A FULLY IMPLICIT STOCHASTIC MODEL FOR HYDRAULIC FRACTURING BASED ON THE DISCONTINUOUS DEFORMATION ANALYSIS

A Dissertation
Presented to
The Academic Faculty

By

William Edmund Morgan

In Partial Fulfillment
Of the Requirements for the Degree
Doctor of Philosophy in Environmental Engineering

Georgia Institute of Technology

December 2014

A FULLY IMPLICIT STOCHASTIC MODEL FOR HYDRAULIC FRACTURING BASED ON THE DISCONTINUOUS DEFORMATION ANALYSIS

Approved by:

Dr. Mustafa M. Aral, Advisor
School of Civil and Environmental Engineering
Georgia Institute of Technology

Dr. Marc Stieglitz
School of Civil and Environmental Engineering
Georgia Institute of Technology

Dr. J. Carlos Santamarina
School of Civil and Environmental Engineering
Georgia Institute of Technology

Dr. Turgay Uzer
School of Physics
Georgia Institute of Technology

Dr. Haiying Huang
School of Civil and Environmental Engineering
Georgia Institute of Technology

Date Approved: November 5, 2014

ACKKNOWLEDGEMENTS

First and foremost, I would like to thank my advisor, Prof. Mustafa Aral, for his support and guidance throughout this whole process. His door was always open, and he never failed to encourage me, even when I couldn't see how everything was going to work out. Many, many thanks.

Additionally, I would like to thank the members of my thesis committee, Prof. Haiying Huang, Prof. J. Carlos Santamarina, Prof. Marc Stieglitz, and Prof. Turgay Uzer, for their helpful comments over the years. There was a lot that I didn't know about rock, fluid, and fracture mechanics before starting this work, and they helped fill in the gaps. Also, I wish to thank Prof. Hao-Min Zhou from the Math department here at Tech, whose advice and ideas proved instrumental in helping my model converge.

I'd like to thank Dr. Andi Zhang, Dr. Ilker Telci, and Dr. Biao Chang for their friendship throughout our years together in the MESL lab. They showed me what life was like as a grad student and how to navigate the day-to-day in MESL. Additionally, I'd like to thank David Trawick for the multitude of lunches and lively discussions shared throughout the course of our years at Tech. They were good times, indeed.

Additional thanks belong to the many members of my church family at Skyland Church here in Atlanta. They supported and prayed for me throughout this journey, and they were with me through both the good times and the bad. Particular mention goes to Andy Hammer, Matt Morton and Tiffany Morton, who were always there when I needed a break from research.

One more note of thanks goes to my parents, who supported me through this process in a variety of ways, most notably by helping to take care of my daughter after she was born. The childcare, as well as the free meals, prayers, and advice they provided were all very much appreciated. Additional thanks belong to my wife's parents, who also contributed greatly to childcare and added their own share of delicious food to the endeavor. Again, many thanks.

Finally, I'd like to thank my beautiful wife, Jenny, for her years of supporting me through this process and encouraging me to stick with it. She is funny, brilliant, and all-around amazing, and without her I'd have quit years ago. Special thanks as well to my daughter, Wren, because she's adorable and awesome. Final thanks belong to God, who despite my many (many) complaints over the course of my dissertation, never abandoned me. "If we are faithless, He remains faithful, for He cannot deny Himself (2 Tim. 2:13)." Hallelujah!

TABLE OF CONTENTS

LIST OF TABLES

LIST OF FIGURES

LIST OF SYMBOLS

Symbol	Dimensions	Meaning
A	-	Matrix of pressure coefficients
A	$[L^2]$	Block area
a	[L]	Fracture half-length
B	-	Vector of terms in fluid matrix equation
C	$[MT^{-1}]$	Mass injection rate
C_0	$[ML^{-1}T^{-2}]$	Cohesive strength,
c_f	$[M^{-1}LT]$	Fluid compressibility
C_L	$[LT^{-1/2}]$	Carter's leakoff coefficient
D	-	Vector of displacement and deformation unknowns in the DDA
d	[L]	Penetration distance
d_0	[L]	Maximum separation distance for hardening
d_c	[L]	Maximum separation distance for softening
dt	[T]	Time step
dx	[L]	Mesh discretization
E	$[ML^{-1}T^{-2}]$	Young's modulus
$\tilde{\mathbf{E}}$	-	Matrix of material constants
F	-	Vector of resultant general forces
f	[-]	Dimensionless function
F_n	$[MLT^{-2}]$	Normal force
F_s	$[MLT^{-2}]$	Shear force
G	$[MT^{-2}]$	Strain energy release rate
G_c	$[MT^{-2}]$	Critical strain energy release rate
h	[L]	Fracture depth
i	-	Index variable
j	-	Index variable
K	-	Stiffness matrix
K	$[ML^{-1/2}T^{-2}]$	Stress intensity factor
k_1	$[ML^{-2}T^{-2}]$	Slope of cohesive zone hardening curve
k_2	$[ML^{-2}T^{-2}]$	Slope of cohesive zone softening curve
K_f	$[ML^{-1}T^{-2}]$	Fluid bulk modulus
K_{IC}	$[ML^{-1/2}T^{-2}]$	Mode I fracture toughness
K_{IIC}	$[ML^{-1/2}T^{-2}]$	Mode II fracture toughness
k_n	$[MT^{-2}]$	Normal spring constant
k_s	$[MT^{-2}]$	Shear spring constant
L	[L]	Fracture length
L	-	Lower triangular matrix
l	[L]	Fracture half-length
L_c	[L]	Contact length
m	-	Iteration counter
N	$[MLT^{-2}]$	Normal force

Symbol	Dimensions	Meaning
n	-	Displacement index
o	-	Displacement index
p	$[ML^{-1}T^{-2}]$	Fluid pressure
$\mathbf{p}$	-	Fluid pressure vector
P	-	Point identifier
p_0	$[ML^{-1}T^{-2}]$	Reference pressure
p_f	$[ML^{-1}T^{-2}]$	Absolute fluid pressure
Q	$[MT^{-1}]$	Flow along a fracture
Q_0	$[MT^{-1}]$	Injection rate at the wellbore
Q_L	$[MT^{-1}]$	Fluid mass leakoff rate
Q_{LV}	$[L^3T^{-1}]$	Fluid volumetric leakoff rate
r	[L]	Radius
r_0	[-]	Rigid body rotation
S	$[MLT^{-2}]$	Shear force
t	[T]	Time
$\mathbf{T}$	-	Displacement transformation matrix
t_0	[T]	Time at which fluid first reaches a node
T_0	$[ML^{-1}T^{-2}]$	Tensile strength
u	[L]	Horizontal displacement in (x,y)-coordinate system
$\mathbf{U}$	-	Vector of horizontal and vertical displacements
u_0	[L]	Rigid body displacement of the centroid along the x-axis
V	$[L^3]$	Volume
v	[L]	Vertical displacement in (x,y)-coordinate system
v_0	[L]	Rigid body displacement of the centroid along the y-axis
w	[L]	Fracture width
w_0	[L]	Initial width
$w_{\min}$	[L]	Minimum fracture width
x	[L]	Coordinate system axis
X	[L]	Fracture length along x-axis
x_0	[L]	Block centroid along the x-axis
y	[L]	Coordinate system axis
y_0	[L]	Block centroid along the y-axis
α	[-]	Propagation angle relative to fracture tips
β	[-]	Angle of fracture orientation to stress axis
Γ	[-]	Normalized fracture half-length
γ_{xy}	[-]	Shear strain
ε_D	[-]	Displacement error tolerance
ε_p	[-]	Pressure error tolerance
ε_{xx}	[-]	Axial strain along the x-axis
ε_{yy}	[-]	Axial strain along the y-axis
ζ	[-]	Dimensionless parameter
η	[LT]	Transmissivity
θ	[-]	Angle
λ_F	[-]	Fluid system stability constant
λ_R	[-]	Rock system stability constant

Symbol	Dimensions	Meaning
μ	$[ML^{-1}T^{-1}]$	Fluid viscosity
ν	[-]	Poisson's ratio
Π	$[ML^{2}T^{-2}]$	Potential energy
ρ	$[ML^{-3}]$	Density
ρ_0	$[ML^{-3}]$	Reference density
ρ_f	$[ML^{-3}]$	Fluid reference density
ρ_r	$[ML^{-3}]$	Rock reference density
σ	$[ML^{-1}T^{-2}]$	Stress
σ_0	$[ML^{-1}T^{-2}]$	Far-field compressive stress
σ_1	$[ML^{-1}T^{-2}]$	Maximum compressive stress
σ_3	$[ML^{-1}T^{-2}]$	Minimum compressive stress
σ_f	$[ML^{-1}T^{-2}]$	Far-field tensile stress
σ_N	$[ML^{-1}T^{-2}]$	Normal stress
τ_f	$[ML^{-1}T^{-2}]$	Far-field shear stress
Φ	[-]	Normalized pressure
ϕ	[-]	Friction angle
ψ	[L]	Fracture length scale
Ω	[-]	Normalized fracture width

SUMMARY

In recent years, hydraulic fracturing has led to a dramatic increase in the worldwide production of natural gas. In a typical hydraulic fracturing treatment, millions of gallons of water, sand and chemicals are injected into a reservoir to generate fractures in the reservoir that serve as pathways for fluid flow. Recent research has shown that both the effectiveness of fracturing treatments and the productivity of fractured reservoirs can be heavily influenced by the presence of pre-existing natural fracture networks. This work presents a fully implicit hydro-mechanical algorithm for modeling hydraulic fracturing in complex fracture networks using the two-dimensional discontinuous deformation analysis (DDA). Building upon previous studies coupling the DDA to fracture network flow, this work emphasizes various improvements made to stabilize the existing algorithms and facilitate their convergence. Additional emphasis is placed on validation of the model and on extending the model to the stochastic characterization of hydraulic fracturing in naturally fractured systems.

To validate the coupled algorithm, the model was tested against two analytical solutions for hydraulic fracturing, one for the growth of a fixed-length fracture subject to constant fluid pressure, and the other for the growth of a viscosity-storage dominated fracture subject to a constant rate of fluid injection. Additionally, the model was used to reproduce the results of a hydraulic fracturing experiment performed using high-viscosity fracturing fluid in a homogeneous medium. Very good agreement was displayed in all cases, suggesting that the algorithm is suitable for simulating hydraulic fracturing in homogeneous media.

Next, this work explores the relationship between the maximum tensile stress and Mohr-Coulomb fracture criteria used in the DDA and the critical stress intensity factor criteria from linear elastic fracture mechanics (LEFM). The relationship between the criteria is derived, and the ability of the model to capture the relationship is examined for both Mode I and Mode II fracturing. The model was then used to simulate the LEFM solution for a toughness-storage dominated bi-wing hydraulic fracture. Good agreement was found between the numerical and theoretical results, suggesting that the simpler maximum tensile stress criteria can serve as an acceptable substitute for the more rigorous LEFM criteria in studies of hydraulic fracturing.

Finally, this work presents a method for modeling hydraulic fracturing in reservoirs characterized by pre-existing fracture networks. The ability of the algorithm to correctly model the interaction mechanism of intersecting fractures is demonstrated through comparison with experimental results, and the method is extended to the stochastic analysis of hydraulic fracturing in probabilistically characterized reservoirs. Ultimately, the method is applied to a case study of hydraulic fracturing in the Marcellus Shale, and the sensitivity of fracture propagation to variations in rock and fluid parameters is analyzed.

1 INTRODUCTION AND LITERATURE REVIEW

1.1 Introduction

Over the past six decades, hydraulic fracturing has emerged as a widely used technique for stimulating wells in unconventional reservoirs. First applied experimentally in 1947 and commercially in 1950, “fracking” has been used to enhance production in over 2.5 million wells, with over a million of those in the United States alone [1]. Worldwide, there are a large number of unconventional reservoirs that may not be produced economically using conventional drilling techniques. These reservoirs, among them tight sands, shales, and coalbed methane deposits, store large quantities of oil and gas that cannot flow due to the reservoirs’ low permeability. Hydraulic fracturing makes production from these formations profitable by increasing their permeability and allowing wells within the formations to produce greater volumes of oil and gas. In the past 15 years in particular, advances in hydraulic fracturing technology and horizontal drilling have led to a boom in oil and gas production throughout the United States. With horizontal drilling, vast areas within a formation may be contacted by a single well, as each well can extend on the order of kilometers along the length of the formation. With traditional vertical wells, however, the area contacted by the well is limited by the height of the formation, which typically ranges on the order of tens to hundreds of meters. Economically, the results of this surge in oil and gas production have been increased wealth, jobs, and more energy independence for the nations developing their unconventional gas resources. In addition, the technology has found additional uses in

geothermal applications, wastewater disposal, and as a tool for measuring reservoir properties, all of which implies that hydraulic fracturing is here to stay.

Hydraulic fracturing of a reservoir begins after a well has been drilled, and steel pipe and well casing have been inserted to protect the overlying formations. The well casing is perforated in the targeted reservoirs, allowing the fracturing fluid to be injected and to contact the gas bearing rock. Eventually, the rate of injection will exceed the rate of fluid absorbed by the rock formation, causing the fluid pressure to build. Once the fluid pressure has reached the breakdown pressure of the formation, the highly pressurized fluid will create new fissures and open pre-existing ones in the impermeable rock. Proppant injected along with the fluid will flow into the fractures, helping to keep them open and maintain their width, while chemical additives help the water and proppant reach the reservoir and penetrate into the formation. In a typical procedure, water makes up 98% to 99% of the fracking fluid mixture, sand or other proppant about 1.0% to 1.9%, and additives make up the remainder of the potentially millions of gallons of fluid injected into each well [1]. Currently, a wide debate is raging as to the impacts that hydraulic fracturing and the associated industry are having on the environment. Below the surface, questions arise concerning the ultimate fate of the injected fluids and concerning the potential for methane and other gases to migrate out of fractured reservoirs. If either the chemicals in fracturing fluid or the gas from targeted formations managed to migrate into drinking water reservoirs during a fracturing treatment, the resulting contamination could prove very detrimental to public health. Additionally, both the injection of fracturing fluid and the re-injection of wastewater are being investigated as sources of increased seismic activity near areas with heavy fracturing. Above the

surface, concern exists regarding the disposal of wastewater, air pollution during the production process, and noise pollution and road degradation caused by the heavy industry associated with hydraulic fracturing. Tying all of these together is the concern for the impacts of these processes on public health.

As fracking and the concerns associated with it have grown more widespread, so too has the need for accurate models of hydraulic fracturing. Historically, modeling hydraulic fracturing has proven to be a very difficult task. A complete model of hydraulic fracturing in its current form requires the coupling of rock and fracture mechanics with the analysis of multiphase fluid mechanics, heat transfer, fluid leakoff and transport dynamics. Adding to the complexity is the inherent uncertainty of subsurface systems, in which stress differentials and natural fractures can lead to very different hydraulic fracture geometries. The purpose of this thesis is to develop a new hydro-mechanical model for hydraulic fracturing that is able to evaluate these uncertainties in a more systematic manner. In particular, this work focuses on the improvement and validation of an existing fully implicit algorithm for hydraulic fracturing, and on the algorithm's extension to the stochastic analysis of hydraulic fracturing in naturally fractured reservoirs. To put the new model into context, this first chapter provides a brief history and review of the hydraulic fracturing models currently available in the literature.

1.2 Planar Analytical and Semi-Analytical Models

Accurate modeling of hydraulic fracturing requires consideration of a few key processes. First, for a purely hydro-mechanical model, a method is required for modeling the deformation of the rock matrix as a response to fluid pressure. Generally, it is

assumed that the matrix deformation is linear elastic, such that linear elastic fracture mechanics (LEFM) can be used to describe the distribution of stress and displacement around the fracture. Second, a fracture propagation criteria needs to be included to account for the formation of new fractures within the system. In typical hydraulic fracturing models, fracturing of new rock is considered to occur in Mode I only, although in hot dry rock geothermal modeling, Mode II fracturing is considered the dominant mechanism (Figure 1.1) [2]. Third, fluid mechanics must be considered, either within the fractures alone, or as a combination of flow within the fractures and flow within the rock matrix. For flow within the fractures, Reynold's lubrication equation and fluid continuity are generally used. For flow in the rock matrix, Darcy flow and fluid continuity are used for the fluids, while Biot's poromechanics equations are used to model the rock matrix's response to the fluid pressure. Introducing the next level of complexity adds proppant into the model and requires the analysis of proppant transport, its effect on fluid flow and the effects of the proppant on fracture deformation. Typically, it is assumed that the fluid-proppant slurry behaves as one fluid for transport modeling, such that the viscosity and physical properties of the combined mixture are used to solve the mass and momentum

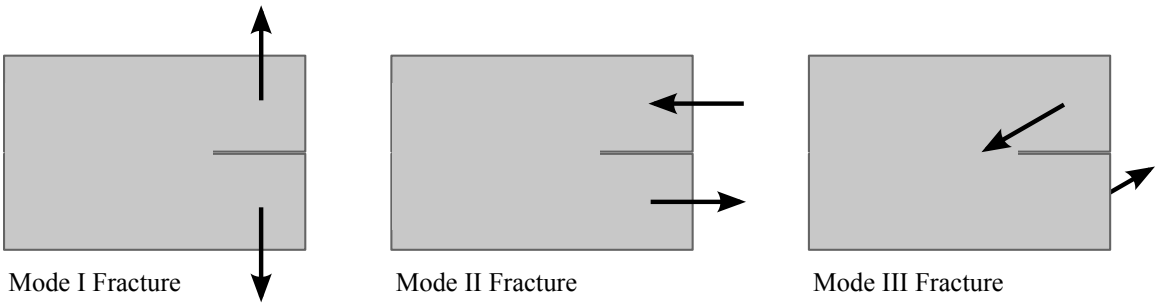

Figure 1.1: Fracturing Modes. Mode I fractures occur in tension, while Modes II and III occur in shear. Mode II fractures are defined as in-plane shear fractures, while Mode III fractures occur out of plane.

continuity equations, rather than just the properties of the original fluid [3]. Finally, chemical and heat processes may be added in, in particular when looking at fracturing models for waste storage or geothermal production. The complexity of the model and its solution are directly dependent on the dimensionality of the original problem, the number of processes modeled, and the level of detail being considered.

Due to the complexity of considering all of these processes, most models rely on a number of simplifications. The earliest models for hydraulic fracturing considered only the elastic response of the rock matrix to fluid pressure, and are based on the assumption of a bi-wing fracture propagating symmetrically away from an injection well. Each of these models finds its roots in fracture mechanics problems from LEFM [4]. For a reservoir with known Young's Modulus (E), Poisson's ratio (v) and far-field stress (σ_0) perpendicular to the fracture, their goal was to determine the geometry of the fracture subject to a given fluid injection rate (Q_0) or pressure at the wellbore (Figure 1.2). The first of these models was introduced by Khristianovich and Zheltov [5] and later expanded on by Geertsma and de Klerk [6], and is often referred to as a 'KGD fracture' in their honor. In the KGD model, plane strain conditions are assumed to exist in the horizontal plane perpendicular to the injection well. The hydraulic fracture is assumed to be of uniform width along the height of the fracture and is assumed to propagate within a two-dimensional (2D) plane. Generally, the KGD model is suitable for situations in which the height of the fracture is significantly greater than its length. The KGD model assumes constant pressure along the length of the fracture except at the fracture tip, giving the fracture an elliptical cross section plane perpendicular to the well. At the fracture tip, the pressure is artificially set to zero to account for both the no flow-

condition out of the fracture and for the stress singularity that arises when modeling a fracture using LEFM. In the vertical plane, the fracture is assumed to have a rectangular cross section. Daneshy [7] later extended these results for the case of power-law fluids, or fluids for which shear stress is not directly proportional to shear rate.

A second analytical solution was developed soon afterward by Perkins and Kern [8], and later expanded on by Nordgren [9], and is referred to as a 'PKN fracture' in their honor (Figure 1.2). For a PKN fracture, plane strain conditions are assumed in the vertical plane, parallel to the injection well. Fluid pressure is constant in the vertical cross sections perpendicular to the direction of fracture propagation, giving the vertical cross sections an elliptical shape with maximum width in the center. Along the direction of propagation, the pressure is a function of the fracture width and falls off at the fracture tip. The PKN model is appropriate when considering a fracture with a significantly larger horizontal extent than height. A third analytical solution investigated by numerous authors ([6, 8, 10, 11]) is that of a radially symmetric fracture, also called a penny-shaped fracture (Figure 1.2). The analytical solutions for penny shaped fractures are generally

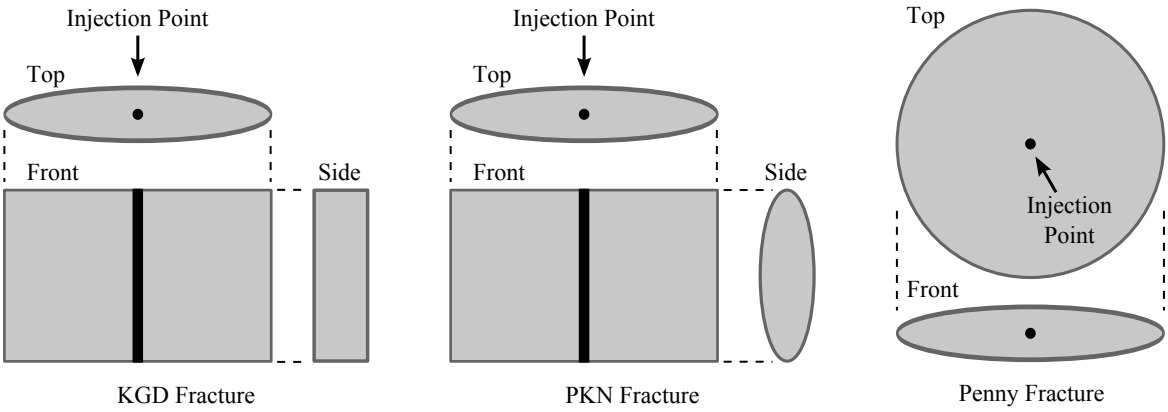

Figure 1.2: Hydraulic fracture geometries for the first-generation analytical solutions.

applicable when the fracture medium and stresses surrounding the injection well are homogeneous, and when the size of the fracture is small relative to the size of the formation. Additionally, penny shaped fractures can occur when the hydraulic fracture occurs near the ground surface, where the primary compressive stress is horizontal. Together, these models represent the most basic descriptions of hydraulic fracturing, and are also the most easily solved. The assumptions required to generate these models, however, are frequently too limiting to allow for their use in actual design problems.

Various authors have sought to make these analytical solutions more rigorous by incorporating additional phenomena into the models. An initial (and ongoing) area of research in this direction has been better characterization of the processes occurring near the tips of hydraulic fractures. Interest in this region developed through the consideration that the fluid pressure changes most rapidly near the tips of propagating fractures, due in part to the square root singularity that occurs in the rock's stress field at the fracture tip. Desroches et al. [12] developed an initial solution for the width and pressure near the tip of the fracture in the case of no fracture toughness and no fluid leakoff, when viscosity effects dominate the rate of propagation. Using the lubrication equations for a power-law fluid, they found that the stress singularity at the fracture tip for a propagating hydraulic fracture is weaker than the classical inverse square root stress singularity predicted at fracture tips by LEFM. They denote their solution as an intermediate asymptotic solution, applicable in the region in between the main body of the crack and the fluid lag zone that may develop at the crack tip. Lenoach [13] extended this solution by adding in leakoff. He found that near the crack tip, leakoff processes will dominate and cause a stronger pressure and stress singularity than in the impermeable case, though still weaker than that

obtained by classical LEFM. Garagash and Detournay [14] added in the effects of fracture toughness and fluid lag. They found that in the presence of fluid lag, the inverse square root stress singularity at the crack tip predicted by LEFM is restored. For small values of toughness, the LEFM solution is contained fully within the lag, while at larger values it can extend beyond the fluid lag. As the fracture grows to infinity, however, their solution becomes independent of toughness and converges to the zero-toughness solution from [12]. As a final addition, Detournay and Garagash [15] extended [14] to account for porous flow in the rock matrix, which can be used to set the proper boundary conditions for pressure at the fracture tip, and derive the conditions under which cavitation might take place ahead of the propagating fracture.

A second area of research has been the characterization of dimensionless groups to generalize the solution of hydraulic fracturing problems. Spence and Sharpe [16] pioneered this effort by developing self-similar solutions for penny shaped and KGD fractures that incorporated the fracture toughness of the rock matrix and allowed the results to be given in terms of dimensionless parameters. Their work paved the way for a large set of studies that sought to characterize hydraulic fracture propagation using dimensionless parameters under a variety of propagation regimes. Using this idea, Hu and Garagash [17] outlined four asymptotic regimes for hydraulic fracture growth based on competing regulatory mechanisms. The first mechanism is based on the manner in which energy is dissipated during fracture growth. As the fracture propagates, energy can be lost both by fracturing of the rock matrix and through viscous dissipation within the fracturing fluid. When fluid viscosity is high and fracture toughness is low, energy is lost primarily to viscous dissipation within the fluid. Conversely, when fluid viscosity is low

and fracture toughness is high, most of the energy is spent fracturing the rock. The second mechanism is based on conservation of fluid mass. As the fracture propagates, fluid can either be stored within the fracture, or it can leak off into the rock matrix. When the leakoff coefficient of the rock matrix is large, the fracture is leakoff dominated, and fracturing is limited by the rate of fluid leakoff into the formation. When the leakoff coefficient is small, the fracture is storage dominated and all of the fluid stays within the propagating fracture. These competing mechanisms can be conceptualized as shown in Figure 1.3 [17]. Each corner of Figure 1.3 corresponds to an asymptotic regime in which the storage and dissipation mechanisms are dominated by only one process. The solutions for these asymptotic regimes have each been derived by various authors. The storage-viscosity solution (no leakoff, no toughness) was given in [18, 19], the leakoff-viscosity solution (no toughness, infinite leakoff) in [20], the storage-toughness solution (no leakoff, zero viscosity) in [21, 22], and the leakoff-toughness solution (zero viscosity,

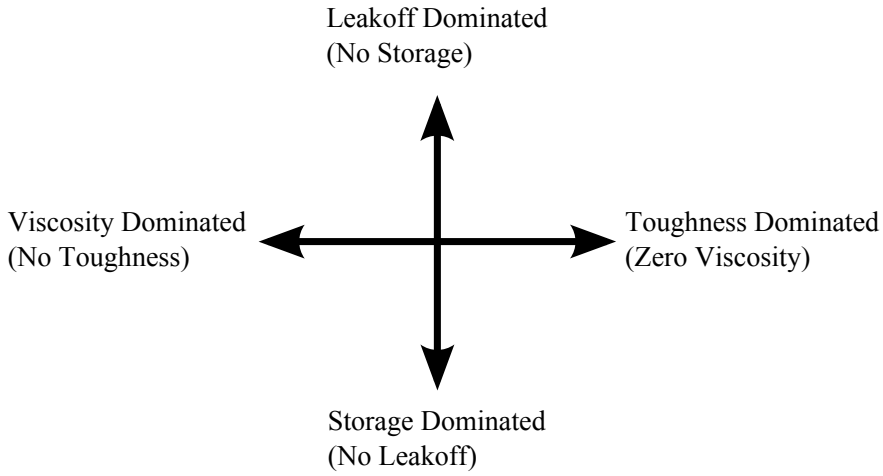

Figure 1.3: Diagram showing the different possible propagation regimes for bi-wing fractures.

infinite leakoff) in [21]. Typical applications of these models include gaining insight into the fundamental mechanisms behind hydraulic fracturing, as well as their use as benchmarks for testing numerical hydraulic fracturing simulators.

1.3 Pseudo-3D and Planar-3D Models

Initially, hydraulic fracturing treatments were small and were used primarily to determine the *in situ* stresses of targeted formations. Hydraulic fracturing to increase well production was not common until the 1960s and was first applied without modeling. Significant increases in well production were observed as a result of fracturing, though proppants would frequently "screen out" and lodge themselves within the fracture, unable to move freely. Proppant transport was soon incorporated into the KGD and PKN models to help characterize this problem, as the incorporation of proppant transport allowed for the calculation of the fluid injection rates needed to prevent proppant screen out. While these models continued to be refined through the 1970s, however, the size of fracturing treatments drastically increased, and it became apparent that new methods were needed to account for conditions encountered in large fracturing treatments [3]. In that decade, the price of gas greatly increased, prompting new research into larger hydraulic fracturing treatments for accessing gas in low-permeability formations. The existing PKN and KGD solutions proved unsuitable for these new treatments, as they did not consider the effects of different layers and confining stresses within the larger reservoirs.

To evaluate the impact of different fracture layers, the PKN model was extended into three dimensions (3D) and developed into the Pseudo-3D (P3D) model. P3D models retain the bi-wing fracture geometry of the PKN model but allow the rock parameters to

vary in layers along the height of the fracture. These models can be used to evaluate the height growth of the fracture in different layers, unlike the PKN and KGD models which assume the height ahead of time. Incorporating different layers into the P3D model changes the cross-section of the fracture such that it will no longer be elliptical. Layers with higher elastic moduli, Poisson's ratio, confining stress, fracture toughness and fluid loss will tend to have narrower cross-sections than layers with lower values of these parameters. Furthermore, large values of these parameters, in particular the confining stress, will lead to shorter fractures, as opening of the fracture requires more energy [23]. Simonson et al. [24] were among the first to capture the effects of multiple fracture layers within a model. They developed a model for fracturing of a three-layered system, in which the top and bottom layers were symmetric. Their work was later extended by Fung et al. [25] for the cases of non-symmetric and multi-layered fractures. The general P3D model was first introduced by Settari and Cleary [26] and later by Morales [27]. A key distinction seen in their work between the P3D models and the PKN model is that the P3D models can account for vertical fluid flow within the fracture. Vertical flow is modeled using pre-defined streamlines for the path taken by the fluid, under the assumption that the fracture length is much greater than its height. Layers are assumed to be perfectly bonded within P3D models, such that shearing between layers is not considered. Generally, P3D models are considered more accurate than their 2D counterparts, and are still solvable within a relatively short amount of time.

The next step in the evolution of planar bi-wing fracture models was the development of Planar-3D models (PL3D), first introduced by Clifton and Abou-Sayed [28]. These models allow for rock property variations along the length and height of the

fracture, using a 2D mesh to solve for the fluid pressure and fracture geometry within the fracture. They allow for a more refined description of the background stresses, and are useful for cases when parameters do not vary monotonically within the same layer. Additionally, situations in which the propagating fracture may result in an hourglass shape, or when the upper and lower layers are less stiff than the middle layers are better suited to a PL3D model [3]. Like the P3D models, rock layers in PL3D models are perfectly bonded and shearing is not considered. Pressure and fracture width are again coupled within these models via the elasticity equation for rock deformation and the equations for 2D fluid flow in a plane. For PL3D models, the fracture system is typically discretized using a mesh of triangles or rectangles which can be fixed, be moving, or be remeshed to track the growth of the fracture. To model the background rock matrix, various options are available. One option is to discretize the matrix into finite elements, which allows for the consideration of heterogeneities in the rock matrix. Use of the fully 3D finite element method (FEM), however, will lead to very large algebraic systems requiring large amounts of computational time to solve. As an alternative, the boundary element method (BEM) may be applied. With this method the elasticity equations are expressed as integral equations over the surface area of the fracture, and are derived as a function of the unknown fracture opening displacements. The integral equations are generally difficult to solve analytically. Instead, they can be discretized as lines (for 2D) or surfaces (for 3D), effectively decreasing the dimensionality of the problem by one and resulting in a much smaller algebraic system than would be generated using the FEM. The computational requirements of the BEM are generally smaller than those for the FEM. The only caveat is that the BEM tends to result in a fully populated elastic stiffness

matrix, while the matrices developed using the FEM are relatively sparse. The vast majority of the PL3D methods developed though the 1980s used the boundary integral technique to solve the equations of elasticity [23].

Among the models that rely on moving meshes or remeshing, Advani et al. [29] generated a moving mesh PL3D model that solves for multi-layered crack growth using the superposition of solutions from a bi-layered system. The number of nodes in the mesh in their system remains constant, but the mesh is allowed to deform at a rate that balances the fluid pressure in the fracture with the amount of energy required to move the fracture forward. A limitation of their bi-layered superposition method is that the layers must be around the same size for the model to function correctly. Siebrits and Pierce [30] developed a planar 3D model that relies on a fixed rectangular mesh, allowing for efficiency in computation time in comparison with moving mesh methods. Their algorithm keeps track of the fracture geometry by assigning one of six different geometry flags to each mesh cell, corresponding to whether or not the cell is fractured and if so, at what angle each cell is fractured. Fluid flow is not specifically considered, but rather a constant pressure is prescribed on the interior of the fracture. A useful feature of their model is its flexibility in dealing with layers of varying thickness, in that very thin layers can be placed next to very thick layers without leading to loss of convergence. A more recent example of a PL3D model, along with a useful literature review of these and other planar hydraulic fracturing models, may be found in [3]. Additional descriptions and comparisons of 2D, P3D and PL3D models may be found in [31].

1.4 Fully 3D Models

Up to this point, all of the models discussed have considered only fracture propagation within a specific plane, ignoring any processes occurring within the rock matrix and ignoring the potential for the fracture to propagate out of plane. The assumption of a perfectly planar fracture is valid when the hydraulic fracture is initialized and propagates perpendicular to the direction of minimum confining stress. In many applications, however, drilling a well can modify the local stress field within a reservoir. Fractures initiated from these wells will initially propagate away from the well in one direction, then turn to align themselves with the minimum confining stress once they have escaped the modified stress field. If the fracture turns too sharply or becomes too tortuous, the flow of proppant can become hindered in the near-well region and the well's productivity can be significantly impaired. This phenomenon is observed particularly with deviated well bores. To accurately model fracturing from deviated wells, and to understand the effects of heterogeneities in the rock matrix and the physics of non-planar fracture growth, various authors have developed fully 3D simulators for hydraulic fracturing. In the literature, many of the models labeled as 3D models are in fact either P3D or PL3D models, so some care must be taken in their classification.

Cleary et al. [32] developed one of the first models to consider three dimensional fractures, using a boundary element representation for the elasticity equations. A key novelty of their work was the development a numerical technique for solving the 3D form of these equations. Fluid flow within the fracture was considered using a 2D finite element mesh. At the fracture boundaries, the authors simplified the problem by defining a process zone of fixed length at the fracture edge, which they use to derive relationships

for flux and pressure gradient at the fracture edge. Fracture propagation is then determined by simple mass conservation of the fracturing fluid. Lam et al. [33] validated the model against the PKN solution and against a laboratory example of fracturing in a cement specimen with regions of varying confining stress. The capability of the model to consider field applications was demonstrated by simulating a fracturing treatment using high-viscosity fluid over several hundreds of feet, though the ability to model out of plane effects was not explicitly demonstrated.

Vandamme's model [34, 35] was one of the first models to account for a completely arbitrary fracture geometry. Elasticity was modeled using the displacement discontinuity (DD) technique, which is a special form of the boundary integral method. With the DD technique, a fundamental solution is used to describe the state of stress at a point in an infinite medium occurring as a result of a unit strength DD. The fracture can be considered as a series of unknown DDs, and the principle of superposition can be applied to evaluate the stress field in the elastic medium as a function of those unknowns. The equations for fluid flow were not discretized in time, but rather were modeled as always being at steady state as a function of the amount of fluid injected. Fracture propagation was considered by incrementing the fracture geometry, then injecting fluid until the Mode I stress intensity of the fracture matched the critical stress intensity of the rock. Propagation direction was controlled by using the maximum circumferential tensile stress. Using this model, Vandamme simulated the growth of two penny shaped fractures occurring along the same wellbore and found that the fluid pressures were larger and the widths at the wellbore smaller than would have been predicted by a single fracture.

Sousa et al. [36] examined how power-law fluids affect 3D fractures. Elasticity was considered using the BEM, while fluid flow was modeled using the FEM. An effective viscosity was used to model the power law fluid. The model begins by considering the solution for a Newtonian fluid, then iterates over pressure, flow rate and effective viscosity until convergence is reached for the non-Newtonian fluid. They provided numerous examples using their model, two of which bear mention here. In the first, they modeled an elliptical crack propagating at an angle of 75° to the principal stresses. As the fracture propagated, it quickly distorted to realign itself planar to the minimum principal stress. In the second, they compared the results of using a Newtonian fluid with those of a power-law fluid in a small well perforated at four locations. They found little difference between the results for the Newtonian and the power-law fluid, due to the small flowrates used in the simulation. They speculated that for higher flowrates and larger fractures, the type of fluid may prove more significant.

Carter et al. [37] developed a fully 3D fracturing model to examine near-wellbore dynamics by coupling the FRANC3D fracturing model with an in-house fracture flow solver. FRANC3D is a fracture mechanics code capable of solving multiple non-planar fractures in complex structures. For speed, the software uses a boundary element method similar to that used by Vandamme [35]. In their method, an influence matrix is generated to describe the response of the overall structure to both the background stress and changes in fluid pressure. As opposed to the fixed and moving mesh methods typically used for fracture propagation, which propagate as a function of injection pressure, FRANC3D models fracture growth by first adding extra elements to the edges of the fracture, then by solving for the amount of injected fluid corresponding to the new

fracture geometry. In addition to the regular lubrication equations for fluid flow, they extended the linear elastic hydraulic fracturing solutions developed by the SCR Geomechanics group [38] and implemented them at the fracture front. Using this model, Hossain and Rahman [39] performed parametric studies of fracture growth near perforated wellbores. They found that fractures initiated in non-preferred directions relative to the background stress field will quickly deviate out of plane, and that well perforations in non-preferred directions will lead to fracture twisting and turning. Additionally, they found that the initiation of multiple fractures along the wellbore will lead to higher treating pressures and reduced fracture volume relative to single fractures, and that multiple fractures can be generated at the base of the same perforation. As a result, the well trajectory and the perforation directions must be optimized to avoid treatment failures resulting from fracture twisting and turning.

1.5 Reservoir and Poroelastic Models

Beyond examination of the fracture itself, many attempts have been made to model the coupled interaction between the growing fracture and the rest of the reservoir. Generally, coupled reservoir models seek to simulate three distinct stages of well production: 1) the initial generation of the fracture geometry, 2) clean-up of the fracture, and 3) long-term well production. The complexity and computational expense in these models is typically higher than in PL3D models, as in these the rock and fluid mechanics in the reservoir must be modeled directly. Early editions of these models considered conditions in plane strain only, such that the reservoir could be considered as a 2D grid of cells, while flow in the fracture could be considered in one dimension (1D). Their goal

was to simulate hydraulic fracturing in medium- to low-permeability reservoirs, with better accounting for the effects of leakoff into the rock matrix. In these models, stress and strain within the reservoir are governed by Hooke-Biot's law for stresses and strains in poroelastic media, the addition of which changes the response of the rock matrix to the hydraulic fracture. Incorporation of Hooke-Biot's law leads to the following effects: 1) the stiffness of the rock matrix will change with time, due to the difference between reservoir properties when the reservoir is drained vs. when it is full; 2) Mechanical deformation of the fracture will be altered, due to the diffusion of pore pressure; and 3) the apparent fracture toughness of the material can change as a function of the rate of fracture propagation [40].

In the first iteration of reservoir models, the hydraulic fracture was considered as a 2D planar element, while the reservoir was modeled using the BEM. Hagoort et al. [41] developed one of the first reservoir models for hydraulic fracturing. In their model, pressure in the fracture was treated as a constant, while pressure in the reservoir varied along a rectangular grid. The elasticity equations were treated in a manner similar to that used in the 2D analytical solutions, and were not explicitly solved within the reservoir. Hagoort et al.'s method relied on an iterative coupling between the reservoir flow equations, the fracture flow equations and the fracture geometry equations which limited the maximum time step allowed. In a later work, Settari [42] extended this model to incorporate heat transfer, two-phase flow, and the presence of other injection and production wells within the reservoir. Nghiem et al. [43] introduced a fully implicit simulator which did not require limitations on the size of the time step. The reservoir flow equations, fluid flow equations and elasticity equations were solved simultaneously

using Newton iterations on a fixed grid. Fracture propagation was required to occur over discrete intervals along the grid, with the assumption that an opened fracture would never close once the hydraulic fracture had propagated into it. Boone and Ingraffea developed a 2D reservoir model which emphasized numerical efficiency using partitioned methods [40]. They applied an explicit dynamic relaxation method to solve the finite element equations of poroelasticity along with an implicit, tri-diagonal solver for the fluid flow equations. Addition of a variable time step option allowed for optimal time steps to be selected, again reducing computation time. Increasing in complexity, Ji et al. [44] developed a reservoir simulator which fully discretized the reservoir using FEM. Their model coupled finite difference multi-phase fluid flow in the reservoir with a 3D finite element geomechanical simulator. Coupling between the two simulators occurred through the porosity and flow properties of the reservoir. Their model considered multiphase flow through the use of the extended black-oil model, which incorporates equations for water, an oil phase and a gas phase to represent the composition of the reservoir fluid. The applications in their work included a waterfrac simulation within 16 different layers, three of which were overburden, three underburden, and the rest were pay zones.

Outside of the reservoir models mentioned, various authors have applied poroelastic effects to smaller 3D models to better understand the physics of hydraulic fracture formation. Ghassemi et al. [45] developed a 3D model for hydraulic fracturing which incorporated poroelastic effects to study the potential for rock failure not just at the tip of the fracture, but also in the surrounding vicinity. Rock media was modeled using the BEM, while the FEM was used for flow within the fracture. Using maximum tensile stress and Mohr-coulomb fracture criteria for failure in the surrounding rock, they found

that the dominant failure mode in the area close to the fracture walls will be tensile, beyond which shear failure becomes dominant over a much larger distance. Injection of a more viscous fluid was found to reduce the extent of the failure zone near the fracture, while rocks with higher moduli of elasticity were found to have larger failure zones. Secchi and Schrefler developed a 3D model for hydraulic fracturing in a fully saturated media [46], extended from the 2D model discussed in [47]. Unlike the other methods discussed, their model was not designed for well production, but rather as a general method for modeling the creation of fluid driven fractures. They assume that the media is saturated with the same fluid being used for fracturing, and flow in the media is modeled using Darcy's Law. Fracture propagation in their work occurred using a remeshing strategy, with propagation controlled by a cohesive law similar to that used by Camacho and Ortiz [48]. Rock media was simulated using the FEM. To validate their model, they compared their solution to fracture propagation occurring at the base of a concrete dam as a wave passes over it. They found that the propagation direction of the crack could not be easily predicted, and thus a remeshing strategy is beneficial over the use of a fixed mesh strategy. Li et al. [49] developed a fully 3D model using a parallel FEM solver for the rock media, Darcy flow for the fluid in the mesh and Biot's poroelastic theory for the coupling between them the media and the fluid. Rock failure was modeled using a damage evolution model for failure, based on the maximum tensile stress and Mohr-Coulomb fracture criteria. A benefit of this formulation is that initial fractures do not need to be assumed at the start of the simulation, but rather will develop naturally. Probability was introduced into the model by sampling mechanical parameters for the rock from a Weibull distribution. A key benefit of their work is the use of parallel

processors, which allows them to model very small rock elements over large areas. With very small elements, the number of elements fractured can be treated as representative of the acoustic emissions associated with fracturing [50]. Results from their study were similar to those developed by Hossain and Rahman [39]. They found that both local heterogeneity in the rock matrix and macro-scale stress fluctuations caused by heterogeneity in rock properties are the major cause of twisting and turning of fractures. Increases in fracture tortuosity led to decreases in fracture volume and required higher fluid pressures to continue propagation of the fracture.

1.6 Boundary Element Network Models

A primary limitation of the models already mentioned is their restriction on the number of fractures, as all of the models mentioned focus on at most a few fractures propagating out from a single well. In the field, however, hydraulic fractures can branch, and propagating fractures will frequently intersect existing natural fractures to form complex fracture networks. As these networks can greatly increase the area of a reservoir impacted by a single fractured well, methods are needed to model them. Typically, fracture network models have relied on coupling between a discrete fracture network (DFN) form of the fluid flow equations and either continuous or discontinuous methods for rock mechanics modeling. The nature of hydraulic fracturing precludes the use of a Representative Elementary Volume (REV) for a fully continuous version of the fluid flow equations, as the pathways induced by hydraulic fracture flow can have conductivities orders of magnitude higher than the surrounding rock matrix, making the determination of an REV extremely difficult. Fracture network models can be categorized

based on the number of dimensions considered. Models can range from zero-dimensional approximations borrowing resistance concepts from electrical engineering to fully 3D simulators that attempt to replicate the most prominent features of the coupled system. Most hydraulic fracturing simulators are solved at the minimum using a 2D spatial field, and in most applications, the dimensionality of the fracture network is one less than that of the rock matrix. For example, if the rock matrix is modeled by a 2D finite element mesh, the fractures would be modeled as one-dimensional (1D) channels with varying widths. Similarly, if the rock matrix is considered in 3D, the fracture network would consist of a 2D network of intersecting planes. A side effect of using these smaller dimensions for the fracture network is that the tortuosity of the actual fracture network cannot be captured, although some of its effects may be captured by adjusting the conductivities of the network. As such, the DFN approach used in these models is at best an approximation of the real system.

In many respects, the network flow models are very similar to the previous models discussed. Rock mechanics are typically treated using either the FEM or BEM, although various models based upon discrete element methods (DEM) have begun to emerge. All of the models described in this section are based upon a form of the BEM, which saves computational costs compared to the FEM and DEM at the price of resolution of the stress field in the rock matrix. Mass balance for fluid flow is considered through continuity at fracture junctions, while flow between junctions is described using Poiseuille's Law. A key difference between these models and their predecessors, however, is that network models must account for the interaction of propagating hydraulic fractures with existing natural ones. In particular, the model must determine if

propagating fractures will cross, arrest or open natural fractures as they are encountered (Figure 1.4). To address this problem, Renshaw and Pollard [51] developed a commonly used criterion for fractures that meet at 90° angles, based on the tensile strength and the coefficient of friction of the natural fracture. Gu et al. [52] later extended this criterion to fractures that meet at non-orthogonal angles. Both criteria were validated experimentally.

Among the various models published, the unconventional fracture model developed at Schlumberger and described in Kresse et al. [53] and Weng et al. [54] is one of the more advanced. Based on the work by Olson and Dahi-Taleghani [55], their model simulates the fracture network using 2D vertical fractures with variable height. For the limiting case of uniform *in situ* stress and constant height, the fractures reduce to those of a PKN model. Otherwise, they are similar to those for a P3D model. Fracture height is evaluated by equalizing the stress intensity factors at the top and bottom of the fractures with the apparent fracture toughness in the vertical direction. Fracture branching is controlled by the intersection criteria developed by Gu et al. [52]. The rock matrix itself is not explicitly modeled, but rather is treated through the elasticity equation as with

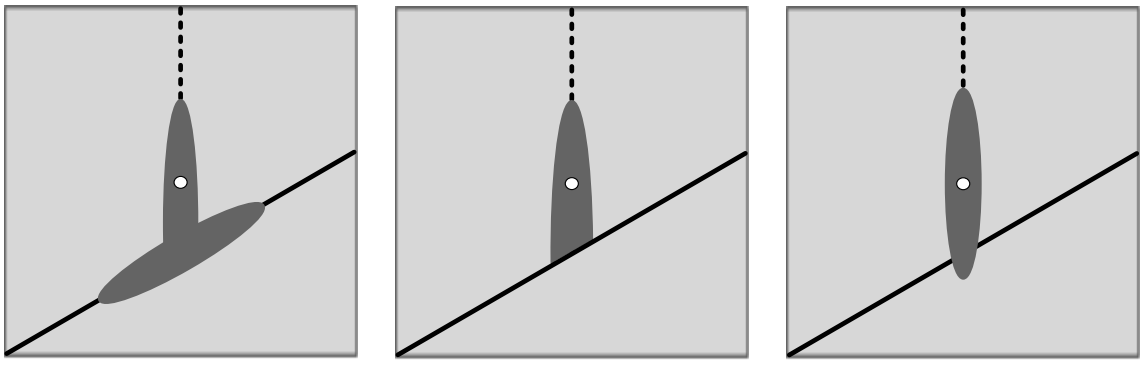

Figure 1.4: Potential interaction modes when a propagating fracture intersects a natural fracture.

simple planar methods, resulting in faster computation times. To account for the changes in rock matrix stress caused by fracturing, they apply the boundary element stress shadow method developed by Crouch and Starfield [56]. The stress shadow method relates the normal and shear stresses acting on one fracture element to the normal and shear stresses acting on all other elements through superposition. In [57], Cipolla et al. demonstrated a workflow for calibrating the unconventional fracture model with microseismic measurements. They found that the complexity of the fractured system is dependent on the stress differential between the maximum and minimum stresses. In their experiments, a stress differential of 500 psi or less resulted in the opening of pre-existing natural fractures, while a stress differential of 1000 psi resulted in a single propagating fracture. Additionally, they found an inverse relationship between the connectivity of the fracture system and the surface footprint of the propagating fracture. As the connectivity of the system increased, the footprint of the fractures decreased as fluid was diverted into natural fractures.

Due to the complexity of modeling fully 3D network systems, many authors use simplified representations of the fractured reservoir to save on computation time. Du et al. [58] introduced a model for network modeling based around the concept of a dual-porosity fracture system. In dual porosity models, fracture networks are approximated by a regularized grid with much higher conductivity than the surrounding rock matrix. Dual porosity models tend to require significantly less CPU time than single porosity models with embedded fractures, but they may struggle to capture the physics of fracture initiation and propagation at non-orthogonal angles or with irregular fracture spacing. Du et al. calibrated their dual porosity model by taking injection and microseismic event data

from a fracturing treatment and using it to generate the model's reservoir properties. They performed a case study of a single horizontal well and used the calibrated model to evaluate the impact of different size proppants on the generated fracture volume. In addition, they performed a sensitivity analysis of rock, fracture and micro-seismic parameters on cumulative well production and found that the degree of fracture connectivity had the greatest impact on well production of the parameters tested. Rogers et al. [59] developed a simplified DFN model for hydraulic fracturing, which eschewed many of the complicated geomechanical relationships discussed previously in favor of computational speed for simulating large numbers of fractures. Their model allowed for the solution of a fully 3D system, with no assumptions placed on the orientation of the fractures. In their model, stress shadow effects are ignored, and fluid flow is governed by a standard transient DFN flow simulation. Fracture volumes are estimated using the elastic solution for elliptical cracks, and fracture propagation into a natural fracture is assigned based on distance from the injection point through the network, the angle of the new fracture with the existing fracture, and the fracture aperture. Fracture propagation into the rock matrix is not considered. The key advantage of their model is its speed, as the examples they considered involved the use of significantly more fractures than those in the other models discussed.

Smith et al. [60] developed a hydraulic fracture model based on percolation theory to examine the likelihood of caprock failure during carbon dioxide sequestration. Flow and geomechanical modeling was performed using the ECLIPSE simulator developed by Schlumberger [61]. ECLIPSE is a poroelastic reservoir simulator based on the three-phase black oil equations. To simulate fracturing, Smith et al. first modeled the

injection of carbon dioxide in a sample aquifer to generate a stress distribution using ECLIPSE. Next, they overlaid a fracture network on top of the distribution and examined if the fractures would fail using maximum tensile strength and Mohr-coulomb fracture criteria. Finally, they evaluated the fracture system to see if a percolating network was produced through the caprock. Probability was introduced by generating numerous fracture networks for each realization of the aquifer stress distribution, and evaluating the number of networks that percolated. A key limitation of this work is that the effects of the fracture network on the system are not incorporated into ECLIPSE. However, their model was capable of evaluating the potential for fracturing in a domain with a depth of 3000 m and a width of 400 km, which represents a domain very much larger than can be reasonably considered with the other network models described in this paper.

1.7 Finite and Discrete Element Network Models

Unlike the previous models, in which the elastic response of the rock matrix was coupled to the fluid pressure through the use of boundary integrals or other methods, the models in this section model the matrix response using discretized elements. These works may be divided into two different types. In the first, the rock matrix is discretized using a continuum representation and is modeled using a form of the finite element method (FEM). In the second, the matrix is discretized using discontinuous elements with a form of the distinct element method (DEM). In the DEM, elements are allowed to deform and separate independent of each other, while unfractured elements are kept together by a series of simple rules. In both methods, fractures may grow only along element boundaries, limiting the potential directions for fracture propagation. One benefit of these

models is that they tend to be partitioned into different solvers, which allows for a degree of interchangeability between the different model components.

Zhang and colleagues [62, 63] used a 2D FEM simulator to examine the different interaction mechanisms that occur when a propagating fracture intersects a natural fracture. In particular, they examined the parameters that influence whether a propagating fracture will cross a frictional confining layer to escape from a targeted reservoir. They found that propagation across interfaces is more likely to occur when the fracture propagates out of a "stiffer" layer with higher Young's Modulus into a "softer" layer with lower Young's Modulus. Additionally, they found that low-viscosity fluids are less likely to penetrate into the confining layer in the case of high *in situ* stress. Dahi-Taleghani and Olson [64] developed a similar model for testing fracture interaction mechanisms. Rather than the regular FEM, however, they used a version of the extended finite element method (XFEM) to allow for fracturing within mesh cells.

Fu and colleagues [65, 66] developed a 2D fully coupled hydraulic fracturing network simulator based around the FEM. Typically, to characterize the stress intensity factors required by LEFM, finite element solvers rely on special quarter-point elements, in which two of the nodes are located not at the midpoint of the element edges, but rather three-fourths of the distance along the open fracture. These elements are limited in their ability to model surface tractions along fractures, and require *a priori* knowledge of the locations of fractures, as discussed in [67]. As such, they are not suited for modeling dynamic hydraulic fracture problems. To overcome these problems, The FEM solver developed by Fu and colleagues uses six node triangular isoparametric elements to discretize the rock matrix with nodes at the endpoints and midpoints along the edges of

the triangles. Fracturing of these nodes is regulated by the stress intensity factor criteria, using the generalized displacement correlation method developed in [67]. The fluid system is discretized into finite volume cells centered at the junctions of fractures. Both the rock and fluid solvers are discretized explicitly in time, requiring the use of small time steps and relatively fine mesh for the rock matrix. Fu et al. validated their model against the KGD solution for fracture growth in a toughness dominated regime, and against the experiments by Blanton [68] for the interaction of a propagating hydraulic fracture with a pre-existing natural fracture. Additionally, they demonstrated the ability of their model to simulate fracturing in a 200 m x 100 m medium with numerous pre-existing natural fractures.

Of the authors who used discontinuous methods, Galindo Torres and Muñoz Castaño [69] developed a 2D model for hydraulic fracturing based upon the explicit form of the DEM. Discretization of the rock mesh was performed using a Voronoi tessellation, which produces irregular-shaped polygons with variable numbers of sides. Fracturing was controlled by the maximum tensile stress and Mohr-Coulomb criteria. Fluid pressure in the fracture was considered using a simplified relationship between the amount of fluid injected and the total volume opened between the rock elements. This pressure was further coupled with Darcy flow to solve for fluid pressure within the rock. The mesh size considered by the authors was fairly coarse, and consisted of a domain of 25 x 25 polygons with an average side length of 2.1 m. Their model was able to capture three different stages of a fracturing simulation, corresponding to the pressure buildup before initial fracturing, pressure drop upon initiation of fracturing, and finally pressure stabilization as the fracture volume grew with a power-law dependence on time. Nagel

[70] developed a 3D hydraulic fracturing simulator based around the DEM, using the commercial software *3DEC*. To discretize the rock matrix, *3DEC* represents the rock domain as an assembly of 3D discrete blocks of varying shape. Discrete fracture networks may be imported into *3DEC* to define blocks around a pre-existing fracture network. All of the equations used for analysis were those already included in *3DEC*. Nagel tested the sensitivity of the rate of tensile and shear fracturing to changes in injection rate and fluid viscosity in a DFN of 350 fractures over a domain of hundreds of feet. He found that increasing the injection rates greatly increased the number of fractures that failed in tension, though it did not have a clear effect on the number of fractures that failed in shear. Increasing the viscosity of the fracturing fluid did not lead to many changes in the number of tensile failures. It did, however, dramatically increase the number of fractures which failed in shear.

A final model under development based on discontinuous methods is the 2D fracturing model developed by Ben and colleagues [71-73]. Their model is based on the implicit form of the distinct element method, called the discontinuous deformation analysis (DDA) [74], which also is the rock mechanics solver used in the current work. The DDA has the advantage of removing the limitation on time step size inherent to the explicit form of the DEM. As a result, it requires fewer time steps to model a given simulation time. However, the computation time required to compute each time step is significantly larger, thus it is not immediately obvious which method will result in faster computation times. The rock matrix in their work was discretized using square elements, with fracturing controlled by the maximum tensile stress and Mohr-Coulomb criteria. Fluid flow is modeled using an implicit finite volume formulation, similar to that in [65].

Like Galindo-Torres [69], they demonstrated the ability of their model to capture three stages of fracturing. Further, they applied their model to a test case of fracturing over a 250 m x 250 m grid and demonstrated its ability to model fracture propagation perpendicular to the direction of minimum *in situ* stress. Some limitations of their model exist, however, which aim to be addressed in the current work. Among these are assumptions regarding the initial state of closed fractures (all are initially opened to fluid), issues concerning the convergence of the algorithm (equilibrium is decided *a priori* after a certain number of iterations), and a lack of verification examples for their solver.

1.8 The Current Model

In this thesis, an algorithm for modeling hydraulic fracturing in complex fracture geometries is presented and verified. The method builds upon the existing methods for modeling hydraulic fracturing with the DDA, using the DDA for consideration of the rock mechanics and a finite volume fracture network model for simulation of compressible fluid flow in fractures. Improvements are made to the fluid, contact and coupling components of the existing algorithm to increase its accuracy and stability, and additional theory is provided to relate the criteria used for fracturing in the DDA with LEFM criteria. Chapter 2 of the thesis provides the model formulation, while Chapter 3 verifies the coupling of the model through comparison with analytical solutions and experimental results for hydraulic fracturing. Chapter 4 relates the maximum tensile stress and Mohr-Coulomb criteria used in the DDA with the LEFM criteria more commonly used in fracturing models and verifies the relationship for hydraulic fracturing through comparison with the semi-analytical solution for bi-wing fracture propagation in

a storage-toughness regime. Chapter 5 demonstrates the statistical application of the model and develops a method for predicting the likelihood of hydraulic fracture propagation to any given location within a reservoir. Finally, Chapter 6 summarizes the findings and implications of this work and provides direction for future research.

2 MODEL DERIVATION

Hydraulic fracturing is a complex process. As mentioned in the previous chapter, accurate modeling of hydraulic fracturing requires the consideration of a few key mechanisms to characterize the coupled rock and fluid system. First, fluid mechanics must be considered, either within the fractures alone, or as a combination of flow within the fractures and flow within the rock matrix. Second, a method needs to be selected for modeling the deformation of fracture walls as a response to fluid pressure, and finally, a mechanism needs to be included to account for the formation of new fractures within the system. In this section, the model used in this work (the HFDDA) is derived in detail. Particular attention is given to the description of each of these processes as they occur in the current model, as well as to the methods used to couple the various processes together.

2.1 Fluid Flow Model

The fluid-flow module in the HFDDA is derived using a finite volume fracture network form of the conservation equations for fluid mass and momentum, and is similar to the method applied by Jing et al. in [75] and Ben and colleagues in [71-73]. The network is comprised of fluid nodes connected by fractures (Figure 2.1), which form the spaces between rock blocks. For a fluid node *i*, conservation of mass is given by the equation

$$\frac{\partial}{\partial t}\left(\rho_i V_i\right) = \sum_{j=1}^{k} Q_{ij} + Q_{L,i} + C_i \tag{2.1}$$

where k is the number of nodes j connected to node i, ρ_i is the fluid density, V_i is the volume of node i, C_i is the mass injection rate, Q_L is the leakoff into the fracture

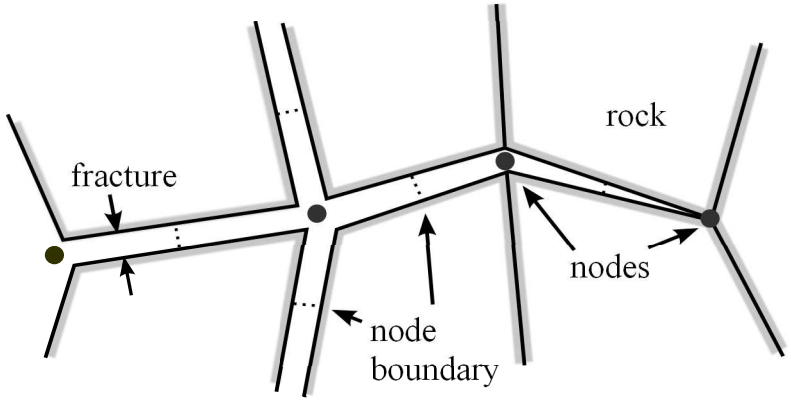

Figure 2.1: Example of fluid and rock system showing components within the HFDDA.

formation, and Q_{ij} is the flow rate along fracture *ij*. For 1D flow, the flow rate along the fracture may be expressed by Poiseuille's Law using the well-known cubic law

$$Q_{ij} = \frac{-\rho_{ij} w_{ij}^3 h_{ij}}{12\mu_{ij} L_{ij}} \left(p_i - p_j \right) = -\eta_{ij} \left(p_i - p_j \right) \tag{2.2}$$

where w_{ij} is the fracture width, L_{ij} is the length, h_{ij} is the depth (equal to unity for plane-strain conditions), μ_{ij} is the fluid viscosity (assumed constant), p_i is the pressure in node *i*, ρ_{ij} is the density in fracture *ij*, and η_{ij} represents the transmissivity of the fracture. The fracture density and fracture widths may be approximated as the average of the densities and widths at nodes *i* and *j*, respectively. Leakoff of the fluid may be expressed using Carter's leakoff coefficient (C_L) and the area opened along the walls of each fracture using the expression

$$Q_{L,i} = -\rho_i \sum_{j=1}^{k} \frac{C_L}{\sqrt{t - t_{0,ij}}} \frac{h_{ij} L_{ij}}{2} = \rho_i Q_{LV,i} \tag{2.3}$$

where $Q_{LV,i}$ is the volumetric rate of leakoff from node *i*, *t* is the simulation time and t_0 is the time at which fluid first arrives at the node from fracture *ij*. Substituting Equations (2.2) and (2.3) into Equation (2.1) yields

$$\frac{\partial}{\partial t}\left(\rho_i V_i\right) = \sum_{j=1}^{k} -\eta_{ij}\left(p_i - p_j\right) + \rho_i Q_{LV,i} + C_i \tag{2.4}$$

Using a forward discretization in time, Equation (2.4) can be discretized as

$$\left(\rho_i V_i\right)^{t+\Delta t} = \left(\rho_i V_i\right)^{t} + \Delta t\left(\sum_{j=1}^{k} -\eta_{ij}\left(p_i - p_j\right) + \rho_i Q_{LV,i} + C_i\right)^{t+\Delta t} \tag{2.5}$$

For compressible flow, fluid density is a function of pressure by the definition

$$\rho_i = \rho_0\left(1 + c_f\left(p_i - p_0\right)\right) \tag{2.6}$$

where c_f is the fluid compressibility, and ρ_0 and p_0 are a reference density and pressure, respectively. Substitution of Equation (2.6) for ρ_i and rearranging yields the final form of the fluid flow equation for each node

$$\begin{aligned}\left(c_f \rho_0\left(V_i^{t+\Delta t} - \Delta t {Q_{LV,i}}^{t+\Delta t}\right) + \Delta t\sum_{j=1}^{k}\eta_{ij}^{t+\Delta t}\right) p_i^{t+\Delta t} - \left(\Delta t\sum_{j=1}^{k}\eta_{ij}^{t+\Delta t} p_j^{t+\Delta t}\right) = \\ \left(\rho_0\left(1 - c_f p_0\right)\left(\left(V_i^{t}\right) - \left(V_i^{t+\Delta t} - \Delta t {Q_{LV,i}}^{t+\Delta t}\right)\right)\right) + \left(c_f \rho_0 V_i^{t}\right) p_i^{t} + \Delta t C_i^{t+\Delta t}\end{aligned} \tag{2.7}$$

Note that this equation differs from the similar equations in [75] and [71, 72], as it accounts for leakoff and uses a fully implicit method to describe the change in pressure resulting from the change in volume of the node itself. For all of the nodes in the fracture system, Equation (2.7) can be rewritten as the matrix system

$$\mathbf{Ap} = \mathbf{B} \tag{2.8}$$

where **p** is the vector of unknown pressures at time $t + \Delta t$, **A** is the matrix of coefficients for the unknown pressure vector, and **B** includes the terms on the right hand side of Equation (2.7). In Equation (2.8), for a given rock geometry, all of the terms in **A** and **B** are known except for the average fracture density ρ_{ij}, which is part of η_{ij} in the matrix **A**, and is dependent on the fluid pressures by the relationship in Equation (2.6). Thus for a

given fracture geometry determined by the DDA, Equation (2.8) must be solved iteratively to reconcile the average densities ρ_{ij} in **A** at time $t+\Delta t$ with the pressures at time $t+\Delta t$.

A question that arose while deriving Equation (2.7) was whether or not the model could be built using an incompressible fluid. For an incompressible fluid, $c_f = 0$ and Equation (2.7) becomes

$$\left(\Delta t\sum_{j=1}^{k}\eta_{ij}^{t+\Delta t}\right)p_i^{t+\Delta t}-\left(\Delta t\sum_{j=1}^{k}\eta_{ij}^{t+\Delta t}p_j^{t+\Delta t}\right)=\rho_0\left(\left(V_i^t\right)-\left(V_i^{t+\Delta t}-\Delta t{Q_{LV,i}}^{t+\Delta t}\right)\right)+\Delta tC_i^{t+\Delta t} \quad (2.9)$$

If the volume of each node remains constant in time $\left(V_i^t = V_i^{t+\Delta t}\right)$ and no leakoff is occurring $\left({Q_{LV,i}}^{t+\Delta t}=0\right)$, the equation becomes the same as that used to solve for flow in pipe networks (e.g., [76]). For pipe network problems, some knowledge of the background conditions at each node is required. First, at every node, either the pressure head or the mass flowrate (into or out of the system) must be known. Second, to solve the system, at least one pressure head must be prescribed. Using the incompressible form of the fluid flow equations for hydraulic fracturing results in the same requirements, and makes the equation suitable for modeling fracturing in an existing pressurized network with a prescribed boundary pressure. Using the compressible form of the equations, however, removes the second requirement, as the system pressure is no longer determined by the *a priori* specification of a boundary pressure head, but rather by the degree of fluid compression at each node. As a result, the compressible form of the equations is more general, as it no longer requires the system to be connected to a pre-existing fracture network. Since many of the examples tested in this work involve the

formation of new fractures in previously intact rock, only the compressible form of the equations is used.

One difficulty that arises when solving Equation (2.8) is that there is no constraint on the pressures in the system to be positive. If the void volume at a fluid node increases beyond the volume of fluid contained within it, the pressure at that node will become negative, a situation which would not happen physically. Two methods were attempted in this work to remedy this problem. First, if a node has a negative pressure in the HFDDA after the solution of Equation (2.8), a zero pressure boundary condition can be assigned to that node, and Equation (2.8) can be resolved. However, to ensure conservation of mass, the amount of fluid that flows into these boundary nodes must also be calculated (Figure 2.2). Returning to Equation (2.7), when a zero pressure condition is assigned to a node, the volume of fluid in the node at the new time ($V_i^{t+\Delta t}$) becomes an unknown variable. Equation (2.7) can be rearranged to solve for $V_i^{t+\Delta t}$, which will then ensure conservation of mass.

A second option for solving the problem is to iterate not just on the volume of the negative pressure node, but rather on the length, width and transmissivity of each fracture

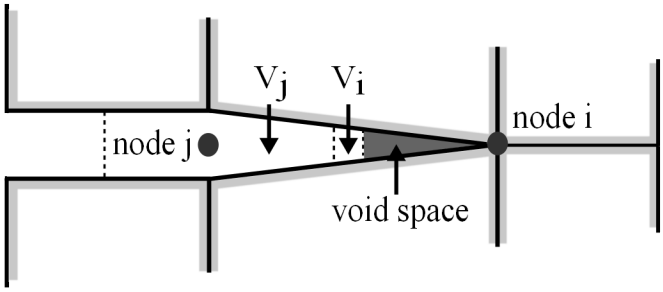

Figure 2.2: Geometry demonstrating the void space and fluid volume at fluid nodes where zero pressure bounds are assigned.

that connects to the node as well. In this method, the tip of the fluid front within each fracture may be tracked more accurately, as the transmissivity and geometry terms in Equation (2.7) would better reflect the volume of fluid actually contained within each fracture. During testing of the algorithm, however, adding in iterations on the transmissivity and geometry terms greatly increased the amount of time required for convergence, without significantly impacting the results. Furthermore, in practice the exact location of the fluid front within each fracture is less important than its location in the overall system. Thus for all of the simulations discussed in this paper, only the first method is used.

Two final aspects of the fluid algorithm also bear mention. First, if a fracture is open to fluid at the end of a time step, that fracture will remain open to fluid throughout the rest of the simulation. To model this process, each fracture is assigned a minimum width ($w_{\min}$) once it has been opened. Physically, this mechanism corresponds to the fact that fractures will be unable to fully close once they have been opened, as a result of roughness generated along the fracture surface when the fracture is first formed. As the overall width of a fracture is calculated using the average of the fracture's width at each end, the width at each end of an open fracture is evaluated separately against the minimum width criteria. Unless otherwise noted, fractures connected to fully open nodes, or nodes with more than two contacts opened, were assigned a minimum width of 0.5 μm. Fractures connected to nodes with only one or fewer nodes opened (corresponding to the fracture tips) were assigned a minimum width of 0.1 μm. Second, to facilitate convergence, the HFDDA requires that fractures close gradually, and that once opened, the width of a fracture may decrease by no more than 5% within each time step. The end

result of these mechanisms is that once a fracture opens, it will remain in contact with the overall fracture network and will never become fully isolated from the main body of the fracture.

2.2 Rock Mechanics Model

For this work, the discontinuous deformation analysis (DDA) was selected to model the rock and fracture mechanics, and was implemented using the open-source software "DDA for Windows" [77]. The DDA is a fully implicit method for analyzing the motion of discrete rock blocks, first developed by Shi in [74]. A review of the theoretical details of the DDA is beyond the scope of this paper, but a summary of the methodology for the two-dimensional DDA, as found in [78], is given here. Similar to the FEM for rock deformation analysis, the DDA solves for deformation and motion of a system of rocks by minimizing the total potential energy of the entire system. As opposed to the continuum representation used in the FEM, rocks are represented in the DDA as individual blocks which are allowed to deform and separate. For a single block, a first order approximation of its displacement can be given by

$$\begin{aligned} u &= u_0 + (x - x_0)\varepsilon_{xx} + (y - y_0)\left(\frac{1}{2}\gamma_{xy} - r_0\right) \\ v &= v_0 + (x - x_0)\varepsilon_{yy} + (y - y_0)\left(\frac{1}{2}\gamma_{xy} - r_0\right) \end{aligned} \tag{2.10}$$

where u and v are the displacements in an (x,y)-coordinate system of the block at point (x,y), u_0 and v_0 are the rigid body motion at the block's centroid (x_0,y_0), ε_{xx} and ε_{yy} are the axial strains in the x and y directions, γ_{xy} is the shear strain, and r_0 is the rigid body

rotation around (x_0,y_0), expressed in radians. In matrix notation, Equation (2.10) may be written for block *i* as

$$\mathbf{U}_i = \mathbf{T}_i \mathbf{D}_i \tag{2.11}$$

where $\mathbf{D}_i^T = (u_0, v_0, r_0, \varepsilon_{xx}, \varepsilon_{yy}, \gamma_{xy})$, $\mathbf{U}_i = (u, v)$, and $\mathbf{T}_i$ is the displacement transformation matrix, which contains the coefficients from Equation (2.10) for each term in $\mathbf{D}_i$. The vector $\mathbf{D}_i$ contains the unknowns for the motion of each rock block *i* and is solved for in each time step. To find them, the total potential energy of the system is minimized, using the equation

$$\mathbf{KD} = \mathbf{F} \tag{2.12}$$

where **D** is a vector containing (6×1) subvectors for the displacement unknowns of each block; **F** is a vector containing (6×1) subvectors of the resultant general forces acting on each block; and **K** is the symmetric positive definite global "stiffness matrix," composed of (6×6) submatrices that correspond to the physical constraints of each block. The on-diagonal submatrices $\mathbf{K}_{ii}$ represent the material properties of block *i*, while the off-diagonal submatrices $\mathbf{K}_{ij}$ $(i \neq j)$ represent the contributions of contacts between blocks *i* and *j*. **K** and **F** are generated by minimizing the sum of all forms of potential energy in the system, including stresses, external or body forces, strain energy, displacement constraints at the block contacts, and so forth. Terms in **K** are generated using the second derivative of the potential energy, while terms in **F** are generated using the negative of the first derivative evaluated at zero displacement. As an example, the potential energy (Π) from strain in each block *i* is given by

$$\Pi = \frac{A_i}{2} \mathbf{D}_i^T \tilde{\mathbf{E}}_i \mathbf{D}_i \tag{2.13}$$

where A is the area of the block at time t, $\mathbf{D}_i$ is the (6×1) subvector of block displacements from time t to time $t+\Delta t$, and $\tilde{\mathbf{E}}$ is a (6×6) matrix of material constants. The second derivative of the potential energy from strain gives

$$\frac{\partial^2 \Pi}{\partial d_{ni} \partial d_{oi}} = \frac{\partial^2}{\partial d_{ni} \partial d_{oi}} \left[\frac{A_i}{2} \mathbf{D}_i^T \tilde{\mathbf{E}}_i \mathbf{D}_i \right] = A_i \tilde{\mathbf{E}}_i; \quad n, o = 1, ..., 6 \tag{2.14}$$

where d_{ni} represents the displacement unknown n in block i, and $A_i\tilde{\mathbf{E}}_i$ forms a (6×6) submatrix which is added back into **K**. The first derivative of the potential energy gives

$$-\frac{\partial \Pi}{\partial d_{ni}} = -\frac{\partial}{\partial d_{ni}} \left[\frac{A_i}{2} \mathbf{D}_i^T \tilde{\mathbf{E}}_i \mathbf{D}_i \right] = -\frac{A_i}{2} \tilde{\mathbf{E}}_i \mathbf{D}_i; \quad n = 1, ..., 6 \tag{2.15}$$

which when evaluated at zero displacement $(\mathbf{D}_i = \mathbf{0})$ results in no contribution to **F**. As with the strain energy, every contribution to the total potential energy will generate a term that may be added into the global **K** and **F**, which may then be used to solve the system of displacement unknowns in Equation (2.12) and the displacement of each block in Equation (2.11). For more information on the derivation of each term in **K** and **F**, see [74].

2.3 Contact and Fracture Model

A unique feature of the DDA is the manner in which it simulates contacts between rock blocks. Within the DDA, blocks are not allowed to inter-penetrate, nor are they allowed to be in tension beyond the tensile or the shear strengths of the bonds holding them together. For the DDA, these conditions are collectively referred to as the no-

tension and no-penetration constraints, and can be expressed between two contacting blocks by the expressions [79]

$$\begin{aligned} &\text{No penetration}: \quad N \geq 0 \\ &\text{No tension}: \quad N \leq L_c T_0, \quad S \leq L_c C_0 + N \tan\phi \end{aligned} \tag{2.16}$$

where N and S are the normal and shear forces between the blocks along the contact, T_0 and C_0 are the tensile and cohesive strengths of the contact, respectively, L_c is the length of the contact, and ϕ is the friction angle between the two blocks. For the no-tension constraints, the tensile constraint is more generally known as the maximum tensile stress or Rankine fracture criteria, while the shear restraint is referred to as the Mohr-Coulomb fracture criteria. T_0 and C_0 only exist along contacts that have not yet been broken; if the normal force or shear force exceeds the strength of the bond, the bond breaks and T_0 and C_0 are set to zero.

In the original DDA, these no-tension and no-penetration constraints are enforced using a penalty method (PM). Contacts are represented mechanically by springs (Figure 2.3), which serve to penalize penetration and tension in the solution of the equations of

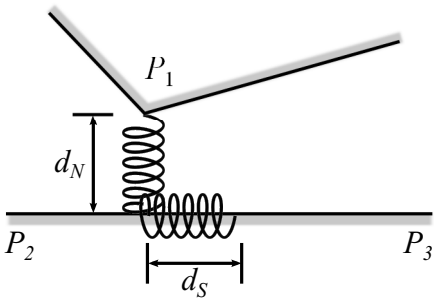

Figure 2.3: Use of springs to represent block contacts in the DDA.

motion. Fracture contacts can have one of three states: locked (normal and shear springs), sliding (normal spring) or open (no springs). To determine which contacts require springs, "open-close" iterations are performed in which springs are systematically applied and removed until the no-tension and no-penetration conditions are approximately satisfied. With the PM, the potential energy from the normal and shear contact springs is given by

$$\Pi_N = \frac{k_N}{2} d_N^2, \quad \Pi_S = \frac{k_S}{2} d_S^2 \tag{2.17}$$

where Π is the potential energy of the spring, d_N and d_S are the normal and shear displacements of the penetration point P_1 along the reference line P_2P_3 (Figure 2.3), and k_N and k_S are the spring constants of the normal and shear springs. To evaluate the no-tension and no-penetration constraints, the contact forces are given by

$$N = \left(\frac{\partial \Pi}{\partial d} \right)_N = k_N d_N, \quad S = \left(\frac{\partial \Pi}{\partial d} \right)_S = k_S d_S \tag{2.18}$$

A key limitation of the PM is that the solution is highly dependent upon the values selected for k_N and k_S. This dependence can be overcome through the use of an Augmented Lagrangian Method (ALM) [79]. With the ALM, forces between contacts are calculated iteratively using the equation updates

$$N^{m+1} = N^m + k_N d_N^m, \quad S^{m+1} = S^m + k_S d_S^m \tag{2.19}$$

where *m* is the iteration counter. As the iteration *m* increases, the influence of the terms $k_N d_N^m$ and $k_S d_S^m$ becomes negligible. The contribution for each contact to the potential energy of the system is given by

$$\Pi_N = N d_N + \frac{k_N}{2} d_N^2, \quad \Pi_S = S d_S + \frac{k_S}{2} d_S^2 \tag{2.20}$$

Incorporation of the normal potential energy terms into the equations of motion (Equation (2.12)) is detailed in [79], while incorporation of both the normal and shear terms is discussed in [80]. More information regarding the original form of the contact constraints and how they are incorporated into the global equations of motion may be found in [81] and [82].

To apply the DDA to hydraulic fracturing simulations, some adjustments were needed in the existing contact algorithm. In their application to the DDA, these adjustments are unique to this work and are specific to the problem of hydraulic fracturing, as they might not apply for general DDA simulations. In particular, they seek to reproduce the Mode I fracture propagation typically observed in hydraulic fracturing experiments. The adjustments include:

i. In LEFM models of hydraulic fracturing, it is generally assumed that fractures will only propagate from pre-existing fractures, rather than forming new nucleation sites within the rock media. Further, in large scale fracturing models, it is typically assumed that any fluid lag between the fracture tip and the fluid is minimal. Thus an added constraint is that locked contacts may only be released if they are connected to an open contact along the same fracture or at the same node, and if they are adjacent to a node that is pressurized. As a result, some fractures may stay closed longer than would be predicted by their tensile or cohesive strengths alone.
ii. Because hydraulic fracturing typically occurs in Mode I, contacts are required to fail in tension before they are allowed to shear. This is accomplished by setting the cohesive strength of every fracture to a very large number. Once the fracture has

failed in tension, the cohesive strength is set to zero and the fracture is allowed to shear.

iii. Occasionally at the tip of the propagating fracture, two or more contacts will fail at the same time in tension. To select the proper propagation direction, the contact with maximum normal stress ($\sigma_N = N / L_c$) is allowed to fail, while the other remains shut. After selection of the propagation direction, another open-close iteration is performed to test for convergence. In the event that the maximum normal stresses are nearly equal, the fracture is allowed to split. In this work, this event was defined as occurring when the maximum stresses were within 0.1 percent of each other.

iv. Because the system is highly compressed, it is not expected that large displacements will occur in the locations of the rock blocks. As a result, the list of potential contacts between blocks is generated only once, and is kept constant throughout the simulation. In the original DDA, the list of potential contacts is refreshed every time step.

v. In the original DDA, contacts were divided into three different types: vertex-vertex, vertex-edge and edge-edge (Figure 2.4). A recognized problem with spring-based

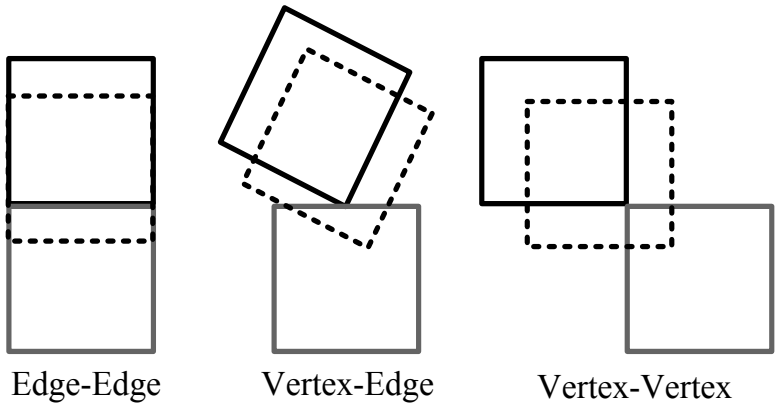

Figure 2.4: Three contact types used within the DDA, in which the upper block penetrates the lower block.

vi. penalty methods is that vertex-vertex contacts can lead to the inaccurate displacement of blocks by requiring the specification of a single reference line for penetration (e.g. [83-85]) (Figure 2.5). Additionally, it was found that unfractured vertex-vertex contacts would frequently struggle to converge when using the ALM, as the penetration distance and force across both reference lines of the contact would be very small. While some efforts have been made to resolve the first of these issues within the DDA by using a trajectory-based method for the initial selection of the reference line ([84, 85]), a fully implicit method for resolving both problems remains elusive. In an effort to minimize these issues, vertex-vertex contacts remain open in the current work until the penetration grows greater than some tolerance, here set at 1 μm. Application of this method requires that the blocks be tightly constrained such that vertex-vertex contacts do not develop independent of other vertex-edge contacts, as is the case in hydraulic fracturing.

vii. In the original DDA, edge-edge contacts are decomposed into two vertex-edge contacts. When the edges share the same endpoints, the springs are divided between

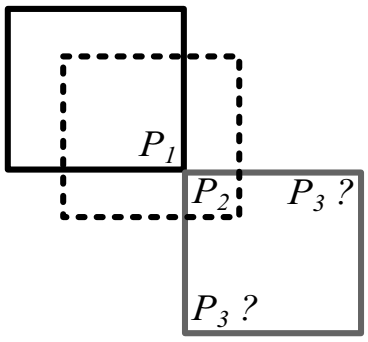

Figure 2.5: Variability of reference line selection in vertex-vertex contacts.

the two contacting blocks, with one spring assigned to each block (Figure 2.6). It was found during testing that using just one spring at each endpoint could cause the fractures to rotate asymmetrically and ultimately lead to the failure of the simulation to converge. A solution for this problem is shown in Figure 2.6. In the new configuration, edge-edge contacts that share endpoints are decomposed into four sets of springs rather than two. To preserve the total energy of the system relative to the original DDA, the energy contribution from each set of springs is averaged. At one vertex-edge pair, the new energy contribution from the normal and shear springs becomes

$$\begin{aligned}\Pi_N &= \frac{1}{2}\left(\Pi_i + \Pi_j\right)_N = \frac{1}{2}\left[\frac{k}{2}d_i^2 + N_i d_i + \frac{k}{2}d_j^2 + N_j d_j\right]_N \\ \Pi_S &= \frac{1}{2}\left(\Pi_i + \Pi_j\right)_S = \frac{1}{2}\left[\frac{k}{2}d_i^2 + S_i d_i + \frac{k}{2}d_j^2 + S_j d_j\right]_S\end{aligned} \tag{2.21}$$

where *i* and *j* are the springs on either side of the contact. The ALM forces are calculated using Equation (2.19) on each individual spring. Using this configuration, the calculation of the contact forces in the no-tension and no-penetration constraints (Equation (2.18)) is modified to become

$$\begin{aligned}N &= \frac{1}{2}\left(\frac{\partial \Pi_i}{\partial d_i} + \frac{\partial \Pi_j}{\partial d_j}\right)_N = \frac{1}{2}\left[k\left(d_i + d_j\right) + N_i + N_j\right]_N \le T_0 \\ S &= \frac{1}{2}\left(\frac{\partial \Pi_i}{\partial d_i} + \frac{\partial \Pi_j}{\partial d_j}\right)_S = \frac{1}{2}\left[k\left(d_i + d_j\right) + S_i + S_j\right]_S \le C_0 + N\tan\phi\end{aligned} \tag{2.22}$$

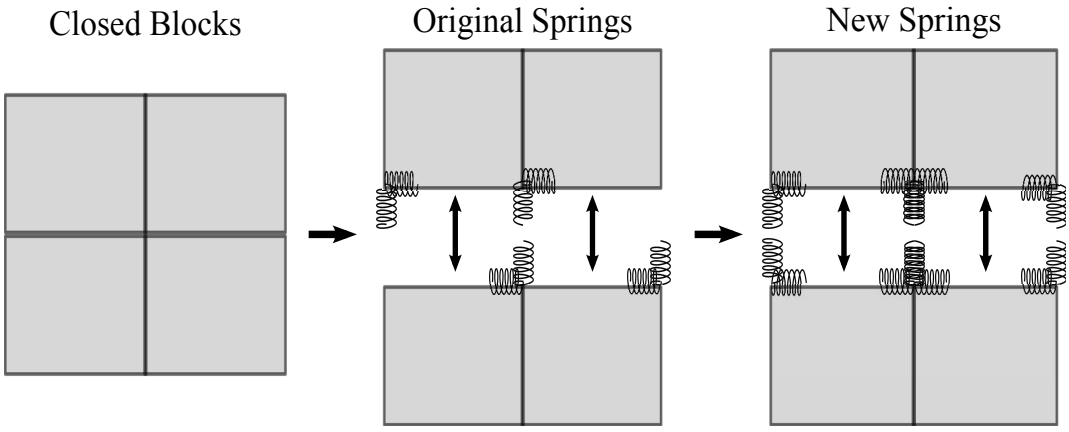

Figure 2.6: Modification of edge-edge contact springs along edges with the same endpoints. The image shows how springs are applied in the original DDA for edge-edge contacts along an unbroken fracture, as well as how they are applied in the HFDDA.

2.4 Coupling Algorithm

In the HFDDA, simulation of the coupled rock and fluid system proceeds in two iterative steps, dubbed inner iterations and outer iterations. Inner iterations are used to solve the global system of equations, while outer iterations are used to resolve the open-close state of the rock contacts and the fractures. Within the inner iteration cycle, fixed-point iterations are used to solve for the rock displacements and the pressure distribution. Fluid pressures are applied to the rock blocks using a trapezoidal pressure distribution [75, 86], which is applied as a single equivalent force onto each rock block adjacent to an open fracture. The applied pressure forces will lead to displacement of the rock blocks, which will cause the geometry of the fracture network to change. New fracture geometries will lead to new estimates of the fracture volume and width, which will in turn cause the pressure distribution to change. The coupling of Equations (2.12) and (2.8) may be expressed by

$$\begin{pmatrix} \mathbf{K} & \mathbf{0} \\ \mathbf{0} & \mathbf{A}\left(\mathbf{D}^{t+\Delta t;\, m}\right) \end{pmatrix} \begin{pmatrix} \mathbf{D}^{t+\Delta t;\, m+1} \\ \mathbf{p}^{t+\Delta t;\, m+1} \end{pmatrix} = \begin{pmatrix} \mathbf{F}\left(\mathbf{p}^{t+\Delta t;\, m}\right) \\ \mathbf{B}\left(\mathbf{D}^{t+\Delta t;\, m}\right) \end{pmatrix} \tag{2.23}$$

where *m* is the iteration counter. The terms in parentheses represent the inter-dependence of the system variables. Due to the highly nonlinear dependence of pressure on displacement, small changes in rock displacement were found to cause wide variation in the system's pressure distribution. Small fracture openings would cause the fluid pressure to become very large, which would lead to wide fracture openings on the next iteration. It was found upon experimenting with the solution of the system that without some form of stabilization, in most cases Equation (2.23) was unable to converge.

To stabilize the system, Equation (2.23) was modified by the addition of stability constants λ_R and λ_F, changing the system to

$$\begin{pmatrix} \lambda_R \mathbf{I} + \mathbf{K} & \mathbf{0} \\ \mathbf{0} & \lambda_F \mathbf{I} + \mathbf{A}\left(\mathbf{D}^{t+\Delta t;\, m}\right) \end{pmatrix} \begin{pmatrix} \mathbf{D}^{t+\Delta t;\, m+1} \\ \mathbf{p}^{t+\Delta t;\, m+1} \end{pmatrix} = \begin{pmatrix} \mathbf{F}\left(\mathbf{p}^{t+\Delta t;\, m}\right) + \lambda_R \mathbf{D}^{t+\Delta t;\, m} \\ \mathbf{B}\left(\mathbf{D}^{t+\Delta t;\, m}\right) + \lambda_F \mathbf{p}^{t+\Delta t;\, m} \end{pmatrix} \tag{2.24}$$

where $\mathbf{I}$ is the identity matrix. When $\mathbf{D}^{t+\Delta t;\, m+1} \approx \mathbf{D}^{t+\Delta t;\, m}$ and $\mathbf{p}^{t+\Delta t;\, m+1} \approx \mathbf{p}^{t+\Delta t;\, m}$, the contribution of λ_R and λ_F to the global solution will cancel out, and the original Equation (2.23) will remain. An additional benefit of the stability constants is that their inclusion can greatly improve the condition number of the matrices **K** and **A**, thus allowing for a more stable iterative solution. This improvement is particularly necessary in **K**, as the DDA is known to suffer from problems of ill-conditioning based on the penalty formulation of the contacts. λ_R and λ_F do not need to remain constant during a simulation, and may be changed if the inner iterations begin to diverge or oscillate.

For the inner iterations, two sets of convergence criteria are employed. The first ensures that the solution in the current iteration is close to the solution to the previous iteration ($\mathbf{D}^{t+\Delta t;\, m+1} \approx \mathbf{D}^{t+\Delta t;\, m}$ and $\mathbf{p}^{t+\Delta t;\, m+1} \approx \mathbf{p}^{t+\Delta t;\, m}$), while the second ensures that each equation is being solved accurately ($\mathbf{KD}^{t+\Delta t;\, m+1} \approx \mathbf{F}$ and $\mathbf{Ap}^{t+\Delta t;\, m+1} \approx \mathbf{B}$). The first set of criteria is given by

$$\left(\frac{\left\langle \mathbf{D}^{t+\Delta t;\, m}, \mathbf{D}^{t+\Delta t;\, m+1} \right\rangle}{\left(\mathbf{D}^{t+\Delta t;\, m} \right)^2} \right)^{1/2} \leq \varepsilon_{D1}, \quad \left(\frac{\left\langle \mathbf{p}^{t+\Delta t;\, m}, \mathbf{p}^{t+\Delta t;\, m+1} \right\rangle}{\left(\mathbf{p}^{t+\Delta t;\, m} \right)^2} \right)^{1/2} \leq \varepsilon_{p1} \tag{2.25}$$

while the second set is given by

$$\left(\frac{\left\langle \mathbf{KD}^{t+\Delta t;\, m+1}, \mathbf{F} \right\rangle}{\left(\mathbf{F} \right)^2} \right)^{1/2} \leq \varepsilon_{D2}, \quad \left(\frac{\left\langle \mathbf{Ap}^{t+\Delta t;\, m+1}, \mathbf{B} \right\rangle}{\left(\mathbf{B} \right)^2} \right)^{1/2} \leq \varepsilon_{p2} \tag{2.26}$$

where in both sets of equations ε_D and ε_p are error tolerances for the displacements and pressures. For each time step, the rate of convergence of the inner iterations was found to be highly dependent on the values of the stability constants. Small values lead to divergence, while large values greatly increase the number of iterations required for convergence, and can even prevent convergence if they are too large. A limitation of the current method is that there is no predefined way of selecting the optimal value for λ_R and λ_F, such that their selection must at first be determined through trial and error.

Figure 2.7 shows a flowchart of the steps involved in the solution of one time step of the coupled solver. Steps 2-8 correspond to the sequence of inner iterations used to solve Equation (2.24), while steps 2, 9 and 10 correspond to the outer iterations. For the inner iterations, a direct LU solver with the Cholesky factorization is used to solve the

rock mechanics equation $\mathbf{KD} = \mathbf{F}$. Because **K** is symmetric positive definite, the matrix can be decomposed into

$$\mathbf{K} = \mathbf{L}\mathbf{L}^{\mathrm{T}} \tag{2.27}$$

where **L** is a lower triangular matrix and $\mathbf{L}^{\mathrm{T}}$ is its conjugate transpose. With the Cholesky factorization, only one copy of the matrix **L** needs to be stored, saving on memory. Additionally, **K** only needs to be factorized once for each outer iteration, as all of the terms in **K** are based on variables at the start of the time step. Factorizing **K** only once saves greatly on computation time, as the equation $\mathbf{KD} = \mathbf{F}$ must be solved anew any time the pressure changes and any time the contact forces are updated. For the fluid equation $\mathbf{Ap} = \mathbf{B}$, similar gains in speed cannot be achieved as the matrix **A** depends on the geometry at the end of the time step and must be refactored after every inner iteration. In the problems tested, however, the speed of the algorithm used to solve the fluid equations proved negligible, as **A** tended to be a very small matrix relative to the size of **K**. For a problem with ~2000 blocks, no more than 100 fractures would typically open, resulting in a $(12,000 \times 12,000)$ matrix for **K**, but no greater than a (100×100) matrix for **A**. Because the size of **A** was so small relative to the size of **K**, the speed of the algorithm used to solve the equation $\mathbf{Ap} = \mathbf{B}$ was not a significant factor in the performance of the overall algorithm.

For the outer iterations, step 9 refers to the DDA's open-close iterations described previously, while step 10 refers to the open-close iterations for the fluid within the fractures. The algorithm for determining if fractures are open or closed for fluid (Figure 2.8) begins with the open-close iterations within the DDA. Each fracture is represented by an edge-edge contact, which may be decomposed into two sets of vertex-edge contacts,

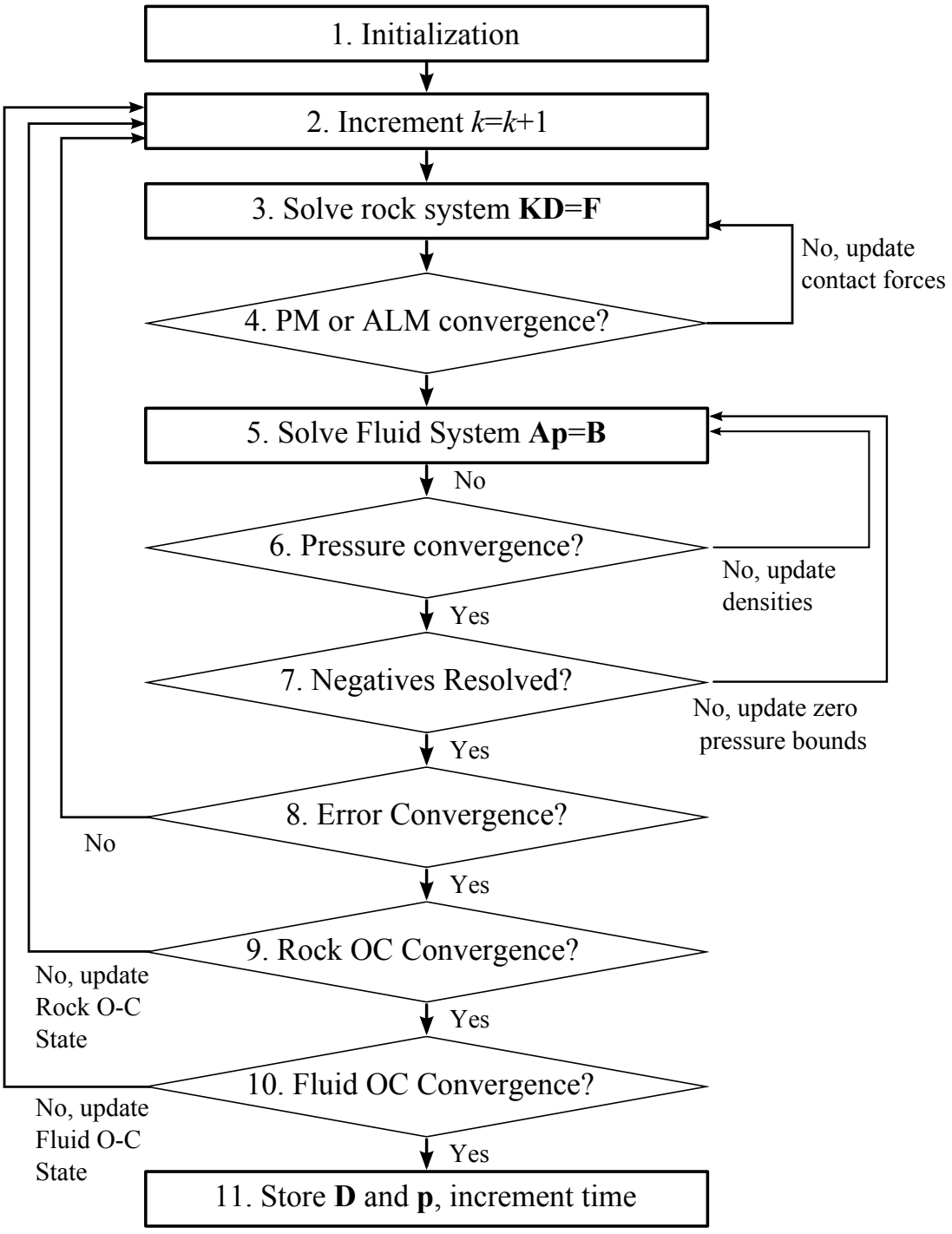

Figure 2.7: Flowchart for solution of one time step of the HFDDA. Steps 2-8 represent the inner iterations of the solution, while steps 2, 9 and 10 represent the outer iterations in which the open-close (OC) states of the rock and fluid are resolved.

one at either end of the fracture. The vertex-edge contacts and the fracture may open independently, such that one end will generally open before the other. If the DDA determines that a vertex-edge contact along a fracture is locked or sliding, then it is assumed to be closed to fluid flow. If the contact is open, then the fracture becomes a potential candidate for fluid flow. Once a fracture has become a candidate based on the DDA, it is next evaluated based on its proximity to the fluid already in the system. At the end of each fracture lies a fluid node, which will either be pressurized or not pressurized, depending on if the fluid has reached that location. Fractures open based on the DDA are included in the solution of Equation (2.8) only if the candidate for opening is directly adjacent to a fluid node that is already pressurized as part of another open contact. Generally, this means that the fluid will propagate until it reaches either fractures that remain locked based on the DDA, or until it leads to negative pressures at the end of a partially-full fracture. Once negative pressures are reached at a fracture tip and a zero pressure condition is assigned, the fluid and fracture cannot propagate from that tip until

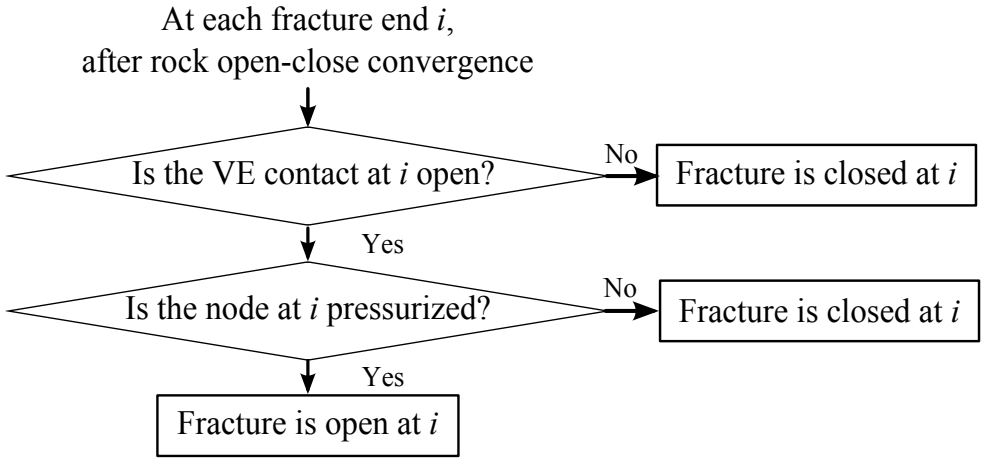

Figure 2.8: Flowchart of open-close selection for fluids in fractures. VE = vertex-edge.

the fracture is fully pressurized and the zero pressure condition is removed. For the outer iterations, convergence is reached when there are no more changes in the open-close state of the block contacts and no more changes in the open-close state of the fluid-filled fractures.

2.5 Model Application

Ultimately, a primary goal of the current work is the development of a model for hydraulic fracturing in reservoirs with pre-existing natural fractures. As will be demonstrated, pre-existing natural fractures can be introduced into the HFDDA both deterministically and stochastically, allowing for the solution of problems in which the fracture location is known with certainty, and for problems in which the fracture characteristics can only be approximated probabilistically. Introduction of a stochastic element into the model allows for a probabilistic assessment of fracture propagation, which in turn will be used to characterize some of the risk associated with hydraulic fracturing. Before diving into the application of the HFDDA to deterministic and stochastic fracture networks, however, the accuracy of the model must first be verified, as will be demonstrated in the following chapters.

3 MODEL VALIDATION

Before the HFDDA can be used to analyze hydraulic fracturing problems, the algorithm must first be verified. In this chapter, the coupling of the algorithm is verified through comparison with different sample problems for hydraulic fracturing. First, the algorithm is compared against the solution for a Griffith crack opening under constant pressure. Second, the algorithm is compared to the semi-analytical solution for a KGD fracture in the limiting regime of no toughness and no leakoff. Third, the method is tested against the experimental results of a fracturing experiment in an impermeable medium. Finally, the logic of the algorithm is examined through a series of numerical experiments which evaluate the model's ability to predict hydraulic fracturing in simple systems.

3.1 Constant Pressure Opening

Before attempting to model a propagating hydraulic fracture, it is worth examining the simpler problem of a Griffith crack of constant length opening under constant pressure (Figure 3.1) [4]. This problem has previously been used by Kim et al. [86] to validate their coupled DDA-fluid flow solver. For this problem, it is assumed that

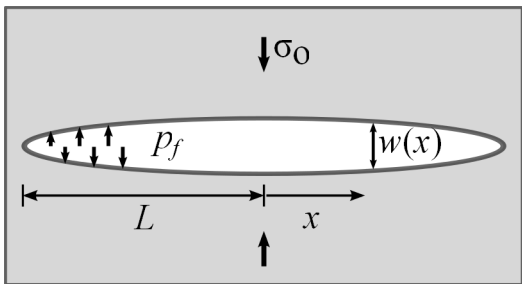

Figure 3.1: Geometry of the constant pressure problem.

the rock is infinite and homogeneous, the system is in plane-strain, and the fluid pressure distribution is constant throughout the length of the fracture. Note that in this problem, the fluid pressure distribution is not a function of time, and thus it is a good benchmark problem for testing the steady-state behavior of the rock mechanics method and the coupling of the fluid solver. It does not, however, provide any information on the transient nature of the solution. At steady-state, the analytical solution for the fracture opening width is given by

$$w(x) = \frac{4(1-\nu^2)(p_f - \sigma_0)L}{E}\sqrt{1-x^2/L^2} \tag{3.1}$$

where w is the fracture opening width, E is the rock modulus, ν is the Poisson's ratio of the rock matrix, p_f is the absolute fluid pressure, σ_0 is the background stress, L is the half-length of the fracture, and x is the distance along the fracture, measured from its center point.

To simulate this problem, an idealization for the rock system was generated consisting of a 36 m x 24 m inner domain contained within a 100 m x 100 m outer domain. A 20 m fracture (L = 10 m) was generated at the center of the domain, with fractures spaced 1 m apart. For this example, two different versions of the geometry idealization were used: one in which the rock matrix was first discretized into quadrilaterals, and one in which those quadrilaterals were further sub-discretized into triangles. In each simulation, a background stress of 5 MPa was applied as force loads along the upper and lower boundaries of the rock matrix, while an internal pressure of 9.81 MPa was assigned to each fluid node within the fracture. Table 3.1 provides the other simulation parameters used in this analysis. In this and all other simulations,

Table 3.1: Constant pressure model parameters

Rock Parameters	
Initial Density, ρ_r	2,650 kg/m^3
Young's Modulus, E	25.0 GPa
Poisson's Ratio, v	0.25 [-]
Fluid Parameters	
Reference Density, ρ_f	1000 kg/m^3
Fluid Bulk Modulus, K_f	2.2 GPa
Viscosity, μ	1 mPa-s
Carter's Leakoff Coefficient, C_L	0.0 m/s
Fracture Parameters	
Friction Angle, ϕ	30.0°
Tensile Strength, T_0	0.0 MPa
Numerical Parameters	
Normal Spring Constant, k_n	100*E
Shear Spring Constant, k_s	100*E
Time Step, dt	1.0 s

background stresses were applied as force loads along the upper and lower boundaries. Each simulation was allowed to continue until the solution reached steady-state, which occurred after two time steps.

Figure 3.2 shows the results of the simulation using different formulations of the geometry idealization and the contact enforcement technique. The first observation from the results of this benchmark problem is that the quadrilateral discretization of the system geometry does not produce the correct fracture opening profile, for both the PM and the ALM case, while the triangular discretization is able to produce the correct profile. A recognized limitation of finite element based methods with linear displacement functions is that quadrilateral or higher-order polygons are unable to resolve correctly the stress and strain within elements [75]. Triangular elements, on the other hand, can correctly resolve the strains. As a result, triangular elements should be used in DDA simulations in which strain is the primary mechanism of rock displacement. For the triangular elements, slight differences were observed between the PM and ALM solutions, but both displayed very

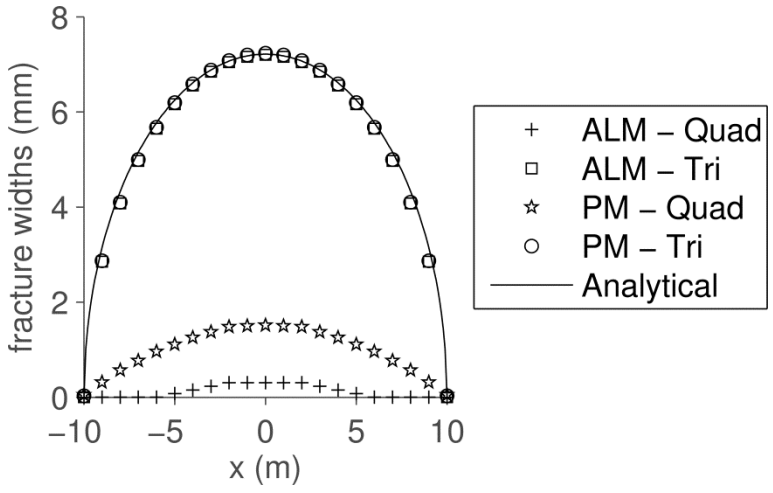

Figure 3.2: Comparison between the HFDDA solution and the analytical solution for fractures widths generated by the constant pressure problem.

good agreement with the analytical solution. The second observation is that the addition of the tolerance for the application of vertex-vertex contacts (item v. of Section 2.3) did not affect the accuracy of the solution. Of particular note is that with the ALM, no vertex-vertex contacts were ever activated. Rather, the normal and shear forces generated by the vertex-edge contacts alone were sufficient to prevent penetration and hold the mesh together. With the PM, however, these forces were not iterated upon and many of the vertex-vertex contacts were activated. These results suggest that when using the ALM, vertex-edge contacts are sufficient to characterize the interior mesh of unfractured rock. With the PM, however, vertex-vertex contacts are required to prevent unrealistic penetration. Based on these results, the ALM was used in the remaining simulations in this work to allow the solution to be independent of the normal and shear spring constants.

3.2 Viscosity-Storage KGD Fracture

The next benchmark problem selected is that of a bi-wing hydraulic fracture propagating under plane-strain conditions in an infinite homogeneous medium. As mentioned in the literature review, this problem was first analyzed by Khristianovich and Zheltov [5], and later by Geertsma and De Klerk [6], and is typically referred to as a KGD fracture in their honor (Figure 3.3). The solution consists of finding the fracture half-length $l(t)$, the fracture aperture $w(x,t)$, and the net pressure distribution within the fracture, $p(x,t)$ (the difference between the absolute fluid pressure $p_f(x,t)$ and the far field compressive stress σ_0). In this problem, *x* is the distance along the fracture away from the injection point and *t* is the time. The primary processes that govern the development of a KGD fracture include the viscous flow of fluid within the fracture,

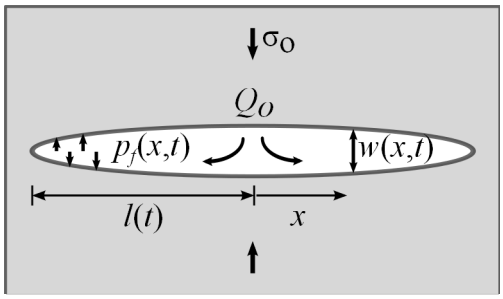

Figure 3.3: Geometry of the KGD problem.

leakoff of the fluid into the rock formation, the propagation of the fracture and the deformation of the rock formation. Using Linear Elastic Fracture Mechanics (LEFM), these processes are found to be dependent on five problem parameters, namely the volumetric fluid injection rate Q_0 and the four material parameters

$$E' = \frac{E}{1-\nu^2}; \quad K' = 4\left(\frac{2}{\pi}\right)^{1/2} K_{IC}; \quad \mu' = 12\mu; \quad C' = 12C_L \tag{3.2}$$

where K_{IC} is the fracture toughness, and the other parameters are as defined previously [17].

Recently, a number of studies have been conducted examining semi-analytical solutions for the KGD problem under varying asymptotic conditions of viscosity, toughness, storage and leakoff (see [17] and references therein). At one extreme, propagation of the fracture is governed by the viscosity of the fluid $(K' \to 0)$, while at the other extreme, propagation is governed by the toughness of the rock matrix $(\mu' \to 0)$. Similarly, fluid volume balance can be governed either by storage within the fracture $(C' \to 0)$ or by leakoff into the rock matrix $(C' \to \infty)$. Four different propagation regimes may be generated from these extremes, as identified in [17]. In each of these

regimes, two of the above four processes are negligible, while the other two dominate their respective mechanisms. For benchmarking purposes, a test of the HFDDA with no leakoff $(C_L = 0)$ and no tensile strength $(T_0 = 0)$ should be comparable to the KGD solution for the limiting case of no leakoff $(C' \to 0)$ and no toughness $(K' \to 0)$ [19]. The HFDDA results can be compared to the semi-analytical solution for half-length of the fracture and the pressure and fracture width at the injection point, all with respect to time. For this problem, the semi-analytical solutions are given by the expressions

$$l(t) = \psi(t)\Gamma(t); \quad w(x,t) = \zeta(t)\psi(t)\Omega(\xi,t); \quad p(x,t) = \zeta(t)E'\Phi(\xi,t) \qquad (3.3)$$

where Γ is the normalized crack half-length, Ω is the normalized crack opening, Φ is the normalized pressure and $\xi = x/l$ is the normalized distance along the fracture. For the no leakoff, no toughness regime, the solutions for Γ, Ω and Φ are each self-similar and may be stated independent of time. At the injection point, Ω takes on the value of $\Omega_0 \simeq 1.8302$ and Φ is given as $\Phi_0 \simeq 0.54495$. For a Newtonian fluid, $\Gamma \simeq 0.61524$. The dimensionless parameter $\zeta(t)$ and fracture length scaling $\psi(t)$ are given by

$$\zeta(t) = \left(\frac{\mu'}{E't}\right)^{1/3}, \quad \psi(t) = \left(\frac{E'Q_0^3}{\mu'}\right)^{1/6} t^{2/3} \qquad (3.4)$$

To model the KGD solution, a rock idealization was generated using a 64 m x 60 m inner domain, contained within a 160 m x 160 m outer domain. Fluid was allowed to propagate up to 24 m along the horizontal fracture leading away from the injection point. For these simulations, it was desired to see how changes to the mesh refinement and the time discretization would affect the HFDDA's ability to reproduce the semi-analytical solution. First, four different mesh discretizations (*dx* = 4.0 m, 2.0 m, 1.0 m

and 0.5 m) were produced, in which the rock mesh along the fracture propagation path was made progressively finer. In each simulation, a fluid injection point was placed at the origin, and a flowrate of $Q_0 = 4.0$ kg/s was applied continuously. To initialize each simulation, the two fractures on either side of the injection point were initially opened. Where applicable, the same physical parameters used in the constant pressure benchmark problem were used here.

The results for p, w, and l from the semi-analytical solution are compared with the values from the HFDDA at different mesh refinements in Figure 3.4 and Figure 3.5. Two different cases are presented. Figure 3.4 shows the results for the case of no background stress ($\sigma_0 = 0$ MPa), while Figure 3.5 shows the results in the presence of background stress ($\sigma_0 = 5$ MPa). For all of these examples, a time step of 0.5 s was used over 10 s of total simulation time. For both cases, when the mesh discretization was fine (dx = 0.5 m), good agreement was observed between the results of the HFDDA and the semi-analytical solution. As the discretization increased in size, however, the results in the absence of background stress continued to show good agreement, but those in the presence of background stress did not. With no background stress, the pressure and width at the injection point matched the semi-analytical solution very well, and the only deviation occurred in the results for the fracture half-length. This deviation results from the fact that fractures can only propagate in discrete intervals within the HFDDA. Thus when the discretization is large, the fracture half-length may increase only in large increments, creating the stair-step pattern observed in Figure 3.4.A. The results do show, however, that even at larger discretizations, the fracture moved forward at the time predicted by the semi-analytical solution. When $\sigma_0 = 5$ MPa , the agreement between the

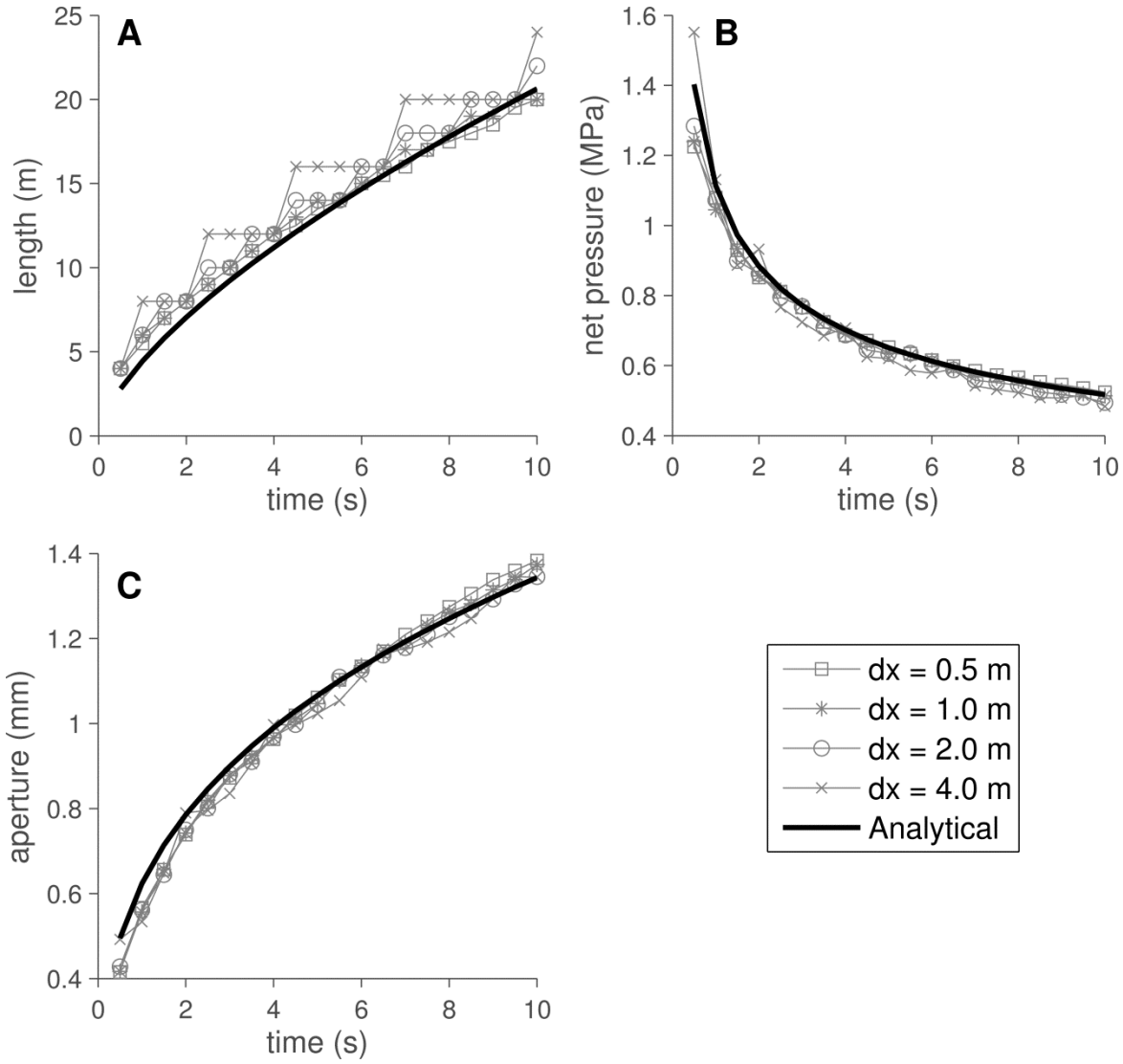

Figure 3.4: Evaluation of the KGD solution for different levels of discretization with no background pressure. **A** shows the half-length of the fracture, **B** shows the pressure at the injection point, and **C** shows the width of the fracture at the injection point.

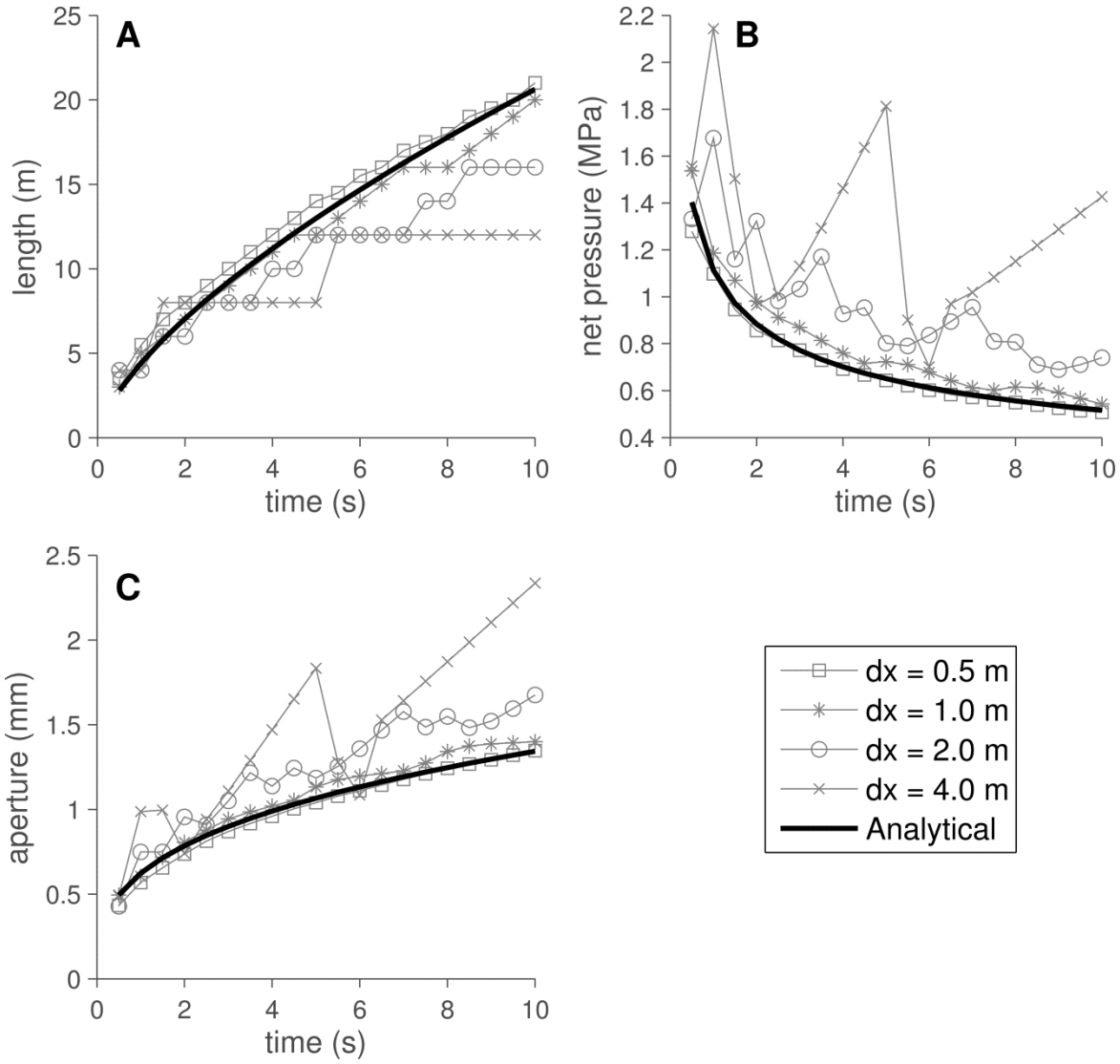

Figure 3.5: Evaluation of the KGD solution for different levels of discretization with background pressure of $\sigma_0 = 5$ MPa . **A** shows the half-length of the fracture, **B** shows the pressure at the injection point, and **C** shows the width of the fracture at the injection point.

HFDDA and the semi-analytical solution worsened as the discretization increased. In this case, the fracture did not propagate as quickly as predicted by the semi-analytical solution. The relative slowness of the propagation caused the pressure and width of the fracture at the injection point to increase beyond the values predicted, with the effect growing worse as the discretization coarsened. Again, the deviation from the semi-analytical solution is a function of the discrete fracture propagation used in the HFDDA. In the presence of a large background stress, the fluid must generate significantly more pressure to overcome the background stress and move the fracture 4.0 m than to move it 0.5 m. When no background stress is applied and the fracture has no tensile strength, no additional force must be overcome in moving the extra distance. Furthermore, in the analytical solution, the additional pressure burden on unbroken fractures from background stress does not appear to be accounted for directly, but instead is only incorporated into the calculation of a net fluid pressure within the fracture. Thus the $\sigma_0 = 0$ MPa solutions show good agreement across a wide range of mesh refinement, while those for $\sigma_0 = 5$ MPa exhibit greater deviation as the mesh refinement grows larger.

Figure 3.6 provides a comparison of the results for *p*, *w*, and *l* from the semi-analytical solution with the values from the HFDDA using different discretizations in time (*dt* = 2.0 s, 1.0 s, 0.5 s and 0.25 s). All of these simulations were performed using a mesh discretization of *dx* = 0.5 m. In general, as the size of the time step increased, the net pressure and aperture at the well bore decreased while the length of the fracture increased. As the time discretization grew, the effect of pressure on the geometry of the fracture was smeared out over a larger time step. As a result, the high pressures observed

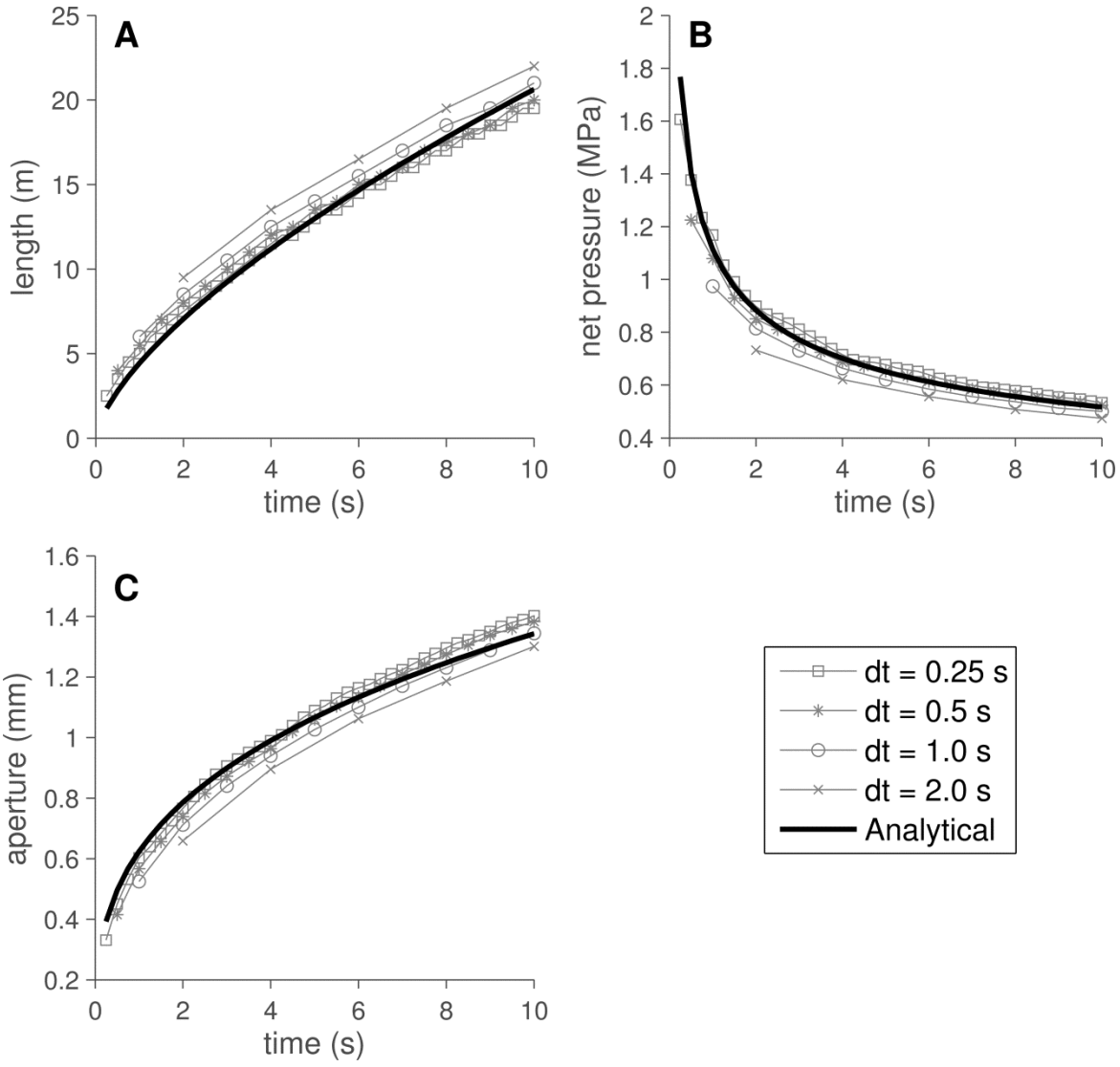

Figure 3.6: Evaluation of the KGD solution using different discretizations of time. **A** shows the half-length of the fracture, **B** shows the pressure at the injection point, and **C** shows the width of the fracture at the injection point.

in the initial time step led the fracture to propagate further than would occur in shorter time steps, in which the pressure and geometry are adjusted more frequently over the same time period. Increases to the length of the fracture led to decreases in the pressure and width, resulting in the trends observed in Figure 3.6. Generally, however, the HFDDA results demonstrated good agreement with the analytical results, with the exception of the largest time step used.

3.3 Experimental Verification in Impermeable Media

To further verify the HFDDA, the model was also compared against the results of a hydraulic fracturing experiment performed by Rubin [87] using a high-viscosity fracturing fluid in an impermeable material. The experimental setup for Rubin's experiment is shown in Figure 3.7. The setup consisted of three layers of polymethyl methacrylate (PMMA) bound together with chloroform, of which the center layer was to be fractured. The chloroform bonding between the layers allowed the center layer to fail in plane strain. A wellbore was drilled into the top and middle pieces, and the well in the top layer was cased with a steel tube of 6.35 mm outer diameter, leaving only the middle layer exposed to the well. Additionally, two 0.56 mm notches were introduced along opposite sides of the borehole, such that the fracture would begin propagating along the longitudinal axis of the layer. For injection fluid, Rubin used high-viscosity Dow Corning 200 silicone fluid that had a kinematic viscosity of 100,000 centistokes. The high viscosity fluid allowed the hydraulic fracture to propagate quasi-statically. Within the center layer, pressure gauges were installed at points A, B and D, and an additional gauge was included at point E, from which the pressure in the borehole (point F) was derived.

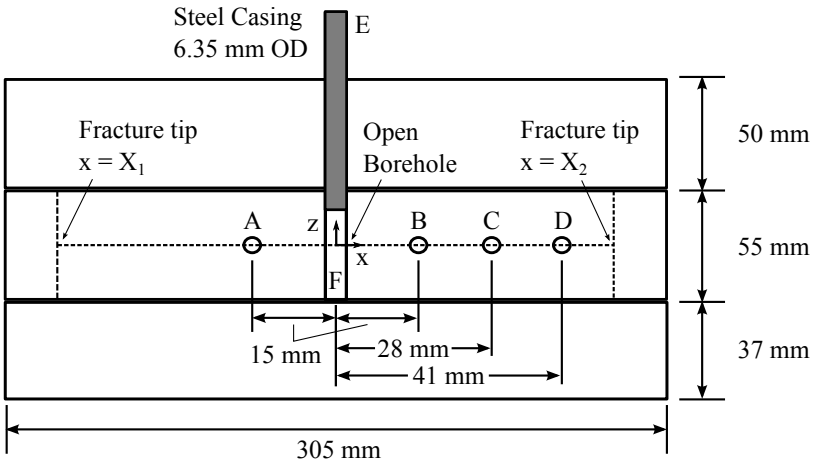

Figure 3.7: Experimental setup used in Rubin's experiment. In addition to the dimensions shown, each layer was 96 mm wide. Pressure was recorded at points A, B, D, and E, while width was recorded at point C.

.

To evaluate the geometry of the fracture, a linear variable differential transducer (LVDT) was used at point C to measure the fracture's width. The experiment was also photographed at 24 frames per second to record the fracture's length at each end as it propagated away from the borehole.

Hydraulic fracturing of the center layer was performed in two phases. First, the center layer was prefractured using a hand pump, which initiated the fracture a short distance to each side and brought it into contact with pressure gauges A and B. The main fracture was then generated using a motorized pump that injected fluid at a constant rate of 73.2 mm^3/s. Fracturing fluid was injected into the center layer until the pressure gauges bottomed out and were unable to record further pressure changes, yielding about 70 seconds of data. Fracture propagation occurred symmetrically, as evidenced by the similar pressures observed at gauge A and B (Figure 3.8), and by the similar propagation lengths at either end of the fracture (Figure 3.9). Furthermore, it was observed that the

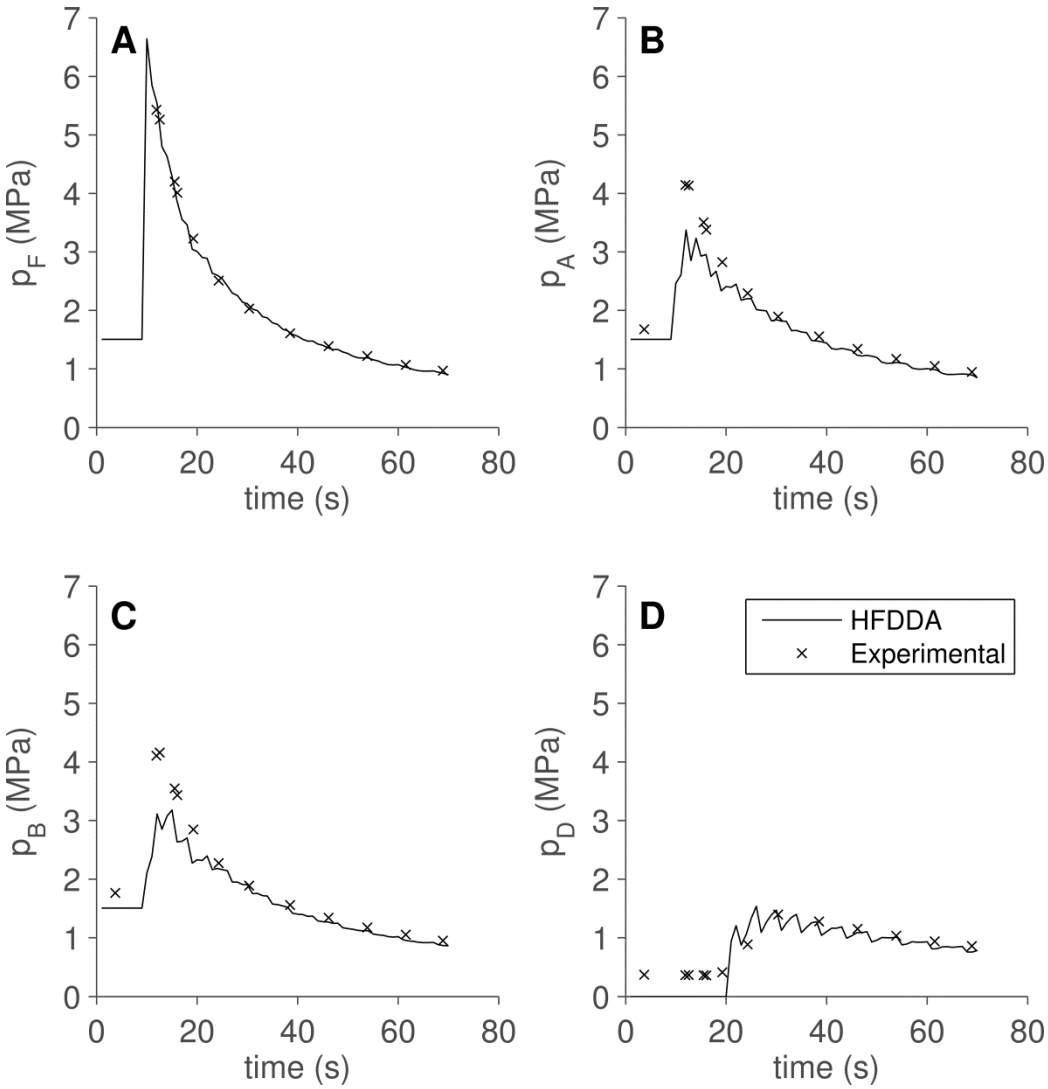

Figure 3.8: Comparison of HFDDA pressure results with experimental results of Rubin experiment. **A** shows the pressure at the borehole, **B** shows the pressure at gauge A (x = -15 mm), **C** shows the pressure at gauge B (x = 15 mm), and **D** shows the pressure at gauge D (x = 41 mm).

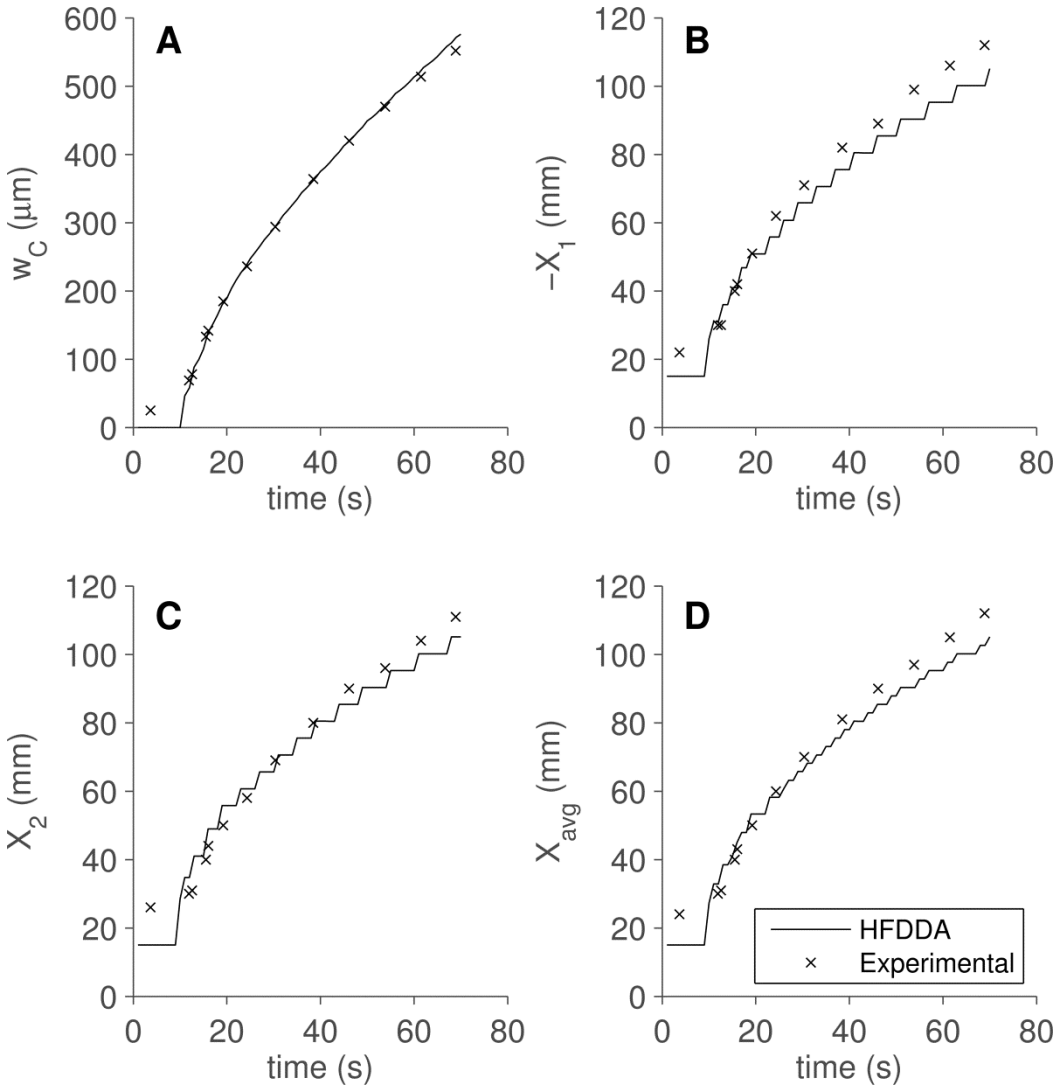

Figure 3.9: Comparison of HFDDA geometry results with experimental results of Rubin experiment. **A** shows the width at point C (x = 28 mm), **B** shows the distance that the fracture traveled to the left of the borehole, **C** shows the distance that the fracture traveled to the right of the borehole, and **D** shows the average distance traveled $\left(-X_1 + X_2\right)/2$.

resulting hydraulic fractures propagated outward from the two original notches in the borehole and curved slightly, rather than remaining perfectly planar.

To model the fracture propagation using the HFDDA, a 305 mm x 96 mm inner area was first generated with two fractures to account for the width of the borehole and the initial notch carved into it. The curved pattern taken by the experimental fracture was approximated by two lines emanating from the ends of the notches at an angle of 5° to the horizontal (Figure 3.10). The PMMA was discretized using a constrained Delaunay mesh generator which restricted the area of each triangle within the mesh to no greater than 30 mm^2, resulting in just over 1800 triangular blocks (Figure 3.11). To simulate the restraining effect of the upper and lower PMMA blocks, an outer boundary of blocks was placed around the inner area and was fixed at the corners. The Poisson's ratio of these outer blocks was set equal to zero, and their Young's Modulus was set equal to 1/10 the Young's Modulus of the inner area. Parameter values for the PMMA and the fracturing fluid are included in Table 3.2. PMMA properties were taken from [87] and [88], while fracturing fluid properties were taken from [87] and [89]. The tensile strength of the PMMA was selected based on the breakdown pressure of the PMMA sample observed in

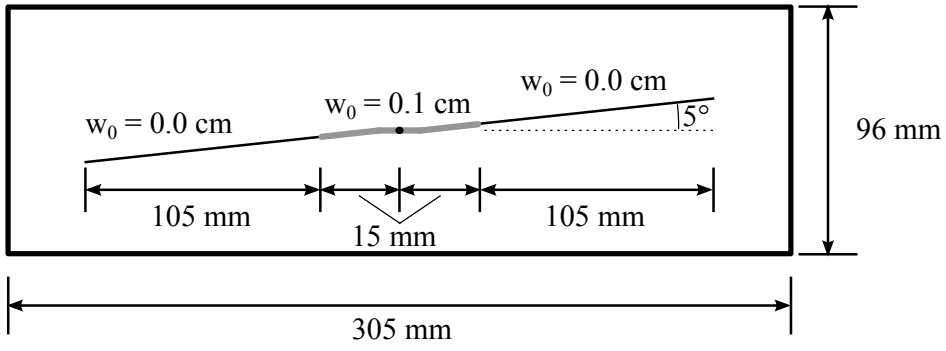

Figure 3.10: Fracture approximation used to generate the mesh for simulation of Rubin's experiment in the HFDDA.

Table 3.2: Parameters for simulation of Rubin's experiment

Rock Parameters - PMMA	
Mass Density, ρ_r	1,185 kg/m^3
Young's Modulus, E	2.0 GPa
Poisson's Ratio, v	0.367 [-]
Fluid Parameters – 100,000 cSt fluid	
Reference Density, ρ_f	977 kg/m^3
Fluid Bulk Modulus, K_f	1.725 GPa
Viscosity, μ	97.7 Pa-s
Injection Rate, Q_0	1.33 cm^3/s
Carter's Leakoff Coefficient, C_L	0.0 m/s
Fracture Parameters	
Friction Angle, ϕ	28.4°
Tensile Strength, T_0	6.0 MPa
Numerical Parameters	
Normal Spring Multiplier, k_n	30*E
Shear Spring Constant, k_s	30*E
Time Step, dt	1.0 s

the experiment. In the absence of background stress and pore pressure, the breakdown pressure and the tensile strength should be the same. Additionally, the original injection rate was normalized by the height of the center layer, as the HFDDA assumes a 1 m height in its derivation. To account for the initial prefracturing performed by Rubin, the fracture was opened 15 mm to either side of the injection point and was given an initial width of 0.1 cm filled with fluid at 0.08% compression by mass (Figure 3.10 and Figure 3.11). To model the delay observed between the time the pump was turned on and the time pressure began to rise in the system, fluid injection was initiated in the HFDDA after 10 seconds.

The results of the HFDDA are compared with the experimental data for pressure in Figure 3.8 and for the fracture geometry in Figure 3.9. All of the experimental data comes from tabular data provided in [87]. In general, the results from the HFDDA

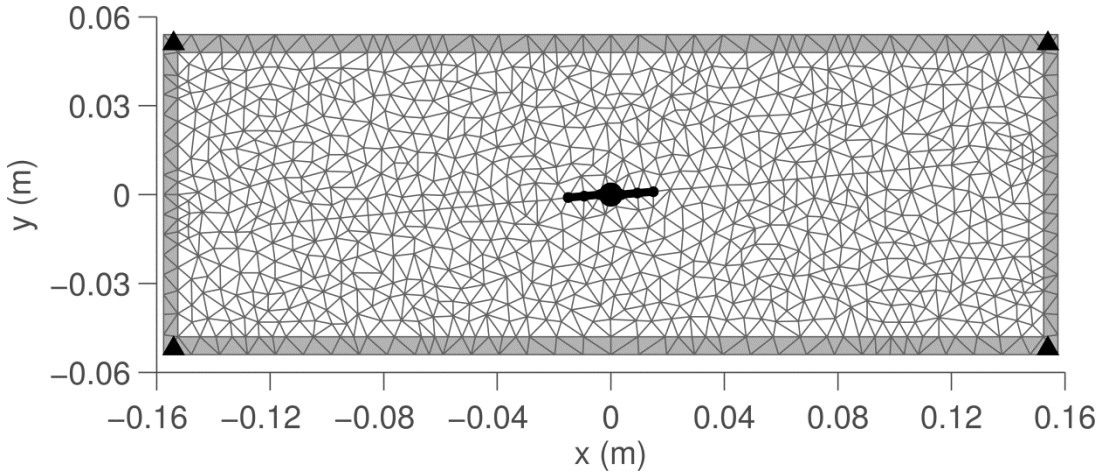

Figure 3.11: Approximation of Rubin's experiment for simulation in the HFDDA. The white triangular mesh represents the middle PMMA layer fractured in the experiment, while the surrounding mesh of gray triangles is used to approximate the restraining effect of the upper and lower PMMA layers. The black line at the center shows the fractures initially open to fluid, while the black triangles at the four corners represent fixed points that cannot move. The injection point is shown by the black circle at the origin.

showed very good agreement with the experimental results. The HFDDA successfully reproduced the propagation pattern of the experiment by generating a hydraulic fracture which propagated at 5° to the horizontal and did not open any other fractures (Figure 3.12). The pressures at all four points showed very good agreement between the HFDDA and the experiment, though differences did occur as the pressure wave first reached each point. At gauges A and B, the pressure did not quite reach the maximum pressure observed at those points, but quickly came into agreement after the fracture had propagated a short distance. At gauge D, the pressure in the HFDDA did not increase until $t = 20$ s , when the propagating fracture reached the gauge. In the experiment, all of the gauges were initially pressurized with fracturing fluid independent of the main fracture, resulting in the constant pressure observed at gauge D up until $t = 20$ s . The oscillations in the pressure observed at gauges A, B and D are due to the discrete length change that occurs each time the fracture propagates. As the fracture tip moved farther away from each gauge, the change in pressures grew smoother. For the geometry, the value recorded for the width at point C was extremely close to that observed in the HFDDA, with the only difference occurring in the first value, before the fracture had reached point C. For the length of the fracture, agreement between the experimental and HFDDA results was close initially, but deviated slightly as the fracture propagated, possibly a result of the simulation's inability to capture the heterogeneity in the PMMA sample that led the fracture to curve. Generally, however, the agreement between the solutions is very good, and the HFDDA is able to capture the trends for pressure, width and length observed within the experimental results, in addition to reproducing the propagation direction and approximate shape of the experimental fracture.

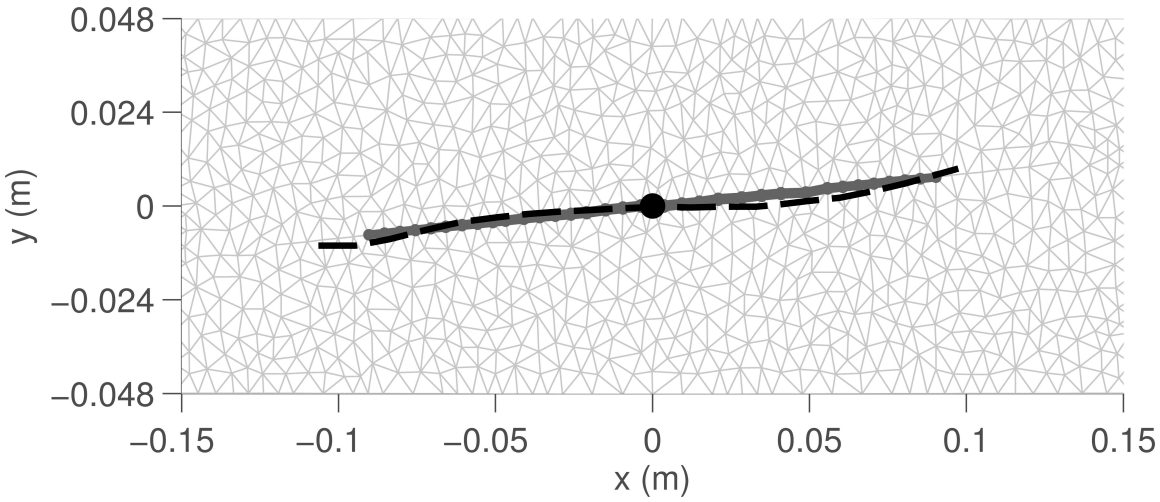

Figure 3.12: Fracture geometry at the end of the HFDDA simulation of Rubin's experiment. The thick grey line shows the open joints within the triangulated mesh, while the superimposed black line shows the path taken by the fracture in the original experiment.

3.4 Fracturing Verification in Symmetric Media

To further verify the model, additional numerical tests were conducted examining the HFDDA's ability to solve simple problems in symmetric and asymmetric media. All of these examples except one use the same numerical mesh, which is composed of a 40 m x 40 m inner domain contained within a 48 m x 48 m outer domain fixed at each corner. Unless otherwise mentioned, horizontal and vertical fractures occur in the inner domain at 2 m intervals, forming squares which are further subdivided into triangles. Injection of fluid occurs at the origin at a flowrate of $Q_0 = 1.0$ kg/s , and the two horizontal fractures adjacent to the injection point are initially open, as in the KGD example. Unless otherwise noted, these examples use the same parameters provided in Table 3.1.

The first set of examples test the algorithm's ability to model fracture propagation in homogeneous media. Included in this set are four cases which each verify different

aspects of the model. In the first case, a tensile strength of $T_0 = 1$ MPa is assigned to each joint, and the fracture is free to propagate in any direction. In the second case, the fractures above and below the injection point are also initially opened, forming a cross pattern at the injection point. For the third case, the fractures are artificially restrained such that they may only propagate along the diagonals of the mesh. In the fourth case, the fractures are once more free to propagate in any direction, but leakoff is added along each open fracture, using a relatively modest Carter's leakoff coefficient of $C_L = 0.02$ mm/s$^{1/2}$. Two different simulations were performed for each case except the one with leakoff, using background stress differentials of $\Delta\sigma = 0$ MPa and $\Delta\sigma = 5$ MPa, respectively. When $\Delta\sigma = 0$ MPa, background compressive stresses of 5 MPa were applied along all sides of the inner domain. When $\Delta\sigma = 5$ MPa, compressive stresses of 5 MPa were applied along the left and right boundaries of the domain, while stresses of 10 MPa were applied along the top and bottom boundaries. To limit the influence of the outer domain on the applied stresses, the blocks in the outer domain were given a Poisson's ratio equal to zero and a Young's Modulus equal to 1/25 that of the inner domain.

The fracture propagation pattern generated by the first case is shown in Figure 3.13. For clarity, in this and all other figures, only the 40 m x 40 m inner domain is shown, and the injection point in each figure is marked by a black circle. The purpose of both this case and the next is to demonstrate the algorithm's ability to select the proper direction for fracture propagation. In this example, the fracture was free to propagate in any direction. In the absence of a stress differential, the fracture proceeded straight outward from the tips of the initially opened fractures, following the same path predicted by a KGD fracture. In the presence of a stress differential, however, the fractures

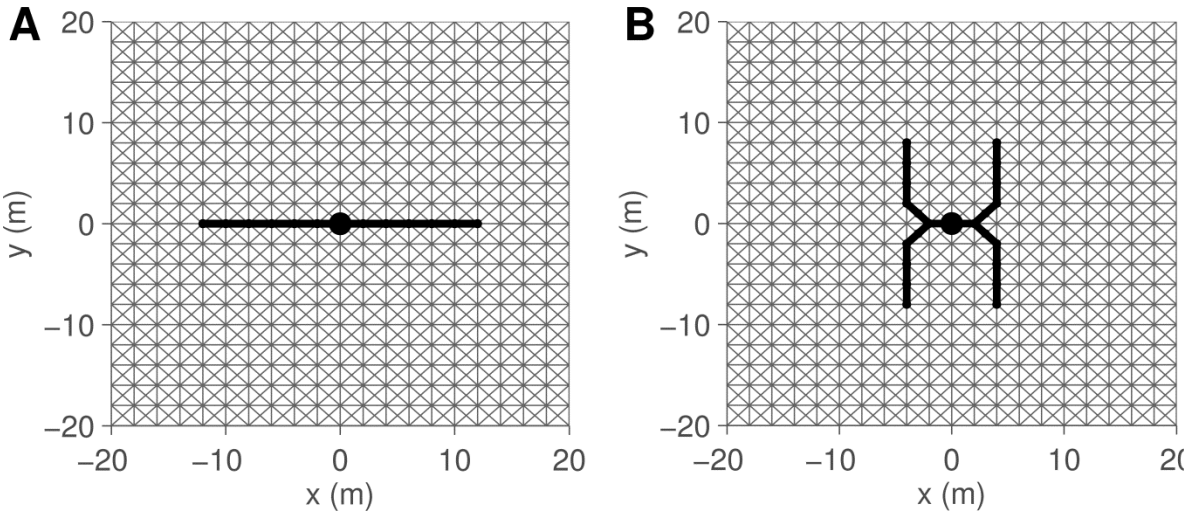

Figure 3.13: Fracture propagation after 30 s when the fracture is allowed to propagate in all directions. **A** shows the pattern when $\Delta\sigma = 0$ MPa **,** while **B** shows the pattern when $\Delta\sigma = 5$ MPa . Open nodes and fractures are noted in black.

immediately turned away from the originally opened fractures. After 6.0 s, the fractures had completely realigned themselves to propagate perpendicular to the direction of minimum compressive stress. It is well known that fractures will turn to propagate perpendicular to the direction of minimum compressive stress [65], and this phenomenon was observed both in this test case and in all of the other cases in which background stress was applied.

For the second case, the fractures immediately above and below the injection point were also opened, forming a cross pattern. The propagation pattern generated by this case is shown in Figure 3.14. In the absence of a stress differential, the fractures proceeded symmetrically away from the origin in four directions, once more proceeding straight outward from the initially opened fractures. However, because propagation was occurring down four fractures rather than just two, each branch of the fracture contained only half as much fluid as in the previous example. As a result, each fracture propagated

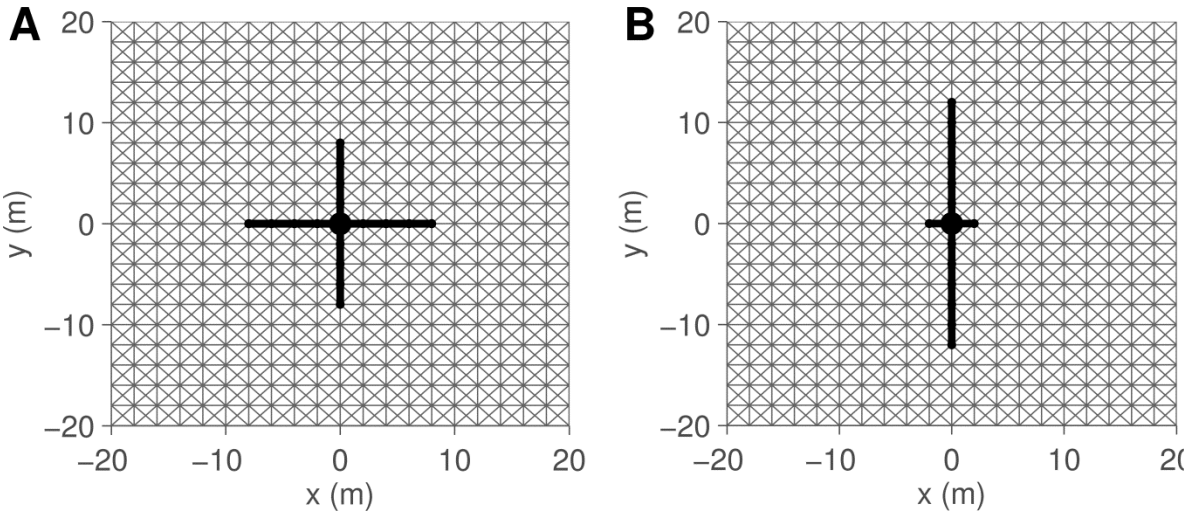

Figure 3.14: Fracture propagation after 30 s when fractures were initially opened in a cross pattern. **A** shows the pattern when $\Delta\sigma = 0$ MPa **,** while **B** shows the pattern when $\Delta\sigma = 5$ MPa . Open nodes and fractures are noted in black.

a distance of only 8 m away from the origin, rather than the 12 m observed in the first case when $\Delta\sigma = 0$ MPa . In the presence of a stress differential, the fracture only propagated perpendicular to the direction of minimum compressive stress. Notably, the original two horizontal fractures did not propagate beyond the distance to which they were initially opened, leaving propagation only in the vertical direction**.**

The fracture propagation pattern generated by the third case is shown in Figure 3.15. The purpose of this case was to verify the algorithm's ability to evaluate fracture branching, using the criteria mentioned in item iii. of Section 2.3. In this example, the fractures were free to propagate only along the diagonals of the mesh. In the absence of a stress differential, the fractures diverged symmetrically away from the initially open fractures. Once each fracture began to travel down a diagonal, it continued in that direction for the duration of the simulation. In the presence of a stress differential, the fractures again propagated perpendicular to the direction of minimum compressive stress,

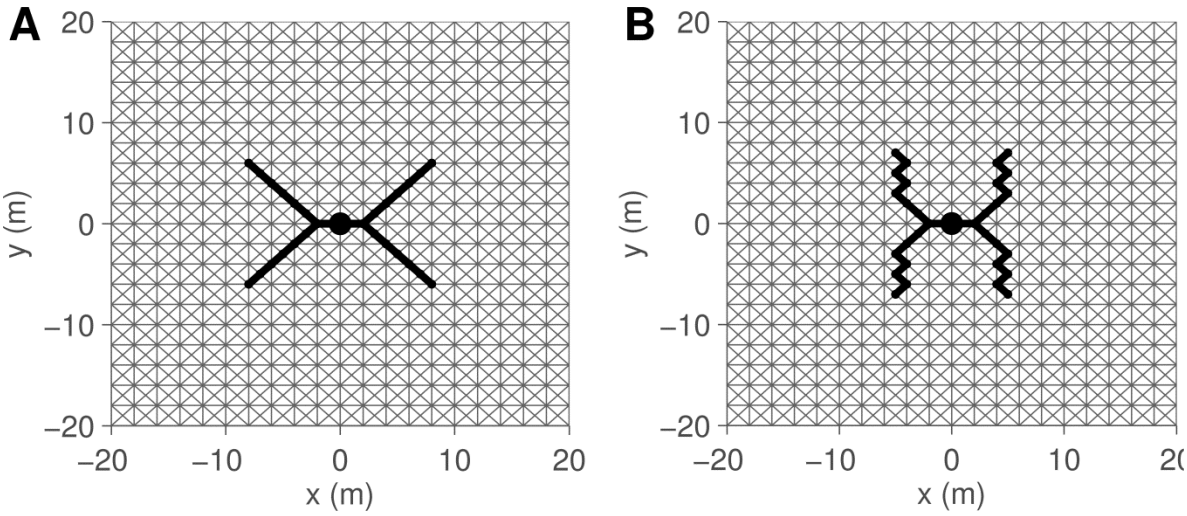

Figure 3.15: Fracture propagation after 30 s when the fractures were limited to diagonal propagation. **A** shows the pattern when $\Delta\sigma = 0$ MPa **,** while **B** shows the pattern when $\Delta\sigma = 5$ MPa . Open nodes and fractures are noted in black.

albeit in a zigzag pattern. Because the fractures were limited to diagonal propagation, they were unable to realign themselves perpendicular to the direction of minimum compressive stress at the scale of individual fractures. At the scale of the overall domain, however, the trend of the fractures was in the correct direction, suggesting that the direction of fracture propagation will be independent of the mesh discretization at sufficiently large scales. Additionally, it is worth noting that this third case was the one that demonstrated the need for the modification of the edge-edge constraints discussed in item vi. of Section 2.3. With the edge-edge contact method from the original DDA, artificial asymmetry would appear on the blocks in the inner domain, and after a few time steps two of the four diagonal branches would close. Using the modified edge-edge method prevented this artificial asymmetry.

The fourth test using the symmetric mesh sought to demonstrate the algorithm's ability to model leakoff. In this case, a Carter's leakoff coefficient of $C_L = 0.02$ mm/s$^{1/2}$

was used, and the fracture was once more allowed to propagate in all directions. Because the primary purpose of this test was to demonstrate the model's ability to conserve mass, only the results when $\Delta\sigma = 0$ MPa are provided. The propagation pattern generated by the simulation is shown in Figure 3.16. When leakoff was applied, the fractures did not propagate as far as they did for the case of no leakoff, which is to be expected. In the absence of a stress differential, the half-length of the fracture extended to only 10 m, as opposed to the 12 m half-length generated without leakoff. Figure 3.17 displays the algorithm's ability to conserve mass in the presence of leakoff. In this figure, the sum of all the mass stored in every fracture is plotted at each time step, as well as the cumulative mass lost to leakoff at each time step. The sum of these two lines gives the total mass in the system. Exact agreement is seen between the total system mass and the cumulative mass injected, indicating that the algorithm is able to conserve mass in the presence of leakoff.

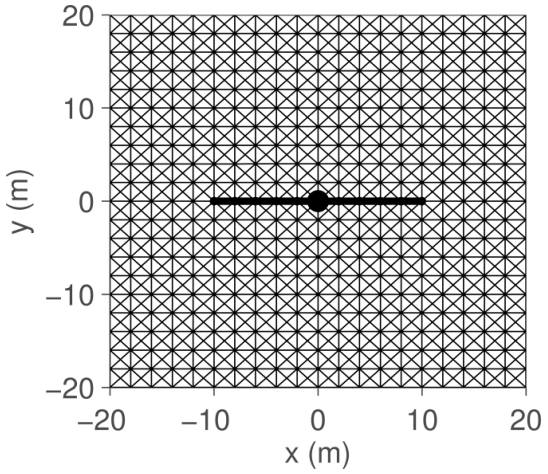

Figure 3.16: Fracture propagation after 30 s when fluid was allowed to leak into the surrounding formation.

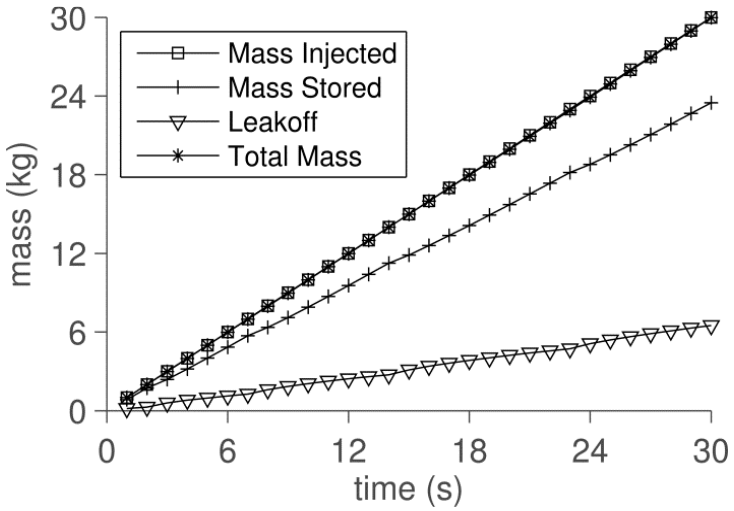

Figure 3.17: Demonstration of conservation of mass in the presence of leakoff, corresponding to the leakoff simulation when $\sigma_0 = 0$ MPa .

3.5 Fracturing Verification in Asymmetric Media

In this next set of examples, the ability of the algorithm to correctly model asymmetric media is considered. Three cases are provided for this set, each modeled in the absence of a background stress differential. In the first case, fracture propagation is limited to the diagonals of the mesh, but different values of the tensile strength are used depending on the orientation of the fractures. Fractures oriented at an angle of 45° from the positive x-axis retained the tensile strength of the previous examples ($T_0 = 1$ MPa), while fractures oriented -45° from the positive x-axis were assigned a weaker tensile strength of $T_0 = 0.1$ MPa (Figure 3.18). The fracture propagation pattern for this case is shown in Figure 3.19. When injection began, the fracture initially propagated along the diagonals oriented at 45° and along those oriented at -45°. After a few seconds, however, the fracture stopped propagating along the direction of stronger joints, but instead continued down only the weaker joints, which appears reasonable.

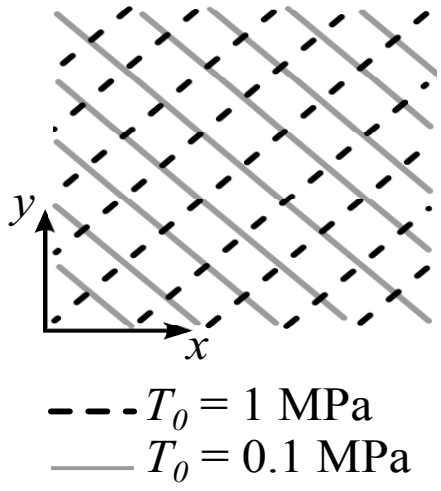

Figure 3.18: Tensile strength distribution when asymmetric tensile strengths were applied along the mesh diagonals.

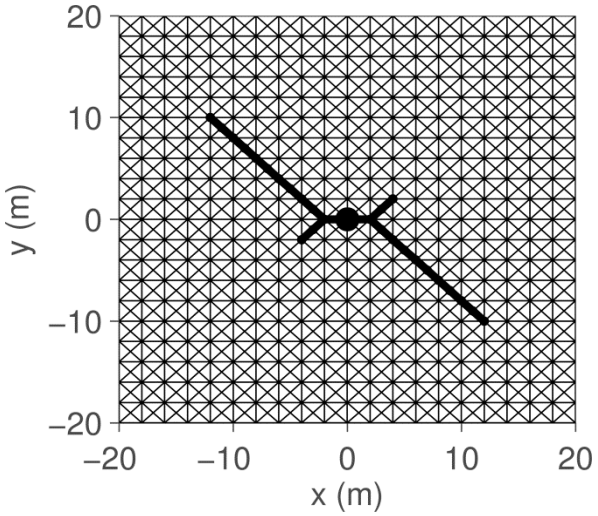

Figure 3.19: Fracture propagation after 30 s when the rock matrix had asymmetric values of tensile strength along the diagonals.

For the second case, the regular grid of the previous examples was eschewed in favor a random triangular grid generated using the Delaunay triangulation program "Triangle" [90]. To generate the triangulation, two initial fractures 2 m long were placed horizontally on either side of the injection point, and each triangle in the resulting grid was constrained to have a maximum area no greater than 1.5 m^2. Both the generated mesh and the results of the simulation are shown in Figure 3.20. The first observation from the triangular grid is that the fracture generated is no longer symmetric. The fracture propagated a distance of 14.0 m to the left of the injection point, but only a distance of 9.1 m to the right. Further, the path taken by the fracture was no longer a straight line, but rather varied along the paths available with the discretization. Overall, however, the fracture did not deviate too far away from the horizontal, and instead followed a path similar to that observed for the first symmetric case in the absence of a stress gradient. These results again suggest that the fracture pattern at the scale of the rock domain will be mesh independent, though variation at the scale of independent fractures will occur.

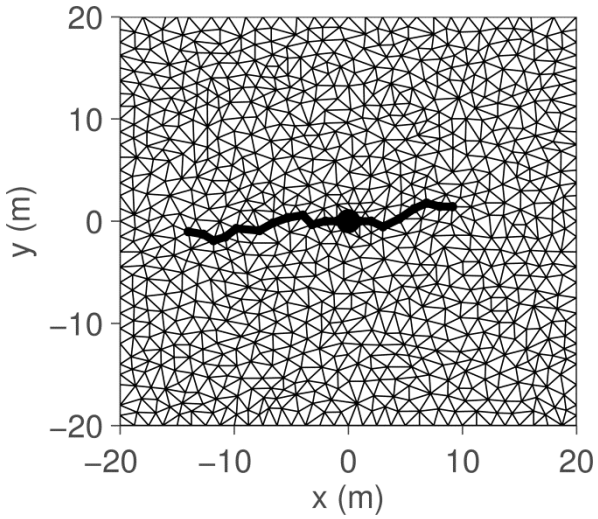

Figure 3.20: Fracture propagation after 30 s when a Delaunay triangulation was used to discretize the rock matrix.

For the final case, the regular grid was again applied, but two different moduli were used for the rock matrix above and below the x-axis (Figure 3.21). For all rocks above the x-axis, the original Young's Modulus of E = 25 GPa was used. Below the x-axis, however, a modulus of E = 5.0 GPa was used. Furthermore, fracturing in this case was limited to the interface between these two domains. The propagation pattern for this case is shown in Figure 3.22, in which the fracture can be seen to propagate along the interface. Figure 3.23 shows a close-up view of the fracture generated as a result of this case. Note the difference in scales along the x and y axes, and that the x axis forms the top boundary of the figure. Two key results may be taken from this figure. First, because the lower domain had a lower Young's Modulus than the upper domain, the boundary stress applied along the top and bottom of the media compressed the lower domain to a greater extent than the upper domain, effectively moving the interface between the two areas down by approximately 5 mm. Second, again because of the disparity between the Young's Moduli of the two domains, the fracture opened to a greater extent in the domain

with a smaller Young's Modulus. Both of these observations are in keeping with the expected results from this simulation. Together, all of these simulations demonstrate that the HFDDA can reliably reproduce basic test cases of hydraulic fracturing.

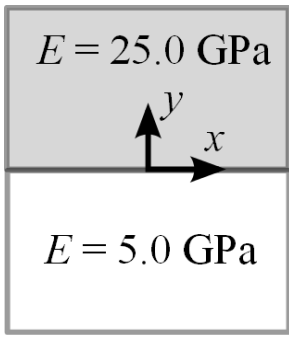

Figure 3.21: Asymmetric Young's Moduli applied in the final asymmetric test case.

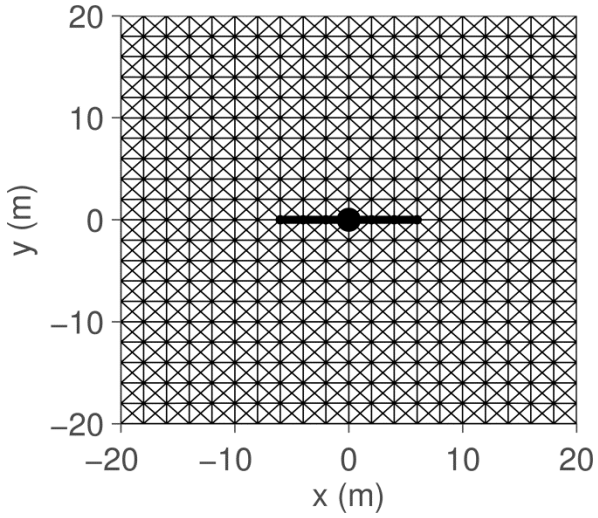

Figure 3.22: Fracture propagation after 30 s when the rock matrix had asymmetric values of Young's modulus.

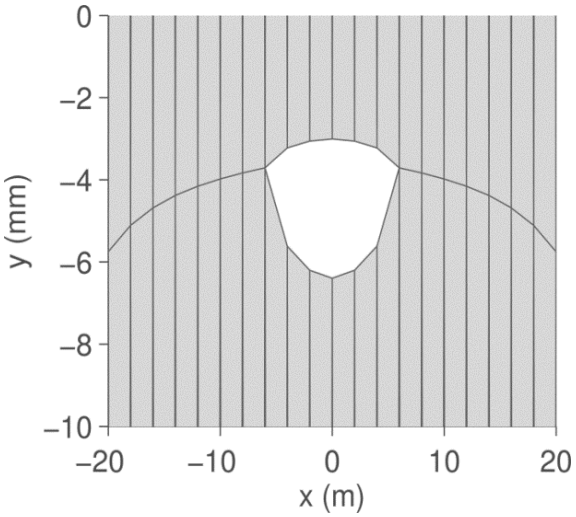

Figure 3.23: Close-up representation of the fracture opening for the case of asymmetric values of Young's Modulus. Note that the *y*-axis is shown in millimeters, while the x-axis is shown in meters.

4 COMPARISON OF FRACTURING CRITERIA

In Chapter 3, the coupling algorithm in the HFDDA was verified, along with its ability to correctly predict fracture propagation direction and branching in simple geometries. In this chapter, the maximum tensile stress and Mohr-Coulomb fracturing criteria used in the HFDDA are investigated and related to the Linear Elastic Fracture Mechanics (LEFM) criteria commonly used in hydraulic fracturing models. The theoretical relationship between these criteria and the LEFM criteria is discussed, and the relationship between the two sets of criteria is demonstrated using the DDA alone. Additionally, the ability of the HFDDA to reproduce the toughness dominated, no-leakoff asymptotic regime for the KGD hydraulic fracturing solution is considered.

4.1 Relationship between the HFDDA and LEFM Criteria

In the HFDDA, fracturing occurs when the normal or shear stress along a joint exceeds a certain threshold. In DDA terminology, the criteria for determining the onset of fracturing are frequently referred to as the no-tension constraints and are described for each joint contact by the equations

$$N \le L_c T_0, \quad S \le L_c C_0 + N \tan\phi \tag{4.1}$$

where all of the terms are as defined previously. In Equation (4.1), the normal stress criteria is also known as the maximum tensile stress or Rankine failure criterion, and is characterized by the tensile strength of the joint, T_0. The shear criterion is known as the Mohr-Coulomb failure criteria, characterized by the cohesive strength (C_0) and the friction angle (ϕ) of the joint. In this work, these criteria are collectively referred to as

the HFDDA fracture criteria. Typically, the maximum tensile stress and Mohr-Coulomb failure criteria are used to define the failure envelope of unfractured materials and to describe the stresses at which new fractures will nucleate. The LEFM criteria, on the other hand, are more commonly used to define the conditions under which an existing fracture will propagate. Unlike the maximum tensile stress and Mohr-Coulomb criteria, which are based on the stresses along each fracture, the LEFM criteria are energy-based, implying that both the stress near the fracture tip and the distance over which it acts will influence fracture propagation. In LEFM, fracturing is determined by the strain energy release rate (G) of the fracture, which is defined as the energy released as the fracture propagates per unit of new fracture surface area. When the strain energy release rate at the tip of a fracture is greater than a critical value (G_c), fracturing will occur. Generally, this criterion is evaluated by examining the stress intensity near the tip of the fracture. For any fracture, a stress intensity factor (K) may be defined as a function of the stress field near the fracture tip. Using a polar coordinate axis with its origin at the crack tip (Figure 4.1), the stress distribution near the tip of the fracture (σ_{ij}) may be defined as [91]

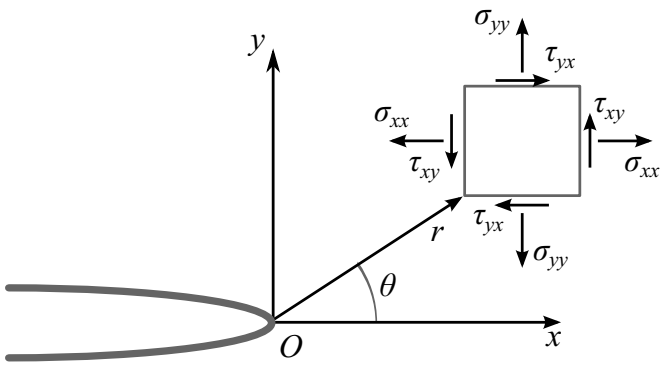

Figure 4.1: Definition of the coordinate axis and stresses at the tip of a fracture.

$$\sigma_{ij}(r,\theta) = \frac{K}{\sqrt{2\pi r}} f_{ij}(\theta) + \text{higher order terms} \tag{4.2}$$

where K is the stress intensity factor with units of stress x length$^{1/2}$, and f_{ij} is a dimensionless function of θ that depends on the system load and geometry. In what is commonly referred to as the square-root singularity for LEFM, Equation (4.2) states that stress near the fracture tip will increase proportional to $1/\sqrt{r}$, with the result that as $r \to 0$, the stress approaches infinity. Due to this singularity, stress intensity factors at the fracture tip are found by taking the limit of the stress distribution with respect to the distance away from the fracture. Typically, stress intensity factors are defined based on the mode of loading. For Modes I and II (the only modes applicable in a 2D environment), the stress intensity factors are given by the equations

$$\lim_{r\to 0} \sigma_{ij}^{(I)} = \frac{K_I}{\sqrt{2\pi r}} f_{ij}^{(I)}(\theta), \quad \lim_{r\to 0} \sigma_{ij}^{(II)} = \frac{K_{II}}{\sqrt{2\pi r}} f_{ij}^{(II)}(\theta) \tag{4.3}$$

In plane strain conditions, the stress intensity factors can be related to the strain energy release rate by the relations

$$G = K_I^2 \left(\frac{1-\nu^2}{E} \right) \tag{4.4}$$

for pure Mode I loading, and by

$$G = K_{II}^2 \left(\frac{1-\nu^2}{E} \right) \tag{4.5}$$

for pure Mode II loading. When fracturing is imminent, $G = G_c$ for both loading modes. The critical value for each stress intensity factor beyond which fracturing will occur in each loading mode may therefore be given by

$$K_{IC} = K_{IIC} = \sqrt{\frac{G_c E}{1-\nu^2}} \tag{4.6}$$

where K_{IC} and K_{IIC} represent the Mode I and Mode II fracture toughness of the material, respectively. When fracturing occurs in tension, the propagation direction for the fracture may be determined by finding the direction which maximizes K_I.

In the HFDDA, a key benefit of the maximum tensile stress and Mohr-Coulomb criteria is their simplicity. The normal and shear stress at each contact can quickly be calculated using the Penalty Method (PM) or the Augmented Lagrangian Method (ALM), resulting in an easily-applied technique for discrete elements of arbitrary shape. Calculation of the stress intensity factors in finite element and discrete element models, on the other hand, is a computationally demanding task, requiring the fine resolution of the stress, strain and displacement fields near the tip of each fracture. To properly evaluate these terms, the mesh at the fracture tip can be refined, or six- to eight-node mesh elements can be used, as opposed to the three-node elements employed in the HFDDA. Calculation of stress intensity factors with six- to eight-node elements is complicated by the fact that two of the mid-side nodes of each element must be shifted to a quarter-point position near the fracture tip (though an alternative approach based on unmodified six- to eight-node elements was recently explored in [67]). Without *a priori* knowledge of the fracture propagation path, methods based on mesh refinement and quarter-point mesh elements are both very expensive computationally, and as a result prove unsuitable for modeling hydraulic fracturing problems in which the fracture may propagate across the entire domain. In light of these observations, it is desired to see if the simpler stress-based HFDDA fracture criteria serve as an appropriate substitute for

the more complicated LEFM fracture criteria frequently used to evaluate crack propagation problems. The key goals of this chapter, therefore, are to relate the HFDDA fracture criteria to the LEFM criteria, and to evaluate the ability of the DDA and the HFDDA to solve LEFM-based problems of fracture growth from pre-existing cracks.

Before examining the relationship between these fracture models, however, it is worth discussing a third method which combines aspects of the previous two. The Cohesive Zone Model (CZM) for fracture separation, whose origins can be traced to the strip-yield model developed by Barenblatt [10] and Dugdale [92], combines the criteria for both the initiation and propagation of fractures into one comprehensive model. In the CZM, separation of the rock media is modeled using a fracture process zone, which develops as the fracture is nucleating and propagating (Figure 4.2). The separation is governed by a stress-displacement curve which can take various shapes, such as the bilinear model shown in shown in Figure 4.3 [93]. In the bilinear model, the stress-displacement curve has two distinct stages. First, during the hardening stage, as the sides of the fracture begin to separate, the stress holding the fracture together steadily increases until it reaches a maximum (T_0). Once the maximum is reached $\left(d = d_0\right)$, as separation

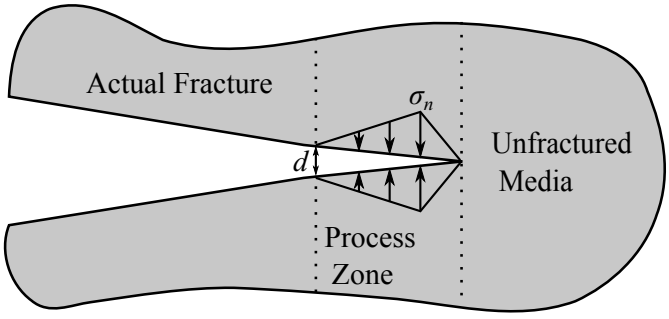

Figure 4.2: Fracture process zone for the cohesive zone model.

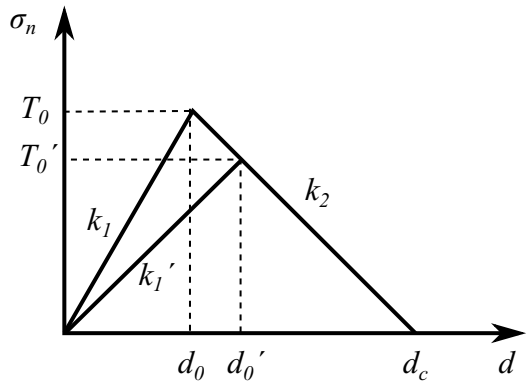

Figure 4.3: Bilinear stress-displacement curve for the cohesive zone model.

continues the tractions begin to decrease until the separation is complete $(d = d_c)$ and the crack is fully formed, in what is referred to as the softening stage. In the softening stage, any deformation that occurs is plastic and will lead to decreases in the slope of the hardening stage (k_1') and tensile strength (T_0') if the load driving the fractures is released. For every stress-displacement curve, the area under the curve represents the critical strain energy release rate (G_c) from LEFM. If only the hardening stage of the bilinear curve is used, in which the contact force is steadily increasing with distance, the algorithm becomes the same as the penalty method employed by the original DDA for Mode I fracturing. The slope of the line is equivalent to the spring constant for the PM, and the maximum stress is equivalent to the maximum tensile stress fracture criteria. Given the similarities between these methods, fracture criteria based on the CZM have been applied in various algorithms, including penalty-based FEM methods (e.g. [94]) as well as a method using the DDA [95].

In light of the benefit that comes from a model explicitly designed to consider both fracture initiation and propagation, implementation of the CZM within the HFDDA

was attempted as part of the current work. Difficulties in the application of the method quickly became apparent, however. First, it was unclear how the stress-displacement curve of the CZM should be implemented using the ALM for the contacts, as opposed to the original PM. With the ALM, the contact forces are iteratively updated, with each update reducing the separation distance between the contact surfaces until the distance approaches zero. Applying the ALM would effectively remove the hardening stage of the stress-displacement curve, resulting in a curve similar to that in Figure 4.4. Second, in what is arguably the larger problem, application of the the softening phase of the CZM as derived by Jiao et al. in [95] can cause the DDA's stiffness matrix to lose its positive definiteness. If the stiffness matrix loses its positive definiteness, the Cholesky-based LU solver employed in the original DDA no longer functions, and it is no longer guaranteed that the stiffness matrix is invertible. To work around this problem, Jiao et al. [95], never actually applied the terms that would arise from the softening side of the CZM in their paper, but instead used only terms based on an iteratively modified spring constant for the hardening side. Using this method in the HFDDA would dramatically increase the

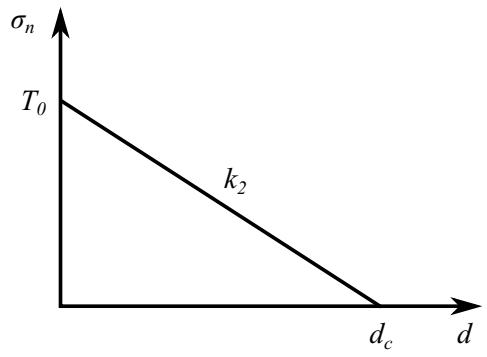

Figure 4.4: Potential stress-displacement curve when applying the Augmented Lagrangian Method within the cohesive zone model.

amount of CPU time required for each simulation, as the DDA's stiffness matrix would need to be refactorized after each inner iteration, rather than only after each outer iteration. Such a change would require the stiffness matrix to be refactorized hundreds of times each time step, rather than the fewer than ten times currently needed. Note that this issue of refactorization is not, however, a problem for explicit solvers such as that in [94], as the displacements in those solvers are not iterated upon in each time step. In light of the difficulties mentioned with application of the CZM to the DDA, the CZM was not pursued any farther as part of the current work.

4.2 Mode I Fracture

To begin the comparison of the HFDDA fracture criteria and the LEFM fracturing criteria, this section examines the stress at which fracturing begins for a pre-existing crack in an infinite plane under Mode I loading. The derivation in this section follows a similar derivation contained in [96], which developed the relationship using circular particles for a DEM model of hydraulic fracturing. Using LEFM, for a fracture with half-length *a* in an infinite isotropic plane subject to a far-field stress σ_f, under linear elastic conditions (Figure 4.5), the normal stress (σ_{yy}, Figure 4.1) near the fracture tips ($r << a$) is given by [97] as

$$\sigma_{yy} = \sigma_f \sqrt{a / 2r} \tag{4.7}$$

where *r* is the radial distance away from the fracture tips. Along the plane of the fracture, the total normal force (F_n) acting between any two points x_1 and x_2 may be found by integrating the stress between them, yielding

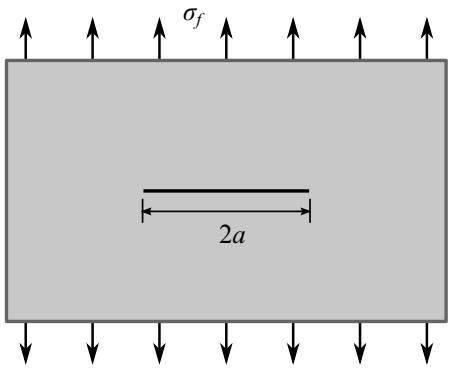

Figure 4.5: Fracture of half-length *a* in an infinite field under Mode I loading.

$$F_n = \int_{x_1}^{x_2} \sigma_f \sqrt{a/2r}\, dr = \sigma_f \sqrt{2a}\left(\sqrt{x_2} - \sqrt{x_1}\right) \tag{4.8}$$

Consider an implementation of the DDA with a joint of length *L* parallel and adjacent to the fracture tip. Using Equation (4.8), the normal force along this joint may be given as

$$F_n = \sigma_f \sqrt{2a}\left(\sqrt{L} - \sqrt{0}\right) = \sigma_f \sqrt{2aL} \tag{4.9}$$

Using LEFM, for this problem the mode I stress intensity factor K_1 may be given as [97]

$$K_I = \sigma_f \sqrt{\pi a} \tag{4.10}$$

Substitution of Equation (4.10) into Equation (4.9) yields

$$F_n = K_I \sqrt{2L/\pi} \tag{4.11}$$

For the two-dimensional plane strain DDA, using the maximum tensile stress criterion, the maximum tensile force sustainable along the joint adjacent to the fracture is given by

$$F_n^{\max} = T_0 L \tag{4.12}$$

where T_0 is the ultimate tensile strength of the joint. Just before failure occurs at the fracture tip, $F_n = F_n^{\max}$ and $K_I = K_{IC}$, where K_{IC} is equal to the critical mode I stress

intensity factor. Using equations (4.11) and (4.12), the relationship between K_{IC} and T_0 may be expressed as

$$K_{IC} = T_0\left(\sqrt{\pi L/2}\right) \tag{4.13}$$

Using this relationship, the maximum far-field tensile stress that can be applied before fracturing occurs is given by

$$\sigma_f^{\max} = T_0\sqrt{\frac{L}{2a}} \tag{4.14}$$

At this point, only the conditions for initiating failure have been discussed, and not those for propagation. Once the fracture has been initiated, LEFM predicts that the fracture should continue to propagate unstably. Consider the case for when the fracture has successfully opened the fracture adjacent to the crack, extending it to half-length $a+L$ subject to the maximum far field tensile force. At this new length, the new normal force at the crack tip (F_n') will be given by

$$F_n' = \sigma_f^{\max}\sqrt{2(a+L)}\left(\sqrt{L}-\sqrt{0}\right) \tag{4.15}$$

which can be reduced to

$$F_n' = \sigma_f^{\max}\sqrt{2aL\left(1+L/a\right)} = F_n^{\max}\sqrt{\left(1+L/a\right)} \tag{4.16}$$

By Equation (4.16), the new force at the crack tip after propagation should be greater than the force which initiated propagation, and the crack should continue to propagate unstably, as predicted by LEFM.

Given this derivation, it was desired to see how well the Mode I failure criteria in the DDA would reproduce the fracture propagation behavior predicted by these equations. For given values of T_0 and L, a fracture in an infinite plane modeled with the DDA

should fail at the value of σ_f predicted by Equation (4.14). To test this theory, a 160 m x 160 m rock domain was generated to represent the infinite plane. The plane for this example (and for all others in this chapter) was characterized by a Young's Modulus of 25 GPa, Poisson's ratio of 0.25, and a rock density of 2,650 kg/m^3. Cracks of initial half lengths ranging from 0.0 m (unfractured) to 5.0 m were placed at the center of the domain, and were allowed to fracture up to 24 m to either side. The mesh along the 24 m was discretized at two different levels (L = 0.5 m and L = 1.0 m), which were separately tested using two different tensile strengths (T_0 = 1 MPa and T_0 = 5 MPa). At the boundaries of the domain parallel to the fracture, tensile stresses were applied and slowly incremented until the fracture exhibited complete failure, defined as when more than 75% of the 24 m half-length had opened. When T_0 = 1 MPa, the stress was incremented in units of 2 kPa, while increments of 10 kPa were used when T_0 = 5 MPa. Each simulation continued until the fracture exhibited complete failure, after which the tensile stress at which failure occurred was recorded.

The results of these tests are shown graphically in Figure 4.6. In each subplot, the final tensile force at which failure occurred in the DDA simulations is shown, as well as the values predicted from the theoretical derivation combining LEFM with the maximum tensile stress criterion. As a testament to the fact that the maximum tensile stress criterion worked as intended, when there was no initial flaw present, the tensile force at which failure occurred was exactly the same as the tensile strength of the rock, independent of the mesh size. When an initial flaw was present, the DDA was able to match the values predicted theoretically by Equation (4.14). The agreement between the two improved as the mesh discretization decreased relative to the length of the initial flaw. When L =

0.5 m, for both T_0 = 1 MPa and T_0 = 5 MPa, the DDA values were very close to the theoretical values for a = 2.0 m aT_0 nd beyond. For half-lengths smaller than a = 2.0 m, the DDA values were less than those predicted theoretically, but still within a reasonable range. Similarly, when L = 1.0 m, for both = 1 MPa and T_0 = 5 MPa, the DDA values were very close to the theoretical values for a = 3.0 m and beyond. Before a = 3.0 m, the joint discretization is still similar to the fracture half-length, and the agreement is still good, but not quite as close as after the discretization becomes significantly smaller than the initial crack length. Regarding the theoretical prediction that fractures will continue propagating once initiated, it was observed that complete fracturing tended to occur over a small range of the applied tensile stress, as opposed to occurring all at once. The magnitude of this range was always small, however, relative to the magnitude of the applied tensile stress. When T_0 = 1 MPa, the difference in far field tensile stress between the initiation of fracture and its completion was no greater than 10 kPa, while for T_0 = 5 MPa, the difference was no greater than 50 kPa. From these results, it appears that the DDA fracture criteria are consistent with the concepts of LEFM, at least for these basic Mode I tensile problems.

An interesting observation for Figure 4.6 is that when an initial flaw is present, the far field tensile stress at which fracture occurred changed as a function of the mesh discretization in both the numerical and theoretical solution. When the discretization was smaller, the stress was smaller for the same initial crack half-length. For instance, in looking at the values from the theoretical derivation, when a = 1.0 m and T_0 = 1 MPa, σ_f = 0.5 MPa when L = 0.5 m, but σ_f = 0.707 MPa when L = 1.0 m. These differences

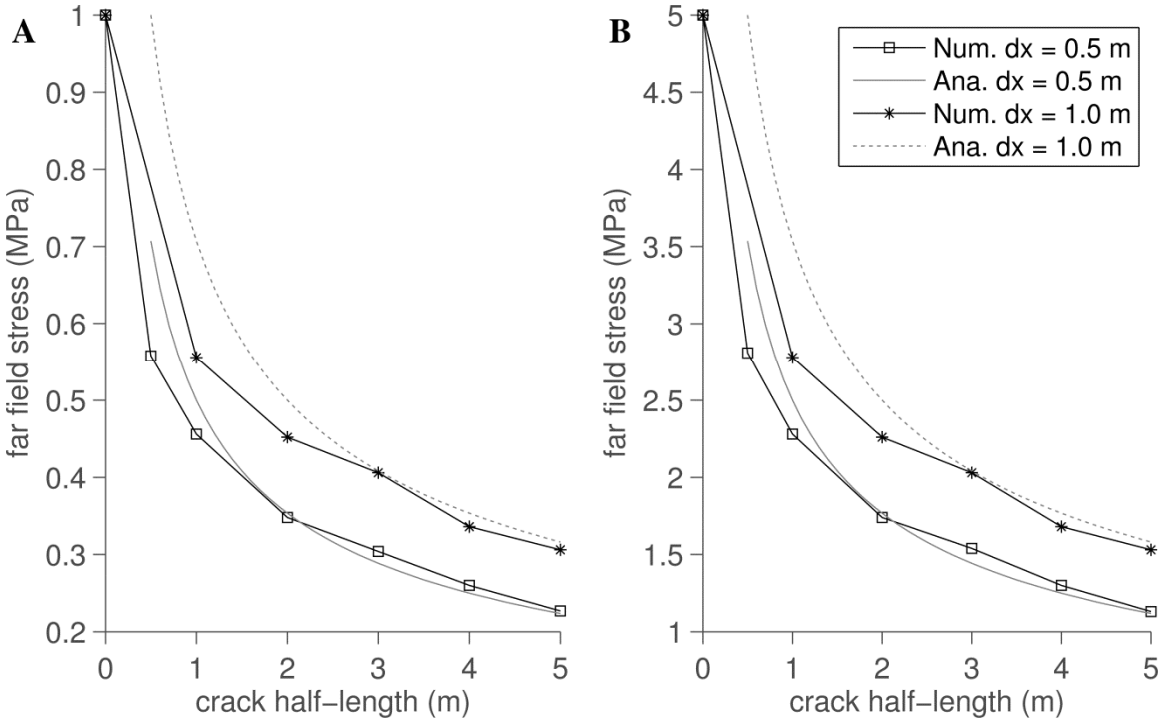

Figure 4.6: Comparison of the DDA results and theoretical results for the far field tensile stress at which failure occurs under Mode I loading. **A** shows the results when T_0 = 1 MPa, while **B** shows the results when T_0 = 5 MPa.

suggest that the tensile strength of the rock domain will not by itself determine the stress at which fracturing begins, but rather that fracturing is a function of both the tensile strength and the discretization of the rock domain. The fact that the discretization has an effect on the onset of fracturing suggests that the maximum tensile stress criterion as applied in the DDA behaves similarly to the Mode I critical stress intensity factor criterion employed in the LEFM. If discretization did not have an effect, the theoretical relationship derived between T_0 and K_{IC} in Equation (4.13) would be invalid. A limitation of using the maximum tensile stress criterion, however, is that two parameters appear to control the extension of existing fractures, as opposed to the single stress

intensity factor criteria used with LEFM. Thus changes to the discretization of a problem in the DDA may have a significant effect on the onset of fracture propagation, even if all of the material parameters remain the same.

4.3 Mode II Fracture

Building upon the previous section, this section examines the stress at which fracturing begins for a pre-existing crack in an infinite plane under Mode II loading. Using LEFM, for a fracture with half-length *a* in an infinite isotropic plane subject to a far-field shear stress τ_f (Figure 4.7), under linear elastic conditions, the shear stress (τ_{xy}) near the fracture tips ($r << a$) is given by [97] as

$$\tau_{xy} = \tau_f \sqrt{\frac{a}{2r}} \tag{4.17}$$

Along the plane of the fracture, the total shear force (F_s) acting between any two points x_1 and x_2 may be found by integrating the stress between them, yielding

$$F_s = \int_{x_1}^{x_2} \tau_f \sqrt{a/2r}\, dr = \tau_f \sqrt{2a}\left(\sqrt{x_2} - \sqrt{x_1}\right) \tag{4.18}$$

Using Equation (4.18) and an implementation of the DDA with a joint of length *L* as before, the shear force F_s along this joint may be given as

$$F_s = \tau_f \sqrt{2a}\left(\sqrt{L} - \sqrt{0}\right) = \tau_f \sqrt{2aL} \tag{4.19}$$

Using LEFM, for this problem the mode II stress intensity factor K_{II} may be given as [97]

$$K_{II} = \tau_f \sqrt{\pi a} \tag{4.20}$$

Substitution of Equation (4.20) into Equation (4.19) yields

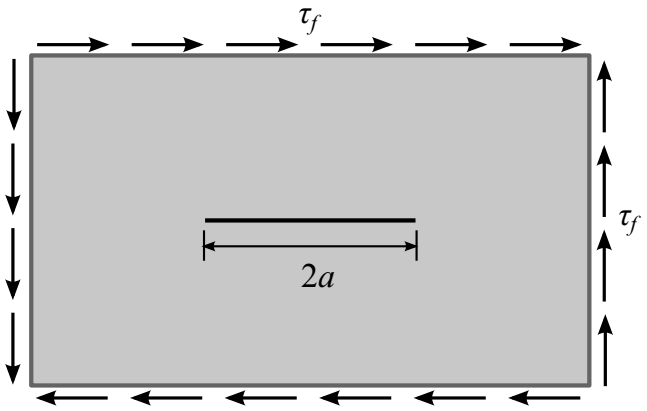

Figure 4.7: Fracture of half-length *a* in an infinite field under Mode II loading.

$$F_s = K_{II}\sqrt{2L/\pi} \tag{4.21}$$

For the two-dimensional plane strain DDA, the maximum shear force sustainable along the joint adjacent to the fracture is given by

$$F_s^{\max} = C_0 L + N\tan\phi \tag{4.22}$$

where C_0 is the cohesive strength of the joint, ϕ is the friction angle and *N* is the normal force acting along the joint. Just before failure occurs at the fracture tip, $F_s = F_s^{\max}$ and $K_{II} = K_{IIC}$, where K_{IIC} is equal to the critical mode II stress intensity factor. Using equations (4.21) and (4.22), the relationship between K_{IIC} and C_0 may be expressed as

$$K_{IIC} = \left(C_0 L + N\tan\phi\right)\left(\sqrt{\pi/2L}\right) \tag{4.23}$$

Using this relationship, the maximum far-field shear stress for given values of cohesive strength, coefficient of friction, discretization and fracture half-length is given by

$$\tau_f^{\max} = \frac{\left(C_0 L + N\tan\phi\right)}{\sqrt{2aL}} \tag{4.24}$$

Similar to the test of the Mode I criteria in the DDA, it was desired to see how well the shear failure criteria in the DDA would reproduce the propagation behavior predicted by these equations. For given values of C_0, ϕ, and L, a fracture in an infinite plane modeled with the DDA should fail at the value of τ_f predicted by Equation (4.24). To examine this relationship, the same 160 m x 160 m rock domain from the Mode I analysis was generated to represent the infinite plane. As before, cracks of initial half lengths ranging from 0.0 m to 5.0 m were placed at the center of the domain, and were allowed to fracture up to 24 m to either side. Two different levels of mesh discretization (L = 0.5 m and L = 1.0 m) were again tested, each using two different cohesive strengths (C_0 = 1 MPa and C_0 = 5 MPa). The friction angle for these problems was set to zero, as no additional compressive forces are applied at the boundaries and the fractures are loaded purely in shear. At the boundaries of the domain, shear stresses were applied and slowly incremented until the fracture exhibited complete failure, using increments of 2 kPa when C_0 = 1 MPa and increments of 10 kPa when C_0 = 5 MPa. The simulations were continued until the fracture exhibited complete failure, defined as when over 75% of the available fracture had sheared, and the shear stress at which failure occurred was recorded.

The results of these tests are shown graphically in Figure 4.8. Again, as testament to the fact that the cohesive criteria and shear portion of the ALM are working properly, in the absence of an initial fracture the domain failed at the cohesive strength of the joints. Also as before, the shear stress at which fracture occurred changed as a function of the mesh size. When the mesh size was smaller, the shear stress at failure was smaller for the same initial crack half-length, as required by Equation (4.24). Unlike for Mode I fractures,

however, the fit between the DDA and the values predicted theoretically for Mode II fractures was not as good. While the relative gap between these values did appear to improve as the size of the initial crack increased relative to the discretization, and the overall trend between the two sets was the same, the DDA values were consistently different from the predicted values. This phenomenon may stem from the DDA's manner of sharing the tensile and cohesive strengths of joints between the two contacts at opposite ends of each joint. In the DDA, each contact is assigned a contact length equal to half of the joint length, resulting in the tensile and cohesive strength being split between the two contacts. For both the Mode I and Mode II fractures, the joint half immediately adjacent to the fracture tip would fail early in the simulation, leaving only

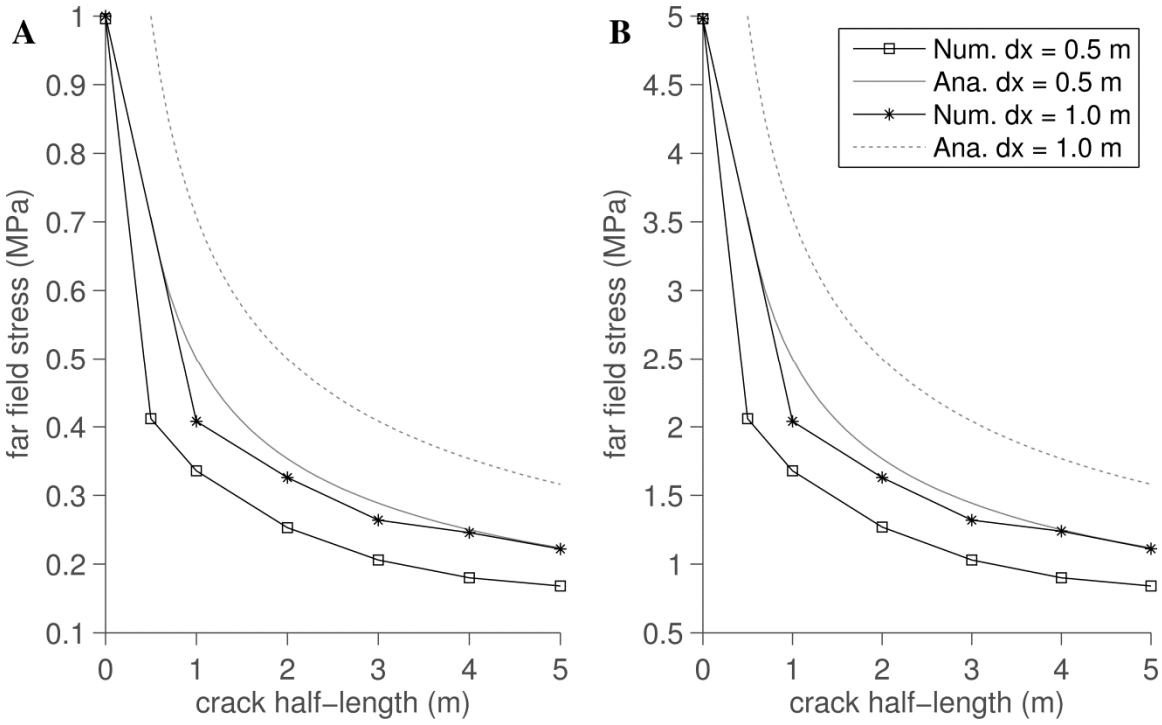

Figure 4.8: Comparison of the DDA results and theoretical results for the far field shear stress at which failure occurs under Mode II loading. **A** shows the results when C_0 = 1 MPa, while **B** shows the results when C_0 = 5 MPa.

the second half of the joint to support the far field load. It is unclear, however, why the second half of the Mode I fracture failed at the value predicted theoretically while the Mode II fracture failed earlier. Even with the discrepancy for Mode II fracture, the general trends for the far field stress with respect to discretization and initial crack half-length are consistent between the DDA and the theoretical results, suggesting that the Mohr-Coulomb criterion can serve as a reasonable replacement for the LEFM criteria in shear for frictionless contacts, or for contacts that are not undergoing significant compressive stress. In the presence of friction, however, shear fracturing becomes a function of both the normal compressive force on the contact and its cohesive strength. In this case, the comparison between the Mohr-Coulomb criteria and the LEFM criteria falls apart, from the observation that the Mode II critical fracture toughness, a material property in LEFM, would be dependent on the stress field (Equation (4.23)) , which is a function of the load. While these differences will prove significant when shear is a dominant mechanism for fracture propagation, they are not expected to be significant in the current application, as hydraulic fracturing is expected to occur primarily in Mode I.

4.4 Mode I Fracture in Mixed-Mode Loading

As a final test of the relationship between the HFDDA and the LEFM fracture criteria, it was desired to see how well the DDA could reproduce characteristics of a Mode I LEFM fracture undergoing mixed-mode loading. To create a mixed-mode stress field, far-field tensile stress can be applied to a crack oriented at an angle β to the stress plane (Figure 4.9.A). When $\beta \neq 0$, the crack is subject to both Mode I and Mode II loading. To facilitate modeling, an equivalent stress system can be defined for a

horizontal crack by using a new coordinate axis that coincides with the angled crack. Using the new coordinate system, the original far-field stress can be resolved into its normal and shear components, as shown in Figure 4.9.B. In general, for stresses applied in an *x-y* coordinate system, an equivalent set of stresses may be defined in a new x'-*y'* coordinate system at an angle β to the original using the definitions

$$\begin{aligned}
\sigma_{x'x'} &= \sigma_{xx}\cos^2\beta + \sigma_{yy}\sin^2\beta + 2\tau_{xy}\sin\beta\cos\beta \\
\sigma_{y'y'} &= \sigma_{xx}\sin^2\beta + \sigma_{yy}\cos^2\beta - 2\tau_{xy}\sin\beta\cos\beta \\
\tau_{x'y'} &= \tau_{xy}\left(\cos^2\beta - \sin^2\beta\right) + \left(\sigma_{yy} - \sigma_{xx}\right)\left(\sin\beta\cos\beta\right)
\end{aligned} \tag{4.25}$$

In the current problem, $\sigma_{xx} = 0$, $\tau_{xy} = 0$, and $\sigma_{yy} = \sigma_f$. Substitution of these expressions into Equation (4.25) yields

$$\begin{aligned}
\sigma_{x'x'} &= \sigma_f \sin^2\beta \\
\sigma_{y'y'} &= \sigma_f \cos^2\beta \\
\tau_{x'y'} &= \sigma_f \left(\sin\beta\cos\beta\right)
\end{aligned} \tag{4.26}$$

For the mixed-mode loading shown in Figure 4.9.B, the stress intensity factors may be given by [97]

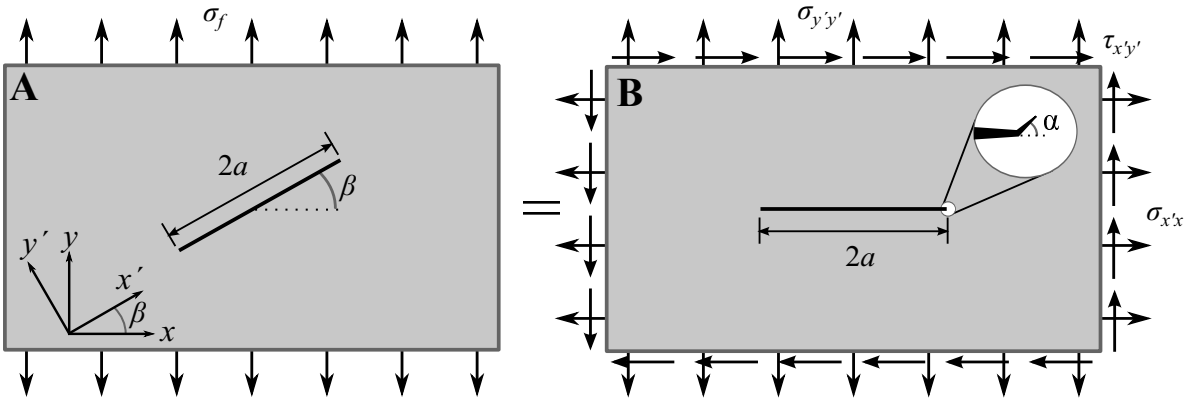

Figure 4.9: Crack in an infinite plane oriented at an angle β to the stress plane. **A** shows the original crack, while **B** shows an equivalent loading on a horizontal crack. The inset on **B** shows the definition used for the propagation angle α relative to the crack tips.

$$K_I = \sigma_{y'y'}\sqrt{\pi a} = \sigma_f \cos^2(\beta)\sqrt{\pi a}$$
$$K_{II} = \tau_{y'x'}\sqrt{\pi a} = \sigma_f \sin(\beta)\cos(\beta)\sqrt{\pi a} \quad (4.27)$$

For fractures subject to mixed loading, the so-called G-criterion can be used to determine the onset of Mode I failure in the component body. In two dimensions, the G-criterion can be expressed as

$$K_{IC}^2 = K_I^2 + K_{II}^2 \quad (4.28)$$

Using the relationship for K_{IC} and T_0 as given in Equation (4.13) and the stress intensity definitions in Equation (4.27), Equation (4.28) may be rewritten as

$$\left[T_0\left(\sqrt{\pi L/2}\right)\right]^2 = \left[\sigma_f \cos^2(\beta)\sqrt{\pi a}\right]^2 + \left[\sigma_f \sin(\beta)\cos(\beta)\sqrt{\pi a}\right]^2 \quad (4.29)$$

Given this relationship, for a defined T_0 and L, Mode I fracture should occur when

$$\sigma_f^2 = \frac{T_0^2 L}{2a\left(\cos^2(\beta)\right)\left(1+2\sin(\beta)\cos(\beta)\right)} \quad (4.30)$$

To simulate the mixed-mode loading in the DDA, a new mesh was generated containing 1 m x 1 m blocks in an inner 30 m x 20 m mesh, surrounded by a coarser 160 m x 160 m outer mesh. Each block in the inner mesh was subdivided into four triangles, and horizontal cracks of half-lengths ranging from 0.0 m to 5.0 m were placed in the center. The background stress field was set to correspond to a crack oriented at an angle of $\beta = 30°$. Using the maximum strain energy release rate criteria as discussed in [97], propagation from a fracture oriented at $\beta = 30°$ should initiate at an angle of $\alpha = -45°$ from the fracture tip (Figure 4.9.B, inset), down the diagonals of the inner domain. For these simulations, Mode I fracturing was allowed along any fracture within the inner domain, and Mode II fracturing was restricted through the use of a large cohesive

strength. Two different tensile strengths (T_0 = 1 MPa and T_0 = 5 MPa) were given to the fractures in the inner domain. At the boundaries of the domain, tensile and shear stresses were applied using the expressions in Equation (4.26). The far-field stress σ_f was incremented in units of 2 kPa when T_0 = 1 MPa and in units of 10 kPa when T_0 = 5 MPa, and was applied to the system until the fracture propagated, defined here as the far field stress at which the first joint fully failed on both sides of the initial crack.

The results of the tests for the mixed-mode stress field are shown graphically in Figure 4.10. In each subplot, the equivalent far field tensile force at which failure occurred in the DDA simulations is shown, as well as the values predicted theoretically in Equation (4.30). In each case, fracturing initiated at an angle of -45° to the horizontal, in

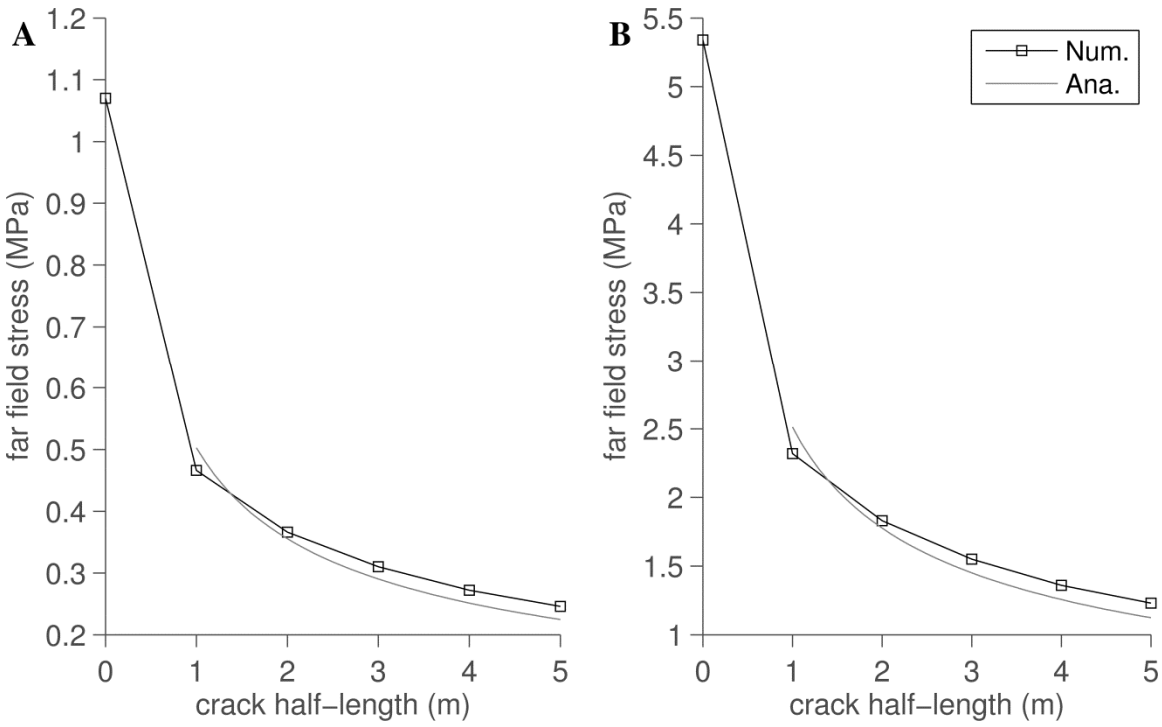

Figure 4.10: Comparison of the DDA results and theoretical results for Mode I fracturing of a crack in a mixed-mode stress field at different tensile strengths. **A** shows the results when T_0 = 1 MPa, while **B** shows the results when T_0 = 5 MPa.

accordance with LEFM. As with the horizontal Mode I fractures, the fit between the DDA values and the values predicted theoretically was very good for both T_0 = 1 MPa and T_0 = 5 MPa. Indeed, in this case the fit was actually better for smaller half-lengths than that observed when the horizontal fracture was fully perpendicular to the direction of the far field stress, while the agreement at larger half-lengths was comparable.

To tie together the results of these three sections, it would appear that the maximum tensile stress criterion as implemented in the DDA yields very similar results to the values that would be predicted by LEFM in Mode I. For each example of Mode I fracturing, when the mesh size was small relative to the size of the initial crack, very good agreement was observed between the DDA and the predicted theoretical values. For Mode II fracturing, the agreement between the DDA and the theoretical values was not as close, but both methods displayed similar trends in the shape of the far field stress curve in the absence of friction. When friction is present, the Mohr-Coulomb criterion in the DDA and the LEFM criteria are inherently incompatible, due to the Mohr-Coulomb criterion's dependence on normal stress. Together, these results suggest that the fracture criteria in the HFDDA can serve as a reasonable surrogate for LEFM criteria in studies of Mode I fracture propagation, as is the case for hydraulic fracturing.

4.5 Toughness-Storage KGD Fracture

Having established the relationship between the HFDDA fracture criteria and the stress intensity fracture criteria used in LEFM, it was next desired to see how well the fracture criteria in the HFDDA extended to LEFM models of hydraulic fracturing. In Chapter 3, the HFDDA was validated against the analytical solution for a viscosity-

storage dominated hydraulic fracture, or one for which the rock matrix has no tensile strength. In this section, the HFDDA is compared against the solution for a toughness-storage dominated KGD fracture [22], or one for which the toughness of the rock matrix is the dominant control of fracture propagation. In particular, it was desired to see if the relationship derived for K_{IC} and T_0 in Equation (4.13) would continue to apply during simulations of hydraulic fracturing.

In the toughness-storage dominated regime, the viscosity of the fluid approaches zero $(\mu \to 0)$ and no leakoff occurs through the fracture walls $(C_L = 0)$. As with the storage-viscosity KGD fracture, the solution is defined by the fracture half-length $l(t)$, the fracture aperture $w(x,t)$, and the net pressure distribution $p(x,t)$, where x is the distance along the fracture away from the injection point and t is the time. The HFDDA results can be compared to the semi-analytical solution for half-length of the fracture and the pressure and fracture width at the injection point, which are given by

$$l(t) = \psi(t)\Gamma(t); \quad w(x,t) = \zeta(t)\psi(t)\Omega(\xi,t); \quad p(x,t) = \zeta(t)E'\Phi(\xi,t) \quad (4.31)$$

where all variables are as defined previously. For the no-leakoff, no-viscosity regime, the solutions for Γ, Ω and Φ are each self-similar and may be stated independent of time. At the injection point, Ω takes on the value of $\Omega_0 \simeq 0.7323$ and Φ is given as $\Phi_0 \simeq 0.1831$. For a Newtonian fluid, $\Gamma \simeq 0.9324$. The dimensionless parameter $\zeta(t)$ and the fracture length scaling $\psi(t)$ are given by

$$\zeta(t) = \left(\frac{K'}{E'(Q_0 t)^{1/4}} \right)^{4/3}, \quad \psi(t) = \left(\frac{E'Q_0 t}{K'} \right)^{2/3} \quad (4.32)$$

where again all variables are as defined previously.

Table 4.1: KGD toughness-storage parameters

Rock Parameters	
Initial Density, ρ_r	2,650 kg/m^3
Young's Modulus, E	25 GPa
Poisson's Ratio, v	0.25 [-]
Fluid Parameters	
Reference Density, ρ_f	1000 kg/m^3
Fluid Bulk Modulus, K_f	2.2*10^9 Pa
Injection Rate, Q_0	4.0 kg/s
Viscosity, μ	1*10^{-3} Pa-s
Carter's Leakoff Coefficient, C_f	0.0 m/s
Numerical Parameters	
Normal Spring Multiplier, k_n	100*E
Shear Spring Constant, k_s	100*E
Time step, dt	0.5 s
Total time, t	10.0 s

For the HFDDA simulation, a grid was generated consisting of a 144 m x 60 m inner mesh surrounded by a 200 m x 180 m outer mesh. Fracturing was limited to the horizontal line passing through the center of the grid, and was confined to the inner mesh. As in the tests between the HFDDA and the LEFM criteria, two different levels of discretization (L = 0.5 m and L = 1.0 m) were tested against two different tensile strengths (T_0 = 1 MPa and T_0 = 5 MPa). To approximate the zero-viscosity condition, the viscosity was set to 1/1000 the viscosity of water, or 1*10^{-3} mPa-s. All other simulation parameters are provided in Table 4.1.

Figure 4.11 and Figure 4.12 show the results of the HFDDA simulations for the different combinations of mesh discretization and tensile strength. Additionally, the analytical solutions from Equation (4.31) are given, with K' derived using the relationship for K_{IC} and T_0 developed in Equation (4.13). As may be seen, all four cases displayed relatively good agreement between the HFDDA and the analytical solutions for

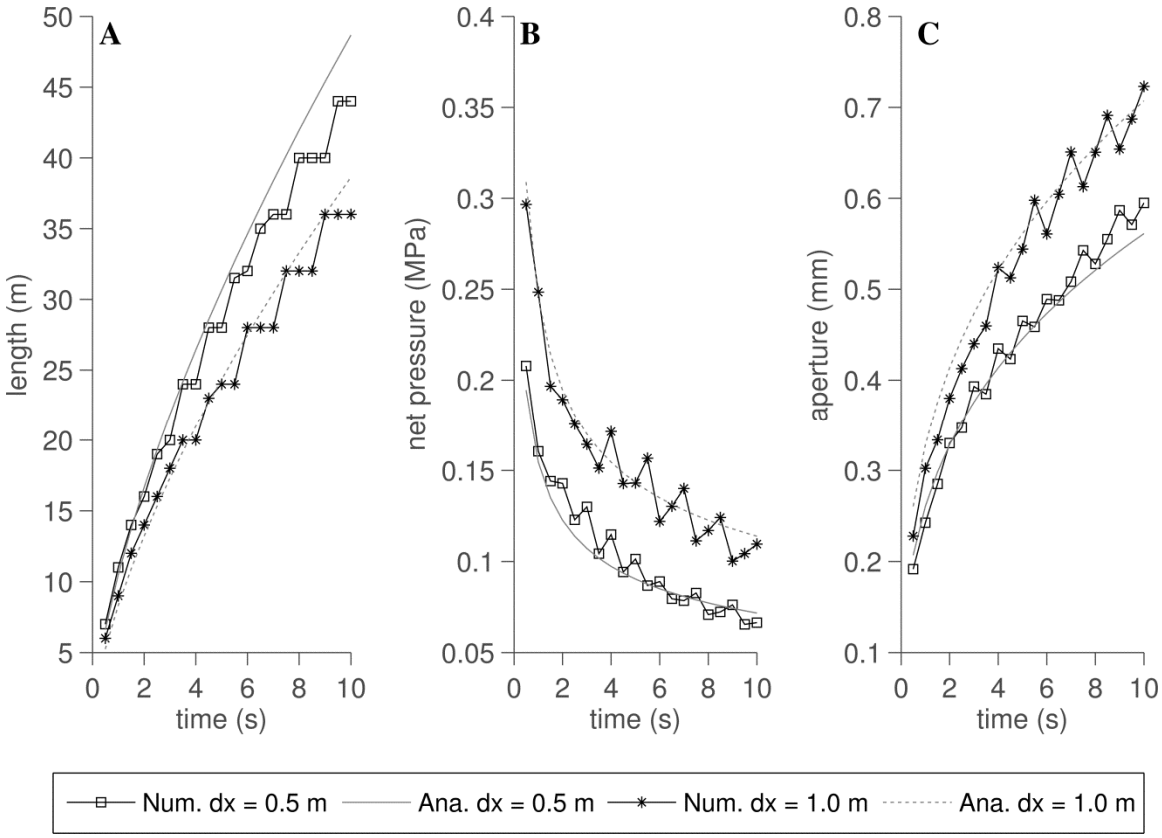

Figure 4.11: Numerical and analytical results for the toughness-storage KGD solution when T_0 = 1 MPa at different levels of discretization. **A** shows the half-length of the fracture, **B** shows the pressure at the injection point, and **C** shows the width of the fracture at the injection point.

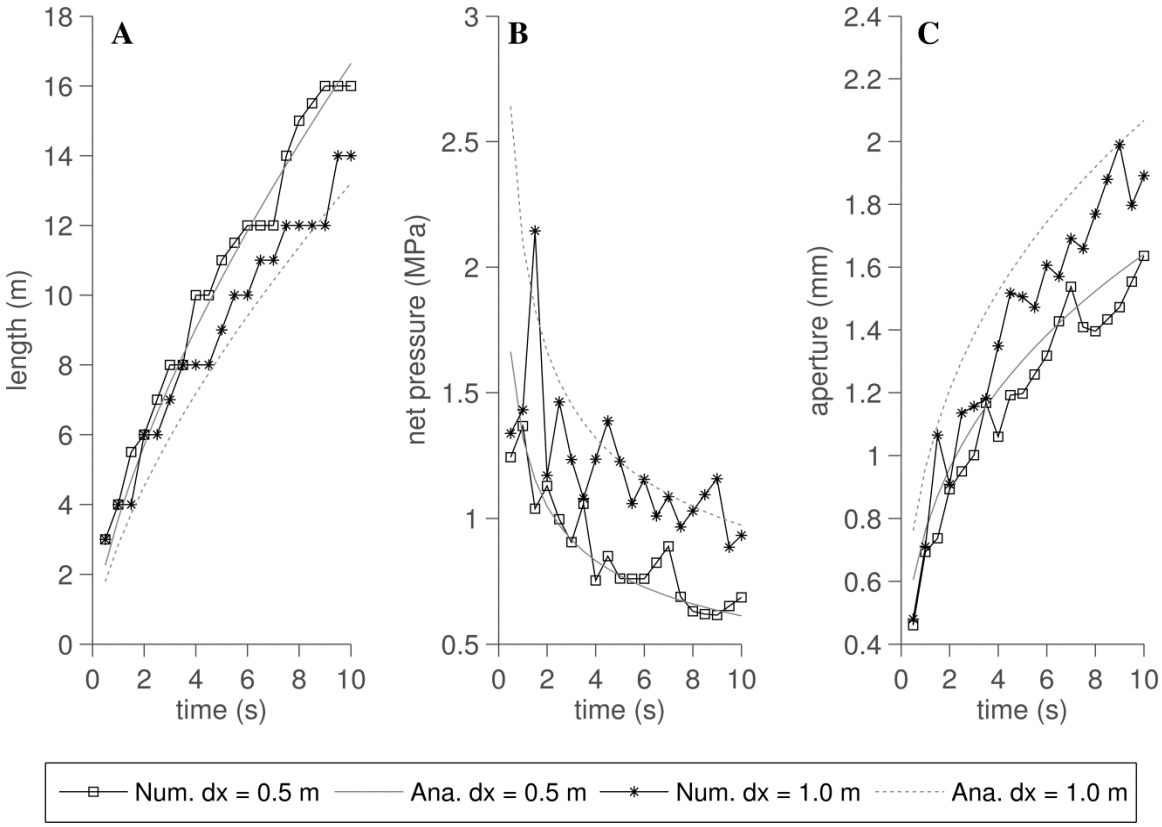

Figure 4.12: Numerical and analytical results for the toughness-storage KGD solution when T_0 = 5 MPa at different levels of discretization. **A** shows the half-length of the fracture, **B** shows the pressure at the injection point, and **C** shows the width of the fracture at the injection point.

injection pressure, fracture width and fracture length. When the tensile strength was lower (T_0 = 1 MPa), the fracture progressed to a farther length and the fracture width was narrower compared with the fracture geometry using a higher tensile strength of (T_0 = 5 MPa). Some discrepancies exist between the HFDDA results and the analytical solution, however, which in general may be explained as the result of the discretization required in the HFDDA, and as a result of the constant growth assumption employed by the analytical solution. In all four HFDDA simulations, the length of the fracture grows in a stair-step pattern which grows increasingly pronounced as the simulation progresses. In Section 4.2, it was demonstrated that the force necessary to continue the propagation of a fracture will be less than the force required to initiate it. In the KGD solution, at later times when the fracture has grown large, each incremental change to the fracture length results in a proportionately smaller change in the pressure magnitude. Once the pressure has risen sufficiently to initiate fracturing at later times in the HFDDA, multiple fractures may open rather than just one, as the pressure may remain high enough to open multiple fractures despite incremental growth in the fracture length. In the analytical solution, it was assumed that the fracture would propagate smoothly as a function of time.

A second discrepancy observed in the HFDDA solutions is that the pressure and width from each simulation oscillate around the values predicted by the analytically. In both the HFDDA and in the analytical solution, as the fluid viscosity goes toward zero, pressure within the fracture becomes more uniform. Because the fluid is modeled as a compressible fluid in the HFDDA, the uniform pressure that develops in the fracture is a direct function of the volume available for the injected fluid. As a result of the discrete nature of the HFDDA, the HFDDA solution cannot grow as smoothly as the analytical

solutions, and as mentioned will cause the fracture length to propagate in discrete intervals. As a result, if the fracture in the HFDDA has propagated slightly beyond the distance predicted by the analytical solution, the width and pressure will each be lower, while if the fracture has not traveled as far, the width and pressure will be greater. Interestingly, this pressure oscillation is not observed in the storage-viscosity solution from Section 3.2, in part because the fracture pressure in that solution decreases over the length of the fracture, rather than remaining uniform across the fracture length as in the toughness-storage solution. These results suggest that the HFDDA is better able to model situations when viscosity is the main determinant of fracture propagation, rather than fracture toughness, though the results for fracture toughness dominated simulations are still very good.

Beyond the relative agreement of the solutions, the key observation for these simulations is to note that for a constant T_0, both the analytical and numerical solutions will change based solely on the discretization. When T_0 = 1 MPa and L = 0.5 m, the fracture traveled a distance of almost 45 m, while when T_0 = 1 MPa and L = 1.0 m, the fracture traveled just over 35 m, an 8 to 9 m difference. Again, the physical interpretation of these results is that by Equation (4.13), the Mode I fracture toughness changes as a function of both the tensile strength of a joint and the discretization of the fracture. These results suggest that the HFDDA can correctly reproduce problems based on LEFM, but that the solution will be dependent on both T_0 and L.

Given this dependence, it was desired to see if the same value of K_{IC} would produce the same results for the KGD solution using different values of L and T_0. To test this idea, two additional simulations were performed, using values of K_{IC} derived to

match those used in the simulations in which (T_0 = 1 MPa, L = 0.5 m) and (T_0 = 5 MPa, L = 0.5 m). For the first simulation, K_{IC} was equal to 0.886 MPa-m$^{1/2}$, while for the second, K_{IC} was equal to 4.33 MPa-m$^{1/2}$. For these new simulations, the mesh was generated using a discretization of L = 1.0 m, leading to tensile strengths of 0.707 MPa and 3.536 MPa respectively. Figure 4.13 and Figure 4.14 show the results for the new simulations and compare them both with the results of the simulations for L = 0.5 m and with the theoretical results. In general, the results match well with the analytical solution and are not significantly different than those from the original simulations using L = 0.5 m. The agreement observed when K_{IC} = 0.886 MPa-m$^{1/2}$ was slightly better than that when K_{IC} = 4.33 MPa-m$^{1/2}$, just as the agreement was better for the original simulations when the lower value of tensile strength was used in comparison with the larger. Thus it may be said that for the same value of K_{IC}, derived using different combinations of T_0 and L, the results generated using the HFDDA will be similar, with the solutions growing closer as the value of T_0 becomes smaller. Altogether, these findings suggest that the fracture criteria applied in the HFDDA are suitable for comparison with hydraulic fracturing problems based on LEFM.

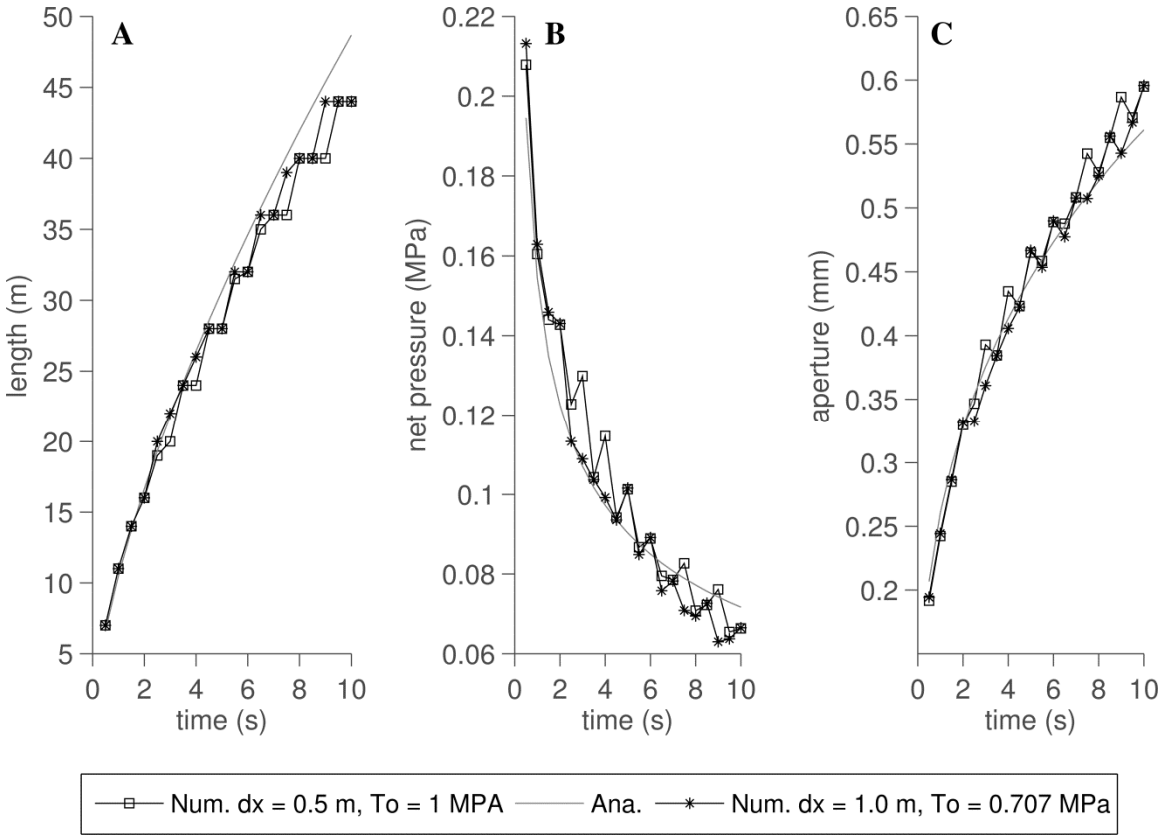

Figure 4.13: Numerical and analytical results for the toughness-storage KGD solution when K_{IC} = 0.886 MPa-m$^{1/2}$ for two different combinations of discretization and tensile strength. **A** shows the half-length of the fracture, **B** shows the pressure at the injection point, and **C** shows the width of the fracture at the injection point.

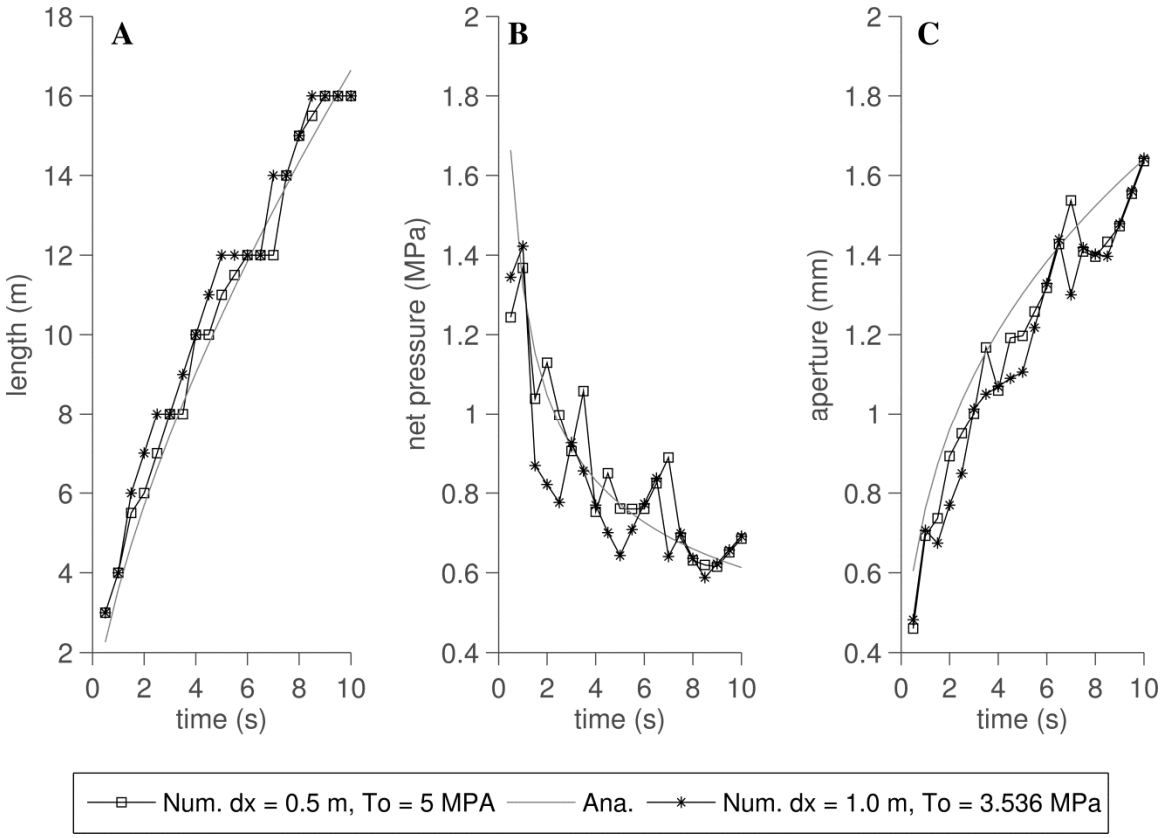

Figure 4.14: Numerical and analytical results for the toughness-storage KGD solution when K_{IC} = 4.33 MPa-m$^{1/2}$ for two different combinations of discretization and tensile strength. **A** shows the half-length of the fracture, **B** shows the pressure at the injection point, and **C** shows the width of the fracture at the injection point.

4.6 Summary

In this chapter, the maximum tensile stress and Mohr-Coulomb model of fracturing as applied in the DDA and the HFDDA was demonstrated to agree well with the LEFM model of fracturing. Additionally, the HFDDA was shown to be capable of reproducing toughness dominated LEFM solutions for hydraulic fracturing, even when the toughness of the rock medium is not explicitly considered as an input parameter. In demonstrating these relationships, it is shown that the HFDDA is compatible with other existing models of hydraulic fracturing based upon LEFM fracturing criteria, and that the maximum tensile stress and Mohr-Coulomb criteria, which are much more easily implemented within distinct element methods than the LEFM criteria, are adequate for hydraulic fracture modeling. Together with the verification studies from the previous chapter, this analysis confirms the suitability of the HFDDA for hydraulic fracturing in homogeneous media and paves the way for the study of hydraulic fracturing in pre-fractured media, which will be seen in the next chapter.

5 HYDRAULIC FRACTURING IN NATURALLY FRACTURED RESERVOIRS

In this Chapter, the HFDDA is extended to model hydraulic fracturing in the presence of pre-existing natural fractures. First, the theory behind the interaction of natural fractures and propagating hydraulic fractures is discussed. Changes to the algorithm needed to accommodate natural fractures are detailed and verified through comparison with the results of the interaction of a propagating hydraulic fracture with a single natural fracture. Finally, the application of the HFDDA in the context of stochastic fracture networks is considered, and the algorithm is applied to a case study of hydraulic fracturing in the Marcellus Shale.

5.1 Hydraulic Fracturing in Naturally Fractured Reservoirs

Up until this chapter, hydraulic fracturing was considered primarily within the context of unfractured, homogeneous media. In practice, however, natural gas reservoirs are frequently interspersed with pre-existing natural fractures which serve as conduits for fluid flow. These natural fractures can have a dramatic impact on the geometry of propagating fractures. Rather than the bi-wing fractures predicted for homogeneous media, pre-existing natural fractures can lead to the formation of complex fracture networks during hydraulic fracturing treatments, as evidenced by microseismic monitoring of fracture propagation (e.g. [57]). These complex networks will have very different fracture “footprints” than their bi-wing counterparts, which will result in very different flow and production properties for targeted reservoirs. Frequently, the presence of natural fractures will serve to greatly enhance reservoir production. For example, in

recent years particular attention has been given to the production of natural gas from the Marcellus Shale, a highly fractured formation within the Appalachian Basin in the Northeastern United States (Figure 5.1). Encompassing over 100,000 square miles from New York to Tennessee, the Marcellus currently holds one of the largest volumes of recoverable natural gas in the United States. This gas was largely thought to be unrecoverable prior to 2008, as new wells drilled into the Marcellus would quickly dry up and gas flows could not be sustained. New advances in horizontal drilling and hydraulic fracturing, however, have allowed the Marcellus to be produced economically and have led to a dramatic increase in natural gas production from the formation. In 2007, the Marcellus region was producing just over one billion cubic feet of natural gas per day (bcf/d). As of September 2014, that number had exceeded 16 bcf/d [98].

Two primary joint sets exist in the Marcellus Shale, both of which serve to increase the reservoir area contacted during any given stimulation treatment of the formation [99]. Due to a unique geological coincidence, one of the primary joint sets in the Marcellus lies almost parallel with the direction of the maximum compressive stress in the region. To maximize production, horizontal wells can first be drilled perpendicular to this joint set, allowing fluid to be drained from each joint intersected by the well. Hydraulic fracturing can then be performed throughout these horizontal wells, causing fractures to propagate perpendicular to the direction of minimum compressive stress and intersect the joints in the second set, greatly increasing the formation area drained during the treatment. Given the potential impact of natural fractures on hydraulic fracture propagation and reservoir production, the study of fracturing in naturally fractured reservoirs and the uncertainties involved deserves further attention. Before diving into

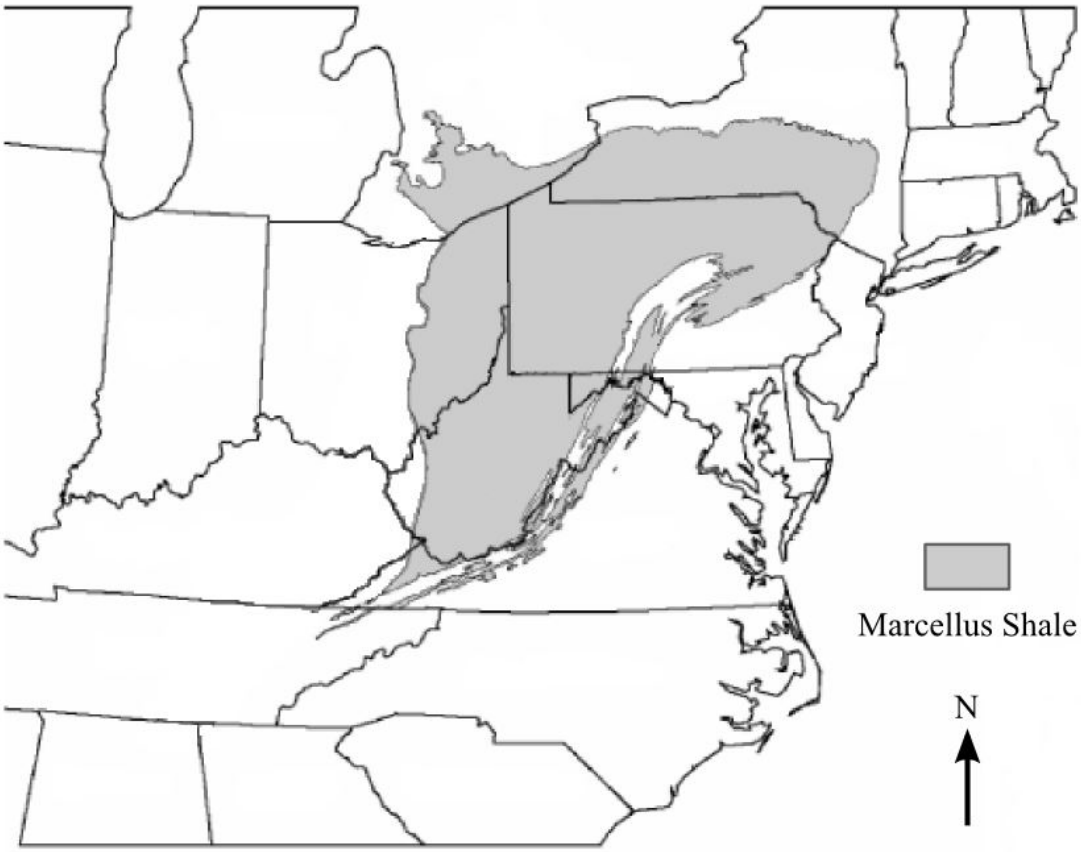

Figure 5.1: Location of the Marcellus Shale in the Northeastern United States. Image adapted from [100].

these topics, however, it is worth looking at the effect that an individual natural fracture might have on a propagating hydraulic fracture.

At the level of individual fractures, various theoretical, numerical and experimental studies (e.g., [68, 101-103]) have shown that hydraulic fractures propagating in two dimensions will interact with natural fractures in one of three different ways. The propagating hydraulic fracture can 1) cross the existing natural fracture, 2) open the existing fracture, or 3) shear at the intersection with the existing fracture and arrest (Figure 5.2). A fourth option, which may be viewed as a combination of the others can occur when the hydraulic fracture opens the natural fracture but then crosses it at an offset point. In the first option, when the hydraulic fracture crosses the natural fracture, no branching occurs and the hydraulic fracture will continue to grow. In the second case, if the fracture opens the natural fracture, the hydraulic fracture will change direction and potentially form multiple branches, leading to the formation of a complex fracture network. For the third option, if the fracture is arrested, the propagating fracture is effectively stopped and further injection serves only to widen the fracture. As a result, arresting fractures can lead to poorer production rates for a reservoir, as premature

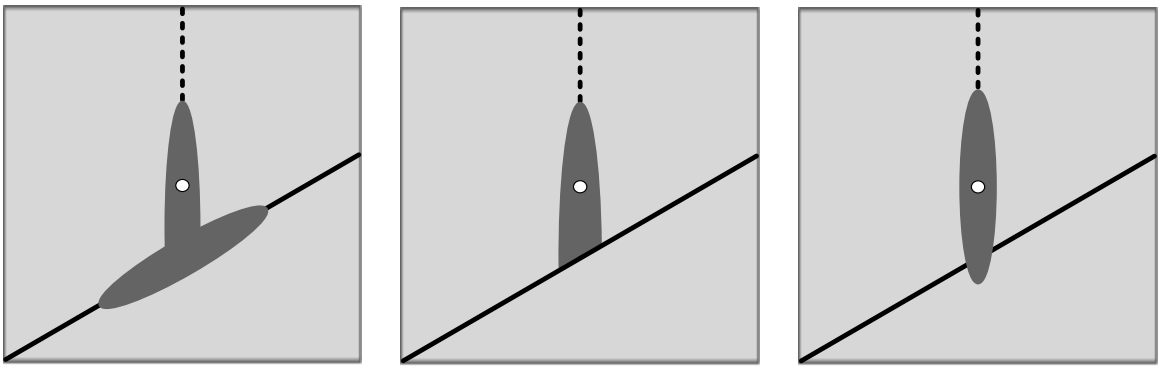

Figure 5.2: Potential opening modes when a hydraulic fracture intersects a natural fracture.

arresting of the propagating fracture will prevent the hydraulic fracture from propagating and contacting more of the reservoir.

To accurately model the interaction of hydraulic fractures with natural fractures within the HFDDA, some changes were required to the contact algorithm. Up to this point, only tensile fracturing had been considered, as hydraulic fracturing in unfractured rock is generally expected to occur in tension. To model the arrest of hydraulic fractures with natural fractures, however, failure in shear must also be considered. Shear failure was incorporated into the HFDDA as follows: First, in all of the current simulations, shear failure of the rock was allowed only along the natural fractures. Confining shear failure to just the natural fractures is enforced by using an extremely high cohesive strength along any contacts forming part of the rock body. Second, in the same manner previously established for tensile fractures, shear failure is allowed only at pressurized nodes and at nodes where another contact has already failed, either in an opening or a sliding mode. Introduction of this criteria localizes any shear failure along a fracture to the fracture tip, rather than allowing multiple contacts along a natural fracture to slide all at the same time. When shear failure was not localized at the fracture tip, convergence difficulties were encountered during testing.

Addition of shear failure into the HFDDA increased the complexity of the contact method, and was found to have a direct impact on the algorithm's ability to converge. To allow the program to converge successfully, a few adjustments were required. When using the version of the algorithm discussed up to this point, it was found that the open-close contact iterations could prove unable to converge, in particular when the propagating hydraulic fracture encountered a junction that consisted of multiple natural

fractures. When the hydraulic fracture reached this type of junction, the contact states would occasionally enter a cycle from which they could not exit and the algorithm would stall. In the original version of the DDA, stalling in the open-close iterations was dealt with by lowering the time step. It was found that in the HFDDA, however, the inability of the open-close states to converge was more a function of the discrete nature of the contact states rather than the time step size, and as a result, lowering of the time step did not lead to improved convergence. To deal with this problem, a workaround was introduced. In the current version of the algorithm, each successive open-close state of the contacts is stored, up to the 50 most recent. After each open-close iteration, the previous states are checked for cycling. If it is determined that the contact states are cycling, the algorithm will search all of the previous contact states for each contact contained within the cycle and find the one that is the most open (no contact springs is more open than only a normal spring, which is more open than a normal and shear spring). Each contact is then assigned the most open state that it had achieved, and the DDA is solved again using these contact states. Upon convergence of the inner fluid-structure iterations, convergence of the new open-close state is not checked, but rather the algorithm proceeds to the next step, checking the convergence of the fractures open to fluid. The obvious limitation of this method is that when invoked, the algorithm can move forward with a non-converged contact state. It was found, however, that the contact states would generally resolve after a subsequent time step or two, once more fluid was injected into the system and fluid pressures were able to rise.

The second change made to the algorithm deals with the application of the Augmented Lagrangian Method (ALM). During testing, it was noticed that resolving the

external forces on shearing contacts could lead to very long convergence times for the ALM. Frequently, pairs of shearing forces would develop in which positive gains to one force were offset by losses to another, leading to the inability of the ALM force updates to converge. To resolve this problem, a two-tiered approach was introduced for the contact forces. Previously, the ALM was used to solve for all of the contact forces. For the simulations involving pre-existing fractures, however, the ALM is used to solve only those contacts that exist at un-fractured joints. For all other contacts (sliding contacts, and any contacts that opened and have since closed again), the original penalty method is used and the contact forces at these contacts are not iterated. This change to the contact algorithm resulted in drastic improvements to the speed of the HFDDA, with only a marginal effect on the accuracy of the overall solution.

The final problem that arose dealt with the closing of open fractures and affected the convergence of the inner iterations. If a fracture closed suddenly during a simulation, its volume and transmissivity would sharply decrease, causing the pressure to drastically increase at that node. Very large pressures coupled with very small fracture volumes and transmissivities led to the failure of the inner iterations to converge, as the fluid iterations in the affected nodes came to be dominated by their stability constants, rather than by the governing fluid flow equations. Two different solutions were developed for this problem. The first, which was applied to all of the natural fractures in general, was to use different values of the stability constant for those nodes on the main fracture branch and those off of it. As before, nodes on the main fracture branch were defined as those having at least two contacts fully open, while those off of the main fracture branch have less than two. For the following simulations, nodes off of the main branch were given a stability

constant of 0.01 times the stability constant for the nodes on the main branch. The second solution developed for this problem was to allow the width of a fracture to close only gradually, as mentioned in Chapter 2.

5.2 Experimental Comparison

To verify these proposed changes, and to verify the HFDDA's ability to model correctly the interaction between hydraulic and natural fractures, the HFDDA was compared against the results of a hydraulic fracturing experiment published by Blanton in [68]. In numerous studies of hydraulic fracture interaction with natural fractures ([68, 101, 102]), the interaction mechanism between the propagating hydraulic fracture and the pre-existing natural fracture was found to be heavily dependent on the differential background stress ($\Delta\sigma$) and the angle of approach (θ) between the two fractures. In Blanton's experiment, the influence of these terms on the interaction mechanism of

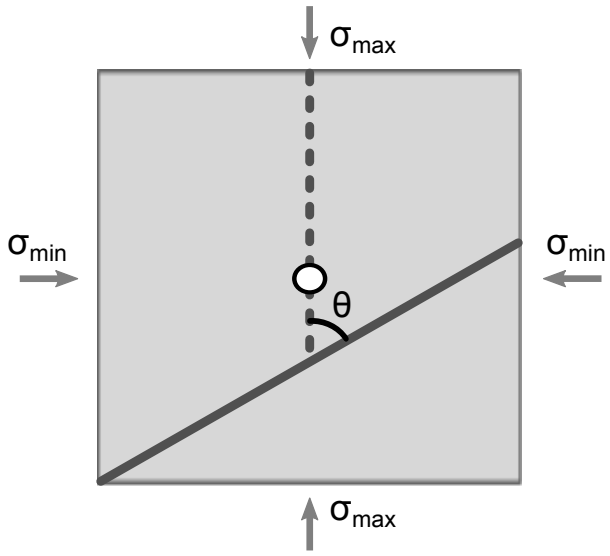

Figure 5.3: Geometry for Blanton Experiment.

intersecting fractures was examined using 11 blocks of hydrostone, each formed with a single pre-existing fracture set at varying angles within the block (Figure 5.3). Various combinations of $\Delta\sigma$ and θ were applied to each block, and the resulting interaction mode of the natural and hydraulic fracture was observed. To create the pre-existing fracture in each block, hydrostone was poured into a 12 in. x 12 in. x 15 in. mold with the long dimension horizontal, tilted at the angle desired for the natural fracture. After pouring the hydrostone to a level approximately 1 in. below where the central borehole would be drilled, the mold was righted and the rest of the mold was filled. A 1/8 in. central borehole was drilled to a depth of 8 in. and cased with 7 in. of steel tubing, leaving a 1 in. area open at the center of the block. Each block of hydrostone was placed into a triaxial load frame and hydraulically fractured subject to varying degrees of background stress. Fracturing fluid was injected into the blocks at a constant rate of 0.05 in^3/s until the propagating hydraulic fracture interacted with the natural fracture, and the interaction mechanism observed in each block was recorded.

To recreate Blanton's experiments using the HFDDA, simulation parameters were applied as shown in Table 5.1. Of the rock parameters listed in Table 5.1, only the Young's Modulus and Poisson's ratio of the rock were given explicitly in [68], though all other parameters fall within a reasonable range. The tensile strength of hydrostone was estimated as 6.0 MPa, which is approximately 1/10 the magnitude of the material's advertised compressive strength of 69 MPa [104]. For the natural fractures formed within the hydrostone, Blanton estimated that their friction coefficient was between 0.5 and 0.75 $\left(\theta = [26.56, 36.86]\right)$. Additionally, it was assumed that the natural fractures did not have any cohesive or tensile strength as a result of the forming process, and that they had a

Table 5.1: HFDDA parameters used to reproduce Blanton's experiment

Rock Parameters	
Initial Density, ρ_r	2,650 kg/m^3
Young's Modulus, E	10 GPa
Poisson's Ratio, v	0.22 [-]
Tensile Strength, T_0	6.0 MPa
Friction Angle, ϕ	35°
Fluid Parameters	
Reference Density, ρ_f	1000 kg/m^3
Fluid Bulk Modulus, K_f	2.2 GPa
Viscosity, μ	20 mPa-s
Carter's Leakoff Coefficient, C_f	0.0 m/s
Injection Rate, Q_0	2.16 cm^3/s
Natural Fracture Parameters	
Tensile Strength, T_0	0.0 MPa
Cohesive Strength, C_0	0.0 MPa
Natural Fracture Width, w_0	1.0 μm
Friction Angle, ϕ	35°
Numerical Parameters	
Normal Spring Constant, k_n	30*E
Shear Spring Constant, k_s	30*E
Time Step, dt	1 min 30 s
Simulation Time	1 hr 7.5 min

uniform initial width of 1 μm. For the fluid parameters, the injection rate of the fluid was derived for plane strain conditions by normalizing the injection rate used in the experiments by the depth of the rock blocks (38.1 cm). The viscosity of the fluid was not specified by Blanton, and as such a viscosity characteristic of a medium-viscosity fracturing fluid was used. Geometrically, the hydrostone blocks used by Blanton were simulated as 30 cm x 30 cm blocks in plane strain, surrounded by a boundary of blocks with fixed points in each corner which served to stabilize the simulation. Natural fractures were placed such that they passed about 4 cm beneath the injection point, slightly farther than the 2.5 cm mentioned by Blanton. The extra 1.5 cm was used to accommodate the initially open fractures required in the HFDDA. Rock blocks were discretized using a constrained Delaunay triangulation generated by the program *Triangle* [90], with the area of each triangle limited to be no greater than 2 cm^2.

The results from Blanton's experiments and the HFDDA numerical results are given in Table 5.2. In general, the HFDDA results showed excellent agreement with the interaction modes observed in Blanton's experiments, as each HFDDA experiment was able to reproduce the interaction mode observed by Blanton. The interaction modes were found to be strongly dependent on the angle of approach and the differential stress applied to the block sample, as demonstrated graphically in Figure 5.4. At lower angles of approach and lower values of differential stress, the natural fracture would open when the propagating fracture intersected it. At moderate values of these parameters, the propagating fracture would arrest, while at larger values, the propagating fracture would cross over the natural fracture. Occasionally in the HFDDA results, there was some overlap between the opening and arresting modes. For instance, in simulation CT14, the

Table 5.2: Results from Blanton's experiments compared with the HFDDA results

Test ID	θ (°)	σ_{max} (MPa)	σ_{min} (MPa)	Δσ (MPa)	Blanton	HFDDA
CT9	30	20	5	15	Arrest	Arrest
CT7	30	19	10	9	Opening	Opening
CT11	45	20	5	15	Arrest	Arrest
CT12	45	18	5	13	Arrest	Arrest
CT13	45	16	5	11	Arrest	Arrest
CT14	45	14	5	9	Arrest	Arrest (+1 Opening)
CT22	45	10	5	5	Opening	Opening
CT8	60	20	5	15	Crossing	Crossing
CT21	60	14	5	9	Arrest	Arrest
CT4	60	12	10	2	Opening	Opening
CT20	90	14	5	9	Crossing	Crossing

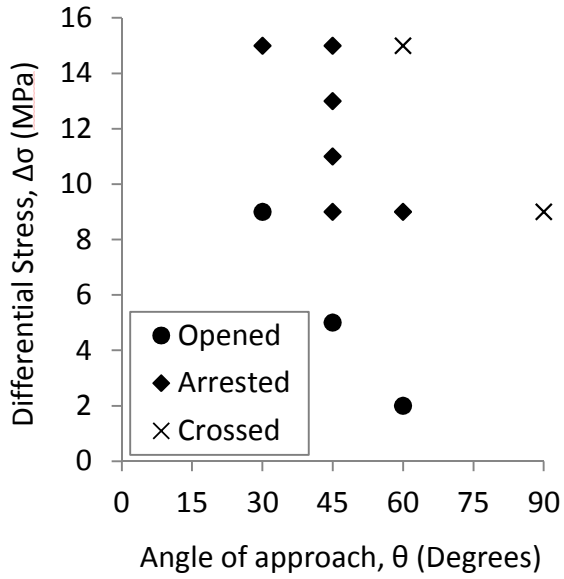

Figure 5.4: Interaction modes observed in Blanton's experiment for different combinations of differential stress and angle of approach. The HFDDA was able to simulate each of these interaction modes correctly.

propagating fracture eventually arrested, but only after opening one joint along the pre-existing natural fracture. At higher stress differentials for the same fracture angle, the joint remain closed. Ultimately, the results of this verification experiment demonstrate the ability of the HFDDA to model accurately the interaction of propagating hydraulic fractures with natural fractures, and lay the foundation for hydraulic fracturing modeling in complex fracture networks.

5.3 Fracture Networks

To apply the HFDDA to hydraulic fracture modeling in complex fracture networks, the first challenge lies in characterizing the pre-existing fracture systems that may exist within a reservoir. In typical discrete fracture network (DFN) models, the spacing and geometry of each fracture in a fracture set is generated stochastically, using different density functions for the length, width and location of the fractures. Fractures are "grown" from points distributed throughout the rock domain, resulting in 2D fracture maps similar to that in Figure 5.5. Fractures can be spaced very close together as a result of this procedure and rarely will intersect precisely. A triangular mesh generated using fractures sampled as in Figure 5.5 would result in widely different block sizes throughout the mesh, as pockets of small blocks will be formed in the interior of closely spaced fractures and at any location where the end of a fracture is close to, but not exactly coincident with another joint. In testing, it was found that these pockets of small blocks greatly hamper the algorithm's speed and ultimately can prevent its convergence. Attempts were made to address these issues by adjusting the length and intersection angle of problematic joints, but ultimately were abandoned, as artificial changes to the length

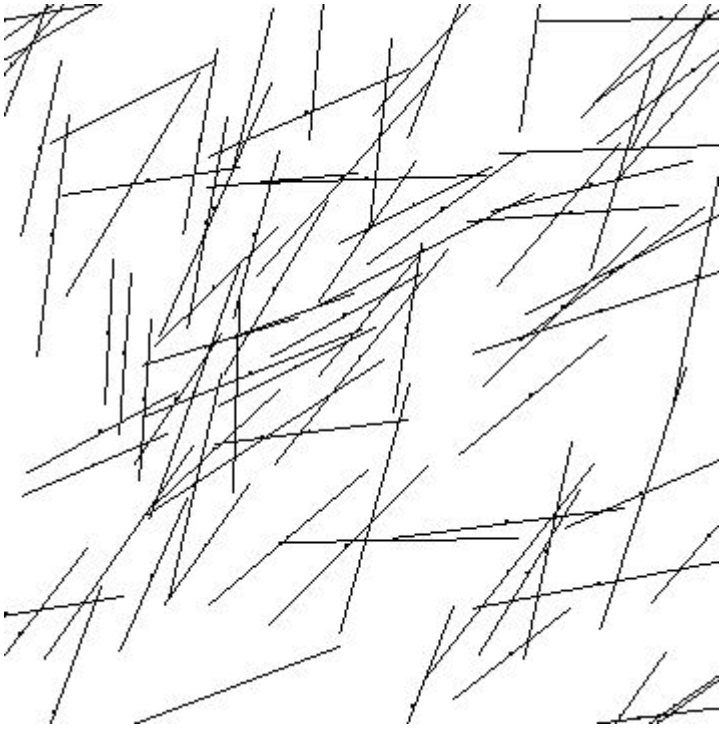

Figure 5.5: Sample 2D discrete fracture network created using typical stochastic methods for network simulation.

and intersection angle of fractures would remove the underlying statistical properties of the fracture network.

To counter these difficulties, a different method for defining fracture sets was developed for the HFDDA. In this method, the rock matrix is first discretized into a Delaunay triangulation with initial fractures placed at each fluid injection point. Next, each fracture set within the domain is assigned a pre-defined azimuth relative to the domain's *y*-axis. All of the joints in the Delaunay triangulation that occur at this azimuth, plus or minus a small range, are then marked as potential candidates for the fracture set. To generate individual fractures, a percentage of these joints are selected as seeds by sampling a value for each joint from a uniform distribution ranging between zero and one. If the sampled value is lower than the specified percentage, the fracture is marked as a

seed. Next, a random length is sampled for each seed fracture from a range defined for the joint set. In the following examples, lengths are sampled using a uniform distribution, though any distribution may be assigned. Once the length is selected, each seed fracture is "grown" by adding in the joint adjacent to the seed with an azimuth closest to that of the fracture set. Joints are continually added onto the ends of each growing fracture until every fracture in the set has reached its sampled length.

Four examples of fracture patterns generated using this method are shown in a 250 m x 250 m domain in Figure 5.6 - Figure 5.9. In each figure, the blocks forming the mesh were constrained to be no greater than 25 m^2 in area. Two fracture sets were generated for each domain, one having a primary azimuth of 45° and the other with an azimuth of 135°. For the generation of these sets, any fracture within ±5° of the azimuth was taken as a candidate fracture. For the first two figures, 12% were selected as seed values from which fractures were grown. For the fracture lengths, both sets were assigned uniform distributions with minimum length of 20 m and maximum length of 40 m. Figure 5.6 and Figure 5.7 represent two different realizations of the fracture domain using these parameters. As seen in both figures, the fractures produced using this method generally follow the azimuth direction predicted for each set, and have lengths that fall within the uniform range assigned. Occasionally, however, the fractures effectively grew into each other, resulting in fractures with lengths larger than those given by the distribution. In the next two figures, Figure 5.8 shows a realization of the network in which the length distribution of each fracture set was halved relative to the values for the first two sets, while Figure 5.9 shows a realization of the network in which the percentage of selected candidate fractures was halved. In both instances, the connectivity of the

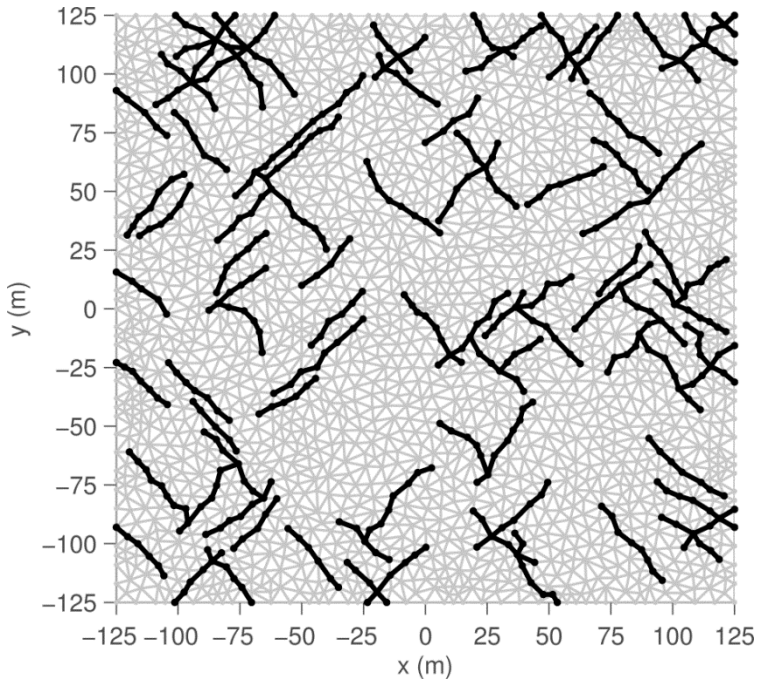

Figure 5.6: Sample fracture pattern generated from two fracture sets oriented at 45° and 135°. Both fracture sets have minimum and maximum lengths of 20 m and 40 m, and were generated using a fracture density of 12%.

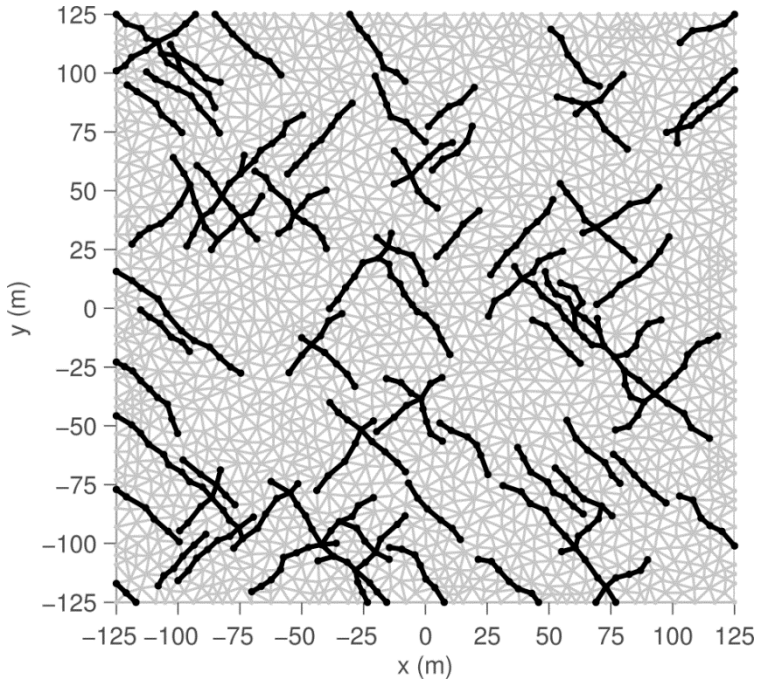

Figure 5.7: Second sample fracture pattern generated using the same fracture set parameters, but a different seed value than the network in Figure 5.6.

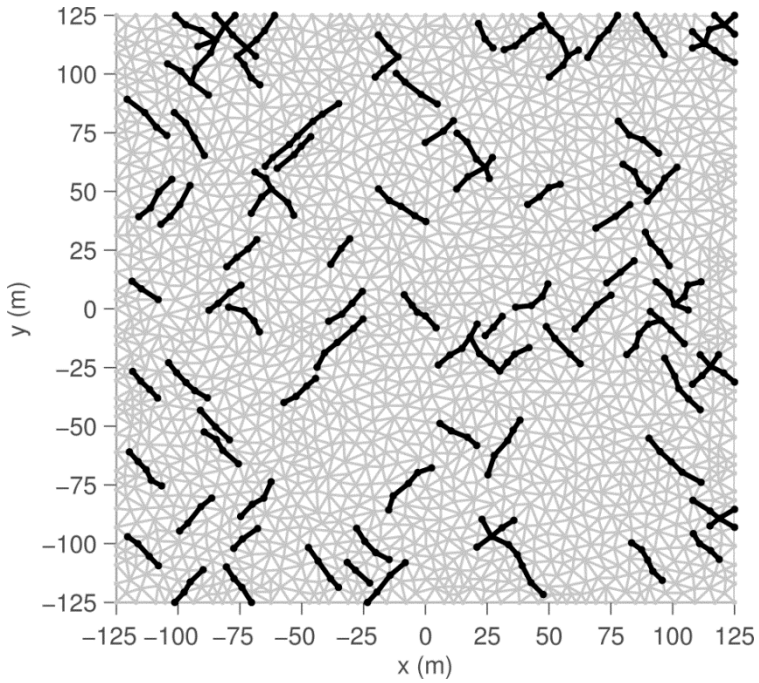

Figure 5.8 Fracture pattern generated using the same fracture set parameters and seed value as those used in Figure 5.6, but with the minimum and maximum fracture lengths reduced to 10 m and 20 m respectively.

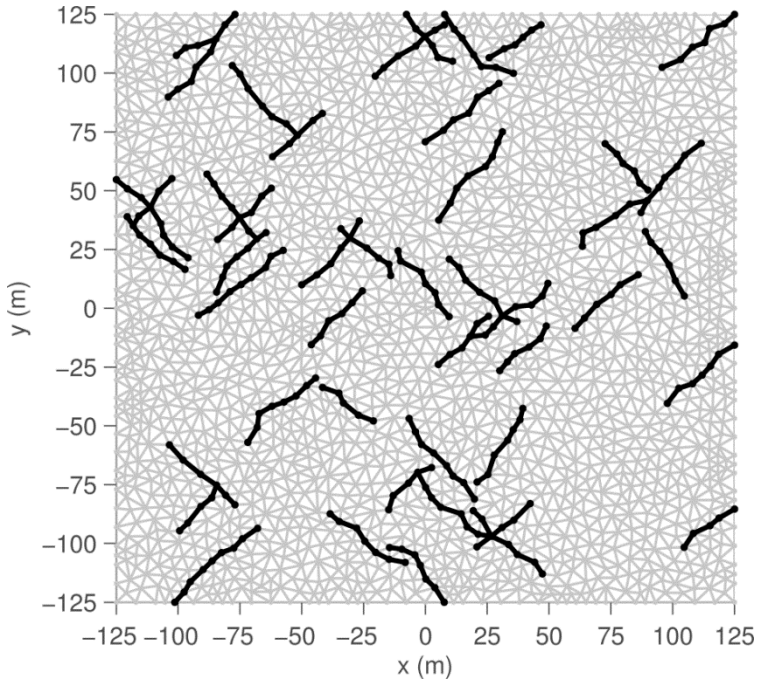

Figure 5.9 Fracture pattern generated using the same set parameters and seed value as those from Figure 5.6, but with the percentage of selected fractures reduced to 6% .

network was greatly reduced. Having shorter fractures decreases the likelihood that each fracture would intersect another fracture, while decreasing the number of candidate fractures creates fewer fractures in the system overall.

Notably, there are a few key limitations of this method relative to actual systems. First, the uniform distributions used for fracture location and length are atypical for discrete fracture network simulations. Uniform distributions were chosen for their simplicity, though other distributions may be used instead. Second, and perhaps more importantly, fractures can be no shorter than the length of a side of a Delaunay triangle, and they can be spaced no closer together than allowed by the triangulation. Thus, very small fractures and very close fractures can be considered only on fine meshes which may prove too expensive computationally for large reservoirs. For large reservoirs, therefore, the current algorithm may best be considered as an approximation of the dominant fracture features in a domain, as opposed to an exact representation of the reservoir's fracture distribution. If one or two fractures are known to be dominant in a reservoir, or if the effects of hydraulic fracturing on a large feature such as a fault are under consideration, these can be included explicitly by incorporating them into the Delaunay triangulation.

To demonstrate the HFDDA's ability to model the hydraulic fracturing of complex fracture networks, fracturing was simulated in two different hypothetical reservoirs. The first reservoir used the natural fracture pattern shown in Figure 5.6, while the second used a network with similar parameters, but with fracture sets generated with azimuths of 0° and 90°. Two simulations were performed for each reservoir, one with $\Delta\sigma = 0$ MPa , and the other with $\Delta\sigma = 12$ MPa . As before, when $\Delta\sigma = 0$ MPa , stresses

Table 5.3: Parameters used in fracture network simulations

Rock Parameters	
Initial Density, ρ_r	2,650 kg/m^3
Young's Modulus, E	10 GPa
Poisson's Ratio, v	0.22 [-]
Tensile Strength, T_0	6.0 MPa
Friction Angle, ϕ	35°
Fluid Parameters	
Reference Density, ρ_f	1000 kg/m^3
Fluid Bulk Modulus, K_f	2.2 GPa
Carter's Leakoff Coefficient, C_f	0.0 m/s
Viscosity, μ	20 mPa-s
Injection Rate, Q_0	1000 cm^3/s
Natural Fracture Parameters	
Tensile Strength, T_0	0.0 MPa
Cohesive Strength, C_0	0.0 MPa
Natural Fracture Width, w_0	100.0 μm
Friction Angle, ϕ	35°
Numerical Parameters	
Normal Spring Constant, k_n	30*E
Shear Spring Constant, k_s	30*E
Time Step, dt	1 min
Simulation Time	1 hr

of 5 MPa were applied to all sides of the reservoir. When $\Delta\sigma = 12$ MPa , a stress of 5 MPa was applied as the minimum principal stress, and a stress of 17 MPa as the maximum. In these and all remaining simulations, the stress differential between the maximum and minimum stress was examined as an input parameter rather than the ratio of the maximum and minimum stress, in keeping with the analysis of fracture interaction modes from the experimental studies of fracturing mentioned previously ([68, 101, 102]). Other parameters common to all of the simulations are given in Table 5.3, and the fracture patterns generated as a result of these simulations are shown in Figure 5.10 – Figure 5.13. In these figures, natural fractures are shown by the thin black lines, joints with at least one open contact by the thick gray lines, and joints for which both contacts are locked or sliding, but which have also been invaded by fluid, are shown by the thin gray lines. When a joint contains at least one open contact, the rock has separated and the hydraulic fracture has successfully propagated along that joint. If both contacts remain locked or sliding, the blocks along the joint are closed, but fluid may still invade the joint, either because the joint is part of a natural fracture, or because the joint was open and then closed at a later point in the simulation, leaving behind a residual width as discussed in Chapter 2.

When $\Delta\sigma = 0$ MPa , the direction of fracture propagation was predominantly influenced by the azimuth of the natural fracture sets. With no background stress differential to govern the direction of fracture propagation, the hydraulic fracture tended to open any contacted natural fractures and subsequently propagate outward from their tips. In the network generated using fracture sets oriented at 45° and 135°, the bulk of the hydraulic fracture propagated parallel to the 135° fracture system, as the first natural

fracture intersected occurred at 135° (Figure 5.10). When the propagating fracture intersected a natural fracture oriented at 45°, however, the natural fracture largely remained closed, due to the stress exerted upon it by the fluid in the main fracture branch and the applied background stress. For the network generated using fracture sets oriented at 0° and 90°, the direction of fracture propagation was again dominated by the orientation of the natural fractures (Figure 5.11). Below the injection point, the fracture intersected a natural fracture and opened it, changing direction by 90° from the direction of the initially opened fractures. As the fracture continued to propagate, it changed direction once more after hitting a second natural fracture. In both simulations, the orientation of the natural fracture network was the primary determinant of the fracture's propagation direction.

It is interesting to note that for these simulations, even though the stress differential was set to zero, not all of the natural fractures opened. Rather, a primary fracture branch is clearly seen to develop in both simulations, while most of the adjacent natural fractures remain closed. Significantly, these results suggest that even in the presence of natural fractures, one primary fracture branch will still develop, as opposed to a web of interlocking fractures. Natural fractures attached to the main branch may still be invaded by fluid, however, allowing the fracturing fluid to spread a sizeable distance away from the main fracture branch. This observation runs contrary to what may have been expected based on Blanton's experiment, in which the mode was found to be independent of the fracture orientation relative to the propagating fracture as $\Delta\sigma \to 0$. Possibly, the creation of a main fracture branch is an artifact of the algorithm itself, as fractures are generally required to open one-at-a-time at the tips of the fractures, as

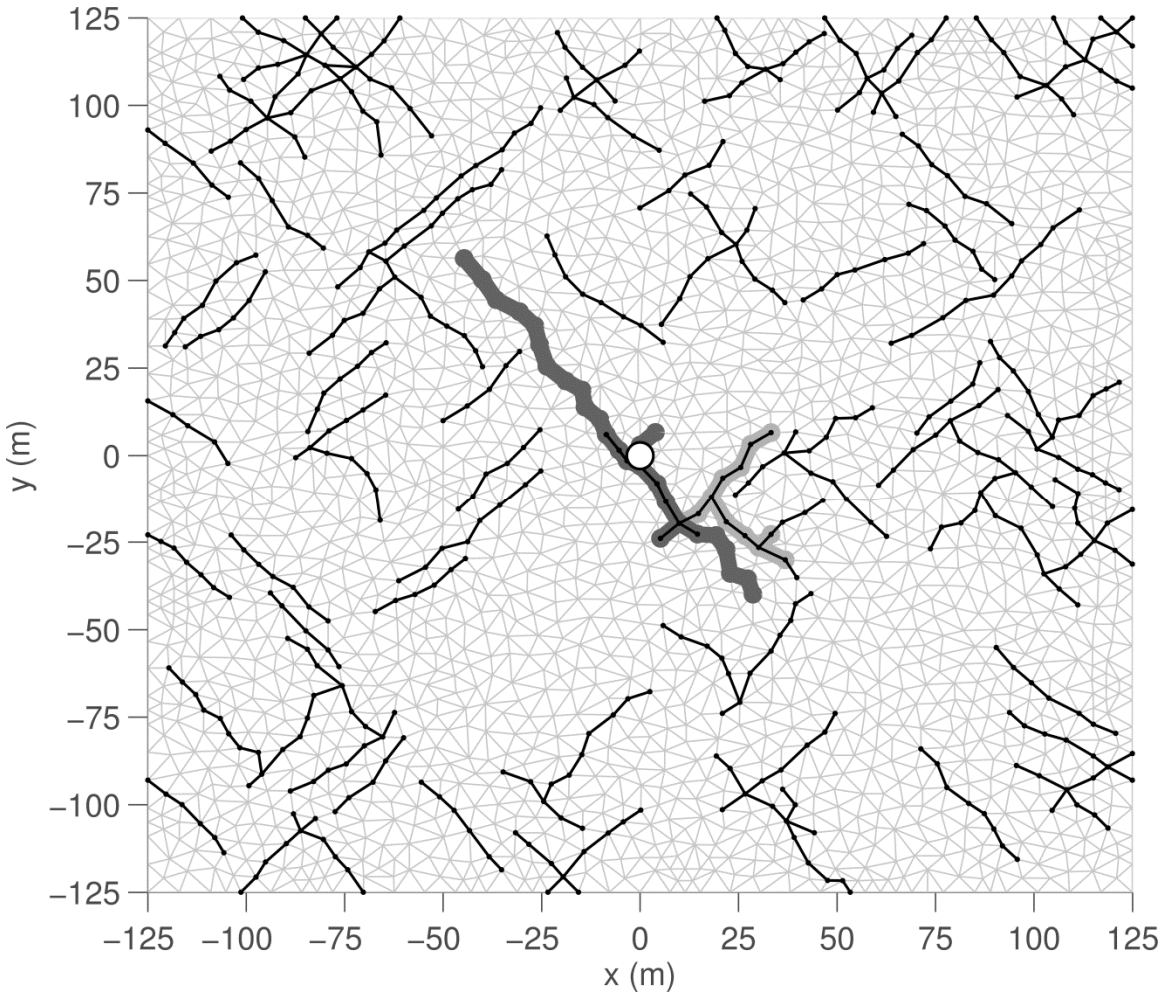

Figure 5.10: Fracture pattern generated for fracture sets oriented at 45° and 135° when $\Delta\sigma$ = 0 MPa, μ = 20 mPa-s, and Q_0 = 1 kg/s. Natural fractures are shown by thin black lines, open fractures by thick dark gray lines, and unopened fractures invaded by fluid by lighter thick gray lines.

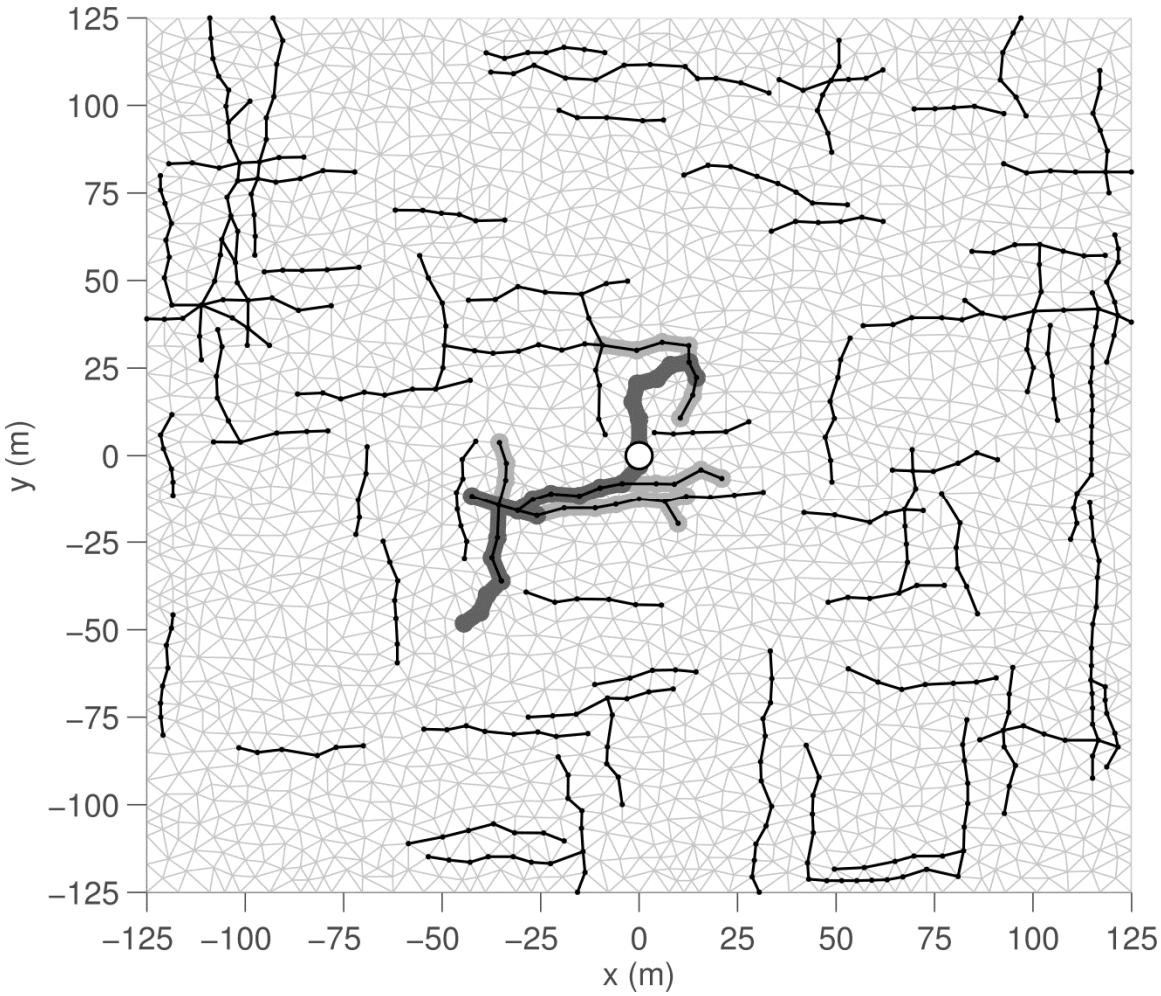

Figure 5.11: Fracture pattern generated for fracture sets oriented at 0° and 90° when $\Delta\sigma$ = 0 MPa, μ = 20 mPa-s, and Q_0 = 1 kg/s. Natural fractures are shown by thin black lines, open fractures by thick dark gray lines, and unopened fractures invaded by fluid by lighter thick gray lines.

discussed in Chapter 2. Given that some of the natural fractures were able to open off of the main fracture branch, however, it appears likely that the phenomenon is not artificial. As a result, these findings are therefore significant in that they suggest that even in a naturally fractured reservoir, most of the fracturing will occur along one primary path.

For the next pair of simulations, in which $\Delta\sigma = 12$ MPa , the propagation direction in the system was dominated by the differential stress. While many of the natural fractures intersected by the hydraulic fracture opened to some degree, fracturing of unbroken rock tended to occur perpendicular to the direction of minimum compressive stress, as opposed to along the natural fractures. In the network with fractures oriented at 45° and 135°, most of the natural fractures connected to the main fracture remained closed (Figure 5.12). Only the natural fracture immediately below the injection point opened along most of its length, likely a result of the small approach angle between the natural fracture and the propagating one. In the network with fractures oriented at 0° and 90°, very few of the natural fractures opened and propagation occurred almost entirely perpendicular to the direction of minimum compressive stress (Figure 5.13). Interestingly, the propagating hydraulic fracture crossed three of the natural fractures located below the injection point, but opened the natural fracture encountered above the injection point. Further, in both simulations, it did not appear that any of the fractures arrested in shear, in contrast to what may have been expected from Blanton's experiment. Based on that experiment, fractures oriented at 45° to the propagating fracture subject to a differential stress of 12 MPa should arrest, as seen in Figure 5.4. Thus it may be said that the experimental results observed by Blanton for individual fracture interaction modes are not generalizable to fracture sets. Rather, the interaction mode appears to be determined

locally, and is subject to the stress conditions created by the background stress, the propagating fracture, and the pressure generated from fluid invasion into nearby natural fractures.

From the results of these four simulations, it would appear that the differential stress is the dominant factor determining the direction of fracture propagation, even within a reservoir with an extensive natural fracture network. When the differential stress was high, the propagation paths taken by the hydraulic fractures were very similar. These results are in stark contrast to those observed when differential stress was low. For those simulations, the fracture propagation path was highly dependent on the orientation of the natural fracture networks. These results are very similar to those observed by Cipolla et al. [57], in which fractures propagating in high differential stress fields were much more independent of the fracture network than those in low differential stress fields. Notably, these results may be particularly relevant during treatments involving multiple fractures initiated from the same well. In high differential stress fields, each initiated fracture may be more likely to remain separate from the other fractures. In low differential stress fields with a high degree of fracture connectivity, however, the fractures may be more likely to travel down natural fractures and merge, which may lead to less overall area contacted during the treatment.

Beyond the analysis of the reservoir characteristics, it was also desired to see what impact changes to the fluid design parameters would have on the fracture propagation pattern. First, the impact of viscosity was examined by increasing the viscosity of the fracturing fluid to $\mu = 100$ mPa-s . Two simulations were performed using this new

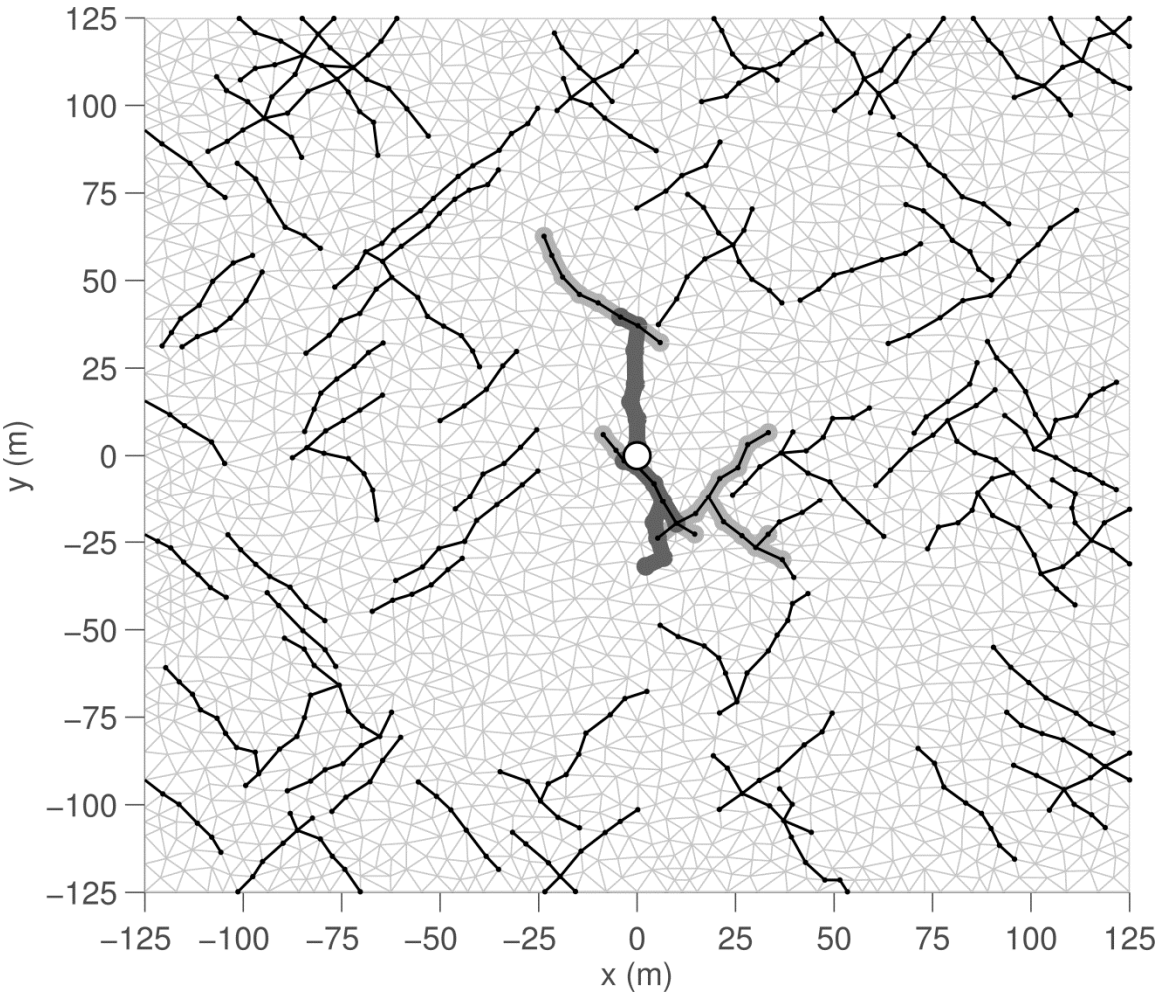

Figure 5.12: Fracture pattern generated for fracture sets oriented at 45° and 135° when $\Delta\sigma$ = 12 MPa, μ = 20 mPa-s, and Q_0 = 1 kg/s. Natural fractures are shown by thin black lines, open fractures by thick dark gray lines, and unopened fractures invaded by fluid by lighter thick gray lines.

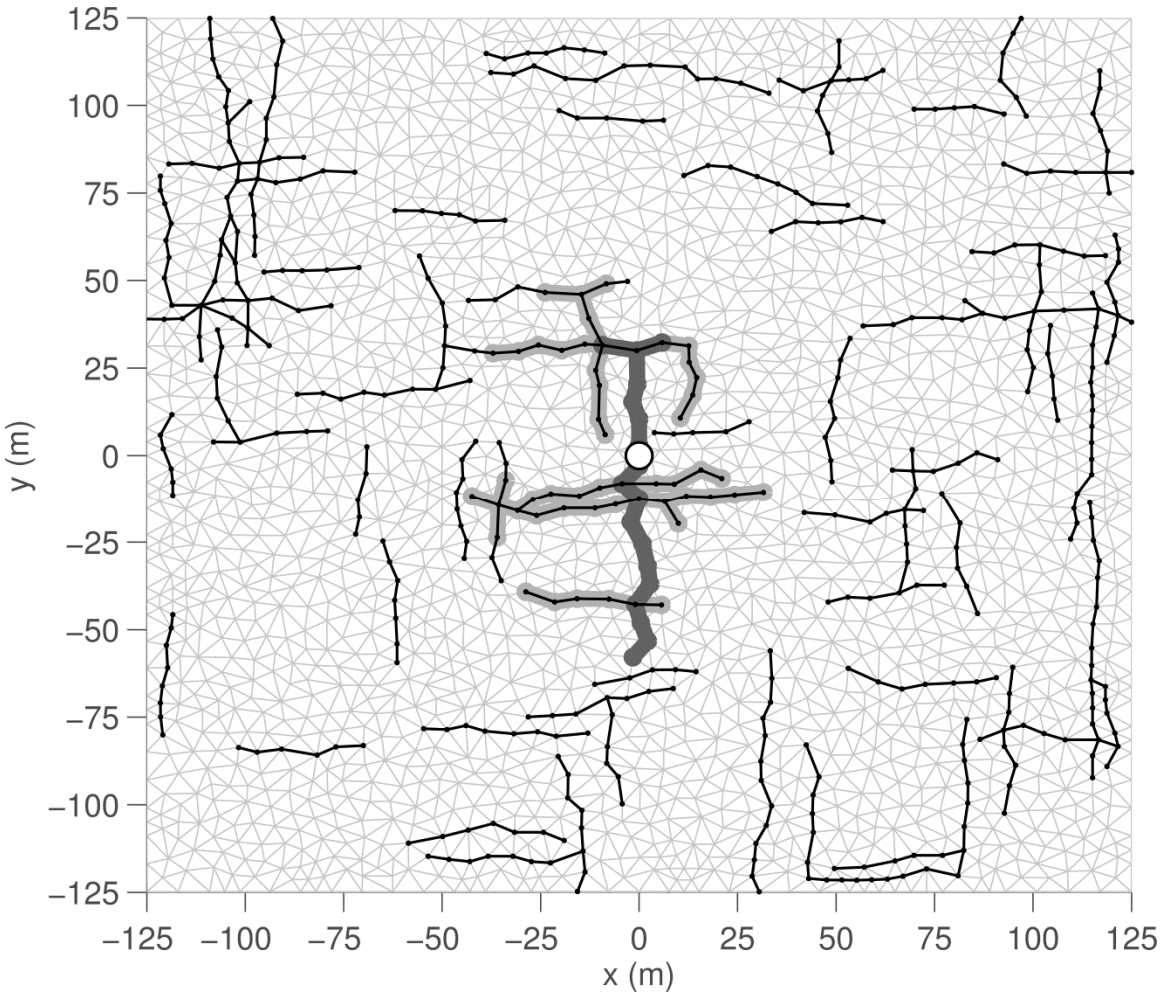

Figure 5.13: Fracture pattern generated for fracture sets oriented at 0° and 90° when $\Delta\sigma$ = 12 MPa, μ = 20 mPa-s, and Q_0 = 1 kg/s. Natural fractures are shown by thin black lines, open fractures by thick dark gray lines, and unopened fractures invaded by fluid by lighter thick gray lines.

viscosity, both using the fracture network shown in Figure 5.6. In the first, $\Delta\sigma = 0$ MPa , while in the second $\Delta\sigma = 12$ MPa . All other parameters are the same as those used in Table 5.3. The results of these simulations are shown in Figure 5.14 and Figure 5.15. With a higher viscosity fluid, it is expected that the fluid will not flow as readily, with the result that the fluid will be less able to invade natural fractures and may be concentrated closer to the fluid's source. In the first simulation, when $\Delta\sigma = 0$ MPa , the fracture pattern generated using the higher viscosity fluid was not significantly different than that generated using the lower viscosity fluid. The only observable change that occurred relative to the lower viscosity fluid is that the fracturing fluid did not invade as far into the natural fracture system below the injection point, but rather stayed closer to the main fracture branch. Similarly, when $\Delta\sigma = 12$ MPa , the higher viscosity fluid did not invade as deeply into the unopened natural fracture networks surrounding the main fracture branch, but the main fracture branch remained unchanged. Based on these results, it would appear that with the viscosities and tensile strengths tested in these simulations, propagation in this system is governed more by the tensile strength of the rock matrix than by the viscosity of the fluid. Had the system been governed by the viscosity, the viscosity should have had a greater effect on the length to which the main fracture propagated, as seen for the viscosity-dominated fracture in Chapter 3. Thus, these results suggest that the primary impact on propagation pattern of lower-viscosity fluids in systems with significant tensile strength is to govern the degree to which fluid will invade the natural fractures. As a design parameter, using a higher-viscosity fluid would therefore be more likely to keep the fracturing fluid closer to the main fracture branch in

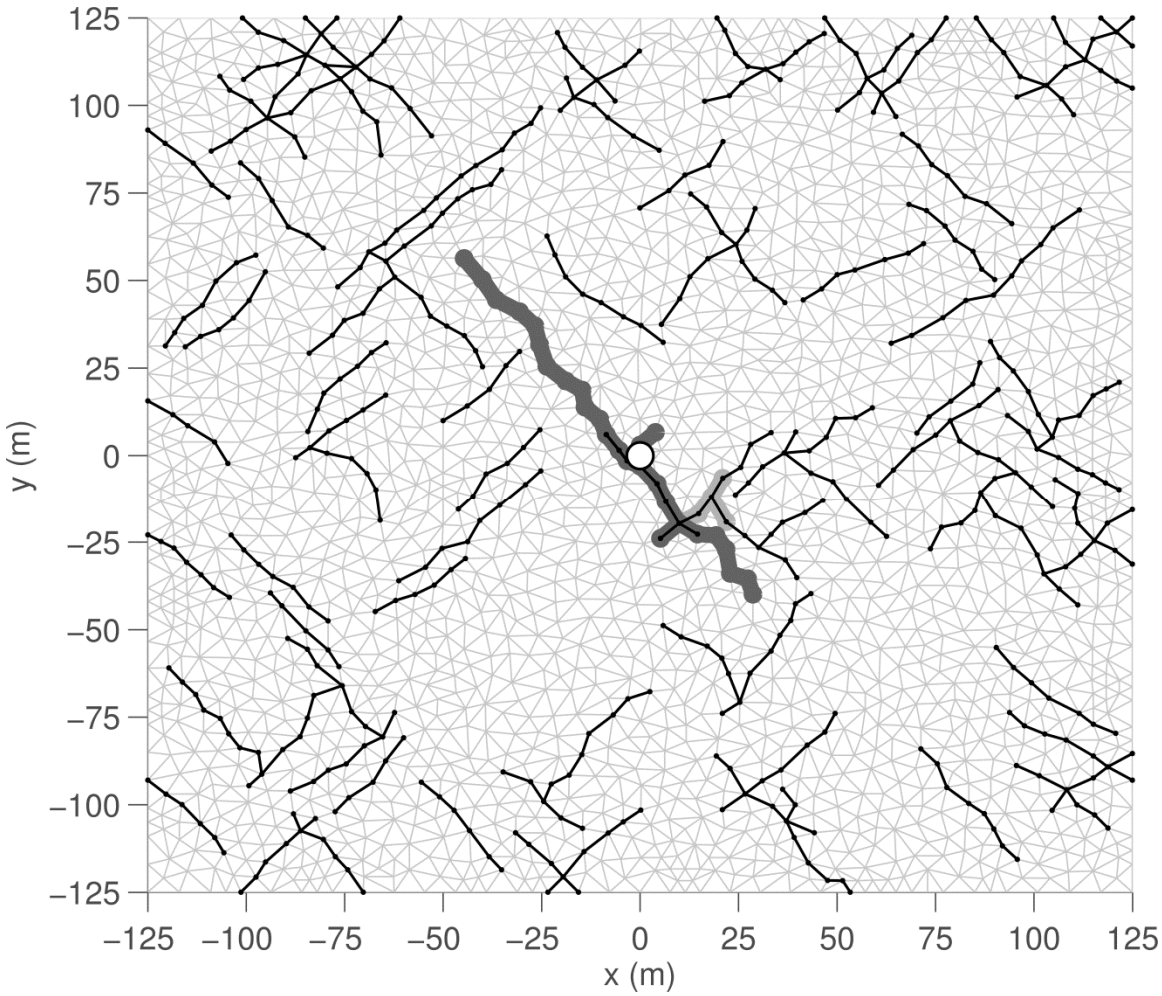

Figure 5.14: Fracture pattern generated for fracture sets oriented at 45° and 135° when $\Delta\sigma$ = 0 MPa, μ = 100 mPa-s, and Q_0 = 1 kg/s. Natural fractures are shown by thin black lines, open fractures by thick dark gray lines, and unopened fractures invaded by fluid by lighter thick gray lines.

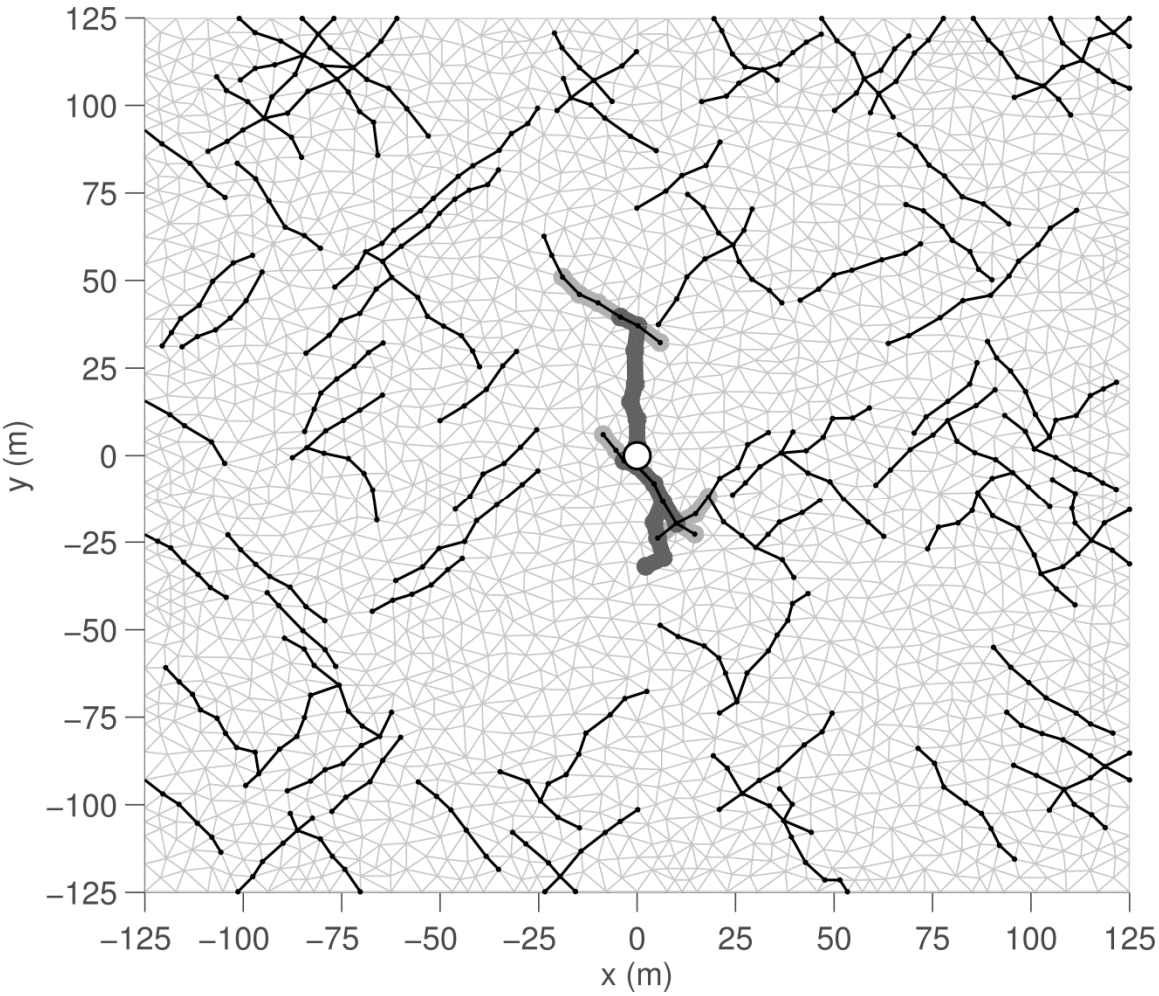

Figure 5.15: Fracture pattern generated for fracture sets oriented at 45° and 135° when $\Delta\sigma$ = 12 MPa, μ = 100 mPa-s, and Q_0 = 1 kg/s. Natural fractures are shown by thin black lines, open fractures by thick dark gray lines, and unopened fractures invaded by fluid by lighter thick gray lines.

these systems, which would prevent it from escaping down natural fractures and leaking off into the rest of the reservoir.

Next, it was desired to see how flowrate might affect the results. The impact of flowrate was examined by doubling the flowrate to $Q_0 = 2$ kg/s, applied to the same fracture network as before. For this simulation, only the background stress of $\Delta\sigma = 0$ MPa was considered. The simulation time was halved to 30 min, such that the simulation reflects the same total mass of injected fluid as used previously, and the time step was halved such that the same mass is injected in each time step as in the previous simulations. With this combination of parameters, doubling the fluid injection rate was found to have very little impact on the propagation pattern generated for the system (Figure 5.16). Relative to the results from the very first simulation, in which $Q_0 = 1$ kg/s, *dt* = 1 min and the simulation time is equal to 1 hr (Figure 5.10), the only difference in the propagation pattern is that the fluid penetration into the natural fractures was slightly less than that observed when $Q_0 = 1$ kg/s.

Taken together, these results suggest that the fluid design parameters will play a much less important role than the differential stress and fracture network orientation in determining the direction of fracture propagation, at least in an impermeable system such as the one modeled. It is worth noting, however, that based on experimental evidence (e.g. [105]), both of these properties can have a strong impact on the propagation of hydraulic fractures. The discrepancy between the results observed here vs. the experimental results is largely due to the assumption of an impermeable material in the HFDDA. For a permeable material, both viscosity and injection rate will control the rate at which fluid leaks off into the rock matrix. While leakoff can be modeled with the HFDDA using

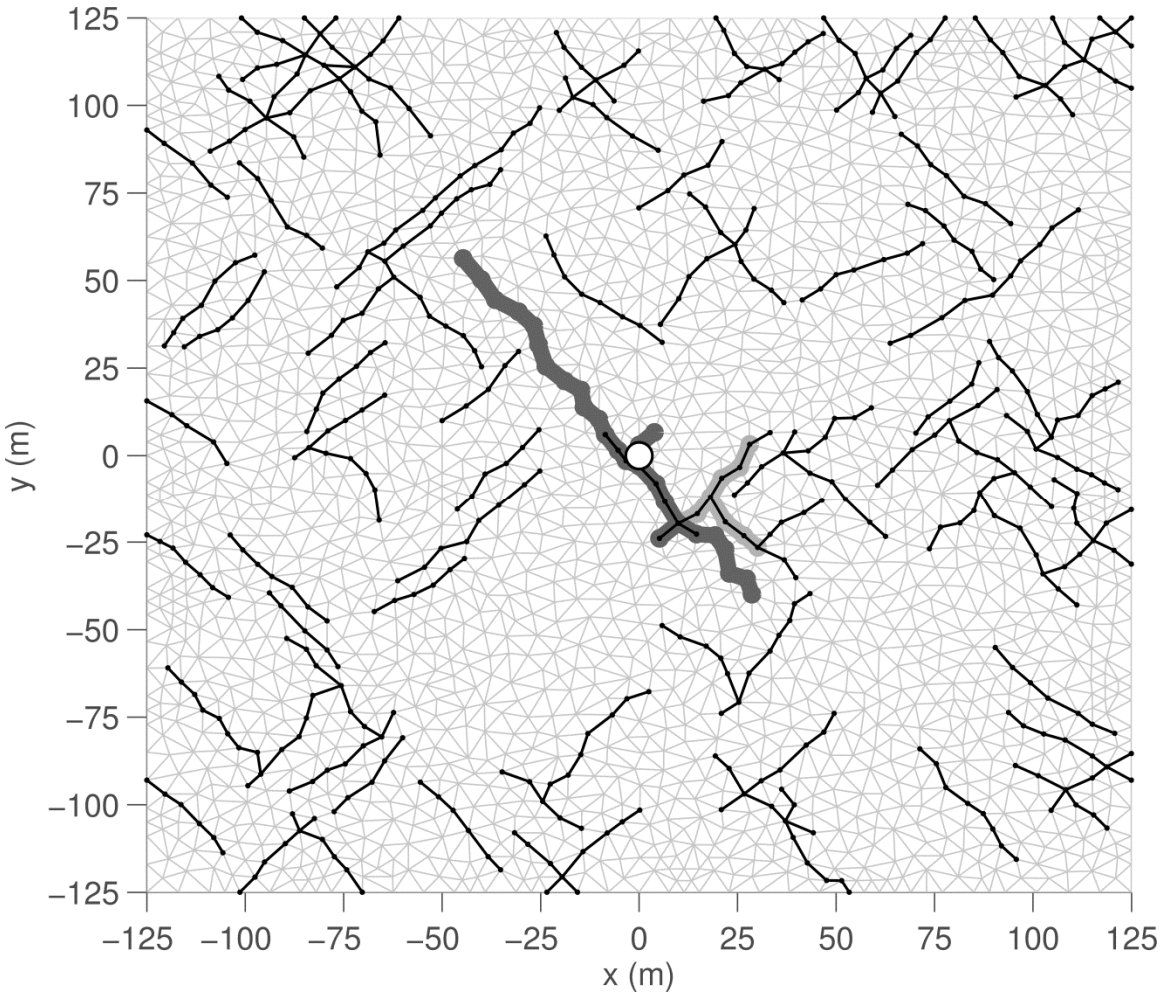

Figure 5.16: Fracture pattern generated for fracture sets oriented at 45° and 135° when $\Delta\sigma$ = 0 MPa, μ = 20 mPa-s, and Q_0 = 2 kg/s and dt = 30 s. Natural fractures are shown by thin black lines, open fractures by thick dark gray lines, and unopened fractures invaded by fluid by lighter thick gray lines.

Carter's Leakoff coefficient as discussed in Chapter 2, a key limitation of the algorithm is that the effect of leakoff on the pore pressure of fluid in the surrounding rock is not considered. Thus, the results observed in this section are only applicable for highly impermeable systems, in which any pore pressure in the surrounding rock is largely disconnected from the propagating fractures.

5.4 Hydraulic Fracture Simulation of the Marcellus Shale

As a case study, the method described in Section 5.3 was used to simulate hydraulic fracturing in the Marcellus Shale. First, an approximation for the two primary joint sets (J_1 and J_2) in the Marcellus was generated using the fracture generation method described at the start of this section. As mentioned previously, characterization of the exact stochastic properties of a joint system is not feasible with the current method. Rather, joint set parameters are selected to provide an approximation of the actual field. In the Marcellus Shale, the first joint set (J_1) is oriented from the southwest towards the northeast [99] across the entire region. The second set (J_2), on the other hand, displays more variation, but generally is oriented from the northwest towards the southeast. Furthermore, as mentioned previously, the direction of the maximum compressive stress happens to run parallel to the orientation of the J_1 fracture set. To approximate this system, the simulation region is rotated such that the J_1 fracture set and the maximum compressive stress run parallel to the *x*-axis (Figure 5.17). Using this orientation for the reservoir system, the J_2 fracture set is approximated as running parallel to the *y*-axis, along with the minimum compressive stress. To represent the high degree of fracturing in the Marcellus Shale, the fracture length distributions for each set were made

comparatively long, using a minimum of 50 m and a maximum of 100 m. To approximate the fracture density, 20% of the J_1 fractures and 15% of the J_2 fractures were selected from the candidate fractures, representing the field observation that the J_1 fractures are more closely spaced in the black shales in the northwest part of the Appalachian Basin where the Marcellus lies [99]. Figure 5.18 shows one realization of this fracture system in a 250 m x 250 m area, generated using a triangular mesh with grid cells no larger than 25 m^2. Both the J_1 set and the J_2 set are clearly seen, resulting in a system that is very highly fractured.

Hydraulic fracturing was simulated in the system using the parameters provided in Table 5.4. Parameters characterizing the rock were taken from various sources in the literature, and were selected to correspond with an approximate reservoir depth of 800 m. All of the parameters from [106] were calculated based on average values from Appalachian black shale samples taken at this depth, while parameters from [107] were estimated based on other values for black shales in the literature. As before, the natural

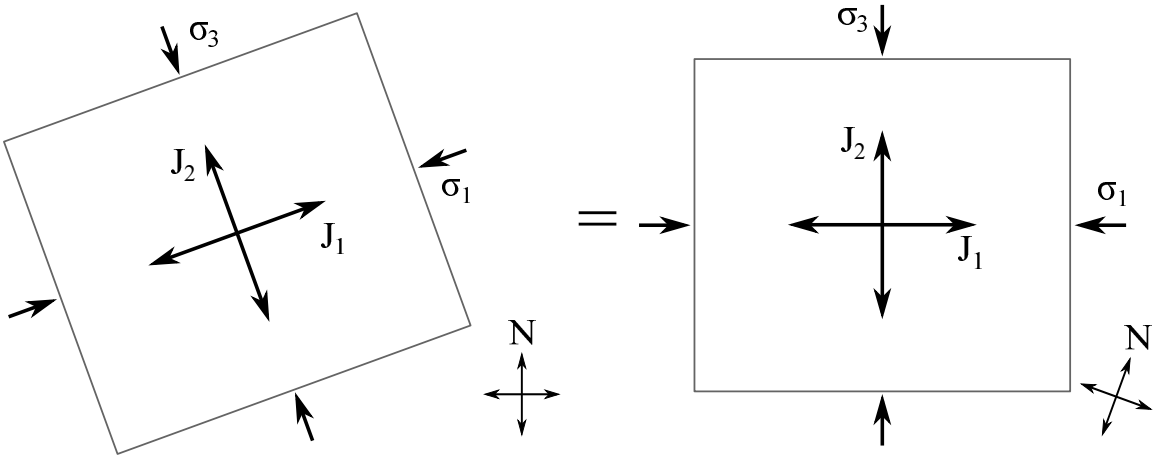

Figure 5.17: Approximate geographic orientation of primary joint sets and principal stresses in the Marcellus Shale, and reorientation for modeling in the HFDDA.

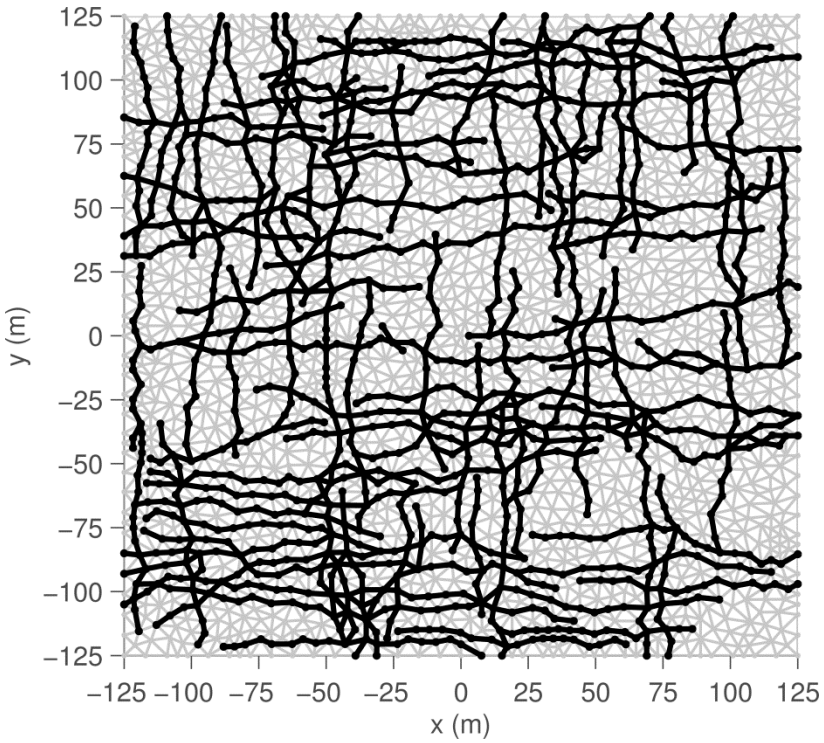

Figure 5.18: One realization of the fracture sets used to approximate fracturing in the Marcellus Shale.

fractures were not assigned any tensile or cohesive strength, and an initial width of 100 μm was assumed for each fracture. For simplicity, no leakoff was assumed in the formation, and the same fluid and numerical parameters were used as in the first example in this section. For this study, the initial fractures in the reservoir were oriented along the *x*-axis such that fracturing is initiated parallel to the direction of maximum principal stress.

The fracture pattern generated at the end of the simulation time is shown in Figure 5.19. As in the theoretical examples, the first observation from this simulation is that despite the extensive natural fracture network, Figure 5.19 clearly shows the development of one primary fracture branch, largely oriented perpendicular to the direction of minimum compressive stress. To the right of the injection point, the propagating fracture

is seen to contact a natural fracture from the J_1 set, which caused it to deviate slightly out of plane. Once this natural fracture was opened, all further propagation appeared to occur to the right of the injection point as the natural fracture was progressively opened. Due to the large stress differential between the maximum and minimum compressive stress, very few of the contacted natural fractures from the J_2 fracture set opened. Even though many of these natural fractures did not open, however, the fracturing fluid was still seen to invade the natural fractures extensively. As a result, the overall "footprint" of the fracturing treatment is rather large, with the result that production from this system would likely be much higher than that from the theoretical examples in which the natural fracturing was less dense. By crossing over the joints from the J_2 fracture system, all of the fluid initially contained in these fractures, in the adjacent fractures, and in the nearby rock matrix would be able to flow into the wellbore. Furthermore, these results represent the potential impact of hydraulic fracturing from only one injection point. If a well was drilled horizontally along the *y*-axis of this system and multiple hydraulic fractures were generated, the well and fractures would intersect multiple joints from both the J_1 and J_2 sets and the resulting footprint of the overall system would be very large. Thus, it is apparent that production in the Marcellus greatly benefits from the numerous natural fractures in the reservoir, as has already been observed in the field.

Table 5.4: Parameters used for simulation of fracturing in the Marcellus Shale

Rock and Reservoir Parameters	
Initial Density, ρ_r	2,500 kg/m^3 [106]
Young's Modulus, E	33.47 GPa [106]
Poisson's Ratio, v	0.17 [-] [107]
Tensile Strength, T_0	9.02 MPa [106]
Friction Angle, ϕ	30° [107]
Max. Compressive Stress, σ_1	32.0 MPa [106]
Min. Compressive Stress, σ_3	10.0 MPa [106]
Fluid Parameters	
Reference Density, ρ_f	1000 kg/m^3
Fluid Bulk Modulus, K_f	2.2 GPa
Carter's Leakoff Coefficient, C_f	0.0 m/s
Viscosity, μ	20 mPa-s
Injection Rate, Q_0	1000 cm^3/s
Natural Fracture Parameters	
Tensile Strength, T_0	0.0 MPa
Cohesive Strength, C_0	0.0 MPa
Natural Fracture Width, w_0	100.0 μm
Friction Angle, ϕ	30° [107]
Numerical Parameters	
Normal Spring Constant, k_n	30*E
Shear Spring Constant, k_s	30*E
Time Step, dt	1 min
Simulation time	1 hr

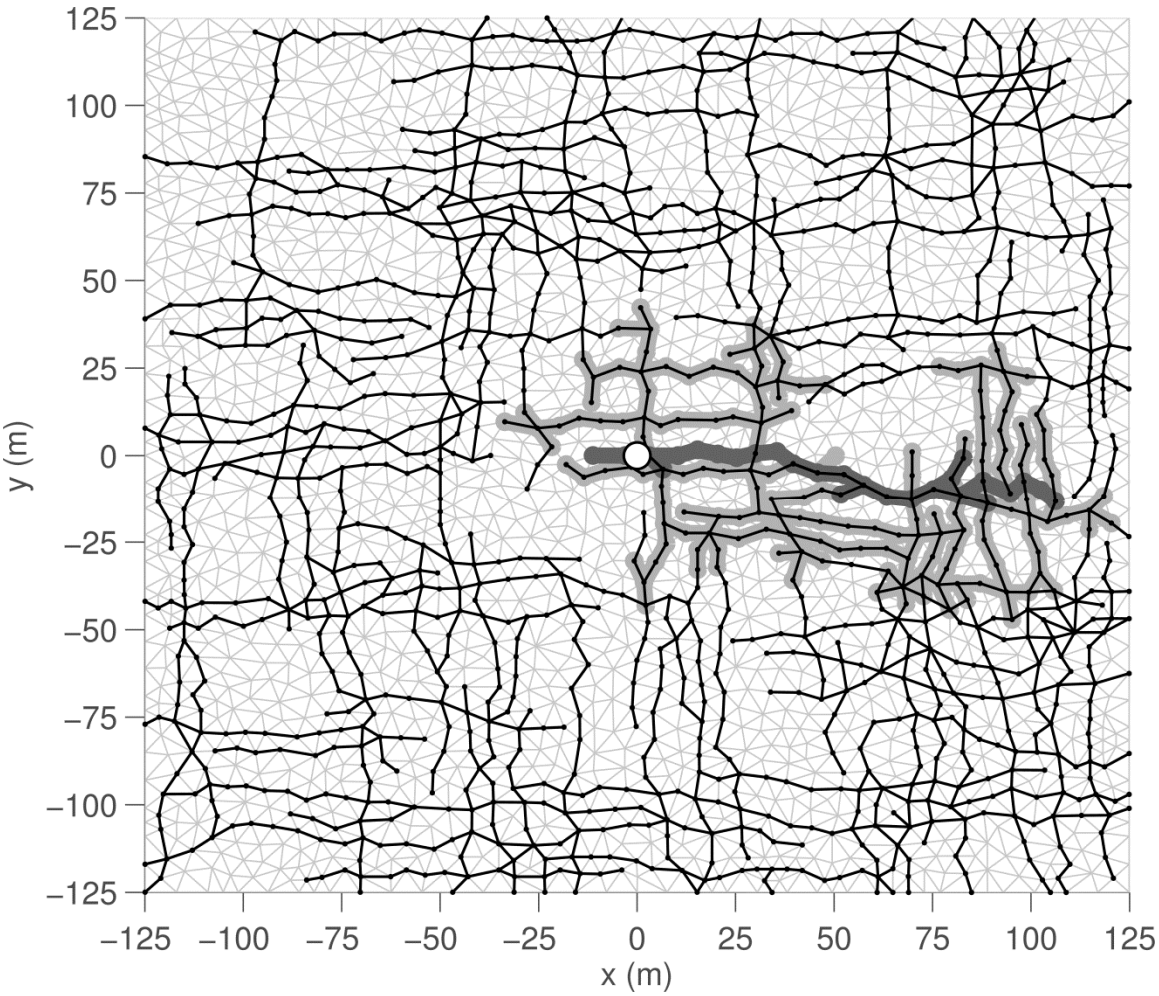

Figure 5.19: Fracture pattern generated after one hour of fracturing simulation for the Marcellus Shale. Natural fractures are shown by thin black lines, open fractures by thick dark gray lines, and unopened fractures invaded by fluid by lighter thick gray lines.

5.5 Monte Carlo Analysis of Fracture Networks

In the previous section, it was demonstrated how hydraulic fracturing in a stochastic fracture network might be modeled using the HFDDA. In this section, that method is extended to create a probabilistic assessment of fracture propagation as a method of characterizing the uncertainty in subsurface systems. Two primary applications are intended for this method. First, in geothermal engineering, hydraulic fracturing is frequently performed to increase the connectivity of naturally fractured reservoirs. For the geothermal system to operate, a pathway of connected fractures is needed between the injection and extraction wells, and thus it is desired to quantify the likelihood that hydraulic fracturing will produce a connected pathway. Second, in gas production and wastewater injection applications, hydraulic fracturing can occur in reservoirs with complicated systems of pre-existing faults, and potentially in areas where other wells have already been drilled. Application of the current method will provide an estimate of the likelihood of propagating hydraulic fractures intersecting or avoiding other features in the subsurface, be they pre-existing faults or pre-existing wells. In both cases, the probabilistic assessment of fracture propagation better characterizes the uncertainty involved with fracturing and allows for better design decisions to be made regarding the location of injection wells and the properties of the fracturing fluid.

In the subsurface, the location and dimensions of fractures and the material properties of a reservoir are difficult to evaluate precisely across an entire domain of interest. Typically, estimates for the rock and fracture properties are taken at individual sampling sites, and values for the rest of the domain are extrapolated from these points. To account for the uncertainty inherent in this process, the Monte Carlo method may be

employed, in which multiple simulations are performed over different realizations of the same reservoir data. With the Monte Carlo method, the material properties of the reservoir are assigned distributions rather than discrete values, and the distributions are individually sampled for each simulation performed using the HFDDA. Additionally, each simulation uses a new realization for the natural fracture network, generated using the method outlined in Section 5.3. For the rock blocks, the Young's Modulus and Poisson's ratio are both assigned triangular distributions, in which the maximum, minimum and mode for each variable are required. For the fractures, triangular distributions were selected for the friction angle of all of the joints, while lognormal triangular distributions were assigned for the tensile strengths and widths of the fractures, as these parameters can vary over orders of magnitude. In each case, triangular distributions were used to reflect reservoirs for which limited sample data is available, based on an available maximum and minimum, as well as an estimate of the modal value.

As an example application of the method, the algorithm was applied to a reservoir

Table 5.5: Triangular distribution parameters for the Monte Carlo Analysis

Rock Parameters			
	Mode	Min	Max
Initial Density, ρ_r	2,650 kg/m^3	2,650 kg/m^3	2,650 kg/m^3
Young's Modulus*, E	10 GPa	8 GPa	12 GPa
Poisson's Ratio, ν	0.22 [-]	0.20 [-]	0.25 [-]
Tensile Strength, T_0	6.0 MPa	5.0 MPa	7.0 MPa
Friction Angle, ϕ	30°	25°	35°
Natural Fracture Parameters			
Tensile Strength, T_0	0.0 MPa	0.0 MPa	0.0 MPa
Cohesive Strength, C_0	0.0 MPa	0.0 MPa	0.0 MPa
Natural Fracture Width, w_0	100.0 μm	80.0 μm	200.0 μm
Friction Angle, ϕ	30°	25°	35°

with the parameter distribution provided in Table 5.5, using the fracture network properties described in Section 5.3 for the fracture sets oriented at 45° and 135°. With the exception of the friction angle, the modal value of each stochastic parameter is the same as the discrete value used in the previous simulations. Each realization of the fracture network was based upon a constant underlying triangular mesh within a 250 m x 250 m domain with injection occurring at the center. For speed, the maximum size of any given triangle was increased to 50 m^2. The distributions were sampled for 50 realizations of the reservoir, and all distributions were sampled using pre-defined seeds such that the results were reproducible. Unless otherwise mentioned, all other parameters are as described in Table 5.3. For this simulation, a constant background stress differential of $\Delta\sigma = 0$ MPa was applied to the system. As opposed to the previous simulations, when stresses of 5 MPa were applied along all sides, for this simulation no stresses were applied to allow for maximum growth of the fracture. Each simulation was applied to 1 hr of simulation time, using a constant time step of dt = 1 min. Evaluation of the results occurs probabilistically. Because the same underlying mesh was used for each realization of the reservoir, the likelihood that the fracturing fluid might open any given joint may be found by averaging the number of realizations in which the joint opened over the total number of realizations. Using this method, the probability of each joint being open at the end of 1 hr is shown in Figure 5.20. For this simulation, the vertical fractures immediately above and below the injection point opened with very high probability, as indicated by the darkest lines in the figure. A well-defined main fracture extended with very high probability to a distance of approximately 17 m above the injection point and approximately 40 m below it. Outside of this main fracture, however, the likelihood of any given fracture opening is markedly

lower and decreases with the distance away from the injection point. The pattern formed by these fractures roughly corresponds to the 45° and 135° azimuths of the natural fracture sets, as fracturing occurred more frequently along joints oriented at those angles compared with joints oriented more parallel to the axes.

To find the likelihood of fracture propagation at any point within the system, a few challenges exist. First, the probability of fracture propagation must somehow be evaluated over the points not explicitly covered by a joint. Second, the method must somehow account for the density of fractures within the system. As seen in the results for individual fractures, the propagating hydraulic fractures in the HFDDA tend to develop along a primary fracture branch. Increasing the density of joints in the system would therefore decrease the likelihood that any particular joint would open, leading to lower estimates of fracture probability. To resolve these issues, a new method is proposed in which the likelihood of propagation for a given area is defined based on the number of realizations in which the area is intersected by an open fracture. For each realization of the reservoir, a grid is placed over the reservoir domain, and each grid cell receives a value of one if it contains an open fracture and a value of zero if it does not. After all of the simulations have been completed, the results are averaged over the total number of realizations to determine the likelihood of fracture propagation within each cell. Use of this method accounts for the points not explicitly covered by a fracture and serves as a method for normalizing the fracture probabilities relative to the density of the joints in the system. A limitation of this method, however, is that the cell size will have a very strong impact on the likelihood of propagation for each cell. The larger the cell, the more likely

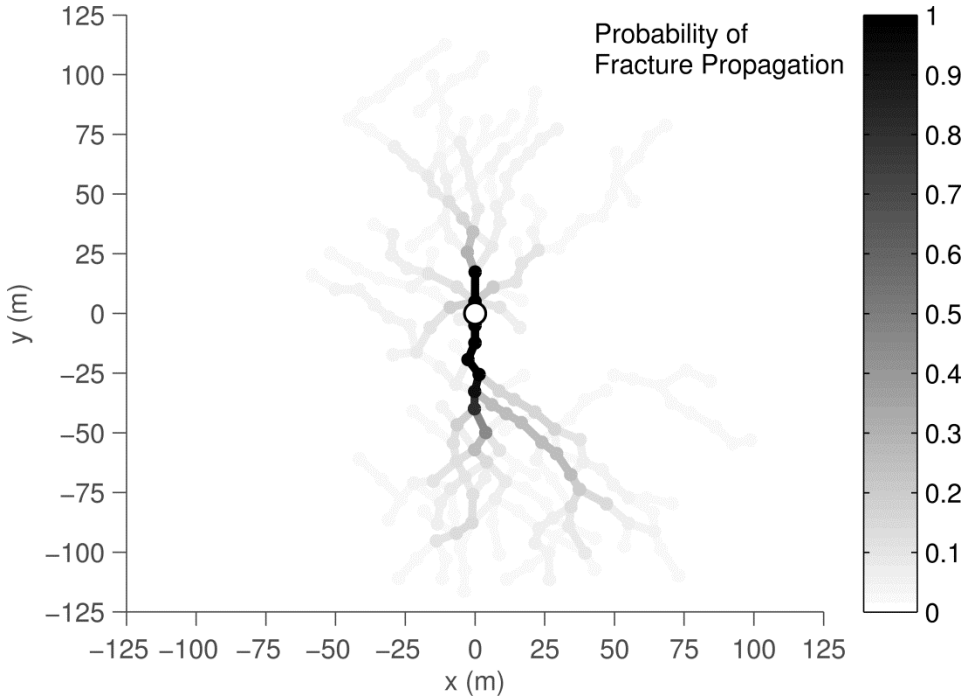

Figure 5.20: Likelihood of individual fracture propagation for fracture sets oriented at 45° and 135°, subject to background stress of $\Delta\sigma = 0$ MPa.

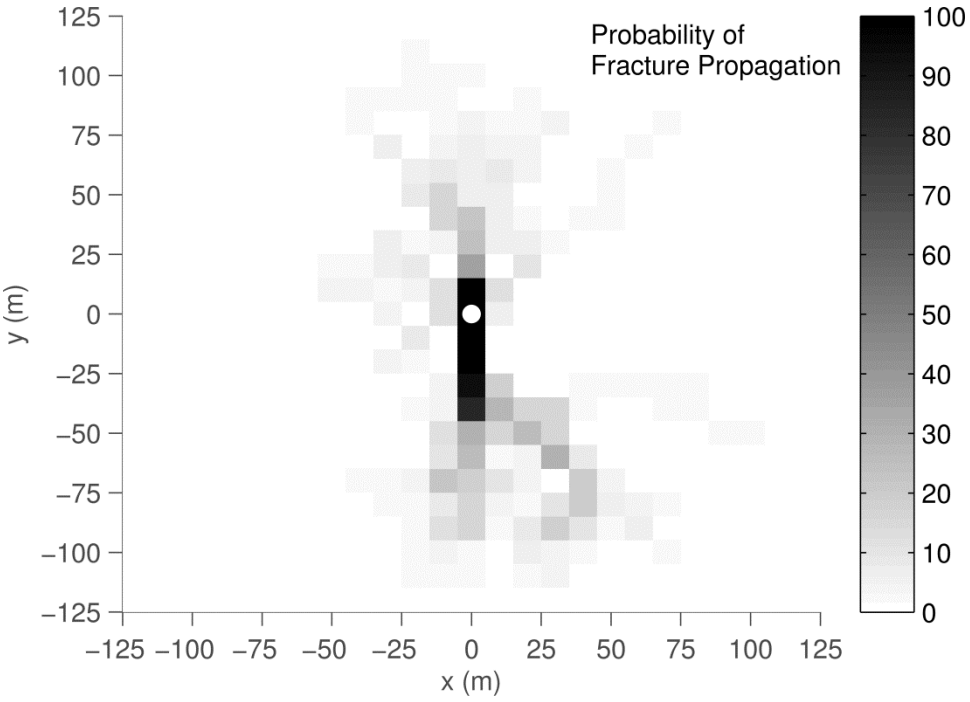

Figure 5.21: Likelihood of fracture propagation within a defined grid for fracture sets oriented at 45° and 135°, subject to background stress of $\Delta\sigma = 0$ MPa.

that it will be intersected by an open fracture, and the less that can be said about which specific locations within the domain are prone to fracturing.

The results of this method using a grid of 10 m x 10 m cells are shown in Figure 5.21. Each grid cell has an area of 100 m^2, double the size of the largest possible triangle in the mesh. Thus, each cell will contain multiple joints. The likelihood distribution displayed in this figure closely mirrors the distribution for fracture propagation shown in Figure 5.20. Effectively, this method serves to smear out the linear information from the first figure over a 2D area. To better analyze the domain, the results of this method can be used to create contours for the likelihood of fracture propagation over time. In Figure 5.22 - Figure 5.25, the likelihood of fracture propagation for the previous simulation is shown in contours after every 15 minutes of simulation time. In these figures, white contours signify any area that has less than a 1% probability of being reached by the hydraulic fracture, while black signifies any area with a probability greater than 50%. Again, the high-probability areas are seen to be located near the injection point and proceed vertically away from it. As seen in Figure 5.22, the fracturing in this area largely occurred within the first 15 minutes, in which fracturing was concentrated relatively close to the injection point. Interestingly, almost all of the fracturing that occurred with medium to high probability (greater than 25%) happened within the first 15 minutes. As time proceeded, the variability in the fracture location grew, and the footprint of areas potentially intersected by the hydraulic fracture greatly increased. Almost all of the area reached by the fracture in the last 45 minutes remained within the lowest quartile of fracture propagation. As mentioned, these results may be used in two ways. For geothermal wells, or any situation in which a particular feature is desired to be intersected

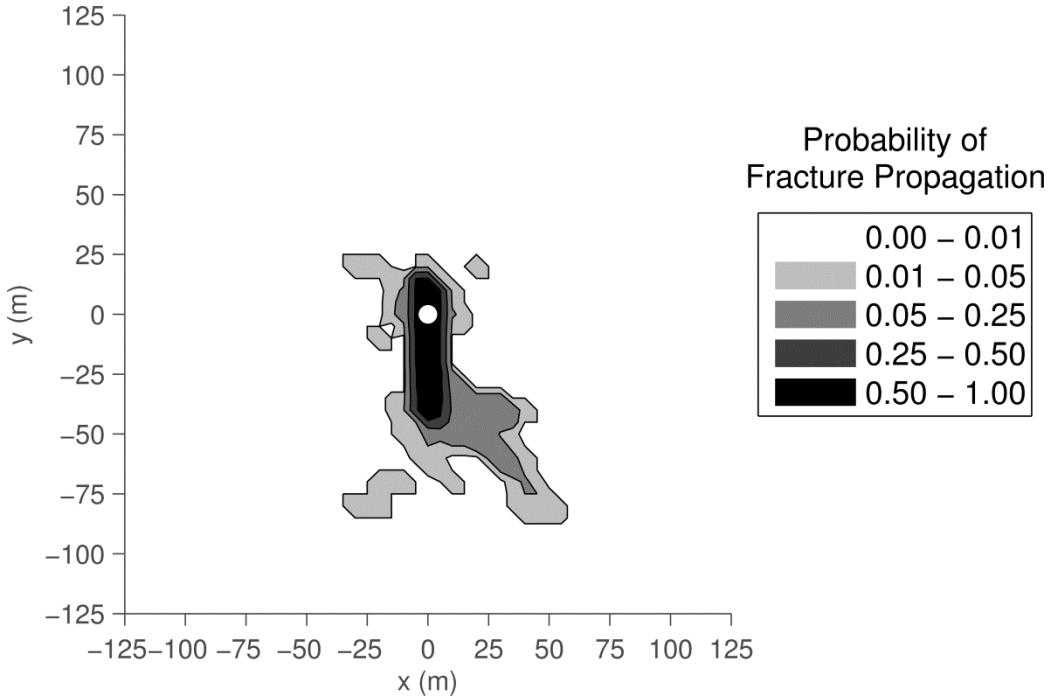

Figure 5.22: Contours for likelihood of fracture propagation after 15 minutes for fracture sets oriented at 45° and 135°, subject to background stress of $\Delta\sigma = 0$ MPa .

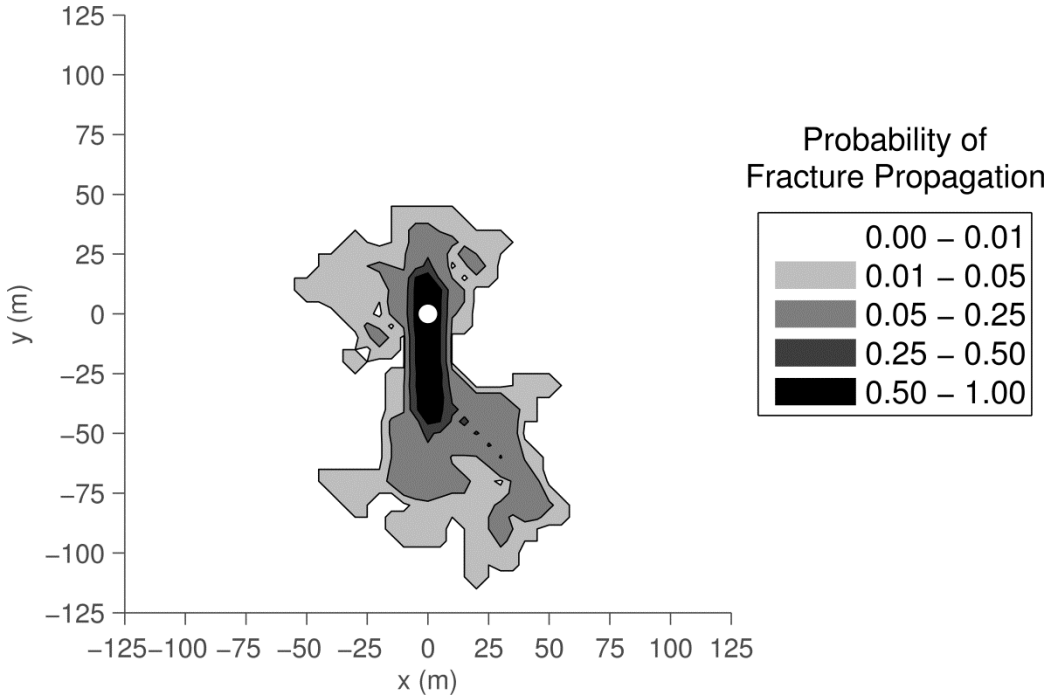

Figure 5.23: Contours for likelihood of fracture propagation after 30 minutes for fracture sets oriented at 45° and 135°, subject to background stress of $\Delta\sigma = 0$ MPa .

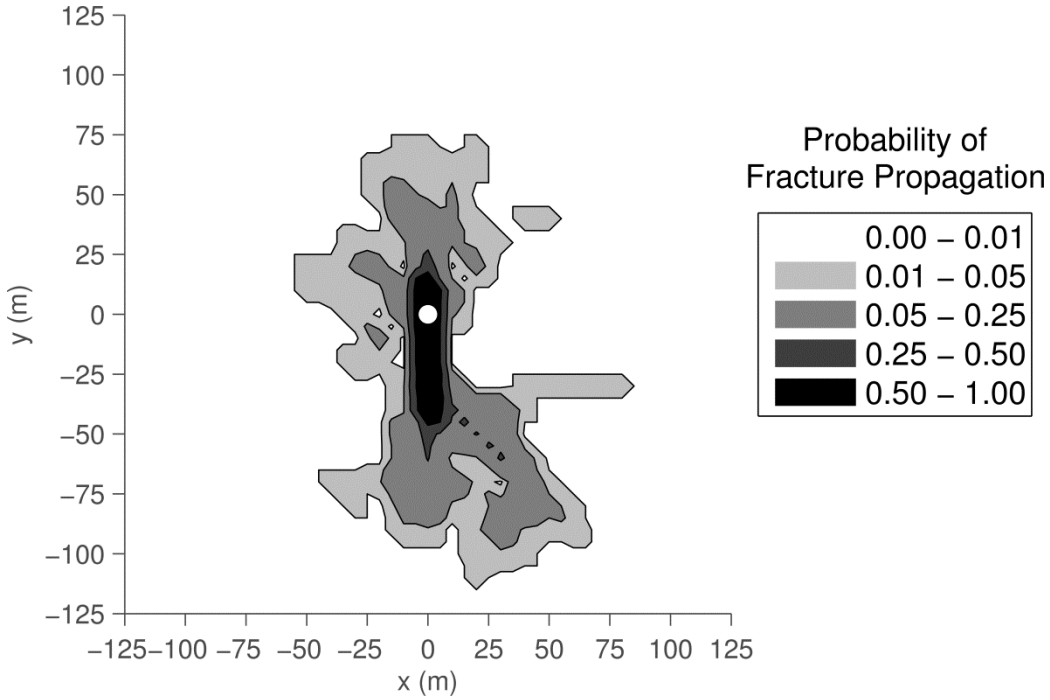

Figure 5.24: Contours for likelihood of fracture propagation after 45 minutes for fracture sets oriented at 45° and 135°, subject to background stress of $\Delta\sigma = 0$ MPa .

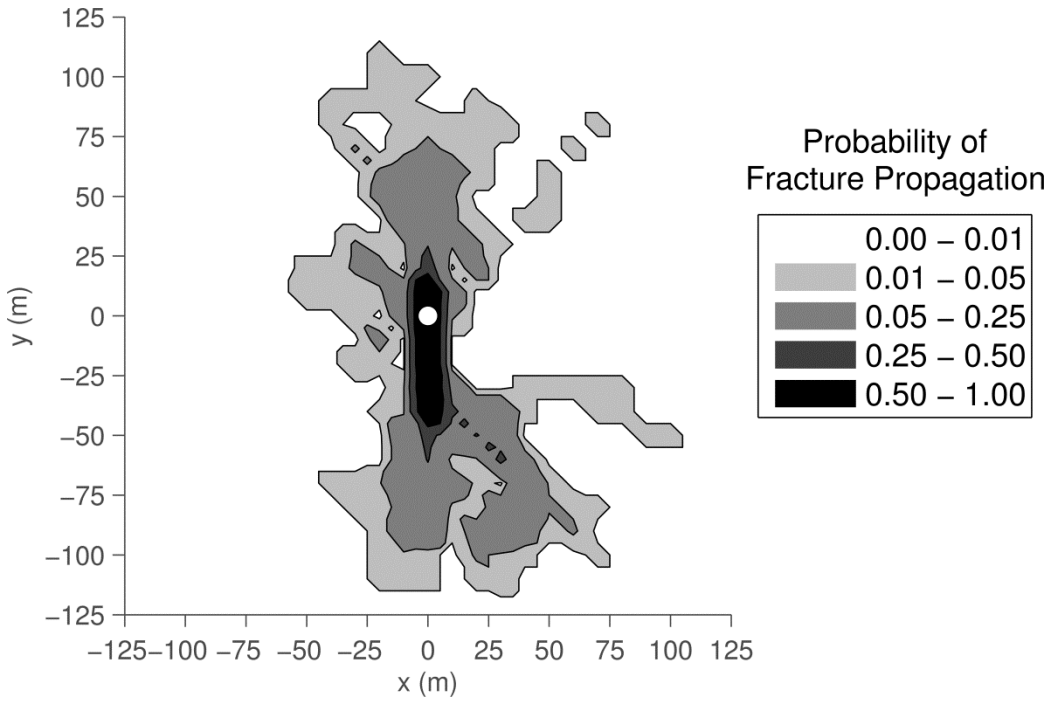

Figure 5.25: Contours for likelihood of fracture propagation after 60 for fracture sets oriented at 45° and 135°, subject to background stress of $\Delta\sigma = 0$ MPa .

by the propagating fracture, these results suggest that the feature should be located relatively close to the injection point in naturally fractured reservoirs with minimal differential stress. Further, the well should be located along the plane in which the hydraulic fractures are initiated, as these areas had the highest probability of being fractured. If, however, the feature in question needed to be avoided, these results suggest that the lateral expansion of the hydraulic fracture may be significant, and care must be taken in locating the injection well far from the feature of interest.

Having examined the results of a Monte Carlo simulation in the absence of background stress, it was next desired to see how they would change in the presence of background stress. For these examples, the same 50 realizations of the reservoir and fracture network were produced as before, but in these a background stress differential of

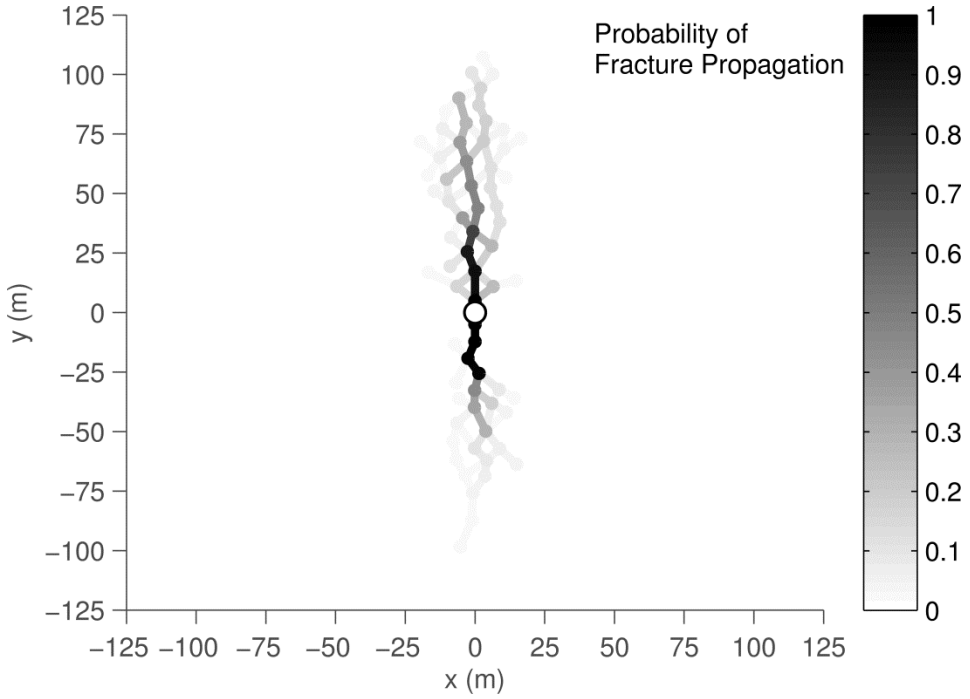

Figure 5.26: Likelihood of individual fracture propagation for fracture sets oriented at 45° and 135°, subject to background stress of $\Delta\sigma = 12$ MPa .

$\Delta\sigma = 12$ MPa was applied. The probability of fracture propagation along each joint is shown in Figure 5.26. A few distinctions are immediately apparent between the results when $\Delta\sigma = 12$ MPa and the results when $\Delta\sigma = 0$ MPa . First, the propagation pattern when $\Delta\sigma = 12$ MPa is much tighter than that when $\Delta\sigma = 0$ MPa . Almost all of the fracturing was localized to within 25 m on either side of the injection point, compared with the growth of greater than 50 m to either side observed when $\Delta\sigma = 0$ MPa . Second, a primary fracture branch developed more clearly in this example than in the previous. Above and below the injection point, high-probability fractures occurred symmetrically, and a fracture branch with moderately high likelihood of fracturing grew up to 75 m above the injection point and down to 50 m below it. The higher likelihood of a distinctly vertical fracture branch developing away from the injection point may more clearly be seen in Figure 5.27 - Figure 5.30, which show the growth of the fracture in 15 min intervals. These figures were generated using the same area-normalizing procedure with 10 m x 10 m grid cells as before. Unlike the results when $\Delta\sigma = 0$ MPa , when $\Delta\sigma = 12$ MPa the mid- and upper- quartiles continue to grow with time. Between the 15^{th} and 60^{th} minute, the 25% - 50% contour expanded from 25 m to 85 m above the injection point, and from -25 m to -45 m below it. These results are in contrast with those from the first simulation, in which minimal growth was observed over the same period.

From these results, it may be determined that in reservoirs with a higher stress differential, the direction and extent of fracture propagation may be determined with more certainty than in those with a low stress differential. Again, these results are similar to those observed for individual fractures. With individual fractures, the presence of a high background stress differential caused the fracture to propagate largely independent

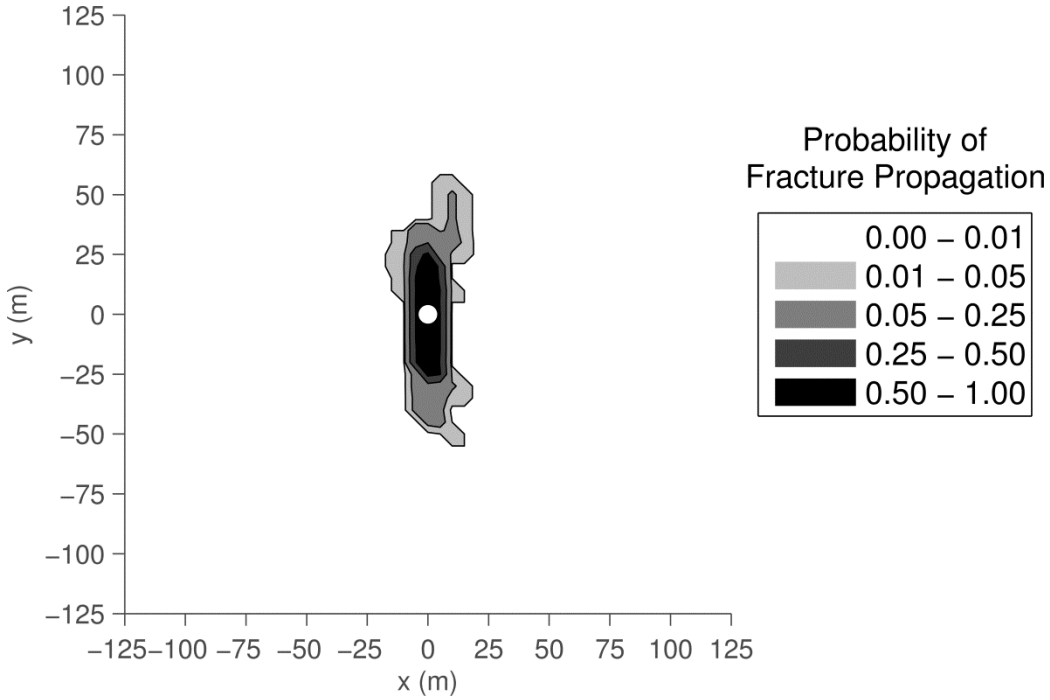

Figure 5.27: Contours for likelihood of fracture propagation after 15 minutes for fracture sets oriented at 45° and 135°, subject to background stress of $\Delta\sigma = 12$ MPa .

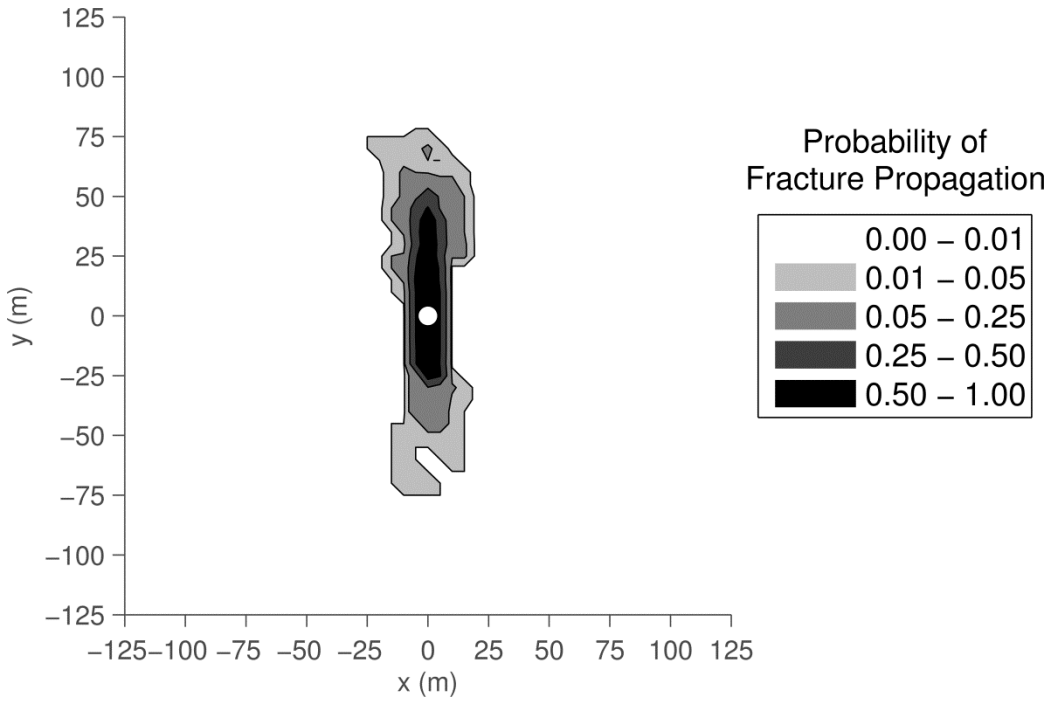

Figure 5.28: Contours for likelihood of fracture propagation after 30 minutes for fracture sets oriented at 45° and 135°, subject to background stress of $\Delta\sigma = 12$ MPa .

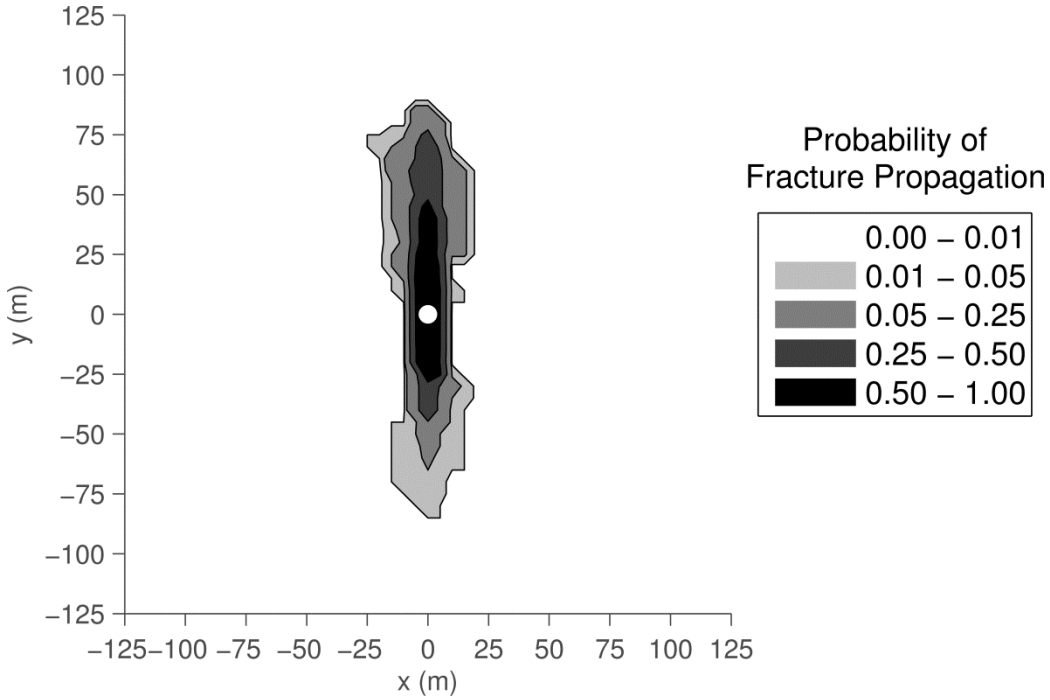

Figure 5.29: Contours for likelihood of fracture propagation after 45 minutes for fracture sets oriented at 45° and 135°, subject to background stress of $\Delta\sigma = 12$ MPa .

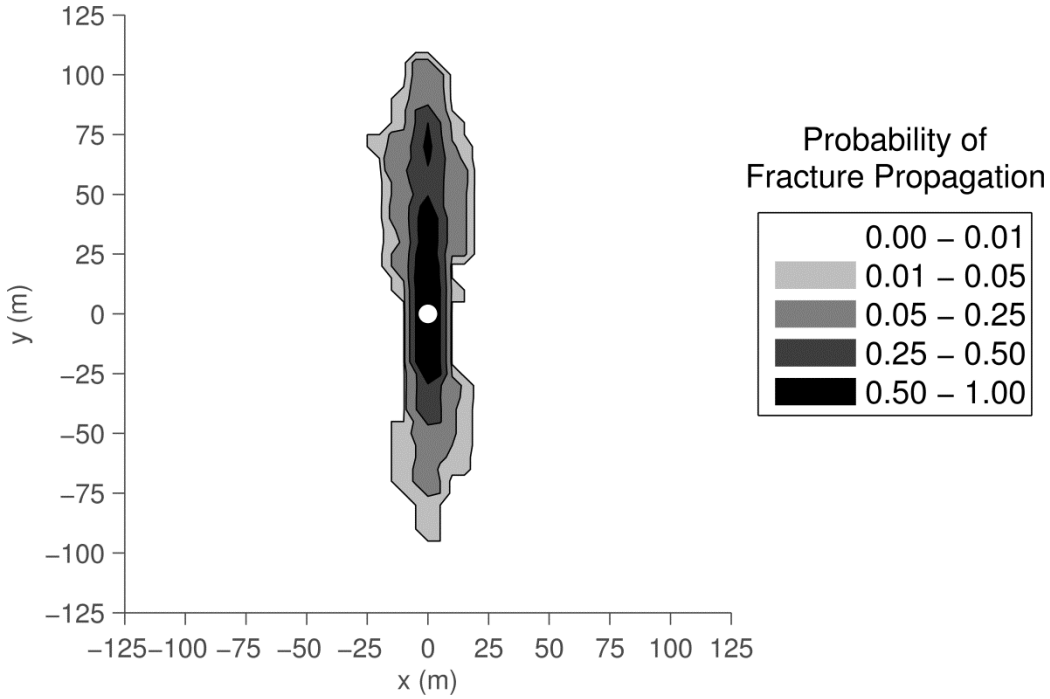

Figure 5.30: Contours for likelihood of fracture propagation after 60 minutes for fracture sets oriented at 45° and 135°, subject to background stress of $\Delta\sigma = 12$ MPa .

from the existing natural fracture network. When evaluated probabilistically, the result is a fracture pattern that occurs with much greater regularity than that when the differential stress is low and the system is heavily influenced by variations in the fracture pattern and other reservoir properties. For geothermal wells, these results signify that extraction wells may be placed farther from the injection well with a higher probability of establishing a connection between the two when the differential stress is high. With extra distance between the wells, the fracture footprint between them will be greater, allowing for greater production from the system. For oil and gas wells, the results signify that features to the left and right of the injection well are much less likely to be intersected by the propagating fracture, allowing fracturing to proceed with more certainty in the presence of pathways that may lead out of the targeted formation.

In a final series of tests, it was desired to see what effect variation in the fluid design parameters might have on the outcome. Two Monte Carlo simulations were performed to test the fluid parameters. In both simulations, triangular distributions were assigned to both the fluid viscosity and the injection range. For viscosity, the modal value was set to 20 mPa-s, the minimum to 1 mPa-s, and the maximum to 100 mPa-s. For injection rate, the modal value was set to 1 kg/s, the minimum to 0.5 kg/s, and the maximum to 2 kg/s. Because these values are design parameters, in an actual hydraulic fracturing operation there would be little uncertainty in their values. Applying a distribution to these parameters, however, allows for a range of values to be simulated and provides an indication of both the likelihood of fracture propagation across the entire range and the effect that variability in these parameters might have on the system. In both simulations, 50 realizations were generated using the distributions for the reservoir and

fluid parameters. For the first Monte Carlo simulation, the reservoir properties were held constant by sampling the rock and fracture distributions only once and using the same sampled values in all 50 realizations. The fluid parameters, however, were sampled individually for each realization. For each realization of the fluid parameters, the HFDDA was run for 120 minutes of simulation time, using a time step of 1 minute. To allow for an accurate comparison with the previous simulations, injection was halted for each realization after 60 kg of fluid had been injected. The likelihood pattern generated for this Monte Carlo simulation is shown in Figure 5.31 and the contour plot at the end of the simulation time is shown in Figure 5.32. For the 50 realizations performed of the fluid parameters, very little variability was observed when the reservoir parameters were held constant. A primary fracture branch above and below the injection point opened in each of the simulations, resulting in these joints opening with very high probability. Some variability was observed at the tips of the fracture, in particular toward the left of the injection point, where a rather large offshoot of the fracture was contacted by the fluid in approximately 15% of the realizations.

Possibly, the variability observed is an artifact of the algorithm. Because the fluid injection rate changes but the time step remains constant, the amount of mass injected into the system within each time step will vary widely. As a result, the pressure will increase much more rapidly when the injection rate is large, as opposed to when the injection rate is small. As more of the system becomes highly pressurized, the likelihood that any given contact will open increases, with the result that the fracture will propagate further when the injection rate is larger. A solution to this problem would be to change the time step such that the fluid injected within each time step remains constant, as in

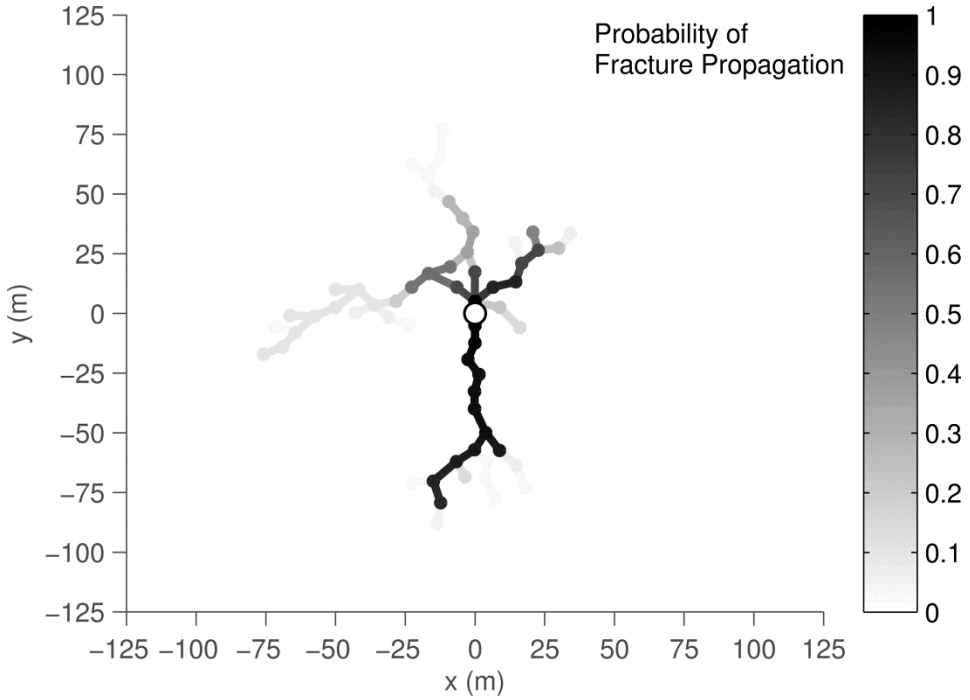

Figure 5.31: Likelihood of individual fracture propagation after all fluid has been injected based on a reservoir sampled once and fluid parameters sampled many times.

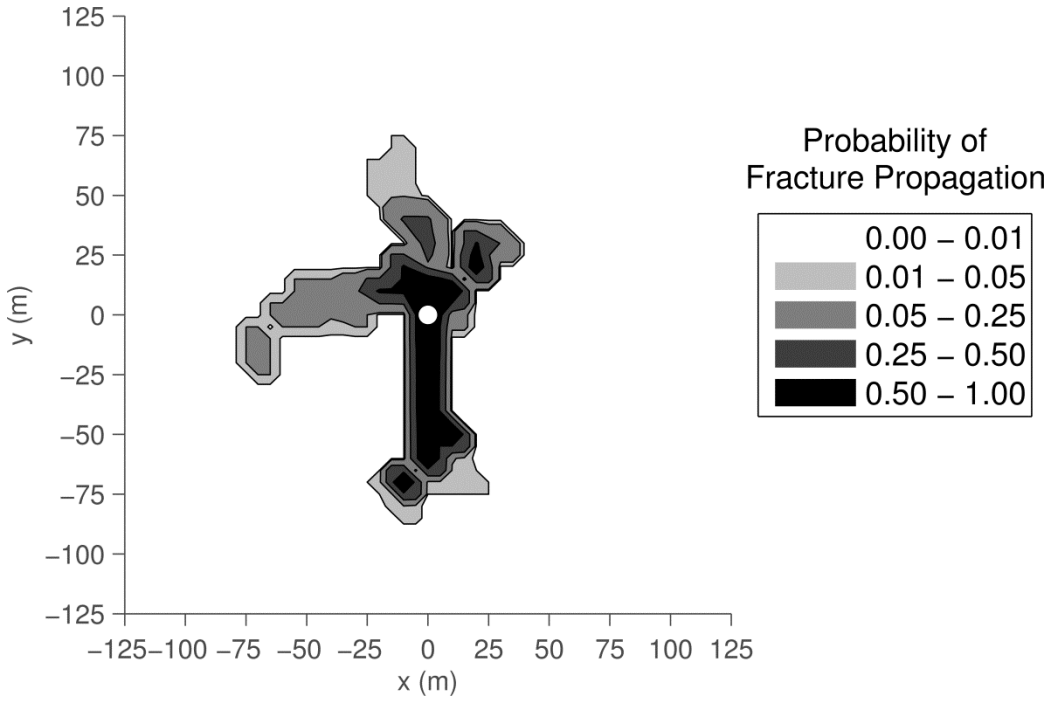

Figure 5.32: Contours for likelihood of fracture propagation after all fluid has been injected based on a reservoir sampled once and fluid parameters sampled many times.

Section 5.3. During testing, however, it was found that changing the time step can affect the ability of the algorithm to converge, as the stability constants used for the rock and fluid matrices are sensitive to changes in the time step. Because there was no way to automate the selection of these constants to ensure convergence, they could not be varied for different values of the injection rate, and a constant time step was required for each realization of the system. Even including this possibility, however, little variability was observed in the propagation pattern using the applied distributions for the fluid parameters, relative to the variability seen in the previous Monte Carlo simulations. These results are consistent with those observed for individual fractures in Section 5.3.

For the second Monte Carlo simulation, both the reservoir parameters and the fluid parameters were sampled individually for each of the 50 realizations. To sample the reservoir parameters, the same initial seed values were used as those in the initial Monte Carlo simulation, in which the fluid parameters were held constant. The likelihood pattern generated for this simulation is shown in Figure 5.33, and the contour plot generated at the end of the simulation time is shown in Figure 5.34. When compared with the fracture pattern (Figure 5.20) and contour plot (Figure 5.25) from the first simulation, very little difference is observed between the results of this Monte Carlo simulation and the results of the first one. Some variability may be seen at the tips of the fractures, but in general the joints opened with roughly the same probability as they did in the first simulation, particularly among those joints that opened with high probability. As a result, it would appear that for the range of parameter values tested, variability in the fluid parameters had little impact on the variability of the fracture network. Again, these results corroborate those from the individual fracture simulations, and suggest that in

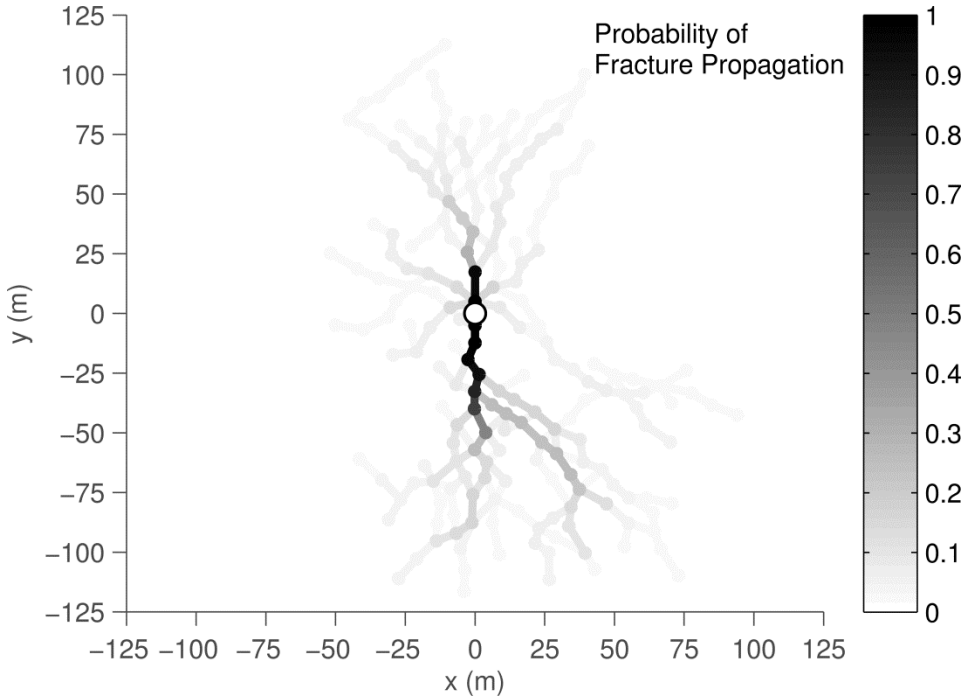

Figure 5.33: Likelihood of individual fracture propagation after all fluid has been injected based on repeated sampling for both the reservoir and fluid parameters.

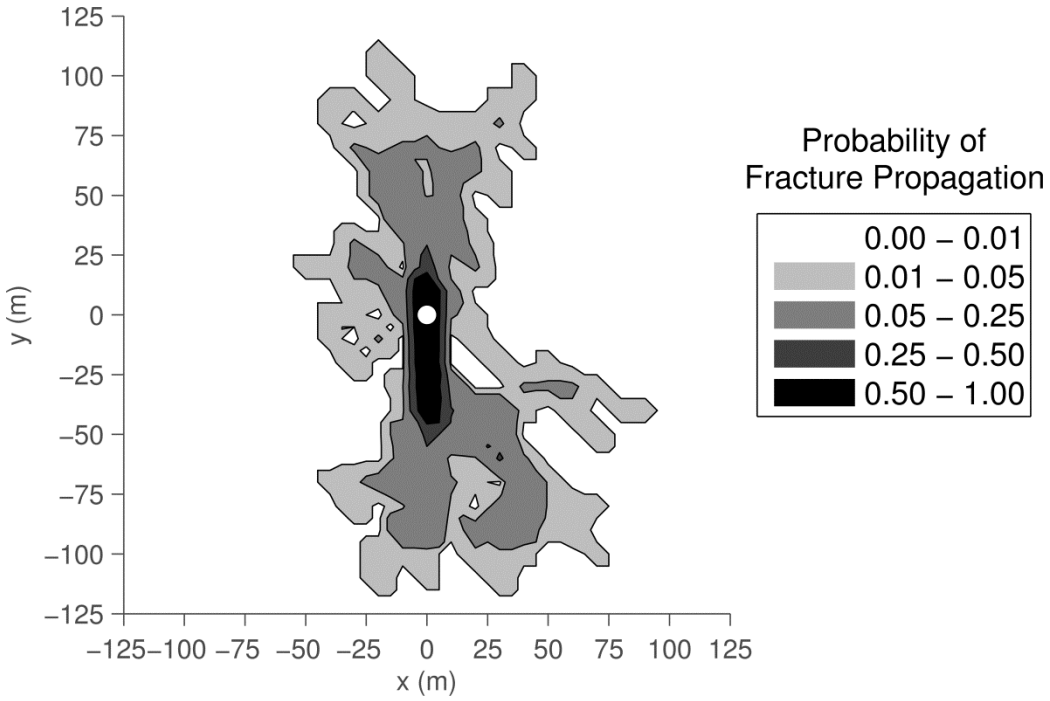

Figure 5.34: Contours for likelihood of fracture propagation after all fluid has been injected based on repeated sampling for both the reservoir and fluid parameters.

impermeable media with significant tensile strength, the fluid design parameters will be of secondary importance to the reservoir parameters in determining the extent and direction of the propagating fracture.

5.6 Monte Carlo Analysis of Hydraulic Fracturing in the Marcellus Shale

As a final test of this method, the Monte Carlo analysis developed above was applied to the Marcellus Shale system detailed in Section 5.4. As before, the distribution parameters were selected to represent a black shale system at a depth of approximately 800 m, and are provided in Table 5.6. For each of the triangular distributions, the mean of the values provided in the reference was selected as the distribution's mode. Additionally, triangular distributions were also applied to the maximum and minimum compressive stress on the system. For these simulations, the length, azimuth and percentage of candidate fractures selected in the J_1 and J_2 fracture sets were characterized using the

Table 5.6: Parameters for the Monte Carlo analysis of fracturing in the Marcellus Shale

Rock Parameters				
	Mode	Min	Max	Reference
Initial Density, ρ_r	2,500 kg/m^3	2,500 kg/m^3	2,500 kg/m^3	[106]
Young's Modulus*, E	33.47 GPa	31.2 GPa	34.2 GPa	[106]
Poisson's Ratio, v	0.17 [-]	0.16 [-]	0.18 [-]	[107]
Tensile Strength, T_0	9.02 MPa	12.4 MPa	5.7 MPa	[106]
Friction Angle, ϕ	30°	25°	35°	[107]*
Max. Comp. Stress, σ_1	32 MPa	28 MPa	36 MPa	[106]
Min. Comp. Stress, σ_3	10 MPa	8 MPa	12 MPa	[106]
Natural Fracture Parameters				
Tensile Strength, T_0	0.0 MPa	0.0 MPa	0.0 MPa	Estimated
Cohesive Strength, C_0	0.0 MPa	0.0 MPa	0.0 MPa	Estimated
Natural Fracture Width, w_0	100.0 μm	80.0 μm	200.0 μm	Estimated
Friction Angle, ϕ	30°	25°	35°	[107]*

*Only the mode was given in the reference, max and min are estimates.

same values as before. For simplicity, the same fluid and numerical parameters provided in Table 5.4 for the simulation of a single fracture were used in this simulation as well. Fifty realizations of the system were made, using a triangular mesh discretized such that each triangle was no greater than 50 m^2 in area. Fracturing was simulated for one hour of injection time, and the likelihood of fracturing at the end of all 50 simulations was observed using the methods described above.

Figure 5.35 shows the likelihood of fracture propagation at the end of the simulation for individual fractures, while Figure 5.36 displays a contour plot generated from this data. In both figures, very little variation is observed in the path taken by the propagating fracture. Due to the high stress differential between the maximum and minimum compressive stresses ($\Delta\sigma \approx 22$ MPa), the hydraulic fracture propagated almost exclusively to the left and right of the injection point, forming a very narrow band in which fracturing was observed. Notably, the width of the band in this simulation was comparable to that observed previously when $\Delta\sigma = 12$ MPa. These results suggest that despite the high degree of natural fracturing in the Marcellus, the high stress differential of the background stress will ensure that the fracture propagates fairly linearly. Furthermore, because the fracture propagates linearly, these results suggest that a bi-wing fracture model may be sufficient for characterizing the growth of individual fractures in the Marcellus, or in any other reservoir in which the stress differential is particularly high.

In addition to the likelihood of fracture propagation in the Marcellus, it was also desired to evaluate the extent to which fracturing fluid would penetrate into the natural fractures surrounding the main fracture. Figure 5.37 shows the likelihood of each

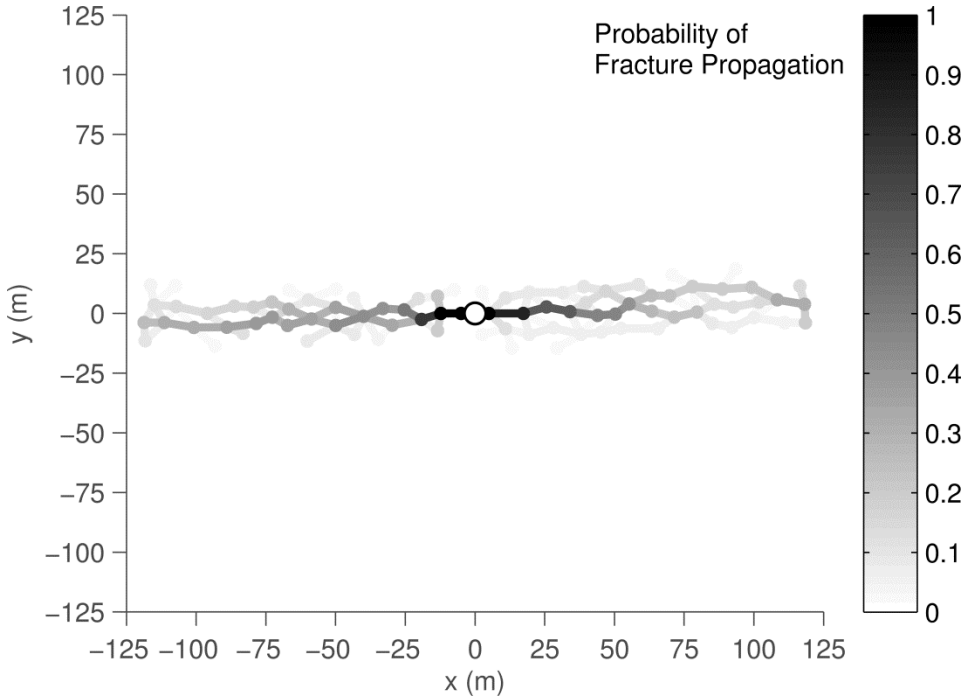

Figure 5.35: Likelihood of individual fracture propagation after one hour of fracturing in the Marcellus Shale.

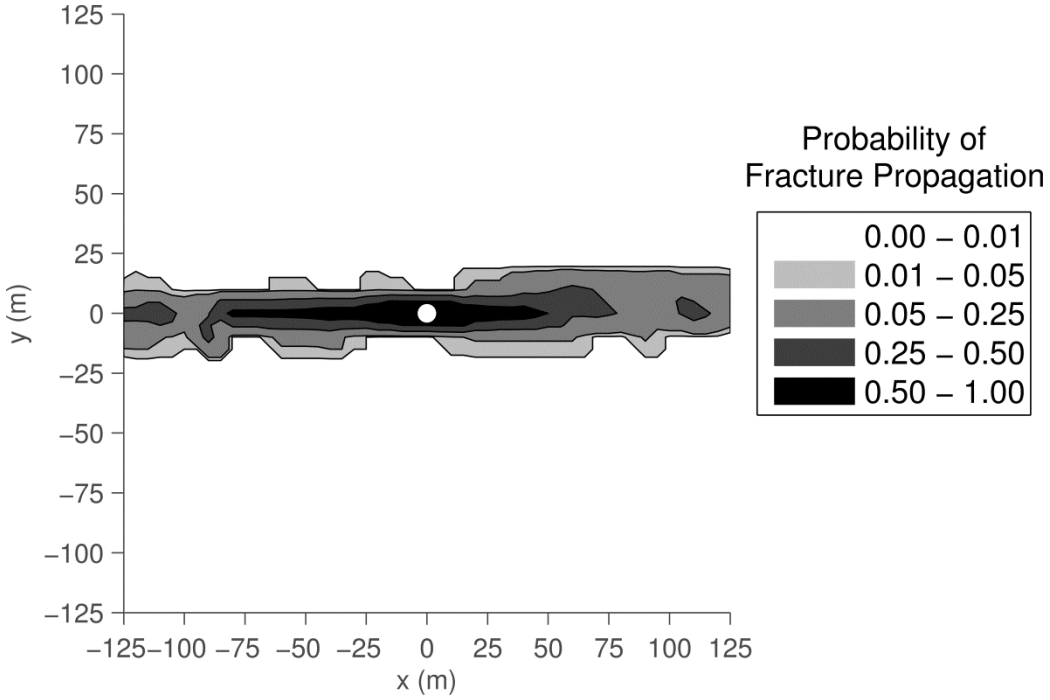

Figure 5.36: Contours for likelihood of fracture propagation after one hour of fracturing in the Marcellus Shale.

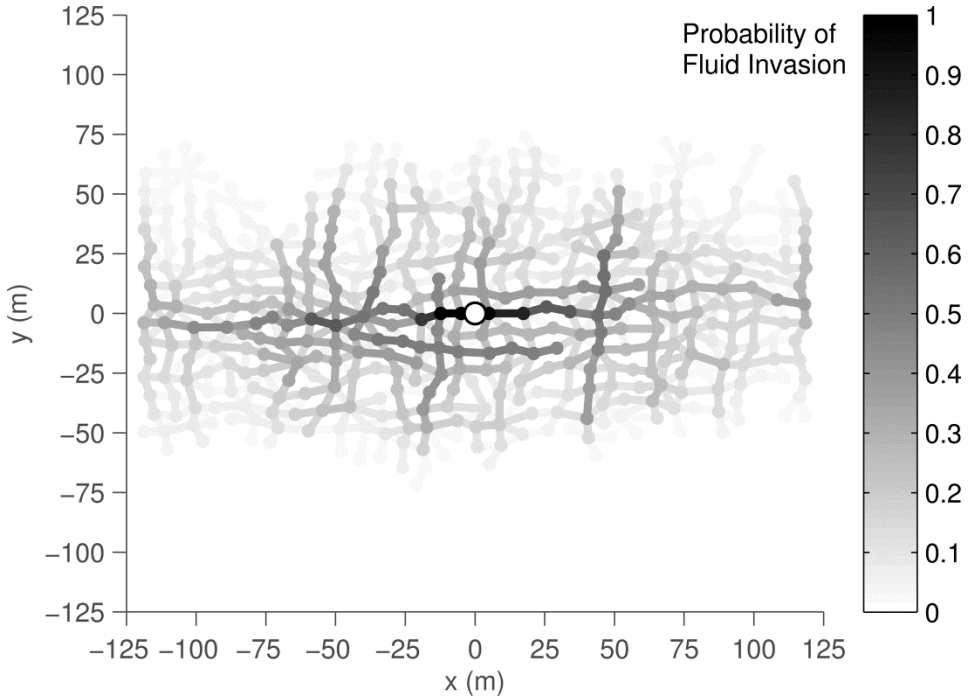

Figure 5.37: Likelihood of fluid invasion in hydraulic and natural fractures after one hour of fracturing in the Marcellus Shale.

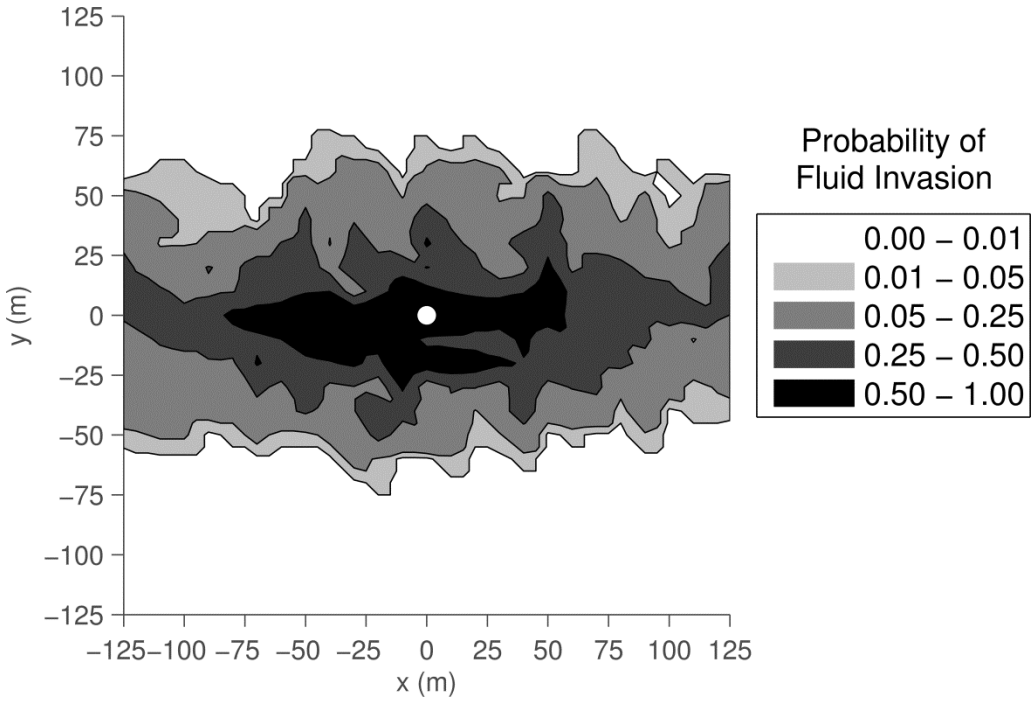

Figure 5.38: Contours for likelihood of fluid invasion in hydraulic and natural fractures after one hour of fracturing in the Marcellus Shale.

individual joint being invaded by fluid, and Figure 5.38 shows a contour plot generated from this data. In these figures, the footprint of the area invaded by the fracturing fluid is clearly much larger than the footprint of the propagating fracture. Fluid invasion occurs in a band over 100 m wide, while fracture propagation occurs in a band approximately 30 m wide. Critically, these results suggest that in heavily fractured reservoirs, fracturing fluid has the potential to migrate far from the location of the main hydraulic fracture. Furthermore, if monitoring is not performed, this migration has the potential to go unnoticed, and the fluid may migrate into faults or fractures that lead out of the targeted formation.

To solve this problem, the impacts of the fluid design criteria available in the HFDDA were examined. First, the Monte Carlo simulations for the Marcellus Shale were performed a second time using a high-viscosity fracturing fluid. Each of the 50 realizations of the reservoir was generated exactly as before. In Section 5.5, it was shown that changing the viscosity from 20 mPa-s to 100 mPa-s did not lead to significant changes in the area impacted by invading fluid. As a result, for this application a fracturing fluid of 1000 mPa-s was applied. Contours of the likelihood of fracture propagation throughout the reservoir using this higher-viscosity fluid are shown in Figure 5.39, while contours showing the likelihood of fluid invasion are shown in Figure 5.40. From these results, the fracture propagation contours observed with the high-viscosity fluid were not noticeably different than those observed with the low-viscosity fluid. Both simulations led to relatively narrow contours of fracture propagation oriented perpendicular to the direction of minimum principal stress. Regarding fluid invasion, however, the high-viscosity greatly limited the extent of fluid invasion relative to that

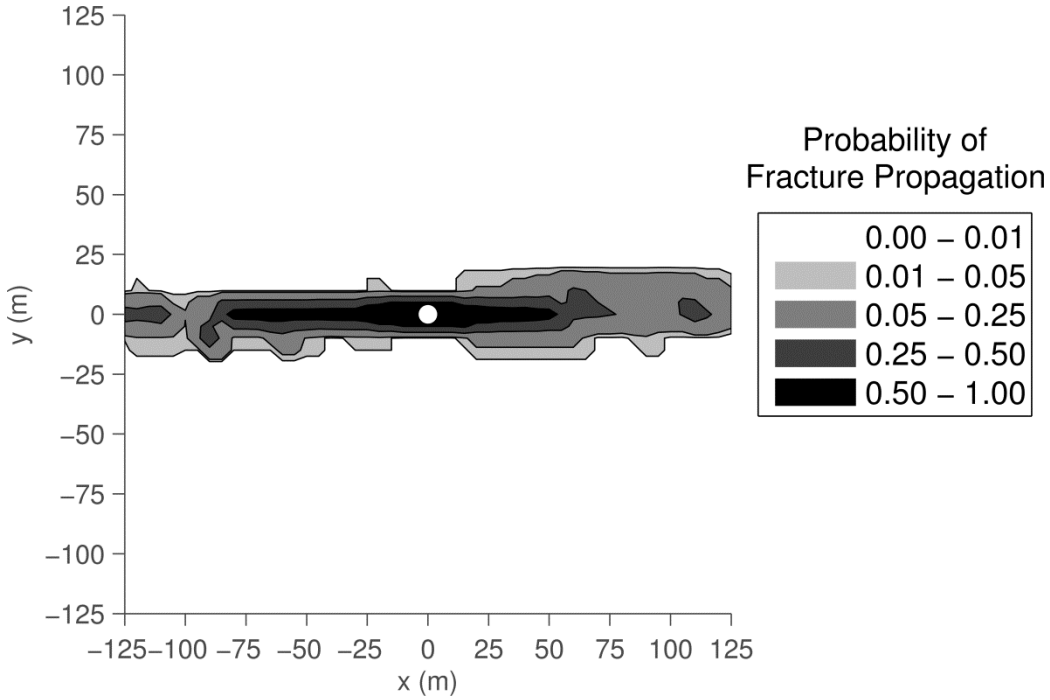

Figure 5.39: Contours for likelihood of fracture propagation after one hour of fracturing in the Marcellus Shale using a high-viscosity fracturing fluid.

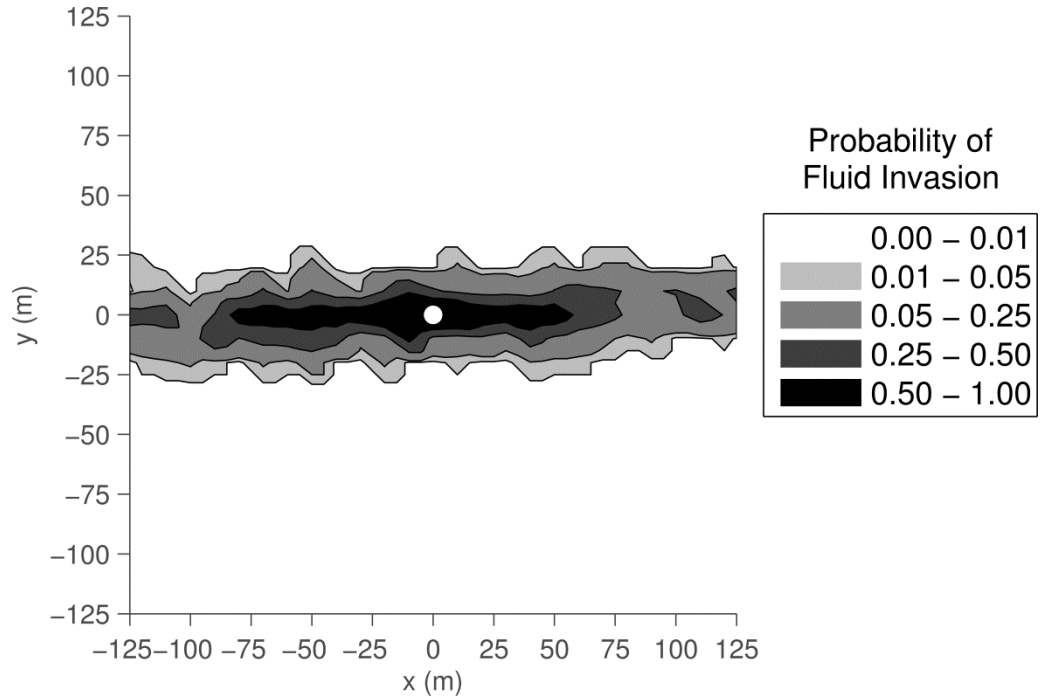

Figure 5.40: Contours for likelihood of fluid invasion in hydraulic and natural fractures after one hour of fracturing in the Marcellus Shale using a high-viscosity fracturing fluid.

observed with the low-viscosity fluid. With the low-viscosity fluid, fluid invasion was observed up to 75 m above and below the injection point. With the high-viscosity fluid, fluid invasion was largely restricted to the 25 m above and below the injection point. Crucially, these results suggest that high-viscosity fracturing fluids can serve to greatly limit the extent of fluid invasion into a surrounding fracture network while still allowing for the production of sizeable hydraulic fractures within a reservoir.

After evaluating the impacts of a high-viscosity fluid, it was next desired to see how changes to the injection rate might impact fracture propagation and fluid invasion throughout the reservoir. For this simulation, the same 50 realizations of the Marcellus reservoir were generated as before. In this case, the fluid injection rate was doubled to 2 kg/s, while the fluid viscosity was returned to 20 mPa-s. Each realization of the system was fractured for 30 minutes using a time step of 30 seconds, such that the same mass of fluid was injected within each time step as in the previous simulations. Contour plots of the likelihood of fracture propagation and fluid invasion for this simulation are shown in Figure 5.41 and Figure 5.42, respectively. Once again, fracture propagation was confined to a narrow band oriented perpendicular to the direction of minimum principal stress. For fluid invasion, in this simulation the fluid invasion pattern appeared similar to that observed in the first Monte Carlo simulation for the Marcellus Shale, in which μ = 20 mPa-s and Q_0 = 1 kg/s. Some differences may be observed, however, in that the fluid invasion in this simulation generally remained within a 50 m band above or below the injection point, as opposed to the 60 to 75 m band that occurred in the first simulation. Furthermore, fluid invasion did not occur as prominently at the corners of the band, suggesting that the larger flowrate used in this simulation did limit the invasion of fluid

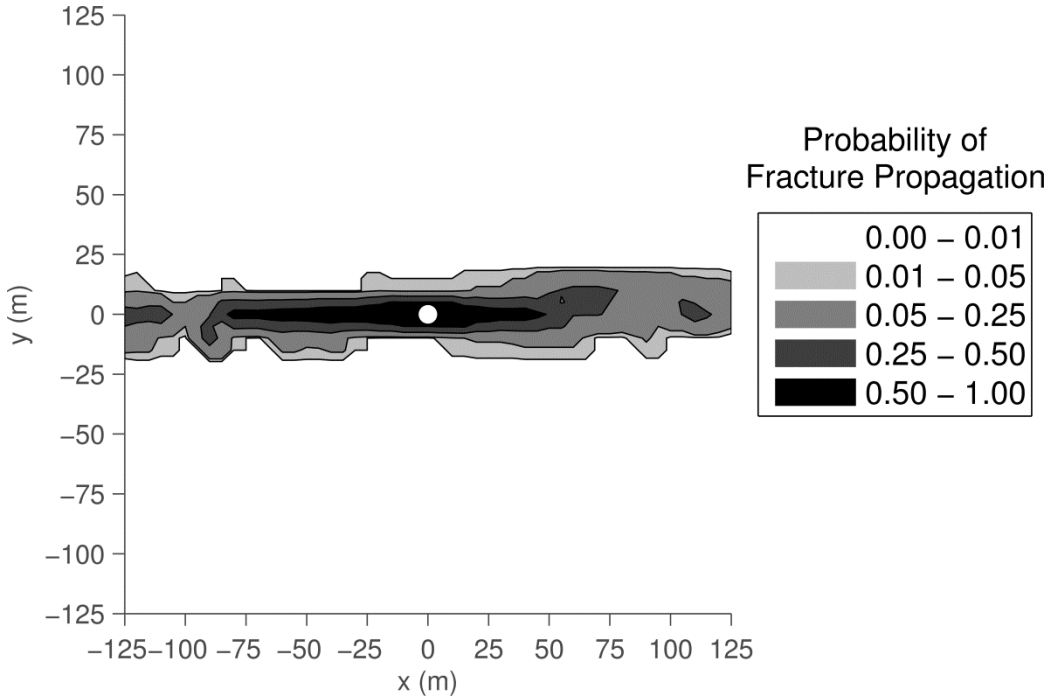

Figure 5.41: Contours for likelihood of fracture propagation after thirty minutes of fracturing in the Marcellus Shale using an injection rate of 2 kg/s.

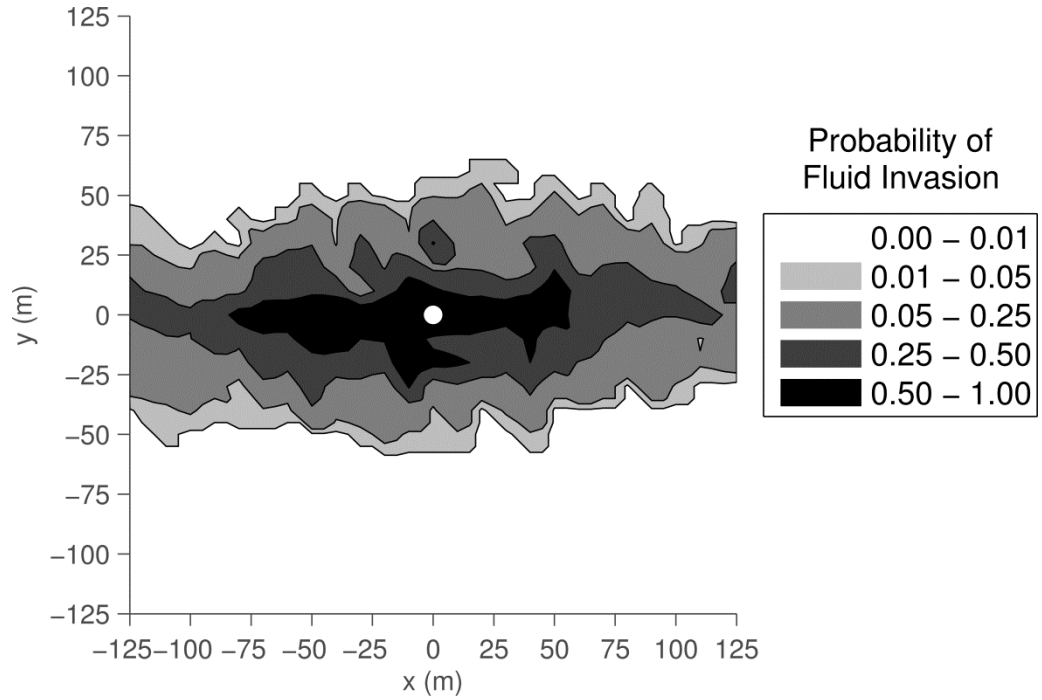

Figure 5.42: Contours for likelihood of fluid invasion in hydraulic and natural fractures after thirty minutes of fracturing in the Marcellus Shale using an injection rate of 2 kg/s.

throughout the domain. From the results of these simulations, therefore, it would appear that the fluid design parameters can have a notable impact on the extent of fluid invasion throughout a reservoir, even if their impact on the likelihood of fracture propagation is less pronounced.

As a final test for the Marcellus Shale, triangular distributions were applied to the fluid design parameters to see how fracturing might vary within a parameter range. For both the viscosity and the injection rate, the maximum and minimum of each parameter was selected to correspond with the values used in the previous simulations. For the fluid viscosity, the minimum was set to 20 mPa-s, the maximum to 1000 mPa-s, and the mode to 100 mPa-s. For the injection rate, the minimum was set to 1 kg/s, the maximum to 2 kg/s, and the mode to 1.5 kg/s. As before, the same 50 realizations were used for the Marcellus reservoir. A time step of 1 min was used for each realization, and injection was allowed to continue in each realization until 60 kg of fluid had been injected. Contour plots of the likelihood of fracture propagation and fluid invasion for these simulations are shown in Figure 5.43 and Figure 5.44. Once more, the fracture propagation contours for this simulation were very similar to those from the previous Marcellus Shale simulations, again suggesting that the fluid parameters will not have a marked effect on fracture propagation, at least over the range of parameters tested. The fluid invasion contours in this simulation remained within a band extending approximately 35 m above and below the injection point and were likely controlled primarily by the fluid viscosity, as the range of fluid viscosity parameters applied was significantly wider than the range of injection rates. As before, these results show that the fluid parameters may have only a secondary impact on the likelihood of fracture propagation throughout the reservoir, but will have a

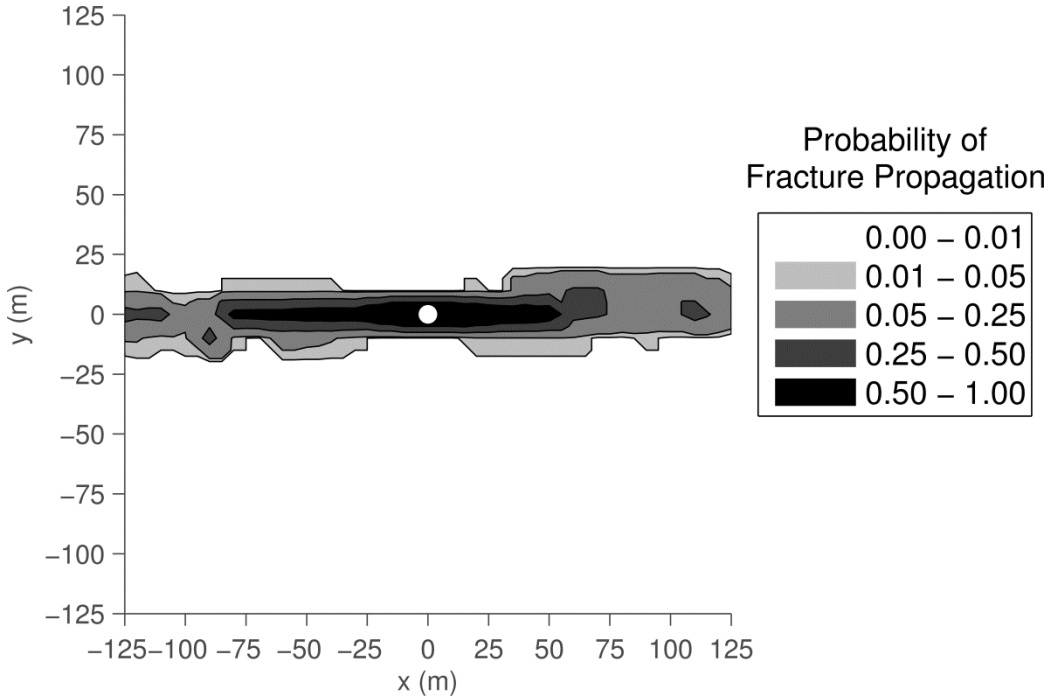

Figure 5.43: Contours for likelihood of fracture propagation in the Marcellus Shale when a triangular distribution is applied to the fluid design parameters.

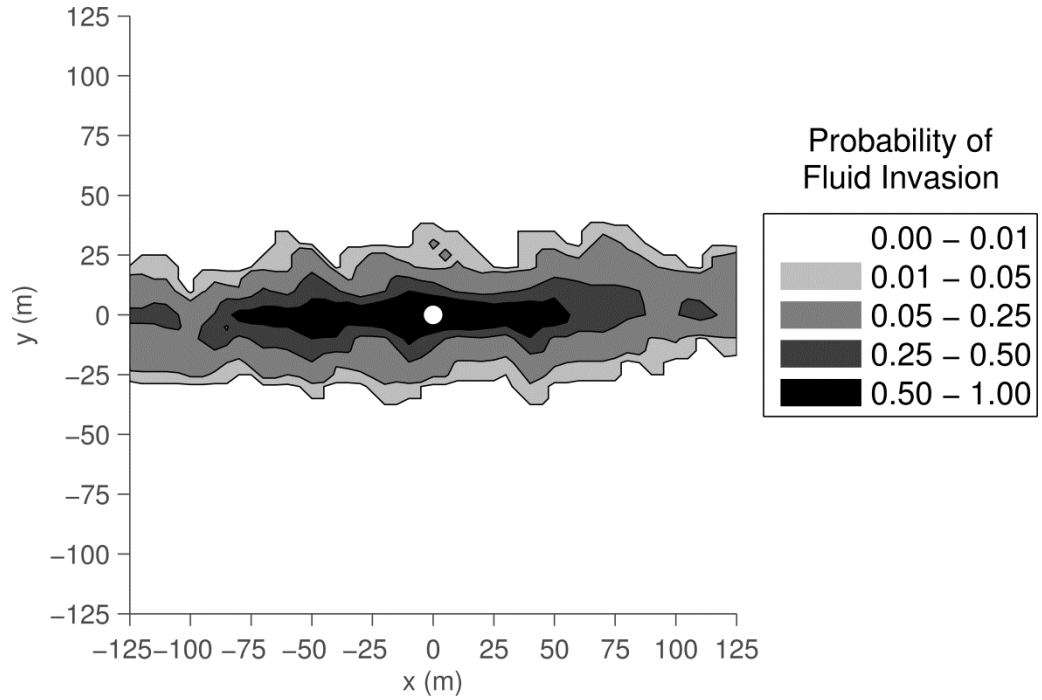

Figure 5.44: Contours for likelihood of fluid invasion in the Marcellus Shale when a triangular distribution is applied to the fluid design parameters.

strong impact on the likelihood of fluid invasion throughout the reservoir when the reservoir is characterized by an extensive pre-existing natural fracture network.

5.7 Summary

In this chapter, it was demonstrated that the HFDDA can effectively model hydraulic fracture propagation in networks of natural fractures. The HFDDA was successfully able to reproduce the fracture interaction mechanisms observed by the intersection of a propagating hydraulic fracture with a natural fracture seen in the experiment performed by Blanton. When elevated to the level of fracture networks, the HFDDA showed that both the angle of approach of the propagating fracture and the differential stress applied to the system will continue to have a strong influence on the direction taken by the propagating fracture. Additionally, for individual realizations of a reservoir, it was demonstrated that both the fluid viscosity and the injection rate can influence the extent to which a fracture will propagate. In the Monte Carlo simulations, however, it was demonstrated that variability in the fluid parameters will have less of an effect on fracture propagation than variation in the reservoir parameters and differential stress. The results of this section are particularly relevant when locating injection wells for hydraulic fracturing, and can be used to facilitate proper well placement in the presence of faults, extraction wells or other pre-existing features in the subsurface. Finally, the methods described in this chapter were applied to a case study of hydraulic fracturing in the Marcellus Shale. In this analysis, it was demonstrated that the high differential stress in the Marcellus will lead to relatively linear fracture propagation, despite the high degree of fracturing already present in the formation. The numerous

natural fractures, however, can allow fracturing fluid to travel far from the main fracture, suggesting that care must be taken when fracturing highly fractured reservoirs to prevent the unwanted migration of fluid.

6 CONCLUSION

In this chapter, the work of the previous chapters is summarized and presented in a unified context. The primary findings of each chapter are highlighted and their significance is discussed. The limitations of the model are also analyzed, and recommendations for further research are provided.

6.1 Thesis Summary and Key Findings

When work began on this research, many models of hydraulic fracturing already existed in the literature. At the most fundamental level were the various analytical and semi-analytical solutions for bi-wing fracture propagation, which analyzed the effect of different fluid and reservoir parameters on the fluid pressure and geometry of a propagating hydraulic fracture. Refinement of these models led to the discretization of the bi-wing fracture into individual cells, and eventually into coupled analyses of bi-wing fractures with reservoir simulators. Recently, various authors had begun to examine hydraulic fracturing in complex networks using a variety of techniques for characterizing the interaction between the rock and fluid components of the reservoir system. It was found upon examining these existing models, however, that very little work had been performed in developing a fully implicit model for hydraulic fracturing in complex fracture networks. Unlike with explicit models, implicit models have no theoretical limitations on the size of time steps or rock elements needed for convergence. While a few studies had been conducted examining fluid flow and hydraulic fracturing implicitly [71-73, 75], a great deal of work remained to stabilize these algorithms and demonstrate

their validity for actual hydraulic fracturing problems in which rock and reservoir parameters are only known stochastically. Thus, the purpose of this thesis was to build upon these studies by stabilizing and validating the existing algorithm, and to extend the algorithm to more accurately account for the uncertainty in hydraulically fractured reservoirs. In this work, the new algorithm generated was labeled the HFDDA.

The first step in the current work was to build upon the existing algorithm developed in [71-73, 75]. In Chapter 2, improvements to the algorithm were made in a few key areas, the vast majority of which were implemented to help the algorithm converge. Among these, the most significant was the introduction of stability constants into the coupled equation system. These terms were directly responsible for the convergence of the fluid pressures and rock displacements, as without them small changes in the geometry of the fractures would cause very large changes to the fluid pressures which would in turn cause the algorithm to fail. Another key development was the order used for the steps in the overall algorithm. The solution steps in the algorithm were arranged such that each change to the open-close state of the joint contacts and the fractures occurred incrementally. This arrangement helped prevent the oscillation of the open-close iterations and ensured that fractures propagated incrementally away from the injection point. Additionally, the open-close logic of both the contacts and the fluid was adjusted to account for issues specific to hydraulic fracture modeling. Among these changes was the requirement that fracturing of the rock matrix occur in tension adjacent to fluid, the use of four sets of springs rather than two for edge-edge contacts, and the restriction on vertex-vertex contacts allowing them to develop only when the penetration distance of the contact exceeded a certain tolerance. Other improvements to the algorithm

included an iterative method to solve for the mass stored in fluid nodes in which the pressure dropped to zero, and the various changes implemented in Chapter 5 to facilitate convergence in the presence of natural fractures. While each of these steps was small by itself, every one of these changes proved instrumental in stabilizing the algorithm and improving its accuracy in the various examples tested.

Upon completion of the model, the next step was to demonstrate its accuracy by validating it against various theoretical and experimental examples of hydraulic fracturing. In Chapter 3, the accuracy of the coupled algorithm was shown through the simulation of two analytical solutions for hydraulic fracturing. Using the solution for the opening of a Griffith fracture subject to constant pressure, it was demonstrated how triangular elements are required to accurately model stress and strain when using first-order expressions for displacement. While this requirement had already been established previously [75], many works currently in the literature continue to incorrectly use non-triangular elements with first-order displacement functions, resulting in incorrect estimates of the strain in the system. Next, the algorithm's ability to model bi-wing fracturing was demonstrated by simulating the semi-analytical solution of a viscosity-dominated KGD fracture. In this example, it was demonstrated how the HFDDA solution was largely independent of both spatial and time discretization when no background stress was applied to the system. In these tests, the results of the HFDDA simulation largely matched the analytical solutions for fracture length, fracture width, and fluid pressure at the injection point regardless of the discretization applied. Critically, these findings demonstrate one of the primary motivations for using an implicit method, namely the ability of the solution to converge to the appropriate result independent of the

system discretization in time and space. When background stress was applied, however, the HFDDA results diverged from the analytical solution as the fracture discretization grew. The divergence appeared largely to be a result of the discretization size, as larger fractures received proportionally more of the background stress and required greater pressures in the system to cause them to open. Because the semi-analytical solution does not directly account for any extra stress on unbroken contacts, however, the divergence observed in this example was not a cause for concern.

After validating the coupled algorithm against analytical solutions, it was next desired to see how well it would perform against experimental results. For this task, the HFDDA was tested against an experiment developed by Rubin [87] for bi-wing fracture growth in a homogeneous medium. Using the data provided for fracture length, width, and pressure at various points along the fracture, the HFDDA was shown to successfully reproduce the experimental results for all of these variables. Notably, these results suggested that the algorithm is suitable for modeling hydraulic fracturing in homogeneous media and is able to reproduce the propagation path of a particular fracture, provided that the path exists within the mesh discretization. In the final section of Chapter 3, various aspects of the algorithm were examined in simple examples. In this section, it was demonstrated that the algorithm was able to conserve fluid mass, model symmetric fracture propagation and fracture splitting, correctly predict the fracture propagation direction in the presence of background stress, and account for asymmetry in the different parameters that define the reservoir. Taken together, all of these examples served to demonstrate both the reliability of the algorithm and its robustness for modeling different types of reservoir systems.

In Chapter 4, the Mohr-Coulomb and maximum tensile stress fracturing criteria employed within the DDA and HFDDA were related to the LEFM criteria more generally used in hydraulic fracturing studies. Implementation of the Mohr-Coulomb and maximum tensile stress criteria in discontinuous studies is much simpler than implementation of the LEFM criteria, as these criteria can be applied to mesh elements of any shape. In the first part of the chapter, an analysis similar to that in [96] was performed to relate the Mode I stress-intensity criteria from LEFM to the tensile failure criteria used in the DDA. In this analysis, it was revealed that the critical stress intensity factor for a joint could be derived as a function of the joint's tensile strength and its length. The validity of this relationship was demonstrated by gradually applying a far-field tensile load to an infinite plane containing fractures of different initial lengths. The load was gradually incremented until failure occurred, after which the failure load was compared to the theoretical failure load derived using LEFM. Excellent agreement was observed in these results, suggesting that the DDA is able to model Mode I fracture propagation as considered by LEFM, even without explicitly evaluating the stress intensity at each contact. Similarly, in an analysis of Mode I fracturing in a Mixed-Mode stress field, the DDA correctly evaluated both the propagation direction of the tensile fracture and the failure load, again suggesting that the DDA is suitable for modeling the propagation of tensile fractures, as based on LEFM. When this analysis was extended to Mode II fracturing, however, the agreement between the DDA and the theoretical predictions was not as close. In Mode II, the DDA was observed to shear with significantly less background shear applied than was predicted theoretically. The reasons for the discrepancy were not immediately clear, as the DDA was correctly able to model

Mode II failure in the absence of an initial fracture. Because, however, hydraulic fracturing is typically expected to occur in Mode I, the inability of the DDA to reconcile exactly with the theoretical results for Mode II hydraulic fracturing is of only secondary importance in the current application. To complete the study of this relationship, the ability of the HFDDA to model a toughness-dominated Mode I KGD fracture was also considered. In this section, it was demonstrated that the HFDDA was able to match the theoretical results for a toughness-dominated LEFM fracture. The critical observation from this example is that in the HFDDA, the geometry and fluid pressure in the fracture can change solely based upon the system discretization even if the Mohr-Coulomb tensile criteria is held constant. While this trait allows the HFDDA to accurately reflect LEFM models for hydraulic fracturing, it also signifies that the propagation observed in the HFDDA simulation will be a direct function of the mesh size. This trait is somewhat undesirable, as in most numerical methods it is typically expected that the algorithm should converge to a constant solution as the mesh becomes finer.

Taken together, Chapters 3 and 4 thoroughly validate the model and its various components for hydraulic fracturing simulation in homogeneous media. The next step in the study was to extend the model into the simulation of non-homogeneous media characterized by pre-existing natural fracture networks, as discussed in Chapter 5. In this chapter, the interaction mechanisms of propagating fractures with natural fractures were discussed, and shear failure was re-introduced into the analysis to allow for the arrest of hydraulic fractures. A few adjustments were made to the initial algorithm to account for the added complexity of natural fractures, most notably changes to the application of the Augmented Lagrangian Method and an *ad hoc* approach for dealing with contact

oscillation. These changes were validated by using the HFDDA to model a series of experiments performed by Blanton in [68], which examined the effect of differential background stress and angle of approach on the interaction mechanism of intersecting fractures. Next, a method was demonstrated for modeling fracturing in networks of natural fractures within the HFDDA. Each fracture set in a sampled reservoir was defined stochastically using parameter distributions for the length and relative frequency of the fractures, along with a definition of their orientation within the domain. Individual natural fractures were then placed and "grown" along the edges of the triangular mesh until each fracture had reached its assigned length. Various examples of fracture networks simulated using this method were demonstrated, and the impact of different parameters on hydraulic fractures propagating in these networks was studied. In this section, it was found that the results of Blanton's experiments are not generalizable to networks of fractures. For instance, in situations in which no background stress differential was applied to the system, many of the natural fractures were observed to remain closed despite being contacted by fluid. Another observation from this section was that the fluid viscosity and injection rate were of secondary importance to the reservoir parameters in determining the fracture propagation pattern when the rock matrix had significant tensile strength. In these simulations, variation in the fluid parameters led to only negligible variation in the propagation pattern of the hydraulic fracture, while variation in the background stress differential and pre-existing fracture network had a much stronger influence on propagation. Further, it was observed that the background stress differential was of greater importance for determining the propagation pattern than the orientation of the fractures. When the method was applied to a case study of fracturing in the Marcellus

Shale, fracture propagation largely occurred perpendicular to the direction of minimum compressive stress, despite the high density of natural fractures already present in the reservoir. The initial fracture network did, however, cause the fracturing fluid to migrate far from the main fracture, suggesting that natural fractures can significantly widen the footprint of area contacted by the fracturing fluid, even if they are not part of the main fracture.

Each of these results for single hydraulic fractures was further confirmed in the Monte Carlo analysis of fractured systems. For the Monte Carlo simulations, a method was demonstrated for evaluating the likelihood of fracture propagation to any point within a reservoir. It was found that for naturally fractured reservoirs in which the applied differential stress was lower, the reservoir area potentially contacted by the fracture was much greater than that when the applied differential stress was higher. When the stress differential was higher, however, the direction of fracture propagation could be known with greater certainty. Both of these observations are very relevant when selecting a potential location for a new well, depending on if other features in the reservoir need to be contacted or avoided by the propagating fracture. Additionally, the Monte Carlo simulations confirmed that variation in the fluid parameters will not lead to large variations in fracture propagation in impermeable systems with significant tensile strength. When applied to the case study of the Marcellus Shale, the Monte Carlo simulations demonstrated propagation occurring almost exclusively perpendicular to the direction of minimum compressive stress, such that a bi-wing fracture model may be applicable in that system or in others characterized by very high differential stress. Furthermore, the Monte Carlo simulations demonstrated that fracturing fluid can migrate

away from the main fracture with very high likelihood, even if the stress differential in the reservoir is high. As a result, care must be taken when fracturing in highly fractured reservoirs to prevent the leakoff and migration of fracturing fluids into the surrounding formation.

6.2 Limitations of the Study

The primary limitations of this study center around two key areas. First are the limitations of the model itself, and second are the limitations of the insights gleaned over the course of this thesis. Regarding the model itself, while the innovations discussed in this thesis represent a significant improvement to the existing algorithm, some notable issues remain. Of these, the most prominent is the computational time required to simulate systems using the HFDDA. When choosing between explicit vs. implicit models, it is frequently unclear which type of algorithm will ultimately prove faster. With explicit methods, small time steps are required for convergence, but iteration is not required to move the algorithm forward. With implicit methods, however, the time steps used can be large, but the computational time required to move the algorithm forward within each time step will likely be extensive. In this work, it was found that increasing the number of blocks within the mesh drastically increased the time required for simulation once the number of blocks had grown to a certain magnitude. With the desktop computers used for each simulation, meshes of around 2250 blocks would require roughly between 3 to 5 hours of computational time, depending on the specific computer used. Doubling the number of blocks to 4500 required anywhere from 12 to 24 hours of computation time. Notably, the rapid growth in computational requirements makes the use of very fine

meshes computationally infeasible, even when required by the physical problem under consideration. This problem is particularly exacerbated by the Monte Carlo simulations, in which multiple realizations are required to find the likelihood of fracture propagation within the system. Thus, it is questionable how useful the model may be in actual field simulations in which the reservoir domain is relatively large, but fractures must be characterized on a smaller scale.

Limits on the minimum size of elements in the mesh will have two primary impacts on the algorithm. First, as discussed in Chapter 5, the size and location of pre-existing natural fractures are directly affected by the discretization. The technique used to generate natural fractures automatically places limits on their length and density, as any fracture smaller than a joint cannot be modeled, nor can fractures be spaced closer together than the mesh allows. To represent an actual fracture system, the parameters of the fracture network would somehow need to be upscaled to be modeled using the current method. At best, the method developed for characterizing natural fractures serves only as an approximation of the existing fracture system. Secondly, as discussed in Chapter 4, the stress at which fractures are initiated in the HFDDA is influenced by the mesh discretization. The fact that the characteristics of the propagating fracture are dependent on the mesh size is troubling, as the discretization size is tied to a number of other characteristics, including algorithm speed. If the tensile strength and critical stress intensity factor of a system are both established *a priori*, then the discretization must automatically be selected by the relationships used in Chapter 4. As a result, this limitation may result in systems which are computationally infeasible to model if both the tensile strength and the critical stress intensity factor must be considered directly.

Beyond the limitations of the model itself, care must be taken in interpreting the results of the various simulations. In its current form, the HFDDA is able to consider two-dimensional fracturing under plane-strain conditions. Leakoff can be incorporated into the analysis, but the poromechanical response of the rock to the leakoff fluid is not considered, nor is the effect of pore pressure in the interior of the mesh elements considered with regard to flow in the fractures. Furthermore, the transport of proppant and its effects on fluid flow and the ability of the fractures to stay open are not considered. Additionally, there are a myriad of other processes not considered that remain important to the analysis of propagating fractures, including geothermal effects, chemical effects, and added tortuosity from fracture propagation in three dimensions. Incorporation of these processes would change the output of the model, in particular regarding the conclusions drawn for natural fracture networks in Chapter 5. Notably, in this chapter the fluid injection rate and viscosity were found to have very little impact on the fracture propagation pattern observed in each simulation. Had porous flow within the rock mesh been considered, the results likely would have been very different. Additionally, if applying the HFDDA for locating wells in geothermal applications, thermal effects could potentially affect the propagation pattern for the fractures in ways not predicted by the current model. Thus, it is recommended that the HFDDA in its current form only be applied to nearly impermeable reservoirs, in which the processes not considered in the HFDDA are negligible relative to the overall outcome.

6.3 Directions for Future Research

Based on the limitations of the current version of the HFDDA, numerous potential directions exist for future research. First and foremost, research into improving the algorithm's speed would be instrumental to facilitating its widespread use. In particular, a method for optimizing the value of the stability constants used in the coupled rock and fluid equations would lead to significant improvements in computation time. Currently, these constants are assigned through trial-and-error as the user gains experience with the model. Additionally, it would be useful to better understand the properties of these constants, which would allow for better convergence of the algorithm. As mentioned in Chapter 2, the algorithm may fail to converge if the stability constants are too low or too high, and thus an upper and lower bound on the parameters would be very useful. Further areas for future study could be the application of more rapid numerical methods for the solution of the coupled equations, or for improvements in the logic of each algorithm step which requires iteration to converge. On the topic of speed, another area of research would be a direct comparison between the HFDDA and various explicit methods for complex fracture modeling, both to evaluate the relative speed of the algorithms and to determine if the results for each method are similar.

Secondly, refinements are still needed to the logic for the open-close contact iterations and the open-close iterations for the fractures adjacent to fluid. In Chapter 5, it was mentioned that the contacts and fractures open to fluid would occasionally oscillate at the fracture tips when the propagating fracture reached an intersection with numerous natural fractures. To resolve this issue, an *ad hoc* algorithm was implemented that selected the most open state of fractures and subsequently allowed the simulation to

move forward. Ideally, the open-close algorithms would be refined such that these oscillations were either not observed or were treated in a more rigorous manner. Additionally, as mentioned in Chapter 2, vertex-vertex contacts are largely avoided in the current work by allowing them to occur only if the penetration distance of the contact exceeds some pre-defined tolerance. A better solution to this problem would be an implicit form of an area-based algorithm for vertex-vertex contacts, as described for explicit algorithms in [83].

With the algorithm in its current form, the most immediate need is for demonstration of the HFDDA's ability to simulate field-scale applications. As part of this work, a method would need to be developed for upscaling an existing fracture network and redefining it as a system that could be modeled using the mesh limitations within the HFDDA. Alternatively, the HFDDA itself could be used to solve fine-scale fracturing, and the results could somehow be extrapolated to account for the entire reservoir. Either way, however, a method is needed for solving large-scale reservoirs without requiring a fine-scale mesh, as the computational requirements would prove too burdensome for the HFDDA in its current form. Validation against a field-scale fracturing study would come next, after which the model could be used for further parametric studies or for actual field-scale design problems. The final step in the model's development would be the addition of the various processes discussed in Section 6.2. Each of these processes would add to the computational burden of the model, however, and would need to be addressed through further improvements in the algorithm's speed.

6.4 Concluding Remarks

In closing, the research presented in this work represents a significant development in the evolution of hydraulic fracture models. The improvements discussed in this work greatly enhanced the stability and convergence properties of the existing implicit hydraulic fracturing methods based on the DDA, and the validation examples demonstrated for the first time the methods' accuracy. Furthermore, the algorithm developed for modeling stochastic natural fracture networks represents a significant extension of the existing methods, and the insights taken from these studies may prove useful in locating fracturing wells. Ultimately, this work provides better understanding of many of the issues faced in complex network modeling, and can be used as a stepping-stone for further studies of fracture propagation in naturally fractured reservoirs.

REFERENCES

[1] King GE. Hydraulic fracturing 101: what every representative, environmentalist, regulator, reporter, investor, university researcher, neighbor and engineer should know about estimating frac risk and improving frac performance in unconventional gas and oil wells. SPE Hydraulic Fracturing Technology Conference, 6-8 February, 2012. The Woodlands, Texas, USA: Society of Petroleum Engineers; 2012.

[2] Willis-Richards J, Wallroth T. Approaches to the modelling of hdr reservoirs: a review. Geothermics. 1995; 24:307-32.

[3] Adachi J, Siebrits E, Peirce A, Desroches J. Computer simulation of hydraulic fractures. Int J Rock Mech Min Sci. 2007; 44:739-57.

[4] Sneddon IN, Lowengrub M. Crack problems in the classical theory of elasticity. New York: John Wiley and Sons, Inc.; 1969.

[5] Khristianovich SA, Zheltov YP. Formation of vertical fractures by means of highly viscous liquid. 4th World Petroleum Conference, June 6-15, 1955. Rome, Italy: Carlo Colombo; 1955. p.579-86.

[6] Geertsma J, Klerk FD. A rapid method of predicting width and extent of hydraulically induced fractures. J Pet Technol. 1969; 21:1571-81.

[7] Daneshy AA. On the design of vertical hydraulic fractures. J Pet Technol. 1973; 25:83-97.

[8] Perkins TK, Kern, LR. Widths of hydraulic fractures. J Pet Technol. 1961; 13:937-49.

[9] Nordgren RP. Propagation of a vertical hydraulic fracture. Soc Petrol Eng J. 1972; 12:306-14.

[10] Barenblatt GI. The formation of equilibrium cracks during brittle fracture. General ideas and hypotheses. Axially-symmetric cracks. J Appl Math Mech. 1959; 23:622-36.

[11] Abé H, Mura T, Keer LM. Growth rate of a penny-shaped crack in hydraulic fracturing of rocks. J of Geophys Res. 1976; 81:5335-40.

[12] Desroches J, Detournay E, Lenoach B, Papanastasiou P, Pearson JRA, Thiercelin M, et al. The crack-tip region in hydraulic fracturing. Proc R Soc London Ser A-Math Phys Eng Sci. 1994; 447:39-48.

[13] Lenoach B. The crack tip solution for hydraulic fracturing in a permeable solid. J Mech Phys Solids. 1995; 43:1025-43.

[14] Garagash DI, Detournay E. The tip region of a fluid-driven fracture in an elastic medium. J Appl Mech. 1999; 67:183-92.

[15] Detournay E, Garagash DI. The near-tip region of a fluid-driven fracture propagating in a permeable elastic solid. J Fluid Mech. 2003; 494:1-32.

[16] Spence DA, Sharp P. Self-similar solutions for elastohydrodynamic cavity flow. Proc R Soc London Ser A-Math Phys Eng Sci. 1985; 400:289-313.

[17] Hu J, Garagash DI. Plane-strain propagation of a fluid-driven crack in a permeable rock with fracture toughness. J Eng Mech. 2010; 136:1152-66.

[18] Carbonell R, Desroches J, Detournay E. A comparison between a semi-analytical and a numerical solution of a two-dimensional hydraulic fracture. Int J Solids Struct. 1999; 36:4869-88.

[19] Adachi JI, Detournay E. Self-similar solution of a plane-strain fracture driven by a power-law fluid. Int J Numer Anal Methods Geomech. 2002; 26:579-604.

[20] Adachi JI, Detournay E. Plane strain propagation of a hydraulic fracture in a permeable rock. Eng Fract Mech. 2008; 75:4666-94.

[21] Bunger A, Detournay E, Garagash DI. Toughness-dominated hydraulic fracture with leak-off. Int J Fract. 2005; 134:175-90.

[22] Garagash DI. Plane-strain propagation of a fluid-driven fracture during injection and shut-in: asymptotics of large toughness. Eng Fract Mech. 2006; 73:456-81.

[23] Economides MJ, Nolte KG, eds. Reservoir Stimulation. 2nd ed. Englewood Cliffs, New Jersey: Prentice Hall; 1989.

[24] Simonson ER, Abou-Sayed AS, Clifton RJ. Containment of massive hydraulic fractures. Soc Petrol Eng J. 1978; 18:27-32.

[25] Fung RL, Vilayakumar S, Cormack DE. Calculation of vertical fracture containment in layered formations. Soc Petrol Eng Form Eval. 1987; 2:518-22.

[26] Settari A, Cleary MP. Development and testing of a pseudo-three-dimensional model of hydraulic fracture geometry. Soc Petrol Eng Prod Eng. 1986; 1:449-66.

[27] Morales RH, Abou-Sayed AS. Microcomputer analysis of hydraulic fracture behavior with a pseudo-three-dimensional simulator. Soc Petrol Eng Prod Eng. 1989; 4:69-74.

[28] Clifton RJ, Abou-Sayed AS. On the computation of the three-dimensional geometry of hydraulic fractures. SPE Symposium on Low Permeability Gas Reservoirs, 20-22 May, 1979. Denver, Colorado, USA: Society of Petroleum Engineers; 1979.

[29] Advani SH, Lee TS, Lee JK. Three-dimensional modeling of hydraulic fractures in layered media: part I - finite element formulations. J Energ Resour. 1990; 112:1-9.

[30] Siebrits E, Peirce AP. An efficient multi-layer planar 3D fracture growth algorithm using a fixed mesh approach. Int J Num Meth Eng. 2002; 53:691-717.

[31] Warpinski NR, Moschovidis ZA, Parker CD, Abou-Sayed IS. Comparison study of hydraulic fracturing models - test case: GRI staged field experiment no. 3. Soc Petrol Eng Prod Facil. 1994; 9:7-16.

[32] Cleary MP, Kavvadas M, Lam KY. Development of a fully three-dimensional simulator for analysis and design of hydraulic fracturing. SPE/DOE Low Permeability Gas Reservoirs Symposium, 14-16 March, 1983. Denver, Colorado: Society of Petroleum Engineers; 1983.

[33] Lam KY, Cleary MP, Barr DT. A complete three-dimensional simulator for analysis and design of hydraulic fracturing. SPE Unconventional Gas Technology Symposium, 18-21 May, 1986. Louisville, Kentucky: Society of Petroleum Engineers; 1986.

[34] Vandamme L, Curran JH. A three-dimensional hydraulic fracturing simulator. Int J Num Meth Eng. 1989; 28:909-27.

[35] Vandamme L, Jeffrey RG, Curran JH. Pressure distribution in three-dimensional hydraulic fractures. Soc Petrol Eng Prod Eng. 1988; 3:181-6.

[36] Sousa JL, Carter BJ, Ingraffea AR. Numerical simulation of 3D hydraulic fracture using newtonian and power-law fluids. Int J Rock Mech Min Sci. 1993; 30:1265-71.

[37] Carter B, Desroches J, Ingraffea A, Wawrzynek P. Simulating fully 3D hydraulic fracturing. In: Zaman M, Booker J, Gioda G, editors. Modeling in Geomechanics. New York: Wiley Publishers; 2000.

[38] Group SG. On the modelling of near tip processes in hydraulic fractures. Int J Rock Mech Min Sci. 1993; 30:1127-34.

[39] Hossain MM, Rahman MK. Numerical simulation of complex fracture growth during tight reservoir stimulation by hydraulic fracturing. J Pet Sci Eng. 2008; 60:86-104.

[40] Boone TJ, Ingraffea AR. A numerical procedure for simulation of hydraulically-driven fracture propagation in poroelastic media. Int J Numer Anal Methods Geomech. 1990; 14:27-47.

[41] Hagoort J. Modeling the propagation of waterflood-induced hydraulic fractures. Soc Petrol Eng J. 1980; 20:293-303.

[42] Settari A. Simulation of hydraulic fracturing processes. Soc Petrol Eng J. 1980; 20:487-500.

[43] Nghiem LX, Forsyth Jr PA, Behie A. Fully implicit hydraulic fracture model. J Pet Technol. 1984; 36:1191-8.

[44] Ji L, Settari A, Sullivan RB. A novel hydraulic fracturing model fully coupled with geomechanics and reservoir simulation. Soc Petrol Eng J. 2009; 14:423-30.

[45] Ghassemi A, Zhou XX, Rawal C. A three-dimensional poroelastic analysis of rock failure around a hydraulic fracture. J Pet Sci Eng. 2013; 108:118-27.

[46] Secchi S, Schrefler BA. A method for 3-D hydraulic fracturing simulation. Int J Fract. 2012; 178:245-58.

[47] Secchi S, Simoni L, Schrefler BA. Mesh adaptation and transfer schemes for discrete fracture propagation in porous materials. Int J Numer Anal Methods Geomech. 2007; 31:331-45.

[48] Camacho GT, Ortiz M. Computational modelling of impact damage in brittle materials. Int J Solids Struct. 1996; 33:2899-938.

[49] Li LC, Tang CA, Li G, Wang SY, Liang ZZ, Zhang YB. Numerical simulation of 3D hydraulic fracturing based on an improved flow-stress-damage model and a parallel FEM technique. Rock Mech Rock Eng. 2012; 45:801-18.

[50] Tang CA. Numerical simulation on progressive failure leading to collapse and associated seismicity. Int J Rock Mech Min Sci. 1997; 34:249-61.

[51] Baumgartner J, Zoback MD. Interpretation of hydraulic fracturing pressure time records using interactive analysis methods. Int J Rock Mech Min Sci. 1989; 26:461-9.

[52] Gu H, Weng X, Lund JB, Mack MG, Ganguly U, Suarez-Rivera R. Hydraulic fracture crossing natural fracture at nonorthogonal angles: a criterion and its validation. Soc Petrol Eng Prod Oper. 2012; 27:20-6.

[53] Kresse O, Weng X, Gu H, Wu R. Numerical modeling of hydraulic fracture interaction in complex naturally fractured formations. Rock Mech Rock Eng. 2013; 46:555-68.

[54] Weng X, Kresse O, Cohen CE, Wu R, Gu H. Modeling of hydraulic-fracture-network propagation in a naturally fractured formation. Soc Petrol Eng Prod Oper. 2011; 26:368-80.

[55] Olson J, Dahi-Taleghani A. Modeling simultaneous growth of multiple hydraulic fractures and their interaction with natural fractures. SPE Hydraulic Fracturing Technology Conference, 19-21 January, 2009. The Woodlands, Texas, USA: Society of Petroluem Engineers; 2009.

[56] Crouch S, Starfield A. Boundary Element Methods in Solid Mechanics: With Applications in Rock Mechanics and Geological Engineering. London: George Allen & Unwin; 1983.

[57] Cipolla CL, Weng X, Mack MG, Ganguly U, Gu H, Kresse O, et al. Integrating microseismic mapping and complex fracture modeling to characterize hydraulic fracture complexity. SPE Hydarulic Fracturing Technology Conference, 24-26 January 2011. The Woodlands, Texas: Society of Petroleum Engineers; 2011.

[58] Du C, Zhang X, Zhan L, Gu H, Hay B, Tushingham K, et al. Modeling hydraulic fracturing induced fracture networks in shale gas reservoirs as a dual porosity system. CPS/SPE International Oil & Gas Conference and Exhibition. Beijing, China. 2010.

[59] Rogers SF, Elmo D, Dershowitz WS. Understanding hydraulic fracture geometry and interactions in preconditioning through DFN and numerical modeling. 45th US Rock Mechanics / Geomechanics Symposium, 26-29 June, 2011. San Francisco, California, USA: American Rock Mechanics Association; 2011.

[60] Smith J, Durucan S, Korre A, Shi JQ. Carbon dioxide storage risk assessment: Analysis of caprock fracture network connectivity. Int J Greenhouse Gas Control. 2011; 5:226-40.

[61] Schlumberger. ECLIPSE Technical Description Manual. 2007.

[62] Zhang X, Jeffrey RG, Thiercelin M. Deflection and propagation of fluid-driven fractures at frictional bedding interfaces: a numerical investigation. J Struct Geol. 2007; 29:396-410.

[63] Zhang X, Jeffrey RG, Thiercelin M. Escape of fluid-driven fractures from frictional bedding interfaces: a numerical study. J Struct Geol. 2008; 30:478-90.

[64] Dahi-Taleghani A, Olson J. Numerical modeling of multi-stranded hydraulic fracture propagation: accounting for the interaction between induced and natural fractures. SPE Annual Technical Conference and Exhibition, 4-7 October, 2009. New Orleans, Louisiana, USA: Society of Petroleum Engineers; 2009.

[65] Fu P, Johnson SM, Carrigan CR. An explicitly coupled hydro-geomechanical model for simulating hydraulic fracturing in arbitrary discrete fracture networks. Int J Numer Anal Methods Geomech. 2013; 37:2278-300.

[66] Fu P, Johnson SM, Hao Y, Carrigan CR. Fully coupled geomechanics and discrete flow network modeling of hydraulic fracturing for geothermal applications. Thirty-Sixth Workshop on Geothermal Reservoir Engineering, 31 January – 2 February. Stanford University, Stanford California. 2011.

[67] Fu P, Johnson SM, Settgast RR, Carrigan CR. Generalized displacement correlation method for estimating stress intensity factors. Eng Fract Mech. 2012; 88:90-107.

[68] Blanton TL. An experimental study of interaction between hydraulically induced and pre-existing fractures. SPE Unconventional Gas Symposium, 16-18 May, 1982. Pittsburgh, Pennsylvania: Society of Petroleum Engineers; 1982.

[69] Galindo Torres SA, Muñoz Castaño JD. Simulation of the hydraulic fracture process in two dimensions using a discrete element method. Physical Review E. 2007; 75:1-9.

[70] Nagel NB, Gil I, Sanchez-nagel M, Damjanac B. Simulating hydraulic fracturing in real fractured rocks - overcoming the limits of pseudo3D models. SPE Hydraulic Fracturing Technology Conference, 24-26 January. The Woodlands, Texas USA: Society of Petroleum Engineers; 2011.

[71] Ben YX, Xue J, Miao Q, Wang Y, Shi GH. Simulating hydraulic fracturing with discontinuous deformation analysis. 46th US Rock Mechanics / Geomechanics Symposium, 24-27 June, 2012. Chicago, IL, USA: Curran Associates, Inc.; 2012. p. 683-90.

[72] Ben YX, Wang Y, Gen-hua S. Development of a model for simulating hydraulic fracturing with DDA. In: Guangqi C, Ohnishi Y, Zheng L, Sasaki T, editors. Frontiers of Discontinuous Numerical Methods and Practical Simulations in Engineering and Disaster Prevention, 27-29 August, 2013. Kukuoka, Japan: CRC Press; 2013. p. 169-75.

[73] Ben YX, J.; Miao, Q.; Wang, Y. Coupling fluid flow with discontinuous deformation analysis. In: Zhao J, Ohnishi Y, Zhao GF, Sasaki T, editors. Advances in Discontinuous Numerical Methods and Applications in Geomechanics and Geoengineering: CRC Press; 2010. p. 107-12.

[74] Shi GH. Discontinuous deformation analysis: A new numerical model for the statics and dynamics of block systems. Berkeley, California: University of California, Berkeley; 1988.

[75] Jing L, Ma Y, Fang Z. Modeling of fluid flow and solid deformation for fractured rocks with discontinuous deformation analysis (DDA) method. Int J Rock Mech Min Sci. 2001; 38:343-55.

[76] Brebbia C, Ferrante A. Computational Hydraulics. London: Butterworth & Co.; 1983.

[77] MacLaughlin M, Sitar N, Doolin D. DDA for Windows. Berkeley, California: University of California, Berkeley; 2004.

[78] Bobet A, Fakhimi A, Johnson S, Morris J, Tonon F, Yeung MR. Numerical models in discontinuous media: review of advances for rock mechanics applications. J Geotech Geoenviron Eng. 2009; 135:1547-61.

[79] Lin CT, Amadei B, Jung J, Dwyer J. Extensions of discontinuous deformation analysis for jointed rock masses. Int J Rock Mech Min Sci. 1996; 33:671-94.

[80] Bao H, Zhao Z, Tian Q. On the implementation of augmented lagrangian method in the two-dimensional discontinuous deformation analysis. Int J Numer Anal Methods Geomech. 2014; 38:551-71.

[81] Doolin DM, Sitar N. Displacement accuracy of discontinuous deformation analysis method applied to sliding block. J Eng Mech. 2002; 128:1158-68.

[82] Ke TC, Bray J. Modeling of particulate media using discontinuous deformation analysis. J Eng Mech. 1995; 121:1234-43.

[83] Feng YT, Han K, Owen DRJ. Energy-conserving contact interaction models for arbitrarily shaped discrete elements. Comput Method Appl M. 2012; 205–208:169-77.

[84] Bao H, Zhao Z. An alternative scheme for the corner-corner contact in the two-dimensional discontinuous deformation analysis. Adv Eng Softw. 2010; 41:206-12.

[85] Bao H, Zhao Z. The vertex-to-vertex contact analysis in the two-dimensional discontinuous deformation analysis. Adv Eng Softw. 2012; 45:1-10.

[86] Kim Y-I, Amadei B, Pan E. Modeling the effect of water, excavation sequence and rock reinforcement with discontinuous deformation analysis. Int J Rock Mech Min Sci. 1999; 36:949-70.

[87] Rubin MB. Experimental study of hydraulic fracturing in an impermeable material. J Energ Resour. 1983; 105:116-24.

[88] Delft University of Technology. PMMA, IDEMAT 2003 database. Delft Univ Tech, Netherlands, 2003.

[89] Dow Corning. Dow Corning 200 fluid product information. 1999.

[90] Shewchuk JR. Triangle. Berkeley, California: University of California, Berkeley; 2005.

[91] Tada H, Paris PC, Irwin GR. The stress analysis of cracks handbook. 3rd ed: American Society of Mechanical Engineers; 2000.

[92] Dugdale DS. Yielding of steel sheets containg slits. J Mech Phys Solids. 1960; 8:100-4.

[93] Williams JG, Hadavinia H. Analytical solutions for cohesive zone models. J Mech Phys Solids. 2002; 50:809-25.

[94] Xie D, Waas AM. Discrete cohesive zone model for mixed-mode fracture using finite element analysis. Eng Fract Mech. 2006; 73:1783-96.

[95] Jiao YY, Zhang XL, Zhao J. Two-dimensional DDA contact constitutive model for simulating rock fragmentation. J Eng Mech. 2012; 138:199-209.

[96] Potyondy DO, Cundall PA. A bonded-particle model for rock. Int J Rock Mech Min Sci. 2004; 41:1329-64.

[97] Anderson TL. Fracture mechanics: fundamentals and applications. Boca Raton, Florida: CRC Press; 1991.

[98] United States Energy Information Administration. Marcellus Region Drilling Productivity Report. 2014.

[99] Engelder T, Lash GG, Uzcategui RS. Joint sets that enhance production from Middle and Upper Devonian gas shales of the Appalachian Basin. AAPG Bull. 2009;93:857-89.

[100] Milici RC. Assessment of undiscovered natural gas resources in Devonian black shales, Appalachian Basin, Eastern USA. United States Geological Survey; 2005.

[101] Warpinski NR, Teufel LW. Influence of geologic discontinuities on hydraulic fracture propagation. J Pet Technol. 1987; 39:209-20.

[102] Zhou J, Chen M, Jin Y, Zhang GQ. Analysis of fracture propagation behavior and fracture geometry using a tri-axial fracturing system in naturally fractured reservoirs. Int J Rock Mech Min Sci. 2008;45:1143-52.

[103] Renshaw CE, Pollard DD. An experimentally verified criterion for propagation across unbounded frictional interfaces in brittle, linear elastic materials. Int J Rock Mech Min Sci. 1995; 32:237-49.

[104] United States Gypsum Company. Hydrostone gypsum cement product data. 1999.

[105] Guo F, Morgenstern NR, Scott JD. An experimental investigation into hydraulic fracture propagation - part 2. single well tests. Int J Rock Mech Min Sci. 1993; 30:189-202.

[106] Blanton TL, Dischler SA, Patti NC. Mechanical Properties of Devonian Shales from the Appalachian Basin. In: Science Applications I, editor. Eastern Gas Shales Project1981.

[107] Dusseault MB. Geomechanical aspects of shale gas development. In: Kwasniewski M, Lydzba D, editors. Rock Mechanics for Resources, Energy and Environment. London, UK: Taylor & Francis Group; 2013.